UNIVERSIDAD COMPLUTENSE DE MADRID

FACULTAD DE CIENCIAS QUÍMICAS
Departamento de Química Física I

TESIS DOCTORAL

Simulación por ordenador de materia condensada: nuevos modelos de agua, cálculo de propiedades y procesos de nucleación

MEMORIA PARA OPTAR AL GRADO DE DOCTOR

PRESENTADA POR

Miguel Ángel González González

Directores

José Luis Fernández Abascal
Chantal Valeriani

Madrid, 2015

Universidad Complutense de Madrid
Facultad de Ciencias Químicas
Departamento de Química Física I

Simulación por ordenador de materia condensada: Nuevos modelos de agua, cálculo de propiedades y procesos de nucleación

Memoria para optar
al grado de Doctor en Ciencias Químicas
realizada por

Miguel Ángel González González

Directores:
Prof. José Luis Fernández Abascal
Dra. Chantal Valeriani

Dpto. Química-Física I

Madrid, 2014

The work in this thesis is based on the following publications:

Results: Chapter 1

Anomalies in water as obtained from computer simulations of the TIP4P/2005 model: density maxima, density, and isothermal compressibility and heat capacity minima.

Helena L. Pi, Juan L. Aragones, Carlos Vega, Eva G. Noya, Jose L. F. Abascal, Miguel A. Gonzalez and Carl McBride.

Mol. Phys., **107**, 365, (2009).

Results: Chapter 2

The shear viscosity of rigids water models.

Miguel A. Gonzalez and Jose L. F. Abascal.

J. Chem. Phys., **132**, 096101, (2010).

Results: Chapter 3

A flexible model for water based on TIP4P/2005.

Miguel A. Gonzalez and Jose L. F. Abascal.

J. Chem. Phys., **135**, 224516, (2011).

Results: Chapter 5

Anomalies in bulk supercooled water at negative pressure.

Gaël Pallares, Mouna El Mekki Azouzi, Miguel A. Gonzalez, Juan L. Aragones, Jose L. F. Abascal, Chantal Valeriani and Frédéric Caupin.

PNAS, **111**, 11, xxxx, (2014).

Results: Chapter 6

Homogeneous bubble nucleation in water at negative pressure: A Voronoi polyhedra analysis.

Jose L. F. Abascal, Miguel A. Gonzalez, Juan L. Aragones and Chantal Valeriani.

J. Chem. Phys., **138**, 084508, (2013).

Results: Chapter 7

Detecting bubbles in water at negative pressure.

Miguel A. Gonzalez, Georg Menzl, Juan L. Aragones, Philipp Geiger, Gael Pallares, Mouna El Mekki Azouzi, Frederic Caupin, Jose L. F. Abascal, Christoph Dellago and Chantal Valeriani.

In preparation.

Results: Chapter 8

Spontaneous bubble nucleation in simple and molecular liquids studied with the largest spherical cavity.

Miguel A. Gonzalez, Jose L. F. Abascal, Chantal Valeriani and Fernando Bresme.

In preparation.

Other publications not in the thesis:

Determining the phase diagram of water from direct coexistence simulations: The phase diagram of the TIP4P/2005 model revisited the TIP4P/2005.
Maria M. Conde, Miguel A. Gonzalez, Jose L. F. Abascal and Carlos Vega.
J. Chem. Phys., **139**,154505, (2013).

Nucleation free-energy barriers using Hybrid Monte Carlo/Umbrella Sampling.
Miguel A. Gonzalez, Eduardo Sanz, Carl McBride, Jose L. F. Abascal, Carlos Vega and Chantal Valeriani.
In preparation.

Índice general

Resumen

Introducción

El agua es una de las moléculas más comunes e importantes para la vida. Esta molécula es una sustancia abundante en la Tierra, que encontramos continuamente en nuestro entorno en forma sólida, líquida y gaseosa. Desde un punto de vista global el papel del agua es importante en la morfología de nuestro planeta. La erosión de ríos y de glaciares ha esculpido poco a poco el relieve de la corteza terrestre. Por otro lado, la presencia de nubes, vapor de agua, hace que la climatología y los procesos en la atmósfera se produzcan de una forma concreta. Destacar también que el agua es considerada el disolvente universal, ya que forma parte como medio de reacción en infinidad de reacciones químicas y sobre todo como medio en el que se desarrolla la vida.

Durante muchos años se han determinado sus propiedades químico-físicas y todavía sigue siendo objeto de estudio. Bernal y Fowler en 1933 fueron los primeros en proponer un modelo unificado de agua líquida, es decir, antes se creía que existían distintos tipos de agua que se mezclaban formando el líquido. Ellos explican las propiedades del líquido a través de un solo modelo basado en el hielo Ih (hielo hexagonal). La estructura de este hielo, el hielo común, tiene una geometría tetraédrica, en la cual una molécula de agua se une a cuatro moléculas vecinas a través de enlaces de hidrógenos. El modelo de Bernal y Fowler mantiene los tetraedros del hielo pero en el líquido se produce una distorsión de los ángulos y distancias de la geometría tetraédrica. Otro aspecto importante del trabajo de Bernal y Fowler es que se trata de una teoría molecular, que explica propiedades macroscópicas a partir de elementos microscópicos. Este planteamiento sólo se puede demostrar a través de la Mecánica Estadística, y más concretamente utilizando la **Simulación Molecular** para comprobar la validez de su modelo. Las bases de esta ciencia se desarrollaron en 1953 por Metropolis *et al.*[1] proponiendo el método de Monte Carlo, y seis años más tarde, Alder y Wainwright[2] presentaron el método de Dinámica Molecular que completa las dos principales técnicas de Simulación Molecular. Las primeras simula-

ciones con modelos de agua fueron realizadas en 1969 por Barker y Watts[3] y en 1971 por Rahman y Stillinger[4] terminaron de consolidar la simulación de este tipo de sistemas. A partir de esos avances la simulación del agua ha crecido exponencialmente. De forma paralela, se han desarrollaron distintos tipos de modelos de agua para reproducir sus propiedades macroscópicas. Los más utilizados son los **modelos rígidos y no polarizables**, porque la relación entre el coste computacional y los resultados obtenidos es óptima. Los más populares son TIP3P[5], SPC/E[6], TIP4P[5], TIP4P/Ew[7], TIP4P/2005[8], TIP4P/ice[9], TIP5P[10], mW[11] y CCM[12], estos dos últimos modelos son igual de famosos pero son modelos de *coarse grained*.

El agua en estado líquido muestra a veces un comportamiento diferente del de la mayoría de los líquidos. Se dice por ello que el agua presenta **anomalías en las propiedades termodinámicas**. Por ejemplo, se presentan mínimos y máximos en las funciones respuesta, como C_V (la capacidad calorifica a volumen constante) o κ_T (la compresibilidad isoterma a temperatura constante). Aunque el ejemplo más claro y conocido es el máximo de densidad que se produce en el agua a 4 ^{o}C y 1 bar. Estas anomalías son mucho más evidentes cuando disminuimos la temperatura o entramos en la región de las presiones negativas. Podemos llamar a esta región del diagrama de fases como región de condiciones extremas. Existe un límite experimental que dificulta el avance en el estudio de las propiedades anómalas del agua líquida: por un lado, cuando se subenfría el agua, ésta acaba transformandose en hielo; por el otro, a presiones negativas el agua líquida termina cavitando (transformandose en vapor). En este punto es donde la Simulación Molecular se hace imprescindible. En simulación no tenemos esos problemas porque los tiempos que se manejan en Dinámica Molecular y Monte Carlo, son suficientes para caracterizar el sistema en condiciones de metaestabilidad. Por lo tanto podremos obtener información relevante sobre el agua metaestable en la region de condiciones extremas, siempre y cuando la Simulación Molecular se lleve a cabo con un modelo de agua robusto y fiable. En nuestras simulaciones, se ha elegido principalmente el modelo de potencial de agua TIP4P/2005.

Es posible simular distintos estados termodinámicos y el comportamiento de las propiedades termodinámicas anómalas del TIP4P/2005 para construir su escenario termodinámico. Llamamos **escenario termodinámico** de una sustancia al plano $p-T$ donde se representan los puntos críticos y triple, las líneas de transición de fase y los lugares geométricos de los máximos y mínimos de las funciones respuesta que presentan anomalías en su comportamiento. Una vez calculado el escenario termodinámico por simulación, es posible compararlo con posibles escenarios propuestos en la literatura. En la Fig 1, cada escenario está explicado en el pie de figura de la misma. Cada uno de ellos ofrece una explicación para las anomalías del agua y por esto es muy

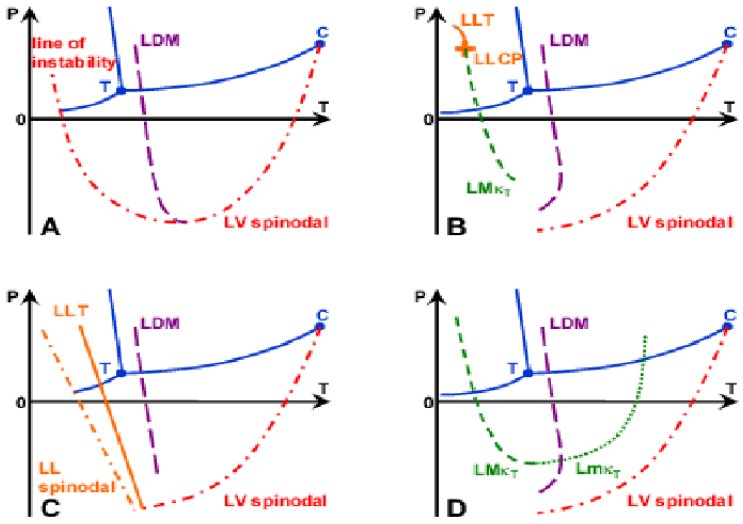

Figura 1: Los cuatro escenarios propuestos en la literatura para explicar las anomalías del agua. En todos ellos nos encontramos con las líneas de equilibrio entre las fases sólido, líquido y vapor (líneas azules), sobre ellas están representados el punto crítico líquido-vapor (C) y el punto triple liquid-vapor-solido (T) , la curva morada y discontinua corresponde a la línea de TMD, temperatura de máxima densidad o LDM, linea de máximos de densidad, la línea roja se ha utilizado en la representación de la espinodal líquido-vapor (LV spinodal). En el escenario A[13], nos encontramos con una espinodal reentrante que aparece a presiones positivas a bajas temperaturas. El escenario B[14], añade un punto crítico líquido-líquido (LLCP) representado por una cruz naranja, la línea de transición líquido-líquido (LLT) corresponde a la línea continua naranja, por último la línea de Widon de la compresibilidad isoterma es la curva verde discontinua. El tercer escenario C[15,16,17] está caracterizado por la línea continua y naranja de la transición líquido-líquido (LLT), con el mismo color pero discontinua tenemos la espinodal líquido-líquido (LL spinodal). Por último el escenario D[18] contempla una prolongación de la línea de Widom, continuando con los mínimos de κ_T, marcados con la línea de puntos.

importante demostrar tanto con datos experimentales como de simulación la validez de cada escenario para el agua

En cada escenario termodinámico nos encontramos con la línea de coexistencia líquido-vapor, también llamada como binodal. Cruzando esta línea se produce una transición de fase de primer orden desde la fase metaestable hacia la nueva fase termodinámicamente estable (fase vapor). Esta transformación se produce en dos etapas, nucleación de los embriones de la nueva

fase y su crecimiento. La **nucleación** es el proceso estocástico de generación de embriones de la nueva fase dentro de la fase metaestable. Este proceso es activado y viene descrito por tres variables característicos: el máximo de la barrera de energía libre, el núcleo crítico y la tasa de nucleación. El máximo de la barrera, ΔG^*, es la energía libre necesaria para poder llevar a cabo la transformación (para que se forme un nucleo crítico de la nueva fase) y la tasa de nucleación, J, es el número de núcleos críticos generados por unidad de volumen y tiempo.

La teoría más utilizada para describir este proceso es la **Teoría Clásica de Nucleación**, (CNT, de las siglas en inglés Classical Nucleation Theory). Fue desarrollada por Volmer y Weber[19] en 1926 y su desarollo está basado en la transición de fase vapor-líquido. Desde un vapor sobreenfriado (fase metaestable) se estudia la condensación de una gota líquida (fase estable), aplicando la formulación para el trabajo reversible de la formación de los núcleos de líquido dentro de la fase metaestable. Existen modificaciones y mejoras de esta teoría, como la de Becker y Döring[20] o la combinación con la Teoría de Funcional de Densidad por parte de Cahn y Hillard[21,22]. Estas mejoras hacen que los resultados obtenidos se puedan extrapolar a otro tipo de transiciones (como la liquido-solido) que sean comparables con los datos experimentales.

Los datos de simulación se comparan también con los valores obtenidos con la CNT, pero tanto comparando con experimentos como comparando con CNT, suele existir una discrepancia con los resultados numéricos. Esto se debe a que los tamaños que se manejan en simulación son menores a las muestras macroscópicas. Por ejemplo, la tensión superficial que se utiliza en CNT es la calculada para una superficie plana mientras que en la simulación no tenemos esta geometría en la interfase (porque el núcleo que crece suele tener simetría aproximadamente esférica). Sin embargo, la ventaja de la utilización de la Simulación Molecular compensa estas diferencias, ya que permite el estudio directo del mecanismo molecular que interviene en el proceso de nucleación.

Las técnicas más utilizada para el estudio de la nucleación se pueden dividir en dos grupos: técnicas para procesos de nucleación espontánea y técnicas para eventos raros. Cuando la barrera de energía libre es pequeña, el sistema es capaz de cruzarla y transformarse en la nueva fase: a este hecho le llamamos proceso de nucleación espontánea. La nucleación de este tipo de procesos se estudia por medio de métodos concretos como la técnica *Mean First Passage Time*[23,24,25], (MFPT). Consiste en analizar el primer tiempo de aparición del núcleo más grande de tamaño n dentro de la fase metaestable, siendo n el número de partículas del núcleo. A partir del análisis de estos tiempos se llegan a obtener los parámetros de nucleación: la tasa de nuclea-

ción, el tamaño del núcleo crítico y la altura de la barrera de nucleación.

En el caso de estudiar la nucleación de eventos raros, es decir, cuando el sistema no es capaz de cruzar la barrera de energía libre porque es demasiado alta, es necesario utilizar otro tipo de técnicas. Como ejemplo de estas técnicas tenemos el método Bennett-Chandler[26,27] Este método se divide en dos pasos: en primer lugar se calcula la probabilidad de que en el sistema aparezca un núcleo crítico en equilibrio con la fase metaestable que lo rodea o que el sistema alcance el maximo de la barrera de energía libre, $\Delta G(n^*)$, y luego se calcula el prefactor cinético, $\kappa(n^*)$, del proceso, obteniéndose la tasa de nucleación por combinación de ambos parámetros, según la relación siguiente,

$$J = \kappa(n^*)P(n^*) = \kappa(n^*)e^{-\beta\Delta G(n^*)}, \tag{1}$$

El valor del máximo de la barrera se puede conseguir a través del método *Umbrella Sampling*[28,29], que se basa en muestrear de forma sesgada el tamaño del núcleo más grande del sistema. Es decir, se favorece el crecimiento del núcleo más grande hasta que sobrepasa el valor crítico y se completa la nucleación. Una vez que conocemos $\Delta G(n^*)$ y el correspondiente n^*, podemos calcular el prefactor cinético, haciendo un estudio de la evolución del núcleo crítico en el máximo de la barrera respecto del tiempo. De este modo, podemos obtener la tasa de nucleación y describir el evento de nucleación.

En nuestra investigación hemos utilizado todas estas herramientas, MFPT y *Umbrella Sampling*, para estudiar la nucleación de burbujas en el agua metaestable a presiones negativas. Como modelo de potencial de agua hemos usado el TIP4P/2005, el mismo que se usa para describir el escenario termodinámico en condiciones extremas en esta memoria.

Objetivos

Cuando nos planteamos realizar el trabajo predoctoral los objetivos era:

1. Encontrar los límites del modelo TIP4P/2005, desarrollado por Abascal y Vega. Para ello se estudió el comportamiento anómalo de las propiedades termodinámicas del agua. Tanto de propiedades estáticas como dinámicas. Reproducir este comportamiento, no sólo implicaba el problema de la precisión del modelo para mostrar esos máximos o mínimos, sino que para encontrarlos debemos simular en condiciones extremas de presión y temperatura, zona sobreenfriada del agua y presiones negativas. La unión de estas dos condiciones hacen que el estudio sea complicado.

2. Desarrollar nuevos modelos con la misma robustez que el TIP4P/2005 y que mejoren los valores de las propiedades que este modelo predice peor: la temperatura de cristalización a 1 bar es de 252 K, 21 grados por debajo del valor experimental y la constante dieléctrica ($\varepsilon/\varepsilon_0$) del modelo es 57,3, un valor menor al 78,4 experimental.

3. Estudiar el fenómeno de la nucleación de burbujas en agua a presiones negativas. Existen estudios de nucleación de líquidos simples como el Lennard-Jones, de condensación[23,24], de cavitación[30,31,32], de cristalización[33,34] e incluso cavitación a presiones negativas[35,36,37]. Pero los estudios de este tipo para el caso del agua son muy pocos y todos orientados a la condensación del agua[38,39] y nunca a la formación de burbujas. Tampoco se han descrito técnicas para determinar y analizar burbujas en un sistema como el agua. Por todas estas razones se hacía imprescindible abordar el estudio de este fenómeno.

Los dos primeros objetivos estaban bien marcados desde el inicio del trabajo predoctoral. Nos propusimos seguir la linea de investigación del grupo, poniendo a prueba el modelo desarrollado en el grupo, reproduciendo el comportamiento anómalo del agua en condiciones extremas. Después de cuatro años de trabajos sobre el TIP4P/2005 y con el espíritu de avanzar y mejorar también se tenía pensado el desarrollo de nuevos modelos de agua para suplir las desventajas del modelo predecesor. Teniendo en cuenta que es un modelo rígido y no polarizable, el primer paso lógico ha sido incorporar la flexibilidad. Esta incorporación debía mantener los buenos resultados del modelo original y mejorar en lo posible las desventajas del mismo.

El tercer objetivo surgió de forma natural durante el trabajo del candidato. Cuando se construyó el escenario termodinámico del TIP4P/2005, se delimitó el límite estable del modelo (línea espinodal líquido-vapor), y nos encontramos con la nucleación espontánea del sistema a presiones negativas. Por lo tanto era necesario su estudio para continuar conociendo el comportamiento del agua.

El estudio se enfocó en la nucleación homogénea de burbujas en agua a presiones negativas, pero se ha avanzado también en un estudio preliminar de nucleación de burbujas a presiones negativas en sistemas heterogéneos (agua + nanotubos de carbono) donde se calcula la tasa de nucleación de diferentes sistemas.

Resultados

Basándonos en los objetivos marcados en el apartado anterior, hemos realizado un estudio exhaustivo de la termodinámica y nucleación de burbujas en agua en condiciones extremas. El modelo de potencial de agua que se ha utilizado durante todo el trabajo predoctoral ha sido el TIP4P/2005. Además ha sido desarrollado el modelo flexible TIP4P/2005f como trabajo del candidato y cuyos resultados resumiremos a continuación. De forma global los resultados en esta memoria se pueden presentar en tres diferentes bloques:

A. **Cálculo de las propiedades anómalas del agua y construcción del escenario termodinámico del modelo.**

   Los capítulos de resultados 1, 2, 4 y 5 forman este bloque. En el primero de ellos se simula el comportamiento anómalo de una serie de propiedades termodinámicas. En el Capítulo 2, se hace un estudio de la reproducibilidad del modelo cuando se calcula la viscosidad, una propiedad dinámica. La elaboración del escenario termodinámico del modelo se llevó a cabo en el Capítulo 4, donde se completaron los datos de la literatura teniendo en cuenta toda la región de presiones negativas. Por ultimo y apoyando estos datos de simulación se presenta el Capítulo 5 con datos experimentales de agua *bulk* a presiones negativas. El estudio experimental ha sido llevado a cabo en el Laboratorio del Prof. Caupin de la Universidad de Lyon. Se midió la velocidad del sonido en dos isócoras a lo largo de una región amplia de temperaturas y se observó un mínimo en los valores de la velocidad del sonido. Este mínimo se corresponde termodinámicamente al máximo de compresibilidad isoterma en la región de presiones negativas y zona sobreenfriada del agua. Los datos experimentales han sido avalados por nuestros datos de simulación que reproducen este comportamiento en las isócoras.

B. **Desarrollo de un nuevo modelo flexible de potencial de agua, TIP4P/2005f.**

   El bloque está formado por el capítulo de resultados número 3. En este artículo se calculan los parámetros moleculares óptimos para un modelo del agua flexible basandonos en las propiedades del TIP4P/2005. A continuación, se calcula una amplia lista de propiedades termodinámicas, con las cuales se describe el potencial del modelo. Este modelo mantiene el nivel de robustez del modelo, TIP4P/2005 y es idóneo para simulaciones donde la flexibilidad se hace imprescindible, como en el caso de estudios espectroscópicos. Además se presenta un método para

ajustar los parámetros de flexibilidad molecular, basado en el espectro de densidades de población.

C. **Estudio de la nucleación de burbujas en agua a presiones negativas.**

Este bloque está formado por el resto de capítulos de resultados: 6, 7, 8 y 9. En el primero de ellos se presenta un método para localizar y analizar burbujas en agua. Este método se basa en el algoritmo de los poliedros de Voronoi. Se analizaron burbujas en distintos entornos termodinámicos, tanto en fases metaestables como inestables. Además se estudió la nucleación espontánea de un estado termodinámico concreto, calculando la tasa de nucleación y el tamaño del núcleo crítico del proceso.

En el Capítulo 7, se describen dos métodos alternativos al presentado en el capítulo anterior, produciendo resultados similares. Estos dos métodos son utilizados para estudiar el mismo estado termodinámico. Además se analiza otro estado donde no se produce la nucleación espontánea y es necesario utilizar las técnicas de eventos raros para nucleación, más concretamente el *Umbrella Sampling*. Cada método fue diseñado por un grupo de investigación diferente: uno se desarrolló en el grupo del que forma parte el candidato y el otro fue propuesto por el grupo de investigación del Prof. Dellago de la Universidad de Viena. En este capítulo se presentan los resultados de la colaboración de los dos grupos. El Capítulo 8, presenta el trabajo durante la colaboración con el Prof. Bresme del Imperial College London, que ha sido posible gracias a dos becas: una del proyecto HPC-Europa2 y otra del Thomas Young Center. En el grupo del Prof. Bresme se desarrolló otro método para el mismo fin, basado en la localización de la cavidad más grande del sistema y su seguimiento en el proceso de nucleación. Una ventaja de este nuevo método es la posibilidad de combinarlo con la *Scaled Particle Theory*[40,41] lo cual nos facilita el cálculo de la barrera de nucleación, aspecto que podria ser más complicado en los anteriores métodos.

El último capítulo de este bloque y de la tesis, Cap. 9, corresponde con los resultados de un estudio preliminar que se ha llevado a cabo sobre nucleación de burbujas en un sistema heterogéneo. Esa heterogeneidad en el sistema la obtenemos por la presencia de nanotubos de carbono de capa simple. Las condiciones de simulación son similares a los otros estudios, presiones negativas y zona sobreenfriada del agua. En esta ocasión se calculó la tasa de nucleación y se comparó con el mismo

sistema homogéneo obteniendo resultados preliminares coherentes.

Conclusiones

El modelo de agua TIP4P/2005 es capaz de reproducir y predicir propiedades termodinámicas en condiciones extremas, tanto valores absolutos como tendencias y comportamientos en amplios rangos de presión y temperatura. Es sensible a ligeros cambios que producen máximos y mínimos en las funciones respuesta y en la línea de densidad máxima. La representación en el plano $p-T$ de este comportamiento permite construir el escenario termodinámico del modelo. Este hecho, es sumamente importante porque apoya activamente un tipo de escenario que explica las anomalías del agua. Además, y confirmando la robustez y fiabilidad del modelo, se presentan datos experimentales de agua a presiones negativas que tienen el mismo comportamiento que los datos de simulación.

Por otro lado, en el caso del desarrollo del modelo flexible de agua TIP4P/2005f podemos concluir que los avances al incorporar la flexibilidad al modelo rígido y no polarizable TIP4P/2005 no son todo lo satisfactorios que hubiésemos querido. Se puede definir como un paso a un lado en el desarrollo de modelos de agua. Con este nuevo modelo de agua flexible, TIP4P/2005f, se ha mantenido la calidad de resultados y predicciones, aumentando los grados de libertad del modelo. Existen otros modelos flexibles basados en modelos rígidos, como por ejemplo el SPC/Fw basado en el SPC, que mejoran sus resultados comparados con su modelo rígido. Este avance se debe a que el modelo de partida es mejorable y no a que la flexibilidad molecular permita unas predicciones mejores en simulación.

Como conclusión para el estudio de nucleación de burbujas en agua a presiones negativas podemos decir que el agua es un sistema muy especial. Cuando estudiamos la transición líquido-vapor, los métodos de análisis de burbujas que se utilizan en otros sistemas, como el Lennard-Jones, no son directemente aplicables a este sistema. Se hace necesario tratar el problema de las burbujas en agua con otras herramientas. El problema consiste en que la nucleación comienza mediante burbujas muy pequeñas. Además el líquido tiene de forma estable cavidades que son pequeñas comparadas con otros sistemas pero de un tamaño similar a las primeras burbujas en la nucleación. La suma de estos dos factores hace que la detección de las burbujas en los primeros estadíos de la nucleación sea difícil y por lo tanto se necesiten métodos especialmente diseñados para ello. Durante la realización del trabajo predoctoral se han desarrollado varios métodos que permiten estudiar este proceso de nucleación. Concretamente de los cuatro métodos presentados en

la memoria tres han sido desarrollados en el grupo del candidato, con la participación activa del mismo y el método basado en la cavidad más grande del sistema ha sido propuesto por el candidato en la estancia del mismo en el grupo del Prof. Bresme del Imperial College London. Con las herramientas adecuadas hemos analizado distintos tipos de estados termodinámicos con distintos tipos de técnicas, MFPT y HMC-US. Con todo este engranaje diseñado para el caso del agua se ha conseguido el estudio general de la nucleación de burbujas en agua a presión negativa.

Summary

Introduction

Water is one of the most common and important molecules for life. This molecule is an abundant substance on Earth that can be found in solid, liquid and vapour form. Globally the role of water is important for the morphology of our planet. On the one hand, the erosion of rivers and glaciers has gradually modified the Earth's crust. On the other hand, the presence of clouds in the atmosphere plays a central role in shaping the climate on Earth. Water is also considered the universal solvent, taking part in many chemical reactions, and it is as the environment in which life can develop.

For many decades researchers have determined chemical-physical properties of water and, even so, studying water can be considered nowadays still a hot topic. Bernal and Fowler in 1933 were the first to propose a unified liquid water model. Before them, it was believed that water existed in different forms, which mixed to create the liquid state. To explain the properties of liquid water, they used a single model based on ice Ih (hexagonal ice). This ice has a tetrahedral geometry, where a water molecule is bound to four neighbour molecules through hydrogen bonds. The liquid model of Bernal and Fowler keeps the tetrahedrality of ice, including distances and angles distortions. Another important aspect of Bernal and Fowler's work is that it is a molecular theory which explains macroscopic properties from microscopic elements. This approach can only be demonstrated through Statistical Mechanics, and more specifically using Molecular Simulations to verify its validity. The foundations of these Molecular Simulations date back to in 1953, when Metropolis *et al.*[1], proposed Monte Carlo method and six years later, when Alder and Wainwright[2] presented the Molecular Dynamics method. These are the two main Molecular Simulations techniques. The first water simulations were performed in 1969 by Barker and Watts[3]. Two years later Rhaman and Stillinger[4] further developed water simulations. Starting from these pioneering works, water simulations have grown exponentially. At the same time, different water models have been developed to predict its macroscopic pro-

perties. The most widely used are rigid and non-polarizable models, given the optimum ratio between computational cost and obtained results. The most popular models are TIP3P[5], SPC/E[6], TIP4P[5], TIP4P/Ew[7], TIP4P/2005[8], TIP4P/ice[9], TIP5P[10], mW[11] y CCM[12] (the last two being coarse-grained models).

At given thermodynamic conditions, liquid water shows different behaviour compared to most liquids, i.e. water presents **anomalies in its thermodynamic properties**. For instance, minima and/or maxima are present in the response functions, such as the heat capacity at constant volume, C_V, or the isothermal compressibility at constant temperature, κ_T. Out of these anomalies, the most notable example is the maximum density that occurs in liquid water at 4 ºC and 1 bar. These anomalies are more evident when liquid water is metastable, either decreasing the temperature or moving into the region of negative pressures. We call this region of the phase diagram as "region of extreme conditions". The an experimental limit that slows down the study of anomalous properties of liquid water, is that liquid water turns into ice when cooled down or it cavitates at negative pressure. Therefore, Molecular Simulations are essential to know the behaviour of the system at these extreme conditions. In simulations, we might be able to circumvent this issue and characterize the system in its metastable region. Hence Molecular Simulations with a robust and reliable water model, might allow us to obtain relevant information on metastable liquid water. In our simulations, we will mainly choose TIP4P/2005 to simulate water.

In order to unravel the thermodynamic scenario of the chosen model potential, it is possible to simulate different thermodynamic states and characterize the behavior of the anomalous properties of TIP4P/2005. We define as **thermodynamic scenario** the p-T plane where we represent the critical and the triple point, the lines of phase transition (liquid-vapor, liquid-solid, vapor-solid) and the loci of the maxima and minima of the response functions. Once we have calculated the thermodynamic scenario via simulations, we can compare it with all different scenarios proposed in the literature, as shown in Fig 2, where each of them gives an explanation for the anomalies of water. However, the most relevant explanation of water anomalies and demonstration of which scenario is valid can be only given with experimental data.

In all thermodynamic scenarios represented in Fig. 2 we can identify the liquid-vapour coexistence line of water (also called binodal). Crossing this line a first order phase transition occurs from the metastable to the thermodynamically stable new vapour phase. This behavior occurs all the way down to the spinodal line (not beyond). This transformation is completed in two stages: first, the stochastic process of **nucleation** of the embryos of the new phase within the metastable one, and then, once they reach a

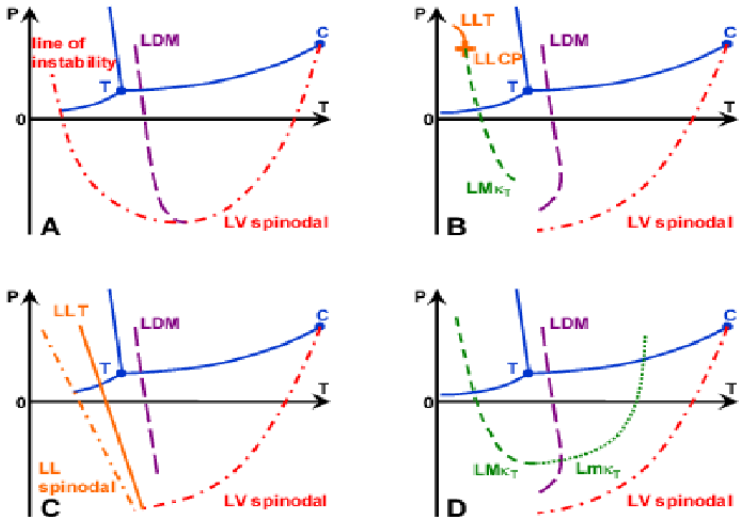

Figura 2: The four scenarios proposed to explain the anomalies of water. In all of them, the equilibrium lines (in blue) are between the solid, liquid and vapour phases, the liquid-vapour critical point (C) and the triple point (T). The purple dashed line corresponds to the temperature of maximum of density, TMD or LDM (line of density maxima), the red dotted-dashed line is the vapour-liquid spinodal (LV). In scenario A[13], we observe the re-entrant spinodal which appears at positive pressure and low temperature. The scenario B[14] involves the liquid-liquid critical point (LLCP) represented by an orange cross, the liquid-liquid transition line (LLT) (in orange) and finally the Widom line of the isothermal compressibility, (LMkT, dashed green curve). The third scenario C[15,16,17] is characterized by the liquid-liquid transition line (LLT), (solid orange line) the liquid-liquid spinodal line (dotted-dashed orange line). Finally the scenario D[18] includes an extension of the Widom line, continuing with the minimum of κ_T, (dotted green line).

critical size, their indefinite growth. Nucleation is the stochastic process of generation of the embryos of the new stage within the metastable phase. Nucleation is an activated process, that can be described by three characteristic variables: the top of the nucleation free-energy barrier, the critical nucleus and the nucleation rate. The top of the barrier, ΔG^*, is defined as the free-energy necessary to carry out the first order phase transition, corresponding to the nucleation of a critical nucleus, and the nucleation rate, J, that is the number of critical nuclei generated per unit of volume and time. The **Classical Theory of Nucleation** (CNT) is the most widely used theory to describe this process. It was developed by Volmer and Weber[19] in 1926

and it is based on the vapour-liquid phase transition. From a supercooled vapour (metastable phase) the condensation of a liquid droplet (stable phase) is studied. Therefore, the formulation of the reversible work is applied to the formation of liquid nuclei within the metastable vapor phase. During the years, there have been modifications and improvements of this theory, such as the one proposed by Becker and Döring[20] or combinations with Density Functional Theory by Cahn and Hillard[21,22]. These improvements allow to extrapolate the obtained results to another type of transitions which are comparable to the experimental data.

Quite often simulation data are compared to the values estimated with the CNT, or to experimental results (when available). However, numerical results present quite often a discrepancy with either CNT or experiments. One reason for this is that, for instance, the surface tension used in CNT is the one of a flat surface at coexistence while the simulated interphase does not have this geometry. However, the advantage of using Molecular Simulation makes up for these differences, allowing the direct study of the molecular mechanism which intervenes in the nucleation process.

The most widely used techniques to study nucleation can be divided into two groups: techniques for spontaneous nucleation processes and rare events techniques. When the free energy barrier is low, the system is able to spontaneously cross it and transform into the new thermodynamically stable: the so-called spontaneous nucleation. This can be studied by methods such as the *Mean First Passage Time*[23,24,25] technique, (MFPT). MFPT is based on the analysis of the first time the order parameter (n) reaches a given value. Using this analysis, it is possible to obtain the nucleation rate, the size of the critical nucleus (n^*) and the top of the free-energy barrier.

When studying nucleation as a rare event, i. e. when the system is not able to cross the free energy barrier because it is too high, other techniques are needed. An example of these techniques is represented by the Bennett-Chandler method[26,27]. This method consists of by two steps: firstly, we calculate the probability that a critical nucleus, in equilibrium with the surrounding metastable phase, appears within the system ($P(n^*)$), so that we can find the top of the free-energy barrier, $\Delta G(n^*)$. Secondly, we calculate the kinetic pre-factor, $\kappa(n^*)$, that corresponds to the frequency to cross the top of the free-energy barrier, obtaining the nucleation rate by combining them according to

$$J = \kappa(n^*)P(n^*) = \kappa(n^*)e^{-\beta\Delta G(n^*)}, \tag{2}$$

The top of the barrier is calculated via a method called *Umbrella Sampling*[28,29], which is based on a biased sampling of the size of the largest

nucleus until it reaches the critical size. From these calculations, we get the top of the free-energy barrier. Once we know $\Delta G(n^*)$ and its corresponding n^*, we can calculate the kinetic pre-factor, studying the time evolution of the critical nucleus from the maximum of the barrier. From this, we obtain the nucleation rate.

In our research, we have used both the MFPT method and Umbrella sampling to study bubble nucleation from metastable water at negative pressure. TIP4P/2005 has been used as a water model; the same potential has been also used in this thesis to characterize the thermodynamic scenario of water at extreme conditions.

Objectives

When we decided to perform the predoctoral work our objectives were:

1. Finding the limitations of the model TIP4P/2005, developed by Abascal and Vega. In order to study these limitations, we studied the anomalous behavior of both static and dynamic properties. Reproducing this behavior not only involved the problem of testing the accuracy of the model, but also the fact that to detect the anomalous properties of water we have to perform simulations at extreme conditions. Therefore, challenged by these difficulties we decided to study this rather complex task.

2. Developing new model potentials with the same robustness than TIP4P/2005 but that could improve the prediction of those properties where TIP4P/2005 performs poorly. For instance, the melting point at 1 bar is 252 K, 21 degrees lower than the experimental data, and the dielectric constant $(\varepsilon/\varepsilon_0)$ of the model is 57,3, which is lower than the experimental value of 78,4.

3. Studying the phenomenon of bubble nucleation in water at negative pressures. Studies about simple liquid nucleation (such as Lennard-Jones) have been carried out in the last few years: condensation[23,24], cavitation[30,31,32], crystallisation[33,34], and also cavitation at negative pressure[35,36,37]. Nevertheless, so far studies about cavitation from overstretched water have not been performed, as far as we are aware (differently from a study on the condensation process[38,39]) Moreover, given the peculiar network-forming structure of liquid water, one might not be able to directly use the already existing numerical techniques to

identify bubbles in metastable water. Therefore, driven by all these issues, we decided to tackle this interesting physical phenomenon.

The first two objectives were well marked at the beginning of the predoctoral work. First, we tested the model developed in the group, TIP4P/2005, by reproducing the anomalous behavior of water at extreme conditions. After four years working on the TIP4P/2005 model, we developed a new water model to improve the limitations of the predecessor model. Taking into account that TIP4P/2005 is a rigid and non-polarizable model, the first logical step was to incorporate flexibility. This incorporation had to keep the good results of the original model, improving its drawbacks.

The third objective came naturally during the candidate's work. Once we constructed the thermodynamic scenario of TIP4P/2005, we identified liquid-vapor coextistence line (binodal) and the spinodal at negative pressure. The region in between these two lines corresponded to the thermodynamic conditions of metastable liquid water, keen to phase transform into the thermodynamically stable vapor phase via a bubble nucleation mechanism (the further the system from the binodal, the easier to spontaneously nucleate at negative pressure).

Our study focused on the homogeneous bubble nucleation of water at negative pressure. Furthermore, we performed a preliminary study of heterogeneous bubble nucleation at negative pressures (water + carbon nanotubes) calculated the nucleation rate.

Results

Based on the objectives presented in the previous section, we have performed an exhaustive study of both thermodynamic properties at extreme conditions and bubble nucleation of water at negative pressure. Throughout the predoctoral work, water has been mainly simulated with the TIP4P/2005 water model potential. Moreover, a flexible model has been developed, TIP4P/2005f. All the results obtained by the candidate are summarized below. Overall the results in this manuscript can be presented in three different blocks:

A. **Calculation of the anomalous properties of water and construction of the thermodynamic scenario of the model TIP4P/2005.**

   This block consists of the results chapters 1, 2, 4 and 5. In the first one, the anomalous behavior of a set of thermodynamic properties is examined. In Chapter 2, a study about the model predictions of the

viscosity, a dynamics property is presented. The development of the thermodynamic scenario of the model is carried out in Chapter 4, where the scenario was completed taking into account the region at negative pressures. Finally, Chapter 5 presents the experimental data of *bulk* water at negative pressures, which was carried out in Prof. Caupin's Laboratory at the University of Lyon, and the simulations performed by the candidate, supporting the experimental data. Sound velocity was measured for two isochores along a wide region of temperature and we observed both in experiments and simulations a minimum in the speed of sound data for each isochores. This minimum corresponds to a maximum of the isothermal compressibility in the region at negative pressures and supercooled water.

B. **Development of a new flexible water model, TIP4P/2005f.**

This block of results consists of the ones presented in Chapter 3. In this chapter we calculated the optimal molecular parameters for a flexible water model based on TIP4P/2005 properties. We have also tested the newly developed flexible water model on a wide list of thermodynamic properties. This model keeps the robustness of TIP4P/2005 and it is ideal for simulations where molecular flexibility is essential, as in the case of spectroscopic studies. Additionally, we present a method to fit the parameters of molecular flexibility, based on the power spectrum.

C. **Study of the water bubble nucleation at negative pressures.**

This block of results comprises the remaining chapters: 6, 7, 8 and 9. In the first one, we present a method to locate and analyze bubbles in liquid water. This method is based on the algorithm of Voronoi polyhedra. Bubbles were analyzed for different thermodynamic liquid states, metastable as well as unstable phases. Moreover, we also examined the spontaneous nucleation of a given thermodynamically metastable state, calculating the nucleation rate and the size of the critical nucleus using the MFPT method.

In Chapter 7, two alternative methods are described, which allow to detect vapour bubbles in water and to predict similar results than the ones presented in Chapter 6. These two methods are used to study the same thermodynamic state as in Chapter 6. Another state is also analysed, where spontaneous nucleation does not occur and it is necessary to use rare events technique, i.e. the Umbrella Sampling method. Each method to detect bubbles in water has been designed by a different research group: one of them has been developed by the candidate's group

and the other one was proposed by the research group of Prof. Dellago at the University of Vienna. In this chapter we present the results of the collaboration between the two groups.

Chapter 8 presents the work carried out in collaboration with Prof. Bresme at Imperial College London, that the candidate could visit twice, having been granted two fellowships (one by the HPC-Europa and one by the Thomas Young Center). In Prof. Bresme's group, another method for the same purpose was developed. This is based on the location of the largest cavity in the metastable liquid and its volume is what one can monitor along the nucleation process. An advantage of this new method is the possibility of combining it with the *Scaled Particle Theory*[40,41] when computing the nucleation free-energy barrier, which can be challenging in the other presented methods.

The last chapter of this block and of the thesis, Chapter 9, shows preliminary results conducted in a heterogeneous system consisting of a single-wall carbon nanotube. The simulation conditions were similar to the ones employed in the other studies, i.e. negative pressure and supercooled water. In this study we calculated the nucleation rate and found that it was higher than the one obtained in the homogeneous system (as one would expect, being the free-energy barrier lower).

Conclusions

The TIP4P/2005 water model has shown to be able to reproduce and predict thermodynamic properties not only in the extreme conditions region, but also in wide ranges of pressure and temperature. It is also sensitive to small changes that produce maxima and minima of the response functions and of the line of density maxima. The representation in the $p - T$ plane of such behavior allows us to construct its thermodynamic scenario and our results seem to support two of the four possible scenarios to explain the anomalies of water. Moreover, confirming the robustness and reliability of the model, we present experimental data of water at negative pressure that show the same behavior as the simulation data.

Furthermore, we developed of a flexible water model, TIP4P/2005f, starting from the rigid and non-polarizable TIP4P/2005, and observe that the results obtained are not as satisfactory as we would have liked, since TIP4P/2005f maintains the quality of the results of rigid model, increasing its degrees of freedom, , differently from what happens with SPC/Ew (that is the flexible version of SPC).

To conclude to the study of water bubbles nucleation at negative pressures we can confirm that water is a very peculiar system. When studying the liquid-vapour transition, the already existing methods to detect bubbles in simple fluids, such as the Lennard-Jones, are not directly applicable to water. It is therefore necessary to address the problem of bubbles in liquid water with other and novel tools. The problem is that the bubble nucleation process begins with very small bubbles, that have the same size as the cavities existing even in thermodynamically stable water. Consequently, the detection of bubbles in the early stages of nucleation is difficult, and we need to develop new approaches specifically designed for water.

During the predoctoral work we have developed several methods that enable us the study of bubble nucleation process. Specifically, out of the four methods presented in this thesis, three have been developed by the group of the candidate, with his active participation, and the method based on the largest cavity has been directly proposed by the candidate during his visit to the group of Prof. Bresme at Imperial College London. With the new tools we have analyzed different types of states with different techniques, such as MFPT and HMC-US. With this ensemble of techniques designed for the case of water, we managed to perform a comprehensive study of bubble nucleation in water at negative pressure.

Bibliografía

1. Metropolis, N., Rosenbluth, A. W., Rosenbluth, M. N., Teller, A. H. & Teller, E., Equation of state calculations by fast computing machines. *J. Chem. Phys.* **21**, 1087 (1953).

2. Alder, B. J. & Wainwright, T. E., Studies in molecular dynamics 1. general method. *J. Chem. Phys.* **31**, 459 (1959).

3. Barker, J. A. & Watts, R. O., Structure of water: A Monte Carlo study. *Chem. Phys. Lett.* **3**, 144–145 (1969).

4. Rahman, A. & Stillinger, F. H., Molecular Dynamics study of liquid water. *J. Chem. Phys.* **55**, 3336–3359 (1971).

5. Jorgensen, W. L., Chandrasekhar, J., Madura, J. D., Impey, R. W. & Klein, M. L., Comparison of simple potential functions for simulating liquid water. *J. Chem. Phys.* **79**, 926–935 (1983).

6. Berendsen, H. J. C., Grigera, J. R. & Straatsma, T. P., The missing term in effective pair potentials. *J. Phys. Chem.* **91**, 6269–6271 (1987).

7. Horn, H. W., Swope, W. C., Pitera, J. W., Madura, J. D., Dick, T. J., Hura, G. L. & Head-Gordon, T., Development of an improved four-site water model for biomolecular simulations: TIP4P-Ew. *J. Chem. Phys.* **120**, 9665 (2004).

8. Abascal, J. L. F. & Vega, C., A general purpose model for the condensed phases of water: Tip4p/2005. *J. Chem. Phys.* **123**, 234505 (2005).

9. Abascal, J. L. F., Sanz, E., García Fernández, R. & Vega, C., A potential model for the study of ices and amorphous water: Tip4p/ice. *J. Chem. Phys.* **122**, 234511 (2005).

10. Mahoney, M. W. & Jorgensen, W. L., A five-site model for liquid water and the reproduction of the density anomaly by rigid, nonpolarizable potential functions. *J. Chem. Phys.* **112**, 8910–8922 (2000).

11. Molinero, V. & Moore, E. B., Water modeled as an intermediate element between carbon and silicon. *J. Phys. Chem. B* **113**, 4008–4016 (2009).

12. Franzese, G. & Stanley, H., Liquid-liquid critical point in a hamiltonian model for water: analytic solution. *J. Phys. Condens. Matter* **14**, 2201–2209 (2002).

13. Speedy, R., A simple equilibrium statistical mechanical theory of dense hard-sphere fluid mixtures-comment. *J. Chem. Phys.* **77**, 2702–2703 (1982).

14. Poole, P., Sciortino, F., Essmann, U. & Stanley, H., Phase-behavior of metastable water. *Nature* **360**, 324–328 (1992).

15. Poole, P., Sciortino, F., Grande, T., Stanley, H. & Angell, C., Effect of hydrogen-bonds on the thermodynamic behavior of liquid water. *Phys. Rev. Lett.* **73**, 1632–1635 (1994).

16. Zheng, Q., Green, J., Kieffer, J., Poole, P., Shao, J., Wolf, G. & Angell, C., Limiting tensions for liquids and glasses from laboratory and md studies, in A. Imre, H. Maris & P. Williams, eds., *Liquids Under Negative Pressure*, vol. 84 of *NATO Science series, Series II: Mathematics, Phys. and Chem.*, 33–46 (NATO, 2002).

17. Angell, C. A., Insights into phases of liquid water from study of its unusual glass-forming properties. *Science* **319**, 582–587 (2008).

18. Sastry, S., Debenedetti, P. G., Sciortino, F. & Stanley, H. E., Singularity-free interpretation of the thermodynamics of supercooled water. *Phys. Rev. E* **53**, 6144–6154 (1996).

19. Volmer, M. & Weber, A., Germ-formation in oversaturated figures. *Zeitschrift Physik. chemie–stochiometrie und verwandtschaftslehre* **119**, 277–301 (1926).

20. Becker, R. & Doring, W., Kinetic treatment of germ formation in supersaturated vapour. *Ann. Physik* **24**, 719–752 (1935).

21. Cahn, J. & Hilliard, J., Free energy of a nonuniform system .1. interfacial free energy. *J. Chem. Phys.* **28**, 258–267 (1958).

22. Zeng, X. C. & Oxtoby, D. W., Gas-liquid nucleation in lennard-jones fluids. *J. Chem. Phys.* **94**, 4472–4478 (1991).

23. Wedekind, J., Strey, R. & Reguera, D., New method to analyze simulations of activated processes. *J. Chem. Phys.* **126**, 134103 (2007).

24. Wedekind, J., Chkonia, G., Woelk, J., Strey, R. & Reguera, D., Crossover from nucleation to spinodal decomposition in a condensing vapor. *J. Chem. Phys.* **131**, 114506 (2009).

25. Chkonia, G., Woelk, J., Strey, R., Wedekind, J. & Reguera, D., Evaluating nucleation rates in direct simulations. *J. Chem. Phys.* **130** (2009).

26. Bennett, C. H., *Molecular Dynamics and Transition State Theory: The Simulation of Infrequent Events*, chap. 5, 63–97 (Am. Chem. Soc., Washington, D. C., 1977).

27. Chandler, D., Statistical-mechanics of isomerization dynamics in liquids and transition-state approximation. *J. Chem. Phys.* **68**, 2959–2970 (1978).

28. Chandler, D., *Introduction to modern statistical mechanics* (Oxford university press, New York, Oxford, 1987).

29. Torrie, G. & Valleau, J., Monte-carlo free-energy estimates using non-boltzmann sampling - application to subcritical lennard-jones fluid. *Chem. Phys. Lett.* **28**, 578–581 (1974).

30. Wang, Z.-J., Valeriani, C. & Frenkel, D., Homogeneous bubble nucleation driven by local hot spots: A molecular dynamics study. *J. Phys. Chem. B* **113**, 3776–3784 (2009).

31. Meadley, S. L. & Escobedo, F. A., Thermodynamics and kinetics of bubble nucleation: Simulation methodology. *J. Chem. Phys.* **137**, 074109 (2012).

32. Torabi, K. & Corti, D. S., Molecular simulation study of cavity-generated instabilities in the superheated lennard-jones liquid. *J. Chem. Phys.* **133**, 134505 (2010).

33. ten Wolde, P.-R., Ruiz-Montero, M. J. & Frenkel, D., Simulation of homogeneous crystal nucleation close to coexistence. *Faraday Discuss.* **104**, 93–110 (1996).

34. Moroni, D., van Erp, T. & Bolhuis, P., Investigating rare events by transition interface sampling. *Physica A-statistical Mechanics and its Applications* **340**, 395–401 (2004).

35. Punnathanam, S. & Corti, D. S., Homogeneous bubble nucleation in stretched fluids: Cavity formation in the superheated lennard-jones liquid. *Ind. Eng. Chem. Res.* **41**, 1113–1121 (2002).

36. Torabi, K. & Corti, D. S., Toward a molecular theory of homogeneous bubble nucleation: I. equilibrium embryo definition. *J. Phys. Chem. B* **117**, 12479–12490 (2013).

37. Torabi, K. & Corti, D. S., Toward a molecular theory of homogeneous bubble nucleation: Ii. calculation of the number density of critical nuclei and the rate of nucleation. *J. Phys. Chem. B* **117**, 12491–12504 (2013).

38. Matsubara, H., Koishi, T., Ebisuzaki, T. & Yasuoka, K., Extended study of molecular dynamics simulation of homogeneous vapor-liquid nucleation of water. *J. Chem. Phys.* **127**, 214507 (2007).

39. Perez, A. & Rubio, A., A molecular dynamics study of water nucleation using the tip4p/2005 model. *J. Chem. Phys.* **135**, 244505 (2011).

40. Reiss, H., Frisch, H., Helfand, E. & Lebowitz, J., Statistical mechanics of rigid spheres. *J. Chem. Phys.* **31**, 369 (1959).

41. Reiss, H., *Scaled Particle Methods in the Statistical Thermodynamics of Fluids* (John Wiley & Sons, Inc., 2007).

Discusión Integradora

El objetivo de este apartado es presentar la conexión entre los artículos utilizados dentro del bloque de resultados y especificar cual ha sido la contribución concreta en los artículos del candidato.

La memoria que aquí se presenta muestra el trabajo del candidato durante los últimos cuatro años. Como miembro del grupo de investigación de la Universidad Complutense de Madrid "Grupo de Termodinámica Estadística de fluidos moleculares" su trabajo se ha enfocado en el estudio de las propiedades anómalas del agua en condiciones extremas de presión y temperatura, concretamente a presiones negativas y en la zona sobreenfriada. Posteriormente y como consecuencia de ese estudio, se ha trabajado en la nucleación de burbujas en agua a presiones negativas. Las herramientas de trabajo durante este periodo han sido la Simulación Molecular y el análisis numérico de los sistemas utilizados. Además se han manejado tanto técnicas de análisis de nucleación para procesos espontáneos, *Mean First Passage Time*[1,2,3] y como para eventos raros, por ejemplo el *Umbrella Sampling*[4], como parte del método Bennett-Chandler[5,6].

Para el estudio del agua se ha utilizado el modelo de potencial TIP4P/2005[7]. Este modelo de agua ha sido desarrollado en el grupo de Madrid en el 2005 y ha demostrado ser el modelo rígido y no polarizable más robusto y con mejores resultados (comparados con experimentos) para un amplio rango de propiedades y condiciones termidinámicas. En la literatura encontramos una larga lista de artículos donde se pone a prueba al modelo[8,9,10,11]. Se han calculado propiedades termodinámicas en equilibrio, fuera del equilibrio y propiedades dinámicas. En esta memoria se presentan los primeros cálculos de algunas de estas propiedades, como viscosidad, compresibilidad isoterma, velocidad del sonido... Y un estudio de la nucleación de burbujas en agua a presiones negativas. Este estudio se ha realizado por medio de nuevos métodos de localización y análisis de burbujas, desarrollados por el candidato, y utilizando nuevos métodos de análisis del proceso de nucleación.

El **objetivo** general del trabajo predoctoral presentado en esta memoria es tanto exponer los novedosos estudios realizados con el TIP4P/2005 en

la región de condiciones termodinámicas extremas, como presentar estudios sobre el proceso de nucleación de burbujas. A continuación se realizará una breve descripción de las partes y capítulos de la memoria. El manuscrito está dividido tres partes: fundamento teórico, resultados y conclusiones.

En la primera parte hemos querido exponer las **bases teóricas** adquiridas por el candidato. Se ha ofrecido una visión general de los temas que se tratan en la memoria, partiendo de los orígenes de cada uno. Así, nos encontramos con un capítulo de Mecánica Estadística, donde se exponen los conceptos básicos, tales como los postulados, los colectivos, las funciones de partición, la utilidad de las fluctuaciones de las propiedades termodinámicas, la conexión con la Simulación Molecular y los modelos de potencial.

Después de esta sección se presenta un capítulo sobre la Simulación Molecular, compuesto por los aspectos básicos sobre cualquier tipo de simulación y una explicación de las distintas técnicas de simulación utilizadas en la memoria: Dinámica Molecular, Monte Carlo, Monte Carlo Híbrido, *Umbrella Sampling* y los modelos de potencial de agua más populares.

El proceso de nucleación se expone en el siguiente capítulo. Se comentará desde las definiciones de estados termodinamicos metaestables hasta las técnicas especiales que se utilizan en simulación para describir el proces de nucelación. Durante este capítulo se explica la Teoría Clásica de Nucleación[12,13] y la forma de obtener tanto la barrera como la tasa de nucleación. Además se exponen algunas de las técnicas que se utilizan en simulación para el cálculo de estas variables. Así, explicamos la técnica *Mean First Passage Time*, para procesos de nucleación espontánea y el método Bennett-Chandler[5,6], específico para eventos raros de nucleación.

Por último, se ha creído necesario presentar los actuales escenarios termodinámicos del agua, ya que buena parte de los resultados se centran en describir las propriedades anomalas a través del escenario del agua apoyados por los datos experimentales y de simulación del modelo TIP4P/2005.

La segunda parte de la memoria se recoge en los diferentes **capítulos de resultados**. En este caso se sigue el orden lógico y continuo que ha regido todo el trabajo predoctoral. Nos referimos a lógico y continuo porque no ha habido un objetivo obligado al final del trabajo predoctoral, al cual había que llegar forzosamente, como es el caso de muchos trabajos de doctorado que tienen una financiación completa de tres o cuatro años. Haciendo de la necesidad virtud, se ha desarrollado una tesis rigurosa, marcada por los proyectos que han financiado el trabajo del candidato.

En el primer capítulo, **Cap. 1**, se expone el cálculo por simulación de las propiedades anómalas del agua. Se determinan para el modelo de potencial de agua TIP4P/2005 la compresibilidad isoterma, κ_T, la capacidad

calorífica a presión constante, C_P y la temperatura máxima de densidad a distintas presiones. La contribución del candidato se centra en el estudio de la compresibilidad isoterma a 1 bar y en un rango amplio de temperaturas $[260 - 360$ K] para distintos modelos de agua TIP4P, SPC/E, TIP5P y TIP4P/2005. Los dos primeros muestran un ligero mínimo en κ_T, pero lejos de los valores experimentales. El modelo TIP5P no es capaz de reproducir el mínimo en la isobara ni el valor experimental en condiciones normales. En el caso del TIP4P/2005, los datos de κ_T se encuentran sobre los datos experimentales. Además el mínimo del modelo, en 37 °C, está bastante cerca del experimental, 46,5 °C. A la vista de estos resultados se decide ampliar el estudio a otra isobara, 1000 bar, donde también observamos la concordancia entre simulación y experimento.

En el capítulo siguiente, **Cap. 2**, se calcula una propiedad dinámica, la viscosidad. En esta ocasión la participación fue completa por parte del candidato. El procedimiento utilizado para calcular esta propiedad dinámica es a través de la ecuación de Green-Kubo. Esta formulación está basada en las funciones de autocorrelación. En nuestro caso utilizamos los componentes del tensor de presión para determinar la viscosidad. Se simularon tres isotermas, 273 K, 298 K y 373 K, en un rango de presiones de 0 a 500 bar. Se comprobó que el modelo predice el mínimo de viscosidad a temperaturas bajas y los datos de simulación se encuentran cerca de los experimentales. Además se comparó con otro potencial de agua, SPC/E, el cual reproduce datos de viscosidad satisfactorios, pero más bajos que los presentados por el TIP4P/2005 y el experimento.

El tercer capítulo, **Cap. 3**, presenta el modelo flexible, TIP4P/2005f, que mantiene la calidad de predicciones introduciendo nuevos grados de libertad al modelo. Esto hace que sea muy útil en determinadas situaciones, como en el caso de estudios espectroscópicos y de dinámicas moleculares regidas por la flexibilidad de las moléculas del agua. La contribución del candidato al artículo es completa, al igual que en el capítulo anterior. Las propiedades termodinámicas que se calculan por medio del modelo son: el valor de la temperatura del máximo de densidad a 1 bar, la función de distribución radial (oxígeno-oxígeno), la entalpía de evaporización, la compresibilidad isoterma en condiciones normales, el coeficiente de difusión a 298 K y presión ambiente, la temperatura de fusión del hielo Ih, la estabilidad relativa de los hielos a 0 k y 0 bar, la constante dieléctrica y el espectro de densidades. No sólo se exponen los resultados del modelo sino que también se propone un método de ajuste de los parámetros de flexibilidad para modelos flexibles, basado en el análisis del espectro de densidad.

El capítulo cuatro, **Cap.4**, describe el escenario termodinámico del modelo de potencial de agua TIP4P/2005, así como el procedimiento a seguir

en la determinación de las líneas que lo forman. Los resultados en este capítulo no están todavía publicados, sino que forman parte de un trabajo que combina datos de simulación y experimentales los cuales son el producto de la colaboración con el laboratorio del Prof. Caupin de la Univerdad de Lyon. Este capítulo presenta los datos de simulación del modelo TIP4P/2005. Parte de los resultados obtenidos a presiones negativas cosntituyeron el trabajo de Máster del candidato y se han utilizado en esta memoria ya que forman parte del trabajo predoctoral. El escenario del modelo está caracterizado por un punto crítico líquido-líquido ligado a la línea de Widom de la compresibilidad isoterma, la cual está formada por los valores máximos y mínimos de esa propiedad a lo largo de una serie de isóbaras. Además esta línea se relaciona con la línea de temperatura máxima de densidad, que se relaciona a su vez con la espinodal líquido-vapor. De esta forma tenemos descrito el escenario termodinámico del modelo.

En el siguiente capítulo, **Cap. 5**, se presentan datos experimentales de agua *bulk* a presiones negativas y los homólogos de simulación usando el modelo TIP4P/2005. En esta ocasión la contribución del candidato al artículo se centra en toda la parte de simulación y análisis numérico que aparece en el capítulo. Se determinó, en un rango de temperaturas, la velocidad del sonido en dos isócoras, tanto de forma experimental como por simulación. Los datos experimentales obtenidos por el grupo del Prof. Caupin en la Universidad de Lyon, han sido exitosamente comparados con los datos de simulación del TIP4P/2005. El resultado principal es la aparición de un mínimo en la velocidad del sonido que se corresponde con el máximo de la compresibilidad. Desde el punto de vista de simulación, el procedimiento para obtener los valores de velocidad del sonido consiste en realizar dos simulaciones diferentes para cada isócora. Por un lado se simula el agua metaestable en el colectivo NVT para obtener la capacidad calorífica a volumen constante, C_V y por el otro a la misma densidad se calculan C_p y κ_T, en el colectivo NpT. La importancia de obtener estos mínimos es que son la primera prueba experimental (ratificada mediante simulación) de la existencia de la línea de Widom. Esta línea apoya los escenarios termodinámicos que tienen en cuenta la línea de Widom para la explicación de las anomalías del agua. Además la concordancia entre el experimento y los resultados del modelo hace más plausible el escenario con un segundo punto crítico líquido-líquido.

Al igual que en los experimentos del grupo de Lyon, en la zona de presiones negativas nos encontramos con el proceso de nucleación. Nuestros sistemas en determinadas condiciones de temperatura y presión, tenden a cavitar espontáneamente y por esa razón realizamos el primer estudio sobre nucleación de burbujas a presiones negativas del TIP4P/2005. Este estudio se presenta en los capítulos siguientes.

En el primero de ellos, sexto capítulo, **Cap. 6**, se propone el algoritmo de poliedros de Voronoi como medio para determinar el volumen de las burbujas que cavitan espontáneamente en agua líquida metaestable en las condiciones termodinámicas elejidas, dado que los poliedros de Voronoi permiten un estudio riguroso de los volúmenes de las moléculas que forman el sistema. La contribución del candidato se basa en la realización de las trayectorias independientes de cavitación espontanea, necesarias en la tecnica del MFPT. En total se simularon 3000 trayectorias en 15 estados termodinámicos diferentes, de los cuales sólo dos fueron elegidos para el artículo. Una vez optimizado el algoritmo de Voronoi para determinar las burbujas en agua, se puede diferenciar entre las moléculas líquidas y vapor, y uniendo moléculas de vapor vecinas entre si (con un algoritmo de *clustering*) para definir las burbujas del sistema, y utilizar sus volúmenes como parámetro de orden para seguir la nucleación.

En el capítulo 7, **Cap.** 7, se presentan otros dos métodos para el análisis de burbujas en agua: un método ha sido propuesto en el grupo de Madrid y otro método en el grupo del Prof. Dellago de la Universidad de Viena. En esta ocasión la participación en el artículo ha sido el desarrollo de las trayectorias de cavitación espontánea necesarias en el MFPT y el análisis numérico de los datos obtenidos por el método presentado por el grupo de investigación de Madrid, tanto en el caso de nucleación espontánea como en el estudio de nucleación "no espontanea" con técnicas específicas para eventos raros (en un sistema de 4000 moléculas de agua). El método desarrollado por el grupo de Madrid está basado en un trabajo de Wang *et al.*[14] sobre nucleación de burbujas en un sistema de Lennard-Jones. Al tratarse del agua, un líquido molecular muy diferente que un líquido simple como el Lennard-Jones, es necesario utilizar distintos criterios para realizar la diferenciación entre moléculas líquido o vapor y además se necesitan criterios *ad hoc* para eliminar las cavidades naturales que se encuentran en el agua líquida en condiciones de equilibrio termodinámico. El otro método esta desarrollado por el grupo del Prof. Dellago de la Universidad de Viena y combina la localización de la burbuja con la variación del volumen de la caja de simulación con respecto al volumen promedio del sistema.

En el capítulo octavo, **Cap.** 8, se presenta otro método para la determinación y el análisis de burbujas en agua, basado en el estudio del Prof. Bresme sobre cavidades de líquidos iónicos[15]. El candidato, durante las dos estancias en el grupo del Prof. Bresme en el Imperial College London (financiadas por una beca Europea, HPC-Europa2, y una inglesa del Thomas Young center), desarrolló el nuevo método para localizar la cavidad más grande en un líquido metaestable y aplicar su estudio al de la nucleación en dos sistemas muy distintos: un líquido simple (como el Lennard-Jones) y uno molecular

(como el agua). Además, el candidato realizó todo el análisis numérico de los resultados de nucleación, obteniéndo la tasa de nucleación, el tamaño crítico de burbuja y las barreras de nucleación. El método presentado consiste en construir en el líquido metaestable una trama con un número suficiente de celdillas. Desde el centro geométrico de cada celdilla se calcula la distancia más corta entre ese centro y todas las moléculas. Por lo tanto cada celdilla tiene una distancia asociada. Entre todas estas distancias se elige la más grande, la cual corresponde a la cavidad más grande del sistema, o al radio de la esfera más grande que no toque ninguna molécula. A partir de la localización de la burbuja más grande se determina su volumen, volumen de la cavidad más grande, que se utilizará como parámetro de orden en el proceso de nucleación espontánea de burbujas en el sistema. En el capítulo se demuestra que este método es muy versátil, ya que puede ser utilizado tanto en líquidos simples (como el Lennard-Jones) como en líquidos moleculares (como el agua).

Por último, y como capítulo final de los resultadods, **Cap.** 9, se han presentado los resultados preliminares del estudio de la nucleación heterogénea de burbujas de agua en presencia de nanotubos de carbono. La contribución por parte del candidato en este capítulo es completa. Los resultados se obtuvieron durante sus estancias en Londres, en el laboratorio del Prof. Bresme del Imperial College London. Para empezar, se construyeron una serie de sistemas heterogéneos con distintos tipos de nanotubos, distinta quiralidad, número de capas... Los resultados presentados en esta memoria sólo son los obtenidos con un nanotubo de carbono simple, rodeado de agua por fuera. La cavitación se consigue simulando el agua que rodea el nanotubo a presiones negativas. Para poder comparar con los resultados obtenidos en estudios previos de nucleación homogénea, se elijeron las mismas condiciones termodinámicas que el el Capítulo 6. Se ha utilizado como método de análisis de burbuja el método de la cavidad más grande descrito en el capítulo anterior ya que es el más adecuado para este tipo de sistemas. Los resultados de nucleación están acorde con los esperados por la CNT, es decir, la tasa de nucleación es mucho menor cuando la nucleación es homogénea que cuando es heterogénea, en el mismo estado termodinámico, siendo la barrera de nucleación más alta en el primer caso que en el segundo.

La memoria termina con la parte de conclusiones, donde se hace una retrospectiva del trabajo realizado durante estos últimos años y se valora la contribución del candidato.

Bibliografía

1. Wedekind, J., Strey, R. & Reguera, D., New method to analyze simulations of activated processes. *J. Chem. Phys.* **126**, 134103 (2007).

2. Wedekind, J., Chkonia, G., Woelk, J., Strey, R. & Reguera, D., Crossover from nucleation to spinodal decomposition in a condensing vapor. *J. Chem. Phys.* **131**, 114506 (2009).

3. Chkonia, G., Woelk, J., Strey, R., Wedekind, J. & Reguera, D., Evaluating nucleation rates in direct simulations. *J. Chem. Phys.* **130** (2009).

4. Torrie, G. & Valleau, J., Monte-carlo free-energy estimates using non-boltzmann sampling - application to subcritical lennard-jones fluid. *Chem. Phys. Lett.* **28**, 578–581 (1974).

5. Chandler, D., Statistical-mechanics of isomerization dynamics in liquids and transition-state approximation. *J. Chem. Phys.* **68**, 2959–2970 (1978).

6. Bennett, C. H., *Molecular Dynamics and Transition State Theory: The Simulation of Infrequent Events*, chap. 5, 63–97 (Am. Chem. Soc., Washington, D. C., 1977).

7. Abascal, J. L. F. & Vega, C., A general purpose model for the condensed phases of water: Tip4p/2005. *J. Chem. Phys.* **123**, 234505 (2005).

8. Vega, C., Abascal, J. L. F., Conde, M. M. & Aragones, J. L., What ice can teach us about water interactions: a critical comparison of the performance of different water models. *Faraday Discuss.* **141**, 251–276 (2009).

9. Vega, C. & Abascal, J. L. F., Simulating water with rigid non-polarizable models: a general perspective. *Phys. Chem. Chem. Phys.* **13**, 19663–19688 (2011).

10. Pi, H. L., Aragones, J. L., Vega, C., Noya, E. G., Abascal, J. L. F., Gonzalez, M. A. & McBride, C., Anomalies in water as obtained from computer simulations of the tip4p/2005 model: density maxima, and density, isothermal compressibility and heat capacity minima. *Mol. Phys.* **107**, 365–374 (2009).

11. Gonzalez, M. A. & Abascal, J. L. F., The shear viscosity of rigid water models. *J. Chem. Phys.* **132**, 096101 (2010).

12. Volmer, M. & Weber, A., Germ-formation in oversaturated figures. *Zeitschrift Physik. chemie–stochiometrie und verwandtschaftslehre* **119**, 277–301 (1926).

13. Becker, R. & Doring, W., Kinetic treatment of germ formation in supersaturated vapour. *Ann. Physik* **24**, 719–752 (1935).

14. Wang, Z.-J., Valeriani, C. & Frenkel, D., Homogeneous bubble nucleation driven by local hot spots: A molecular dynamics study. *J. Phys. Chem. B* **113**, 3776–3784 (2009).

15. Bresme, F. & Alejandre, J., Cavities in ionic liquids. *J. Chem. Phys.* **118**, 4134–4139 (2003).

Parte I

Fundamento teórico

Fundamento Teórico: Capítulo 1

Mecánica estadística. Conectando el mundo microscópico con el macroscópico.

Las bases de la Mecánica Estadística surgen con los trabajos de Maxwell y Boltzmann sobre la cinética de los gases, aunque fue Gibbs quien, en 1902, las asentó con su libro *Elementary Principles in Statistical Mechanics*. Hasta principios del siglo XX no se había consolidado la nueva idea atomística propuesta por Boltzmann, aunque empezaban a existir evidencias que apoyaban pero no demostraban las conjeturas del austriaco. La Termodinámica Clásica y sus principios están fundamentados en la medición de unas pocas propiedades macroscópicas de un sistema dado. La relación existente entre éstas nos permite obtener otras magnitudes termodinámicas y así describir el comportamiento del sistema. Pero existe otro punto de vista complementario para el mismo objetivo y éste se basa en la descripción del comportamiento de los constituyentes del propio sistema por medio de la Mecánica. La estadística, como veremos en líneas sucesivas, es la encargada de unir el mundo de los átomos y las moléculas con las propiedades macroscópicas, tales como entropía, energía, capacidades caloríficas... De este modo se constituye la Mecánica Estadística que es la rama de la ciencia que estudia los sistemas macroscópicos a partir de las características de sus componentes fundamentales, los átomos y/o las moléculas[1].

1.1. Conceptos básicos. Macroestado y Microestado

En poco más de 100 años de existencia de esta ciencia, la Mecánica Estadística se ha aplicado con excelentes resultados al estudio de diferentes tipos de sistemas:

1. Sistemas en **equilibrio termodinámico**, en este caso la Mecánica Estadística se suele denominar Mecánica Estadística de Equilibrio o Termodínamica Estadística, y se aplica al cálculo de propiedades termodinámicas.

2. Sistemas **fuera del equilibrio termodinámico**, aquí el estudio se centra en las velocidades de reacciones químicas y en fenómenos de transporte de calor, de materia... Como no podía ser de otra forma de este campo se encarga la Mecánica Estadística de No Equilibrio.

Todos estos sistemas tienen en común que están compuestos por un gran número de partículas (átomos o moléculas), una cantidad del orden de la constante de Avogadro, $N_A = 6{,}0221415 \cdot 10^{23}$ mol^{-1}. Este hecho hace que la resolución (de forma cuántica o clásica) de las ecuaciones de movimiento para cada una de las partículas sea inabordable, pero como se comentará en las siguientes secciones podemos utilizar aproximaciones matemáticas para resolver estos problemas. Para entender la Termodinámica Estadística debemos de tener como punto de partida que la medida de una propiedad macroscópica es el resultado del promedio de las medidas de una magnitud microscópica en cada uno de los estados representativos de ese sistema termodinámico. Esto quedará mucho más claro cuando definamos qué es un macroestado, qué un microestado y cúal es la relación entre ambos.

Se define **macroestado**, estado macroscópico o estado termodinámico aquel estado del sistema que se puede describir completamente por medio de unas pocas variables llamadas funciones de estado. Éstas provienen de una ecuación de estado que las ponen en conexión directa. Del mismo modo, podemos calcular otras funciones de estado en base a una relación de tres de ellas. Por ejemplo, en un gas ideal tenemos como funciones de estado: la presión (p), en número de moles (n) y el volumen (V). A través de la ecuación de estado $pV = nRT$ obtenemos la temperatura (T), siendo R la constante de los gases ideales. Y además es posible calcular otras funciones de estado, como la energía interna del sistema (U), en función de tres variables de estado $U = U(n, p, T)$

Por otro lado tenemos el estado microscópico o **microestado**, que es fácil de explicar si comprendemos cual es la conducta molecular del sistema. Las partículas están en contínuo movimiento e interactúan entre ellas, generando una sucesión continua de nuevas posiciones y velocidades, correspondientes a distintos valores de energía. Podemos definir microestado a cada una de estas formas en las que se encuentran las partículas dentro del sistema. Existen dos maneras de espeficicar la conducta molecular, una es desde el punto de vista clásico, mediante la resolución de las ecuaciones clásicas de movimiento, como por ejemplo las ecuaciones de Newton. Para ello se

necesita conocer las posiciones y velocidades de las N partículas en cada instante del sistema. De esta forma el microestado queda determinado por las coordenadas,

$$\{x_1, y_1, z_1, x_2, y_2, z_2, .., x_N, y_N, z_N\} = \{\mathbf{r}_1, \mathbf{r}_2, .., \mathbf{r}_N\} \tag{1.1}$$

y las velocidades,

$$\{v_{x1}, v_{y1}, v_{z1}, v_{x2}, v_{y2}, v_{z2}, .., v_{xN}, v_{yN}, v_{zN}\} = \{\mathbf{v}_1, \mathbf{v}_2, .., \mathbf{v}_N\}\,. \tag{1.2}$$

Para conocer la energía, E, de cualquier microestado en necesario calcular previamente su energía potencial V_p y energía cinética K de la siguente manera,

$$E = K + V_p = \sum_{i=1}^{N} \frac{1}{2} m_i v_i^2 + V_p(\mathbf{r}_1, \mathbf{r}_2, ..., \mathbf{r}_N) \tag{1.3}$$

El cáculo completa implica el manejo de $6N$ variables para cada microestado.

Después de definir lo que es un macroestado y un microestado el siguiente paso es determinar la relación que existente entre ambos. El punto de partida es muy intuitivo. Si nos paramos a pensar en un macroestado y en la forma de caracterizarlo, lo que haremos es una medición de dos funciones de estado, en el transcurso de un tiempo concreto. Por ejemplo, mediremos el volumen y la temperatura. Damos por definido el estado cuando estas variables se mantienen constantes y no existe ningún efecto externo que lo perturbe y/o saque de su equilibrio. Si ahora, en esa misma "calma" macroscópica, pensamos sobre el comportamiento de las partículas del sistema, inmediatamente imaginaremos como cambian de posición y velocidad contínuamente. Esto nos lleva a la necesidad de definir otro concepto que nos ayude a conectar los microestados con el macroestado, el **colectivo.** Un colectivo es un conjunto mental de un gran número de réplicas del sistema de estudio (todas ellas compatibles con el estado termodinámico) en distintos estados moleculares (microestados)[2]. Es el conjunto de todas las posibles posiciones y velocidades que tienen las partículas mientras están en esta *calma* macroscópica. Pero sobre la definición de colectivo y sus cualidades volveremos a hacer hincapié en las páginas siguientes. Ahora continuemos con la dualidad entre visiones del mismo sistema la cual se conecta por medio de los dos postulados fundamentales de la Termodinámica Estadística.

El primero de ellos se enuncia de esta forma *la medida temporal (para un tiempo suficientemente grande) de una variable mecánica X en un sistema termodinámico es igual al promedio del colectivo de X en el límite cuando el número de microestados tiende a infinito, siempre que los sistemas del colectivo reproduzcan el estado macroscopico.*[2] Y el segundo hace referencia a

que *existen muchos microestados compatibles con un macroestado siendo la probabilidad de ocupación de cada uno de ellos diferente dentro del macroestado. A no ser que se trate de microestados con igual energía, degenerados, los cuales tendrán la misma probabilidad dentro del colectivo.*[2] Este último postulado es conocido como el *principio de igualdad de probabilidad* y sucede en el colectivo *microcanónico*, concepto que se explicará en líneas sucesivas.[2] Estos dos aspectos se combinan en la **hipótesis ergódica** la cual explica que podemos definir las propiedades macroscópicas de nuestro sistema por medio de mediciones, contínuas en el tiempo, de magnitudes mecánicas microscópicas o por medio de las mismas medidas, en un instante dado, de un gran número de réplicas del sistema dentro del colectivo. Esta hipótesis no es demostrable y se acepta por la validez de los correctos resultados que se generan a partir de ella[3]. Si aplicamos la hipótesis ergódica al estudio de la energía, podemos escribir la siguiente expresión matemática,

$$E = \langle E \rangle_t = \langle E \rangle_{col} = \sum_i^M P_i E_i = \frac{1}{N_r} \sum_j^{N_r} E_j, \tag{1.4}$$

donde $\langle\rangle_t$ significa que se promedia sobre el tiempo, mientras que $\langle\rangle_{col}$ simboliza el promedio realizado sobre los colectivos, j y i son los indices para las réplicas y los microestados respectivamente, P_i es la probabilidad de ocupación del microestado i, E_i, la energía del mismo microestado, M es el número total de microestados, N_r el número de réplicas dentro del colectivo, y E_j la energía de la replica j. Para una propiedad mecánica cualquiera X se puede utilizar la relación general,

$$\bar{X} = \sum_i P_i X_i, \tag{1.5}$$

No todas las propiedades macroscópicas tienen su homóloga microscópica por lo que hay que encontrar otra forma de describirlas en el microestado y relacionarla con el estado termodinámico. Tenemos el caso de la entropía, la cual no es un propiedad mecánica y está directamente relacionada con el número de microestados que forman el sistema, suponiendo que la probabilidad de que aparezcan sea la misma para todos los microestados, es decir, suponiendo el segundo postulado de la termodinámica estadística. Para su demostración ver apéndice (5),

$$S = -k_B \sum_i P_i \ln P_i, \tag{1.6}$$

siendo S la medida macroscópica de la entropía, k_B la constante de Boltzmann y P_i la probabilidad de ocupación de un microestado i, el cual pertenece

a la distribución más probable. Lo cual se demuestra también en el mismo apéndice (5). La utilización de la probabilidad del microestado como nexo con las propiedades no mecánicas del macroestado cierra y engloba el cálculo de todas las magnitudes que caracterizarán nuestro sistema.

1.2. Colectivos

En líneas anteriores hemos adelantado una definición de colectivo para poder introducir los postulados de la Termodinámica Estadística pero no hemos desarrollado este importantísimo aspecto. Retomando esa definición, podemos partir del concepto de conjunto mental que engloba a todas las réplicas de un sistema las cuales mantienen una representatibilidad entre sí y con el macroestado. Siguiendo esta idea, enmarcamos un colectivo conservando constantes unas propiedades, forzando a que todos los microestados tienen que mantener esas magnitudes también constantes para que sean aceptados dentro del colectivo. Existen muchos tipos de colectivos, ya que el macroestado puede estar definido por muchas combinaciones de tres magnitudes macroscópicas: número de partículas, temperatura, presión, entalpía... pero los que más se utilizan son:

1. *Colectivo microcanónico (NVE).* Son sistemas definidos por las magnitudes N, V y E. Estos parámetros se conservan durante todo el estudio por lo que no puede existir ni intercambio de materia ni de energía. Los sistemas con estas características son conocidos como sistemas aislados.

2. *Colectivo canónico (NVT).* Este colectivo es similar a un sistema cerrado, porque sólo puede producirse un intercambio de energía. Las variables que definen el colectivo son N, V y T.

3. *Colectivo isotérmico-isobárico (NpT).* Este colectivo permite fijar la temperatura y la presión, siendo unas condiciones más semejantes a las utilizadas experimentalmente.

4. *Colectivo macrocanónico o gran canónico (μVT).* Como ejemplo de un sistema abierto tenemos a esta clase de coletivo. Se produce el intercambio de materia y energía, ya que lo que debe conservarse es el potencial químico μ.

Para tener una imagen mental de los colectivos, vamos a dejarnos llevar por la nomenclatura de los mismos y basarnos en las figuras (1.2) y (1.2) del texto. Tomemos como referencia el colectivo canónico y lo utilizamos como

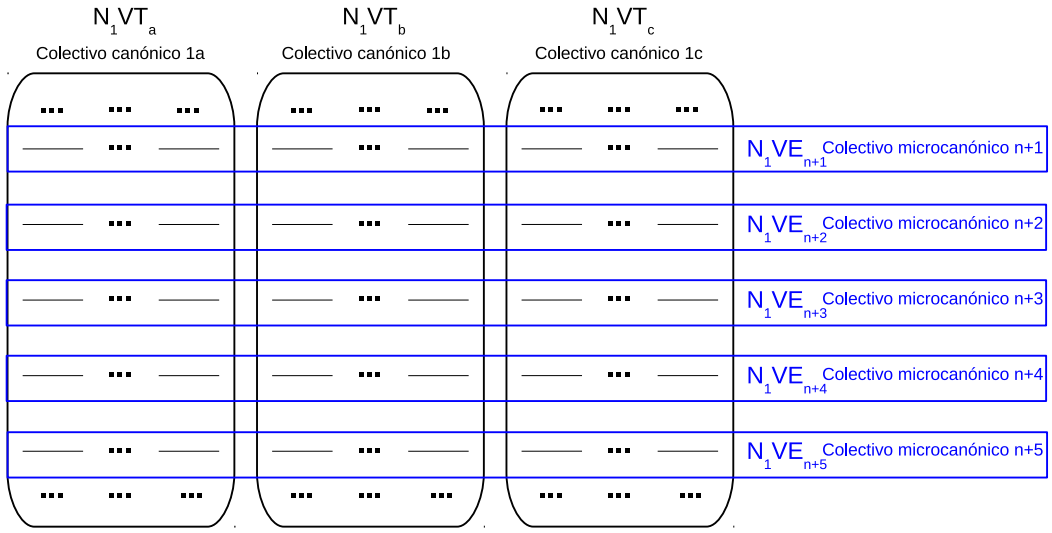

Figura 1.1: Colectivos canónicos, representados en negro y colectivos microcanónicos representados en azul. Las rectas negras dentro de los colectivos corresponden a los microestados del sistema.

raíz de los demás. Nuestro colectivo de partida *colectivo canónico* $1a$ está caracterizado por las variables N_1, V y T_a. A partir de éste podemos construir otros muchos colectivos canónicos. Una forma es mantener constante el número de partículas y cambiar a diferentes valores de temperaturas, T_b y T_c, como se hace en la Fig. (1.2). Generaremos dos nuevos colectivos que se denominan *colectivo canónico* $1b$ y *colectivo canónico* $1c$. De esta forma, obtenemos también una serie de microestados que tienen la misma energía y podemos agruparlos "horizontalmente" formando un mismo colectivo. Así, se definen los *colectivos microcanónicos* (N_1VE_n). La otra forma consiste en conservar la temperatura y modificar la variable N, ver la Fig. (1.2). En este nuevo grupo de microestados nos encontramos con que existe un conjunto global de estos colectivos canónicos formando un nuevo colectivo, llamado *colectivo macrocanónico* (μVT_a), siempre que μ se conserve.

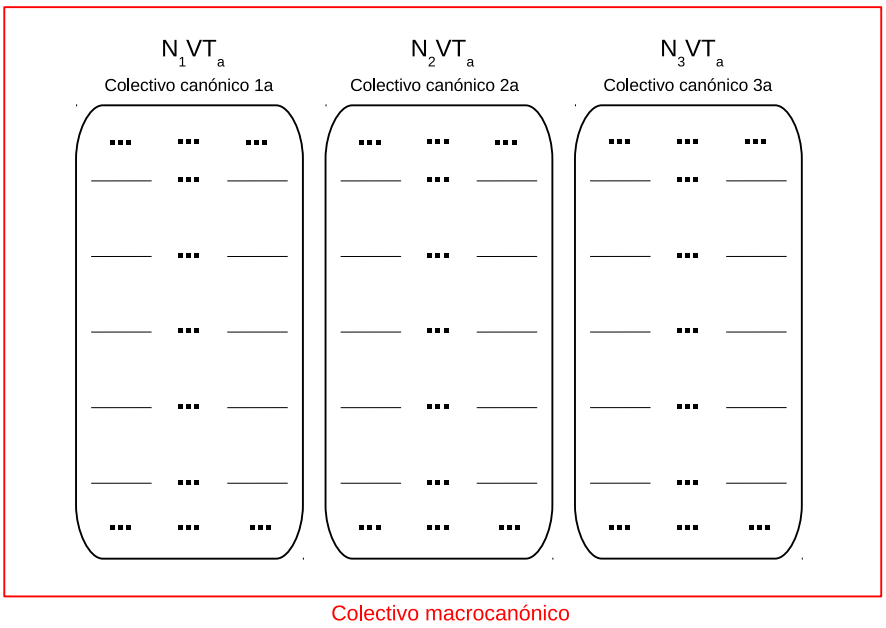

Figura 1.2: Colectivos canónicos, representados en negro y colectivo macrocanónico representado en rojo. Las rectas negras dentro de los colectivos corresponden a los microestados del sistema.

Es muy importante determinar el colectivo de estudio para luego extraer la información termodinámica que nos interesa. Como ejemplo, si queremos calcular la capacidad calorífica del sistema a volumen constante $C_V = \left(\frac{\partial E}{\partial T}\right)_V$, no podemos calcularla a partir de un colectivo microcanónico NVE o del colectivo NpT. El primero de ellos mantiene constante la energía y la C_V está ligada intrínsecamente con las fluctuaciones de energía del sistema, por lo tanto si no hay fluctaciones energéticas no tenemos medidas de C_V. El segundo colectivo tampoco es adecuado porque es necesario que el volumen sea constante como dice la propia definición de la capacidad calorífica. Por todo ello, el adecuado para el cálculo de C_V será el colectivo canónico NVT.

1.3. La Función de partición

La función de partición se define como la sumatoria de las probabilidades de ocupación de todos los microestados, asegurando la normalización en el cálculo de la probabilidad de los microestados que forman el colectivo (ver apéndice (5)). En el caso del colectivo microcanónico, como se cumple el principio de igualdad de probabilidad, su función de partición se obtiene como la suma de las probabilidades del total de estados microscópicos que conforman el coletivo NVE,es decir, $\Omega(N,V,E) = \sum_i P_i$. Para el cálculo de la probabilidad de uno de estos microestados sólo hay que seguir la siguiente relación:

$$P_i = \frac{1}{\Omega(N,V,E)}, \tag{1.7}$$

siendo $\Omega(N,V,E)$ la función de partición microcanónica. Esta misma función es la base para el cálculo de propiedades termodinámicas, como en el caso de la entropía.

$$S = -k_B \ln \Omega(N,V,E). \tag{1.8}$$

Siguiendo con el resto de colectivos, cada uno de ellos tiene asociado una función de partición. En el colectivo NVT, nos encontramos con $Q(N,V,T)$ y viene definida por la siguiente relación:

$$Q(N,V,T) = \sum_i e^{\left(-\frac{E_i(N,V)}{k_B T}\right)}, \tag{1.9}$$

la cual es función de la temperatura y de la energía de los microestados i a N y V constantes. Ayudandonos de esta definición podemos calcular $\Xi(\mu,V,T)$ y $\Delta(N,p,T)$, las funciones de partición del colectivo macrocanónico y colectivo NpT, respectivamente. Siendo,

$$\Xi(\mu,V,T) = \sum_N Q(N,V,T) e^{\left(-\frac{N\mu}{k_B T}\right)}, \tag{1.10}$$

el sumatorio se realiza sobre las N partículas. Y en el segundo caso

$$\Delta(N,p,T) = \sum_i Q(N,V,T) e^{\left(-\frac{pV_i}{k_B T}\right)}. \tag{1.11}$$

En este punto sólo conocemos los tipos de colectivos y su respectivas funciones de partición. Podemos calcular las propiedades macroscópicas del sistema por medio de las relaciones que se exponen en la Tabla (1.3) basadas en Ω, Q, Ξ y Δ. Nótese que siempre existe una propiedad macroscópica que se relaciona directamente con el logaritmo de la función de partición.

Tabla 1.1: Propiedades termodinámicas calculadas a partir de la función de partición correspondiente a cada colectivo.

Colectivo canónico Q(N,V,T)
$A = -k_B T Ln Q$ $S = k_B Ln Q + k_B T \left(\frac{\partial Ln Q}{\partial T}\right)_{N,V}$ $p = k_B T \left(\frac{\partial Ln Q}{\partial V}\right)_{N,T}$ $\mu = -k_B T \left(\frac{\partial Ln Q}{\partial N}\right)_{V,T}$ $E = k_B T^2 \left(\frac{\partial Ln Q}{\partial T}\right)_{N,V}$
Colectivo microcanónico Ω(N,V,E)
$S = k_B Ln\Omega$ $\frac{1}{k_B T} = \left(\frac{\partial Ln\Omega}{\partial E}\right)_{N,V}$ $\frac{p}{k_B T} = \left(\frac{\partial Ln\Omega}{\partial V}\right)_{N,E}$ $\frac{\mu}{k_B T} = \left(\frac{\partial Ln\Omega}{\partial N}\right)_{V,E}$
Colectivo macrocanónico $\Xi(\mu$,V,T)
$pV = -k_B T Ln\Xi$ $S = k_B Ln\Xi + k_B T \left(\frac{\partial Ln\Xi}{\partial T}\right)_{\mu,V}$ $N = k_B T \left(\frac{\partial Ln\Xi}{\partial \mu}\right)_{V,T}$ $p = k_B T \left(\frac{\partial Ln\Xi}{\partial V}\right)_{\mu,V}$
Colectivo NpT Δ(N,p,T)
$G = -k_B T Ln\Delta$ $S = k_B Ln\Delta + k_B T \left(\frac{\partial Ln\Delta}{\partial T}\right)_{N,p}$ $V = -k_B T \left(\frac{\partial Ln\Delta}{\partial p}\right)_{N,T}$ $\mu = -k_B T \left(\frac{\partial Ln\Delta}{\partial N}\right)_{p,T}$

En el caso de que el sistema este compuesto por N partículas indistinguibles la función de partición se calcula por medio de la función de partición molecular, q. La cual se relaciona con la función de partición, por ejemplo la canónica, de la siguiente forma:

$$Q(N,V,T) = \frac{[q(T)]^N}{N!} \int e^{-\beta E(r^N)} dr^N, \tag{1.12}$$

donde $\int e^{-\beta E(r^N)} dr^N$ es la intergal configuracional que se define como la contribución a las fuerzas intermoleculares a propiedades termodinámicas.

1.4. Fluctuaciones

Se han clasificado los colectivos según las propiedades termodinámicas que se conservan constantes en todos los microestados. Pero, ¿qué sucede con el resto de magnitudes que no se conservan constantes? El comportamiento de estas variables está basado en una distribución de valores determinada por una varianza, σ_X^2. La distribución más probable que genera en colectivo tienn un valor promedio de la propiedad X pero dentro del colectivo se acepta una serie de microestados cada uno con valores similares al promedio de la propiedad X pero no iguales. La fluctuación entre los valores de la propiedad X de cada microestado y el valor promedio de X produce una dispersión característica que se puede evaluar estadísticamente[1,3,4].

La varianza que genera las fluctuaciones en las propiedades es característica del estado termodinámico, es decir, el valor de varianza depende de las condiciones en las que se encuentra el sistema y de la naturaleza del mismo. De forma general se expresa de la siguiente forma:

$$\sigma_X^2 = \left\langle X^2 \right\rangle - \left\langle X \right\rangle^2. \tag{1.13}$$

En el apéndice (5), tenemos un ejemplo de cómo podemos calcular una propiedad del sistema, κ_T, a partir de las fluctuaciones de la energía y del volumen, respectivamente. En esta parte de la memoria sólo escribiremos las relaciones finales. En el caso del cálculo de la compresibilidad isoterma, κ_T, asociada a las fluctuaciones de volumen, el colectivo correcto es el NpT y la ecuación que las relaciona es,

$$\sigma_V^2 = \left\langle V^2 \right\rangle - \left\langle V \right\rangle^2 = k_B \left\langle V \right\rangle \kappa_T. \tag{1.14}$$

Tenemos que conocer la naturaleza de la propiedad de estudio para poder elegir de forma efectiva el colectivo en el cual vamos a caracterizar nuestro sistema.

1.5. El papel de los modelos de potencial y la simulación molecular

El conocimiento exacto de las propiedades termodinámicas de equilibrio sólo se consigue en unos pocos sistemas basados en modelos simples, como el gas ideal o el cristal armónico[1]. En general los sistemas son demasiado complejos para su estudio sin la utilización de aproximaciones teóricas. Las cuales intentan tener en cuenta aspectos importantes de cada sistema, facilitando su estudio. Con la llegada de los ordenadores y el gran incremento en su capacidad de cálculo, se ha abierto un amplio abanico de posibilidades en torno al tratamiento y enfoque de los sistemas ya que los métodos de simulación computacional y cálculo numérico permiten obtener soluciones esencialmente exactas sobre modelos que pretenden imitar los sistemas reales. Estos modelos son lo suficientemente complejos para poder reproducir de forma aceptable el comportamiento de los sistemas reales.

Las soluciones obtenidas con la simulación computacional y/o cálculo numérico tienen una doble función. Por un lado, permiten comprobar la validez de un modelo propuesto para representar el sistema real. Como ejemplo, el modelo de potencial de interacciones intermoleculares, potencial de Lennard-Jones (LJ) desarrollado para simular argón[5]. Además este modelo es válido para el estudio de un sistema constituido por moléculas esféricas o coloides. Por otro lado, una vez demostrada la fiabilidad de un modelo, se compara el resultado real con el obtenido en la simulación y así hacer predicciones para que finalmente sean juzgadas por el experimento que es el último y verdadero criterio de verificación de la realidad.

Las simulaciones por ordenador tienen como finalidad de obtener las propiedades de un sistema modelo mediante la generación de un gran número de microestados del mismo. El sistema que se simula está formado por un número limitado de moléculas que interaccionan mediante un potencial lo más realista posible. Los microestados, que llamaremos configuraciones en simulación, pueden generarse por dos técnicas diferentes. La primera de ellas es conocida como el método de Monte Carlo (MC)[6] (1953) por la utilización de números generados al azar en el estudio de los sistemas líquidos. La segunda, conocida como Dinámica Molecular (DM)[7] (1956), consiste en el estudio del sistema por medio de la solución de las ecuaciones del movimiento de las moléculas que lo forman.

Fundamento Teórico: Capítulo 2

Simulación. Experimentos *in silica*

2.1. Consideraciones generales en simulación

El capítulo que a continuación se expondrá tiene como meta presentar por un lado los métodos de simulación (Monte Carlo y Dinámica Molecular) y por otro lado las herramientas de simulación, las cuales disminuyen el coste computacional y el número de partículas N necesarias para recrear el sistema macroscópico.

Como para cualquier sistema, el número de componentes, en nuestro caso moléculas y átomos, es básico ya que afecta tanto a sus propiedades como a la forma de abordar el estudio del mismo[4,8]. En la simulación por ordenador se utilizan generalmente un número reducido de moléculas, típicamente $100 \leq N \leq 100000$. Estas limitaciones vienen determinadas por la velocidad de la ejecución del programa[1]. La relación existente entre el tiempo necesario para evaluar las fuerzas o energía potencial del sistema y el número de moléculas es en principio proporcional a N^2. Una buena parte de las técnicas de simulación desarrollades tienen justamente como objetivo reducir esa dependencia cuadrática.

2.1.1. Condiciones de contorno periódicas

Para simular un sistema hay que conseguir generar mediante ordenador un gran número de microestados sobre los que es posible obtener un valor de la propiedad de estudio. Posteriormente se promediarán los valores obtenidos de cada micorestado para dar como resultado el dato final macroscópico[1]. Una vez establecido el potencial de interacción que regirá el comporamiento de las moléculas, se necesita asignar las coordenadas y velocidades de las N partículas que forman el sistema. Según la descripción clásica hay que establecer $6N$ variables.

Los primeros trabajos en simulación[6,7], aparte de desarrollar las técnicas básicas de simulación, demostraron que es posible obtener resultados

termodinámicos correctos utilizando un número reducido de partículas en vez de manejar una cantidad similar a la constante de Avogadro. Pero los problemas que se generan con este procedimiento son los efectos de superficie. Por ejemplo, en el caso del estudio de propiedades macroscópicas del agua, a una temperatura de 25 ^{o}C y con 10^4 moléculas se podría simular un sistema de geometría cúbica de 67 Å o una gota de 41 Å de radio. Con estas dimensiones la proporción de moléculas que se situarían en la superficie sería demasiado grande frente a las que estaría en el seno del sistema. Por lo que estos efectos superficiales generarían una respuesta diferente a las propiedades termodinámicas de *bulk*.

En general en una muestra macroscópica de agua se pueden despreciar los efectos de la materia superficial[1]. Para reproducir el mismo comportamiento en las simulaciones se ha ideado un mecanismo por el que se pueden eliminar los efectos superficiales del sistema. Este metodo se denomina **condiciones de contorno periódicas**[4,8]. Normalmente el método más utilizado es la utilización de cajas de simulación cúbicas, pero existen métodos que aplican las condiciones de contorno periódicas en otro tipo de cajas de simulación, dodecaedro romboédrico u octaedro truncado. En esta memoria se explicará el método estandar que está basado en replicar la celda de simulación de modo que las moléculas siempre encuentren moléculas vecinas con las que interaccionen, evitando así los efectos de superficie, Fig. (2.1). La implantación del método es muy sencilla: cuando una partícula abandona el sistema por un lado, otra molécula en las mismas condiciones aparece por la pared opuesta manteniendo el número de partículas constante. La eliminación de los efectos de superficie genera otro problema y es que existe una periocidad infinita y constante durante todo el sistema. Por ello es necesario que el número de moléculas que contenga el sistema sea suficiente como para evitar que se generen correlaciones entre una partícula y sus imágenes, falseando los valores calculados durante la simulación. A ésto se le conoce como *efecto finito* del sistema.

Otra dificultad que surge con este método es la evaluación de las interacciones, porque el número de moléculas es infinito debido a la periocidad. No es posible medir las interacciones intermoleculares de todas las partículas. Si tenemos en cuenta que las interacciones dependen inversamente de la distancia entre moléculas, podemos ignorar las interacciones entre moléculas situadas a una distancia mayor que un valor denominado *distancia de corte*, r_c, del cual se hablará con detalle en el siguiente apartado.

A pesar de las aproximaciones anteriores, la experiencia previa en la simulación ha demostrado que las condiciones de contorno periódicas tiene, en general, efectos mínimos sobre las propiedades de equilibrio termodinámico cuando se elige adecuadamente el número de moléculas de la caja de

simulación.

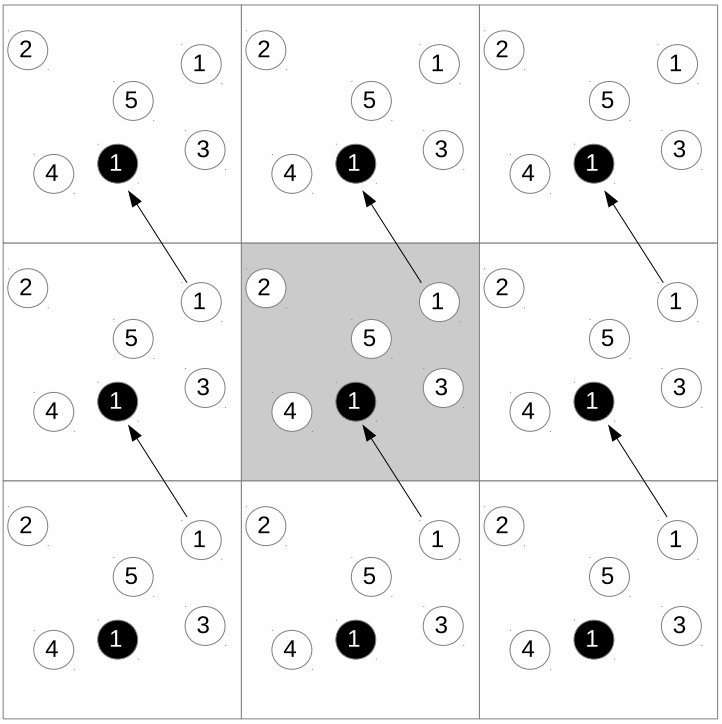

Figura 2.1: Sistema periódico en dos dimensiones. Se repica la celda en negrita 8 veces. Las moléculas pueden entrar y salir de cada caja a través de cada una de las cuatro fronteras. En un ejemplo de tres dimensiones, las moléculas serían libres para cruzar por cualquiera de las seis caras del cubo hacia una de las 26 celdas de simulación que lo rodean.

Imagen mínima

Los programas que utilizan los métodos de Monte Carlo y de la Dinámica Molecular se basan en el cálculo de la energía potencial de cada configuración. En el caso de la Dinámica Molecular también se calculan las fuerzas de cada una de las partículas, a partir del potencial de interacción. Si se considera la contribución a la energía potencial que involucran a una molécula dada (1) suponiendo un potencial de tipo par aditivo, se deben incluir las interacciones entre la molécula (1) y todas las otras moléculas que pertenecen al sistema. En un principio, hay $N-1$ términos en la ecuación de

cálculo de esas fuerzas. Pero se deben incluir también todas las interacciones entre la molécula (1) y las réplicas de esa partícula de las cajas vecinas generadas por las condiciones de contorno periódicas. Esto hace que los términos necesarios para el estudio del sistema tienden a infinito y por supuesto es imposible de evaluar la energía en la práctica.

Una solución es utilizar una función de energía potencial de corto alcance, restringiendo esta suma por medio de una aproximación. Se considera la molécula (1) como centro de una región del mismo tipo y tamaño que la caja de simulación, Fig. (2.2). La molécula (1) interacciona con todas las moléculas cuyo centro se encuentre dentro de esta región, es decir, con las réplicas periódicas más cercanas de las otras $N-1$ moléculas. A este proceso se denomina **criterio de imagen mínima**[4,8]. Esta técnica está implementada en los algoritmos de simulación como consecuencia natural de las condiciones periódicas y fue utilizada en las simulaciones realizadas por Metropolis y colaboradores[6] en 1953.

Los términos de interacción involucrados en el cálculo de la energía potencial son del orden de $N(N-1)/2$. Si pensamos en un sistema de 10000 moléculas este procedimiento resulta dificil de abordar. Existe una aproximación adicional que se denomina **truncamiento del potencial**. Supongamos que el potencial intermolecular se hace cero a partir de una cierta distancia que denominamos distancia de corte, r_c (cutoff). Este valor puede ser igual al radio de corte utilizado para generar la imagen mínima. Durante la simulación sólo se considerarán las energías y fuerzas debidas a las moléculas que se situan a una distancia inferior a r_c. El círculo de la Fig. (2.2) delimita esa área, y en este caso las moléculas 2, 5 y 3 contribuyen a las fuerzas de (1), mientras que la molécula 4 no contribuyen ya que su centro cae fuera del cutoff.

En una caja de simulación de lado L, el número de partículas vecinas consideradas se reducen por un factor de aproximadamente $4\pi r_c^3/3L^3$. La utilización de un radio de corte esférico supone una perturbación pequeña en el sistema, por lo tanto, ese parámetro tiene que ser suficientemente grande para asegurar la fiabilidad del estudio del sistema. En el caso de átomos con potencial tipo Lennard-Jones (LJ), Fig. (2.3),

$$U(r) = 4\epsilon\left[\left(\frac{\sigma}{r}\right)^{12} - \left(\frac{\sigma}{r}\right)^{6}\right], \tag{2.1}$$

el potencial intermolecular se suele truncar a una distancia en torno a $2{,}5-4\sigma$ donde σ es la distancia en la cual el potencial se hace cero y ϵ es la profundidad del potencial. Para asegurar que las dos réplicas de una misma molécula no

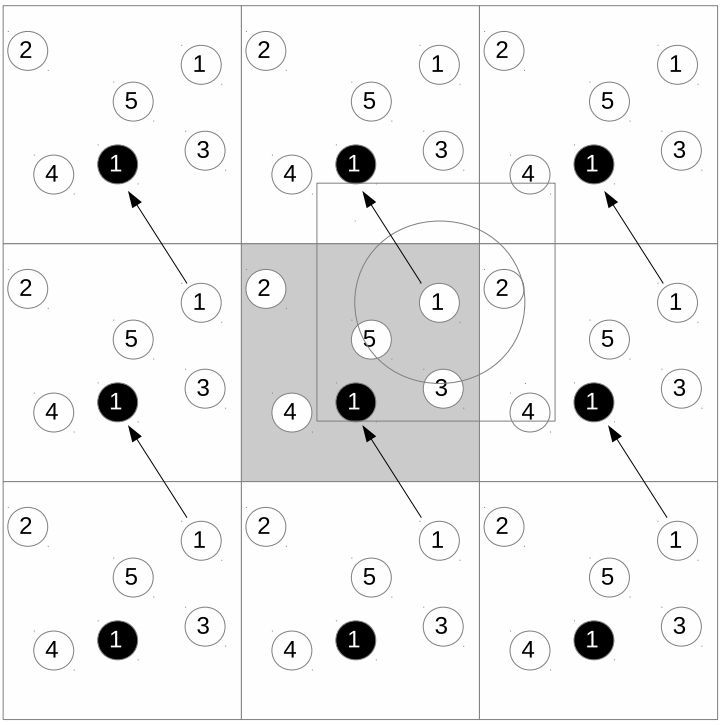

Figura 2.2: Criterio de imagen mínima en un sistema de dos dimensiones. La caja central contiene cinco moléculas. La caja construida en torno al centro de la molécula (1) también contiene cinco moléculas. El círculo representa la distancia a la que se trunca el potencial, r_c.

interaccionan entre sí, es necesario que la distancia de corte del potencial (cutoff) no sea mayor que la mitad del lado de la caja de simulación, L:

$$r_c \leq \frac{L}{2}. \tag{2.2}$$

El método de condiciones de contorno periódicas junto con la utilización del algortimo de la imagen mínima suponen un gran ahorro computacional. No hay que calcular las infinitas distancias entre la molécula (1) y el resto de partículas del sistema. Sino que sólo se determinan las que estén a una distancia menor que el radio de corte. El truncamiento del potencial afecta algo al cálculo de propiedades con respecto al sistema real. Suele realizarse una corrección de largo alcance para diversas propiedades como la energía y la presión[8]. Para ello se supone que a valores de distancias superiores a r_c no hay correlaciones por lo que la función de distribución par es igual a 1.

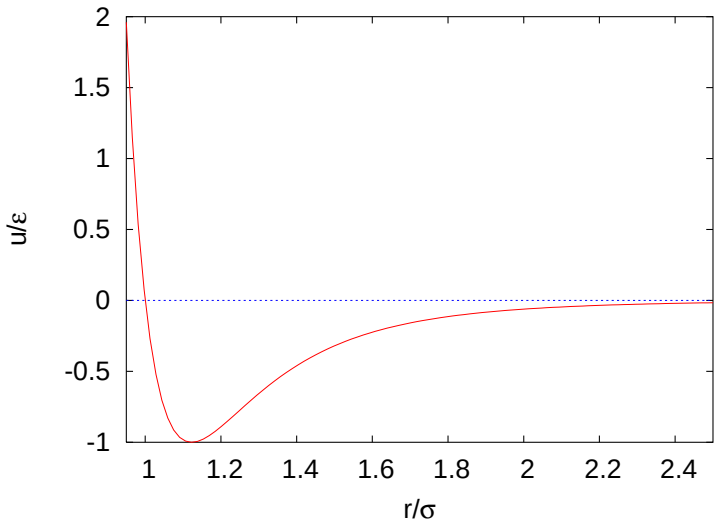

Figura 2.3: Potencial de Lennard-Jones (12-6). σ es valor donde $U(r) = 0$ y ϵ es la profundidad del potencial. Para una fácil localización de estos parámetros se ha representado los valores en unidades reducidas[8]

2.1.2. Fuerzas electrostáticas

Las fuerzas de largo alcance se definen como las fuerzas en las que la interacción espacial no decae a valores menores de r^{-d}, donde d es la dimensionalidad del sistema[4]. Tenemos como ejemplo las interaciones carga-carga entre dos iones o las interacciones dipolo-dipolo entre moléculas. En los apartados anteriores se ha comentado que una forma de simplificar el cálculo de las interacciones del sistema es considerar sólo las que se encuentren a una determinada distancia r_c y dentro de una imagen mínima. Pero nos encontramos con una dificultad cuando lo que nos interesa es evaluar las fuerzas electrostáticas. Porque eliminar las contribuciones que se hacen a esos valores superiores del radio de corte, implica que estamos perdiendo información muy relevante sobre este tipo de fuerzas. Para tener en cuenta las correcciones de largo alcance en sistemas con interacciones culómbicas y/o dipolo-dipolo es necesario utilizar técnicas diseñadas para estos casos concretos.

El **método Ewald**[9,10,11,12], también conocido como sumas de Ewald se aplica a un sistema de cargas puntuales. El cálculo de las interacciones entre una carga q cualquiera y todas las demás, incluyendo las réplicas de las cajas de contorno periódico, se basa en apantallar a cada carga con una gausiana de signo contrario a q quitando la contribución de la propia carga q. Estas

gausianas pueden ser muy anchas, con lo que el apantallamiento es muy poco efectivo o pueden ser estrechas aumentando el apantallamiento.

La introducción de estas funciones hace que la interacción culómbica que hay entre la carga q y todas las demás decaiga de forma más rápida y converja a distancias menores de lo normal. Otra consecuencia de la utilización de las gausianas es que se hace imprescindible contrarrestar las aportaciones de las gausianas acopladas a cada carga. Esta suma se lleva a cabo en el espacio recíproco. Gracias a la utilización de las transformadas de Fourier podemos tratar matematicamente la suma en el espacio recírpoco lo que acelera enormemente la simulación. Con este método, la dependencia del costecomputacional decae a $N^{3/2}$, siendo N el número de cargas.

Otro procedimiento, basado en las sumas de Ewald, es el **método PME**. Esta técnica[13,14] trata a las cargas del sistema como puntos dentro de una malla y después se estudian las interacciones agrupadas en dos categorías: interacciones partícula-partícula y partícula-malla. Lo primero que se realiza es interpolar las cargas dentro de una malla la cual se define por la ecuación de Poisson. Luego se resuelve esta ecuación usando una Transformada de Fourier Rápida (FFT), lo que hace dismimuir el coste computacional a $NlogN$, donde N es el número de de puntos de tranformadas de Fourier discretas[8].

2.2. Dinámica Molecular

La Dinámica Molecular es la solución natural a los problemas propuestos por la Mecánica Estadística ya que se basa en la solución de las ecuaciones de movimiento de las N partículas que forman el sistema obteniendose las posiciones y velocidades de las misma[1,4,8]. Integrando la ecuaciones de Newton, ls configuraciones generadas corresponden al colectivo NVE. Con estos datos es posible calcular cualquier propiedad macroscópica realizando un promedio temporal sobre las propiedades microscópicas:

$$\bar{X} = \langle X \rangle_t \tag{2.3}$$

De este modo, la diferencia fundamental con el otro método de simulación (MC) es el hecho de que la secuencia de microestados obtenidas no es aleatoria, sino que se genera en cada configuración al solucionar las ecuaciones de movimiento. Esto permite el cálculo de propiedades dependientes del tiempo y de propiedades de transferencia de calor y materia, las cuales no son directamente accesibles por el método de Monte Carlo. Para una molécula j

dada perteneciente a un sistema será necesario resolver una ecuación del tipo

$$m_j \frac{d^2 r_j}{dt^2} = F_j = -\nabla_j U(\mathbf{r}^N), \tag{2.4}$$

donde m_j es la masa de la partícula, r_j su vector posición y F_j la fuerza que actua sobre ella, la cual se puede obtener como el gradiente del potencial $U(\mathbf{r}^N)$. Es fácil darse cuenta de que la ecuación (2.4) es la aplicación de la segunda ley de Newton, por lo cual el movimiento de las mismas dependerá de sus masas.

Como método práctico para resolver estas ecuaciones podemos utilizar un desarrollo de Taylor, con lo que es posible obtener las coordenadas y velocidades tras un cierto intervalo de tiempo Δt[1]:

$$r_j(t + \Delta t) = r_j(t) + v_j(t)\Delta t + \frac{1}{2} a_j(t)\Delta t^2 + \frac{1}{3!}\left(\frac{d^3 r_j}{dt^3}\right)\Delta t^3 \ldots \tag{2.5}$$

$$v_j(t + \Delta t) = v_j(t) + a_j(t)\Delta t + \ldots \tag{2.6}$$

Este desarrollo matemático se simplifica truncando la serie en un cierto término. Una posibilidad es truncar despreciando los términos de orden superior a las aceleraciones. Este hecho implica que las aceleraciones se mantengan constantes durante el estudio del sistema, es decir que las fuerzas se conserven en el tiempo total de simulación. De esta forma se obtiene la trayectoria del sistema calculando la aceleración a partir del campo de fuerzas e introduciendola en la expresión (2.5) y (2.6), quedando entonces:

$$a_j(t) = -1/m_j \nabla_j U(\mathbf{r}^N). \tag{2.7}$$

A continuación se obtienen las nuevas coordenadas y velocidades a un tiempo $t + \Delta t$ y se puede además recalcular las fuerzas que actuan sobre cada partícula y resolver el sistema para un segundo tiempo $t + 2\Delta t$. Existen varios algoritmos que disminuyen el error que se comete por el truncamiento de las Ec. (2.6) a un segundo orden sin incrementar por ello los cálculos necesarios para resolver las ecuaciones. Uno de estos procedimientos más sencillos y que mejor comportamiento presenta es el **algoritmo de Verlet[15]**, el cual se expondrá brevemente. Si partimos del desarrollo de Taylor en un tiempo t, obtenemos una ecuación del tipo:

$$r_j(t + \Delta t) = r_j(t) + v_j(t)\Delta t + \frac{1}{2} a_j(t)\Delta t^2 + \frac{1}{3!}\left(\frac{d^3 r_j}{dt^3}\right)\Delta t^3 + O(\Delta t^4), \tag{2.8}$$

$$r_j(t - \Delta t) = r_j(t) - v_j(t)\Delta t + \frac{1}{2} a_j(t)\Delta t^2 - \frac{1}{3!}\left(\frac{d^3 r_j}{dt^3}\right)\Delta t^3 + O(\Delta t^4), \tag{2.9}$$

donde $O(\Delta t^4)$ son los términos que dependen del incremento Δt a la cuarta o potencias superiores a este orden. Si sumamos las ecuaciones Ec. (2.8) y Ec. (2.9) resulta:

$$r_j(t+\Delta t) + r_j(t-\Delta t) = 2r_j(t) + a_j(t)\Delta t^2 + O(\Delta t^4), \tag{2.10}$$

si despreciamos $O(\Delta t^4)$.

$$r_j(t+\Delta t) = 2r_j(t) + a_j(t)\Delta t^2 - r_j(t-\Delta t). \tag{2.11}$$

Por medio de esta expresión podemos conocer las futuras posiciones de las moléculas a un tiempo $t+\Delta t$ a partir de la aceleración y de las coordenadas de las mismas en tiempos anteriores, cometiendo sólo un error del orden de $O(\Delta t^4)$.

La dificultad de este método reside en la elección del valor de Δt. Debe ser lo suficientemente pequeño para que el error que se cometa en el truncamiento de la serie de Taylor no afecte a la fiabilidad de los resultados. Por este motivo el valor de Δt tendrá que ser, por ejemplo, menor que el tiempo característico de las vibraciones moleculares que se intenta estudiar. Y por otro lado, el valor debe ser lo bastante grande como para que el sistema tenga un tiempo razonable en el que se produzcan los cambios necesarios o que los puntos recogidos de los microestados sean estadísticamente aceptables. Normalmente se suele utilizar un tiempo en torno a 1 fs como Δt. Con este parámetro es obligado cubrir un tiempo de simulación del orden del nanosegundo, lo que equivale a simular 10^6 microestados[1]. El objetivo de este método es que la generación de estas configuraciones permita estudiar el sistema en un determinado estado termodinámico (recordar que también se pueden hacer estudios fuera del equilibrio) del que sólo se conocen unas pocas variables.

Al tratarse de una dinámica newtoniana, en la cual se conserva la energía total del sistema, estaríamos trabajando el colectivo microcanónico, NVE. Pero es posible realizar las simulaciones bajo otros colectivos (como se ha realizado durante el doctorado). Por ejemplo en el caso del colectivo canónico, NVT, para mantener la temperatura constante se puede aumentar o disminuir las velocidades de las partículas, de forma que la temperatura calculada a partir de ellas en un determinado instante coincida con la temperatura requerida para la simulación. Esta relación viene determinada por la siguente ecuación[8]:

$$\sum_{i=1} \frac{1}{2} m_i v^2 = \frac{N_{gl}}{2} kT, \tag{2.12}$$

donde N_{gl} es el número de grados de libertad del sistema completo. Si la temperatura calculada según la ecuación (2.12) es demasiado alta, "sólo" hay

que disminuir las velocidades, mientras que si es demasiado baja se aumentan. Para que las configuraciones generadas con el reescalado de la velocidades correspondan con el colectivo se introduce un factor λ. Para cada tipo de termostato nos encontramos con diferentes expresiones de este factor, en esta memoria sólo describiremos el factor λ para el termostato de Berendsen[16].

$$\lambda = \left[1 + \frac{\Delta t}{\tau_T}\left(\frac{T_0}{T} - 1\right)\right]^{1/2}, \tag{2.13}$$

donde Δt es el paso de tiempo del algoritmo de integración de las ecuaciones de movimiento de las partículas, T_0 es el valor de la temperatura objetivo, T es la temperatura instantánea de la simulación y τ_T es una constante.

El caso de los barostatos utilizados en DM es más complicado. Se basan en modificaciones, en la caja de simulación, en las posiciones y en los momentos de las partículas para mantener la presión del sistema controlada. Pero al igual que el termostato de Berendsen, el procedimiento de su barostato[16] también están basados en un factor μ_{ij}, el cual viene definido por un tensor de dimensiones ij:

$$\mu_{ij} = \delta_{ij} - \frac{n_{PC}\Delta t}{3\tau_p}\beta_{ij}\left(p_{0ij} - p_{ij}\right), \tag{2.14}$$

siendo δ_{ij}, n_{PC} y τ_p constantes, Δt es el paso de tiempo elegido durante la simulación, p_{0ij} es la presión objetivo y p_{ij} la presión actual en cada paso.

2.3. Monte Carlo

Este método es una herramienta fundamental en la simulación molecular por ordenador y se basa en la obtención de las propiedades macroscópicas del colectivo mediante un promedio de configuraciones (microestados) del mismo[8]. Estas son generadas al azar por un procedimiento que garantiza que las distintas configuraciones aparecen en la proporción dada por la función de partición del colectivo NVT (o NpT).

Vamos a hacer un pequeño paréntesis para ilustrar la potencia de un estudio de un sistema basado en la probabilidad. El objetivo es conocer si un dado está trucado y tiene una cara más pesada que las otras, lo cual sería muy útil si somos el responsable de un casino. Podemos aplicar las dos visiones de la hipótesis ergódica a nuestra investigación. Generar réplicas al azar para obtener un conjunto suficientemente grande para formar un colectivo o analizar minuciosamente nuestro sistema, el dado, durante una tirada. Esta última visión se podría hacer de la siguiente manera. Se monotoriza la trayectoria de los 8 vértices del dado colocando un pequeño sensor en cada uno

de ellos, todos los sensores deben pesar lo mismo y estar en las posiciones correctas para no afectar a la medida. Con pocas tiradas, si somos realmente perfectos con una tirada valdría, podremos observar que existe una posición predominante, la cual equivale a la que mantiene la cara más pesada orientada hacia el tapete. Esa es el lado del dado que pesa más, es el que está más atraido por la gravedad. Por otro lado, podemos dejarnos en manos de la probabilidad y lanzar el dado unas miles de veces. Puede resultar más cansado para nuestro brazo pero es mucho más efectivo desde el punto de vista matemático y tecnológico. Después de las suficientes tiradas nos daremos cuenta de que hay una cara del dado que sale mayoritariamente. Por lo tanto la cara sobrepesada es la opuesta. La segunda forma de abordar el problema nos ofrece una solución más rápida e inmediata. Este es un sencillo ejemplo sobre cómo a veces es más útil para estudiar un sistema utilizar la probabilidad asociada al mismo que una descripción minuciosa.

Pero volvamos a la descripción del método de análisis que está basado en probabilidad y números al azar. Existen simulaciones de Monte Carlo en todos los colectivos. Básicamente lo que se hace en este tipo de simulación es calcular propiedades promedio a lo largo de millones de configuraciones del sistema. A continuación se expondrán y desarrollarán las expresiones necesarias para obtener las propiedades macroscópicas del colectivo NpT, pero de forma análoga se puede hacer el mismo estudio y desarrollo para el colectivo NVT. Para generar una configuración perteneciente al colectivo NpT, necesitamos conocer la posición de todas las partículas del sistema y el volumen del mismo. El valor de propiedades como la energía interna U o el volumen V de cada configuración fluctuará en torno a un valor medio una vez que el sistema se encuentre en equilibrio termodinámico. El promedio de estas variables es lo que se obtiene como resultado de una simulación NpT. Es necesario especificar que el método de Monte Carlo sólo se aplica a sistemas en equilibrio termodinámico, ya que el balance detallado que acepta las nuevas configuraciones, se basa en la evaluación de propiedades enmarcadas en esas condiciones termodinámicas.

La utilización del balance detallado nos asegura que las configuraciones que estamos generando en la cadena de Markov (en líneas sucesivas se definirá), están dentro del colectivo y podemos obtener la función de partición del mismo. Podríamos basarnos en el principio de reversibilidad microscópica para obtener estas configuraciones pero si cumplimos el balance detallado, un nivel más de exigencia, nos aseguramos la representatibilidad de las nuevas configuraciones.

Entremos en más detalle sobre el **balance detallado**. Se basa en que el número medio de movimientos aceptados desde la configuración inicial, i, es exactamente igual al numero de movimientos que regresan a la configura-

ción inicial. Pero antes debemos presentar el **principio de reversibilidad microscópica**, que dice que la probabilidad de flujo de una configuración a otra debe ser igual. Esto de representa en la siguiente relación matemática:

$$P_i \pi(i, i+1) = P_{i+1} \pi(i+1, i), \tag{2.15}$$

siendo P_i y P_{i+1} las probabilidades de encontrar al sistema en la configuración i y $i+1$, respectivamente, $\pi(i, i+1)$ es la probabilidad de transición de i a $i+1$ y en el caso de $\pi(i+1, i)$ la transición es de $i+1$ a i. Si aplicamos el sumatorio de i a la expresión anterior, llegamos a la siguiente definición:

$$\begin{aligned} \sum_i P_i \pi(i, i+1) &= \sum_i P_{i+1} \pi(i+1, i) = P_{i+1} \sum_i \pi(i+1, i) = P_{i+1} * 1 \\ P_{i+1} &= \sum_i P_i \pi(i, i+1) \end{aligned} \tag{2.16}$$

A partir de la Ec. (2.15), podemos llegar a la criterio de aceptación de Metropolis Ec. (2.22) que hemos escrito en la memoria. La probabilidad de transición $\pi(i, i+1)$ depende directamente de dos tipos de factores: la probabilidad de generar una configuración $i+1$ a partir de la configuración i, y de la probabilidad de acceptación de un cambio en la configuración i para llegar a la nueva configuración $i+1$. Es decir,

$$\pi(i, i+1) = \alpha(i, i+1) P_{ac}(i, i+1) \tag{2.17}$$

y lo mismo para la transformación de $i+1$ a i

$$\pi(i+1, i) = \alpha(i+1, i) P_{ac}(i+1, i). \tag{2.18}$$

Si sustituimos la Ec. (2.17) y (2.18) en la relacion general (2.15) obtenemos,

$$P_i \alpha(i, i+1) P_{ac}(i, i+1) = P_{i+1} \alpha(i+1, i) P_{ac}(i+1, i), \tag{2.19}$$

además como α es una matriz simétrica, $\alpha(i, i+1) = \alpha(i+1, i)$ y la expresión de arriba se simplifica,

$$\begin{aligned} P_i P_{ac}(i, i+1) &= P_{i+1} P_{ac}(i+1, i) \\ \frac{P_{ac}(i, i+1)}{P_{ac}(i+1, i)} &= \frac{P_{i+1}}{P_i}. \end{aligned} \tag{2.20}$$

Por lo tanto, para poder generar y aceptar una nueva configuración $i+1$ desde i se tienen que evaluar la relación de P_i y P_{i+1}, para que $P_{ac}(i, i+1)$

sea favorable. La forma de evaluar la aceptación de la nueva configuración es comparar las probabilidad P_i y P_{i+1} de la siguiente manera.

$$\begin{aligned} P_{ac}(i,i+1) &= 1 \qquad\qquad P_{i+1} \geq P_i \\ P_{ac}(i,i+1) &= P_{i+1}/P_i \qquad P_{i+1} \geq P_i \end{aligned} \tag{2.21}$$

Esto significa que si la probabilidad de encontrar la configuración $i+1$ es mayor que la probabilidad de encontrar la configuración i, la probabilidad de aceptación es de 1, es decir, se acepta la nueva configuración. Si por el contrario P_{i+1} es menor que P_i, la probalidad de aceptación es P_{i+1}/P_i. Otra forma de expresar esta misma condición es:

$$P_{ac}(i,i+1) = minimo\left(1, \frac{P_{i+1}}{P_i}\right) \tag{2.22}$$

En el primer apéndice hemos definido el término P_i en función de la energía del microestado o configuración (5.36) para el colectivo NVT, pero si suponemos que estamos en el colectivo NpT y que no sabemos cual es la función de partición, lo cual es cierto, sólo podremos conocer el factor de Boltzmann para cada configuración de dicho colectivo:

$$P_i \propto e^{-\beta(E_i+pV_i)+N\ln(V_i)} \tag{2.23}$$

donde V_i y U_i son el volumen y la energía interna de la configuración i respectivamente. El cociente de estas probabilidades de aparición en el colectivo NpT viene dado por el cociente de los factores de Boltzmann de las mismas:

$$\frac{P_{i+1}}{P_i} = \frac{e^{-\beta(E_{i+1}+pV_{i+1})+N\ln(V_{i+1})}}{e^{-\beta(E_i+pV_i)+N\ln(V_i)}} = \frac{e^{-\beta H_{i+1}}}{e^{-\beta H_i}}. \tag{2.24}$$

De acuerdo a la Ec. (2.22), si $H_{i+1} > H_i$ el cambio se acepta con probabilidad 1. Si $H_{i+1} < H_i$ el cambio se acepta con probabilidad $e^{-\beta(H_{i+1}-H_i)}$. En caso de rechazo, la configuración $i+1$ se sustituirá por i, y sus propiedades se cuentan de nuevo para el promedio que se hace a lo largo de la simulación según la ecuación (2.25). Una vez explicado este procedimiento se puede definir la **cadena de Markov** como la serie de configuraciones donde una nueva configuración es una modificación de la configuración inmediatamente anterior, siendo esta modificacion aceptada por medio del criterio del balance detallado.

Básicamente, el algoritmo propuesto por Metrópolis[6] para generar la cadena de Markov se resume en el siguiente esquema:

1. Determinar el factor de Boltzmann de la configuración i, Ec. (2.23).
2. Modificar la configuración i para obtener la configuracion $i+1$.
3. Determinar el factor de Boltzmann de la nueva configuración $i+1$, Ec. (2.23) para $i+1$.
4. Aceptar o rechazar el cambio sobre la configuración i de acuerdo al criterio de Metrópolis, Ec. (2.22).
5. Volver al primer paso con la configuración que haya resultado.

La evaluación de factores de Boltzmann es la esencia de toda simulación de MC. Pero existen aspectos concretos de cada colectivo que hay que tener encuenta para la generación correcta de las nuevasa configuraciones. Por ejemplo en el colectivo NpT, el volumen V de la configuración se halla muy fácilmente como el lado de la caja de simulación al cubo, si la caja es cúbica, o a partir del producto mixto de los vectores que definen la caja de simulación, si no lo es. Entendiendo el cálculo del factor de Boltzmann de una configuración, podremos realizar fácilmente los pasos 1, 3 y 4 del algoritmo. El paso 2 conlleva una modificación en la configuración i para producir la $i+1$. Ésta puede ser un cambio de la posición de una partícula o en el cambio de volumen del sistema (con el consiguiente reescalado de las coordenadas de todas las partículas).

Después de haber generado todas las configuraciones necesarias dentro del colectivo pormedio del método de Monte Carlo, expuesto en los párrafos anteriores, podemos calcular el promedio del colectivo de las propiedades termodinámicas. Para calcular el promedio de una magnitud X como

$$\langle X \rangle = \frac{\sum_{i=1}^{M} X_i}{M}, \tag{2.25}$$

donde M es el número de configuraciones que se generan a lo largos de la simulación y X_i es el valor de la magnitud X en la configuración i.

2.4. Monte Carlo Híbrido. *Hybrid Monte Carlo* (HMC)

Existe una técnica que combina los dos métodos anteriores de forma que aprovecha las ventajas de ambos algoritmos. Esta técnica es el *Hybrid Monte Carlo* (HMC)[17,18], al igual que con otros términos se usará el nombre en inglés. Este nuevo método de simulación fue desarrollado por Duane *et al.*

en 1987 y se basa en la idea de obtener los movimientos de las partículas por medio de una dinámica molecular y posteriormente se evalua la aceptación de las nuevas configuraciones con un algoritmo de Metropolis[8,4]. En un primer momento puede parecer que no hay ninguna ventaja en este procedimiento, sin embargo el paso de tiempo que se puede utilizar en el la DM bajo el control del MC es muy superior al que se maneja en el una DM convencional, llegando hasta los 15-25 fs. Así el muestreo se hace de forma más rápida y eficaz en sistemas con un gran número de partículas. Muy relacionado con este método, se ha desarrollado una aproximación del HMC, que reproduce los mismos resultados en los procesos de nucleación estudiados. Se basa en la acceptación del 100 % en los algoritmos de Metropolis y la utilización de una dinámica molecular en el colectivo NpT[19]. Este hecho nos permite sortear el problema de las rígidas condiciones de microrreversibilidad y simplecticidad que deben cumplir las configuraciones generadas según un HMC estricto. En el caso de la nucleación (tema de esta memoria), la combinación de HMC y el algoritmo de *Umbrella Sampling* (ver Sección 2.5) es ya un procedimiento estandar para el cálculo de barrera de energía libre[20].

2.5. Umbrella sampling (US)

Esta técnica de simulación se basa en el cálculo de propiedades que están en fuera del equilibrio a través de una simulación de Monte Carlo. Imaginemos que el estado que queremos evaluar está a una distancia energética de ΔU respecto del estado en equilibrio, U_0.[21] Esto quiere decir que su función de partición (por ejemplo en NVT) se puede escribir como:

$$\begin{aligned} Q(N,V,T) &= \sum e^{-\beta\Delta U} e^{-\beta U_0} = Q_0(N,V,T)\frac{\sum e^{-\beta\Delta U} e^{-\beta U_0}}{Q_0(N,V,T)} \\ &= Q_0(N,V,T)\left\langle e^{-\beta\Delta U}\right\rangle_0, \end{aligned} \tag{2.26}$$

donde $\left\langle e^{-\beta\Delta U}\right\rangle_0$ es el promedio del factor del Boltzman para la diferencia de energia calculada a través de una simulación en el equilibrio.

De esta forma podremos calcular propiedades termodinámicas de un sistema que se encuentra en casi equilibrio:

$$\begin{aligned} \langle A\rangle_{NVT} &= \frac{\sum A e^{-\beta\Delta U} e^{-\beta U_0}}{Q(N,V,T)} = \frac{Q_0(N,V,T)}{Q(N,V,T)}\frac{\sum A e^{-\beta\Delta U} e^{-\beta U_0}}{Q_0(N,V,T)} \\ &= \frac{\left\langle A e^{-\beta\Delta U}\right\rangle_0}{\left\langle e^{-\beta\Delta U}\right\rangle_0}, \end{aligned} \tag{2.27}$$

En todo este desarrollo es necesario conocer ΔU y es ahí donde radica la complicación del método. La forma de acceder a esa energía es por medio de

una función de "bias", W, es decir, una función que genere esta contribución equivalente a la diferencia de energías en el factor de Boltzman, $U_0 = U + W$.

Esta técnica es muy utilizada en el cálculo de propiedades que estan fuera del equilibrio, como es nuestro caso que calculamos barreras de nucleación. A través del *Umbrella Sampling* podemos "dirigir" el crecimiento del núcleo de la fase estable dentro de la fase metaestable para que se produzca la transformación completa a la fase estable. Para más detalle sobre este proceso se recomienda ir al Cap. 4 donde se explican estos conceptos sobre la nucleación e ir a la Sec. 4.5.2 para encontrar una explicación más detallada sobre esta técnica aplicada al cálculo de barrera de nucleación.

Fundamento Teórico: Capítulo 3

Modelos de potencial de agua

Desde los primeros estudios por simulación del agua, se han propuesto una gran cantidad de modelos de agua. Sabemos que la molécula de agua es flexible, polarizable y de unas determinadas dimensiones y geometría. Por lo tanto el modelo que se debería utilizar para representar la molécula de agua tendría que seguir estas directrices. Pero es en este punto del diseño de un modelo de potencial donde cabe preguntarse por el coste computacional que deberemos invertir en cada simulación para representar todas las propiedades del agua. Como respuesta de esta pregunta aparecen los modelos rígidos y no polarizables, es decir, no presentan flexión en el enlace H-O-H, ni vibración de los enlaces O-H, ni modificaciones en la distribución electrónica molecular. Aceptamos que se pierde información sobre la flexibilidad y la polarización de la molécula del agua, pero a cambio se gana rapidez computacional. El coste de simulación de la representación de los grados de libertad vibracional es elevado frente a la información adicional que se obtiene de esos modelos. Sólo recientemente, se han propuestos modelos polarizables con buenos resultados globales? [22] pero el el coste computacional sigue siendo una gran desventaja de estos nuevos potenciales. Por esa razón y porque el cálculo de las propiedades del sistema es muy similar a los valores experimentales, se utilizan de forma estandar y generalizada los modelos rígidos y no polarizables.

Los modelos de potencial de agua[23,24,25,26,27,28] que se muestra en la Tabla (3.1) son los más "populares" y usados en la mayoría de los trabajos de simulación sobre agua. Los modelos que mejor resultados dan en simulación tienen el centro Lennard-Jones (LJ) sobre el átomo de oxígeno y una geometría molecular determinada, habitualmente con una distancia O-H de 0.9572 Å y un ángulo de 104,52º a excepción del modelo SPC, del cual se hablará a continuación. En general se pueden hacer tres grupos de modelos atendiendo al número de centro que se han utilizado para describir el modelo:

1. **Modelos de tres centros:** TIP3P[23], SPC[24]

   Propuestos por Jorgensen y Berendsen, respectivamente, se caracteri-

zan porque la carga negativa está localizada sobre el átomo de oxígeno y la positiva está colocalada sobre los dos átomo de hidrógeno. En el modelo SPC no se utilizan valores experimentales de los parámetros moleculares como las distancias O-H o los ángulos H-O-H; sino que se toma como distancia O-H 1 Å y 109º como ángulo H-O-H. Una modificación de este potencial es el SPC/E, también hecha por Berendsen, aumenta ligeramente la carga, ya que esto supone que la energía de polarización puede ser sumada a la energía interna del líquido cuando se ajustan los parámetros del potencial a la entalpía de vaporización del agua real, mejorando las predicciones del modelo original.

2. **Modelos de cuatro centros:** TIP4P[23], TIP4P/Ew[29], TIP4P/2005[27], TIP4P/Ice[28]

   El modelo base, TIP4P, fue desarrollado por Jorgensen. Emplean los parámetros experimentales de distancias O-H y ánguloH-O-H. El centro de interacción Lennard-Jones está también sobre el átomo de oxígeno y las dos cargas positivas localizadas en las posiciones de los Hidrógenos. Pero la colocación de la carga negativa, que en el modelo anterior se situaba sobre el oxígeno, en estos modelos se situa a lo largo de la bisectriz del ángulo molecular H-O-H.

3. **Modelos de cinco centros:** TIP5P[25]

   Propuesto por Mahoney[25] y el propio Jorgensen, la carga negativa se divide en dos cargas parciales negativas en las posiciones de los "pares de electrones no enlazantes del oígeno". Este modelo recuerda mucho al utilizado en la década de los 70, el modelo ST2[26].

4. **Modelos Coarse-Grained:** mW[30], CSW[31,32], CCM[33]

   Este tipo de modelos se están haciendo muy populares y utilizados por la comunidad científica por la rapidez computacional que conllevan. Cada uno de los tres modelos presentados tienen sus propias características y se recomienda para más detalle leer las respectivas citas que se ofrecen en la memoria. Sólo decir que con el modelo desarrollado por V. Molinero[30] se ha estudiado la cristalización del modelo[34], ofreciendo información importante sobre la controversia de los escenarios teóricos del agua (ver Sección (5) de esta memoria). Sobre este mismo tema nos encontramos el trabajo de Stokely *et. al*[35] donde utilizano el modelo CCM, consiguen reproducir un escenario sin punto crítico líquido-líquido pero con la línea de equilibrio líquido-líquido, a partir de un escenario con punto crítico líquido-líquido.

Tabla 3.1: Parámetros de potencial para los distintos modelos de agua. d_{OH} es la distancia entre oxígeno e hidrógenos, H-O-H el ángulo formado por los hidrógenos y el oxígeno, σ cuando el potencial se hace cero para cada modelo, ϵ/k la profundidad del potencial en cada caso, q_H la carga sobre el hidrógeno, d_{OM} y d_{OL} son las distancias entre los puntos M y L característicos para cada modelo como se explico en el texto.

Modelo	d_{OH} (Å)	H-O-H	σ (Å)	(ϵ/k) (K)	q_H (e)	d_{OM} (Å)	d_{OL} (Å)
TIP3P	0.9572	104.52	3.1506	76.54	0.417	0	-
SPC	1.0	109.47	3.1656	78.20	0.41	0	-
SPC/E	1.0	109.47	3.1656	78.20	0.423	0	-
TIP4P	0.9572	104.52	3.1540	78.02	0.52	0.15	-
TIP4P/Ew	0.9572	104.52	3.1643	81.90	0.524	0.125	-
TIP4P/Ice	0.9572	104.52	3.1668	106.1	0.5897	0.1577	-
TIP4P/2005	0.9572	104.52	3.1589	93.2	0.5564	0.1546	-
TIP5P	0.9572	104.52	3.1200	80.51	0.241	-	0.70

Después de la enumeración de los tipos de modelos se expondrán las características más importantes de alguno de los modelos citados. El modelo TIP4P[23] tiene la carga negativa localizada en un punto M, que está situado a una distancia d_{OM} del átomo de oxígeno en la bisectriz del ángulo H-O-H en dirección a los hidrógenos. En el modelo TIP3P[23], la carga negativa se localiza directamente sobre el oxígeno. Ninguno de estos modelos son capaces de reproducir correctamente propiedades termodinámicas, tales como el máximo de densidad o el punto de fusión del agua por lo que es necesario modificaciones de sus parámetros moleculares. De esta manera y con el espíritu de poder reproducir de la mejor forma la mayor cantidad de propiedades termodinámicas, nacen los nuevos modelos de potencial del agua. Estos modelos son: TIP4P/Ew[29], TIP4P/2005[27] y TIP4P/Ice[28]. Más concretamente los dos primeros se ajustaron para la reproducción del máximo de densidad a presión ambiente del agua líquida en función de la temperatura y el último TIP4P/Ice para dar un buen valor de la temperatura de fusión.

Las diferencias de parámetros entre los modelos de agua son muy importantes porque se ven reflejadas directamente en los tiempos de simulación

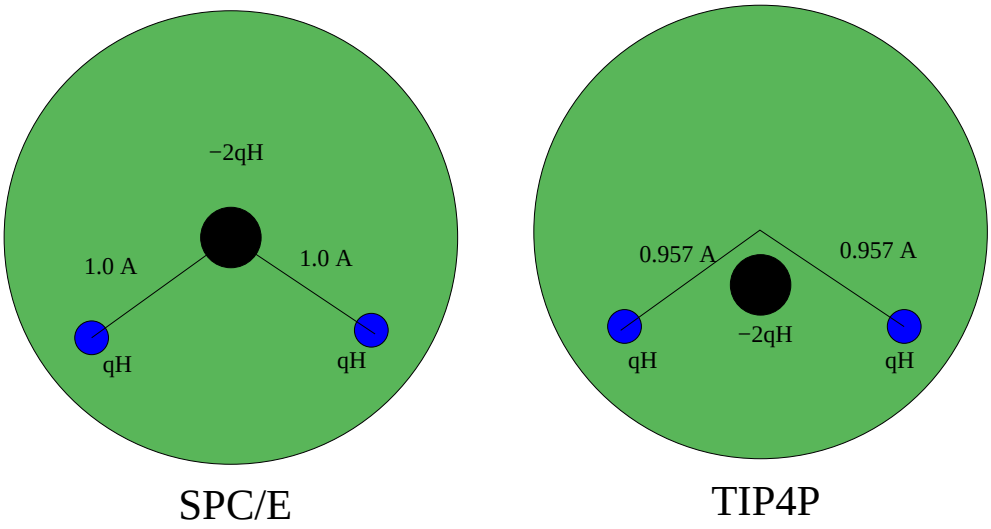

Figura 3.1: Representación esquématica de los modelos SPC/E y TIP4P. Los círculos verdes representan las esferas LJ. Los círculos negros los puntos de carga negativa y los círculos azules los de carga positiva. Las líneas representan los enlaces.

requeridos para el cálculo de las propiedades de estudio. Por ejemplo, los modelos SPC requieren la determinación de 9 distancias centro-centro. Los TIP4P requieren 10 (9 distancias carga-carga y la interacción LJ) y el modelo TIP5P necesita 17 (16 distancias carga-carga y la interacción LJ). El coste computacional guarda una relación $1 : 1{,}1 : 1{,}9$ respectivamente.

En la actualidad los avances en el diseño de los modelos de agua se basan en la incorporación de la flexibilidad y polarizabilidad. Estas nuevas modificaciones mejoran las propiedades predichas por los anteriores modelos. Además nos permiten calcular las magnitudes a las cuales los modelos rígidos y no polarizables son incapaces de acceder, véase el caso de reproducir un espectro de IR o Raman por un modelo rígido. En esta memoria se presenta un nuevo potencial de agua flexible el cual mantiene el nivel de exigencias y calidad que se le pide al modelo TIP4P/2005 y además ofrece información sobre la flexibilidad molecular y espectroscópica del agua. Este modelo lleva por nombre, TIP4P/2005f y se explicará, tanto sus parámetros como los resultados del mismo en el Capítulo (3).

Fundamento Teórico: Capítulo 4

Nucleación. El fin de los estados metaestables

4.1. Introducción

En esta sección de la memoria se darán unas pinceladas sobre el fenómeno de la nucleación. Pero antes es necesario enmarcar este proceso en un escenario termodinámico. Para ello partiremos de los estados metaestables. El ejemplo con más recurrencia académica es el diamante. Esta estructura no es estable termodinámicamente en condiciones ambientes, la configuración atómica estable para estas condiciones es el grafito. Aún así, seguimos comprando diamantes y decimos que son para toda la vida, lo cual es cierto. Esto se debe a que en la estabilidad participa una variable cinética: el tiempo que necesita el diamante para que se transforme a grafito es muy elevado. La combinación de factores cinéticos y de termodinámicos hacen que una sustancia sea un estado metaestable, en este ejemplo un sólido metaestable. Termodinámicamente no es estable pero existe en la naturaleza por motivos cinéticos.

La Termodinámica contempla y estudia los estados metaestables a partir de la definición de los límites de estabilidad. Existe la **linea binodal** entre dos estados termodinámicos, la cual establece el punto donde los potenciales químicos de dos estados son iguales. Por otro lado, podemos calcular la línea espinodal, que es la frontera entre los estados metaestables y los inestables. De esta forma queda definida por estas dos líneas una región donde se encuentra una fase metaestable de una sustancia, como el agua sobrecalentada y sobreenfriada. Podemos encontrar una respresentación esquemática sobre la línea binodal y las espinodales en la Fig. 4.1.

El agua hierve a 100 ^{o}C (temperatura que define la binodal líquido-vapor a presión ambiente) y congela a 0 ^{o}C (temperatura de la binodal líquido-sólido a presión ambiente). Es posible tener agua líquida a más de

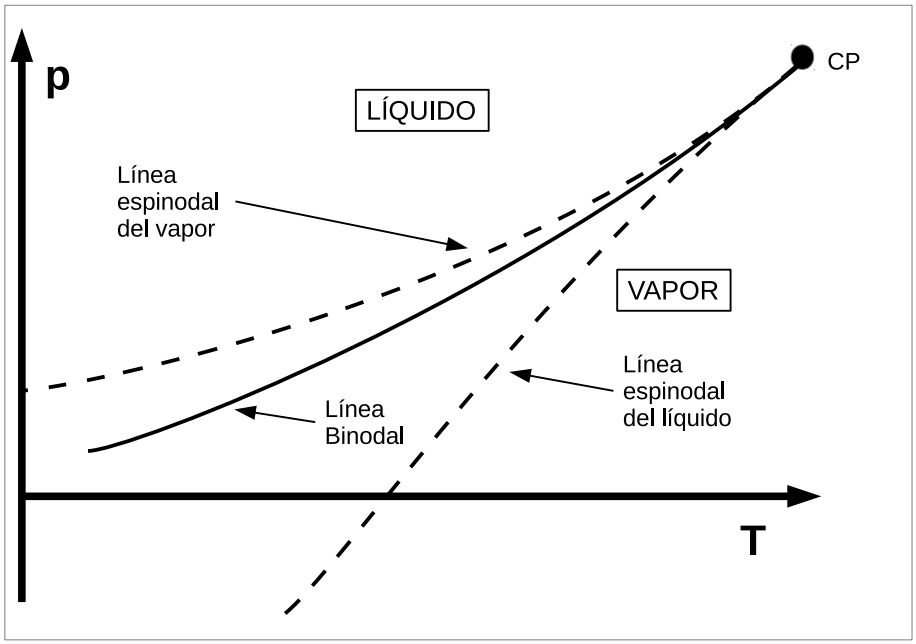

Figura 4.1: Diagrama de fases en el plano $p-T$ donde se representa la línea binodal y dos líneas espinodales, la correspondiente al líquido y al vapor. Notese que las tres líneas parten del punto crítico líquido-vapor (CP).

100 ^{o}C o a menos de 0 ^{o}C, ya que nos encontramos fuera de la zona de equilibrio (cruzando la línea binodal), pero dentro de la zona de estabilidad termodinámica del agua (antes de cruzar la línea espinodal). Obtendremos una fase metaestable durante un periodo de tiempo indefinido hasta que el sistema no entre en contacto con la fase estable y cinéticamente sea lábil la transformación a la fase estable en esas condiciones. Esta transición se basa en una transformación de fase de primer orden y lleva por nombre **nucleación**. Este es el mecanismo de relajación para los estados metaestables y se fundamenta en la aparición de embriones (núcleos o *cluster*) dentro de la fase metaestable. A través del crecimiento de estos núcleos toda la fase metaestable se tranformará en la nueva fase. El fenómeno de nucleación es un proceso activado, es decir, existe una barrera de energía libre que es necesario sobrepasar para poder acceder a la transformación total de la fase metaestable en la fase estable. Esta barrera depende de lo alejado que nos encontremos de la binodal. Así, si nos situamos cerca a esta línea el coste de energía libre tiende

a infinito, lo que quiere decir que los embriones que tenemos de la nueva fase son infinitamente grandes (nos encontramos en equilibrio de fases). Por otro lado, cuando estamos muy alejados de la binodal, cerca de la espinodal la barrera disminuye hasta desaparecer y los embriones que tenemos de la nueva fase también disminuyen de tamaño. Cuando se cruza esta última línea se produce la **descomposición espinodal**, en le que las dos fases se separan de manera homogénea, instantánea y espontánea. Éste es el mecanismo de relajación utilizado por los estados inestables para conseguir la transformación a la fase estable. Volviendo al proceso de nucleación, este fenómeno depende de una barrera de energía libre llamada **barrera de nucleación**, la cual depende a su vez de dos aspectos: el grado de metaestabilidad de la fase de partida y el trabajo necesario para la creación de la interfase.

Habiendo enmarcado nuestro proceso a estudiar, ahora estamos en condiciones de abordar el problema de descripción y análisis desde el punto de vista de la teoría.

4.2. Teoría Clásica de Nucleación

Como se dijo en el apartado anterior la nucleación es el proceso por el cual una fase metaestable se tranforma en la fase estable a partir de la aparición de embriones de la nueva fase. También se puede definir como el mecanismo de relajación para los estados metaestables. Antes de explicar cómo se determina este proceso por la Teoría Clásica de Nucleación es preciso decir que existen dos tipos de nucleación:

1. **Nucleación homogénea,** cuando la nucleación se produce a partir de una sola fase, de forma espontánea debido a fluctuaciones de la densidad que caracteriza la nueva fase.

2. **Nucleación heterogénea,** similar a la homogénea pero el proceso da comienzo en presencia de paredes y/o impurezas de otra sustancia. Esta coexistencia acelera la nucleación y disminuye la sobresaturación necesaria para la transformación a la nueva fase.

La Teoría Clásica de Nucleación, normalmente citada por sus siglas en inglés (*Classical Nucleation Theory*, CNT) es una teoría fenomenológica basada en la observación de la transición de fase vapor-líquido, a través de la formación de una gota líquida en un vapor sobresaturado. Esta sobresaturación no se refiere al grado de disolución de un soluto en un disolvente sino a la diferencia de potencial químico $|\Delta\mu|$ entre una fase estable y una fase metaestable que están implicadas en el proceso de nucleación. Para poner

la definición de CNT en los mismo términos que hemos utilizado durante la memoria diremos que partimos de una fase metaestable, vapor sobresaturado o vapor sobreenfriado, que se transforma irremediablemente en la fase estable en esas condiciones, la gota líquida. Un aspecto muy importante a tener en cuenta de esta teoría es que describe un proceso macroscópico. Los criterios utilizados están acorde con el mundo macroscópico, por ejemplo, se utilizan normalmente valores de tensión superficial basados en superficies totalmente planas. Este hecho será relevante cuando tengamos que analizar los resultados de sistemas microscópicos.

Los primeros en desarrollar esta teoría fueron Volmer y Weber[36] (1926), su trabajo está basado en aplicar la formulación de Gibbs sobre un trabajo reversible de la formación de un embrión de la nueva fase dentro de la fase metaestable. De esta forma se puede calcular la tasa de nucleación y ponerla en relación con la formación del núcleo crítico en procesos de estas características, concepto que definirá en páginas sucesivas. Seguidamente en 1935, en el trabajo de Becker y Döring[37] se propone la utilización de la distribución del estado estacionario (*steady state*) en sustitución de la distribución de núcleos en equilibrio propuesta por Volmer *et al.*. Además obtuvieron, al utilizar este tipo de distribución, una ecuación donde se define la tasa de nucleación independiente del número de partículas. Utilizando este mismo sistema, Zeldovich[38] en 1943, hizo aportaciones y modificaciones importantes a la CNT, pero no se aplicó en materia condensada hasta el trabajo de Turnbull y Fisher[39] (1949).

A partir de esta teoría se han realizado sucesivas mejoras y se han abierto otros camino no tan clásicos. Como la aproximacion al fenómeno de la nucleación por medio de la Teoría del Funcional de Densidad (TFD), mejor conocida como DFT, de sus siglan en inglés, *Density Functional Theory.* Esta nueva visión se la debemos al trabajo de Cahn y Hillard[40] en 1959, y a la posterior revisión de Oxtoby y Evans[41]. En este caso se trata al embrión y su evolución como una inhomogeneidad de la estructura, medida a través de la densidad. La energía libre del sistema se vincula con la densidad por medio de un funcional con el cual podemos calcular directamente la energía libre de la formación del núcleo de la nueva fase[42].

Como dijimos en un comienzo, la Teoría Clásica de Nucleación nos permite determinar, a través de una formalismo riguroso, la barrera de nucleación, ΔG y la tasa de nucleación, J. A continuación daremos unas pinceladas sobre el tratamiento de estos dos conceptos según la CNT.

4.3. La Barrera de Nucleación según la CNT

Sabemos que el proceso de nucleación es un proceso activado, lo cual implica la existencia de una barrera de energía libre denominada barrera de nucleación. Para calcular esta barrera partiremos de dos sistemas A y B en condiciones termodinámicas de presión y temperatura constantes. El sistema A está compuesto por la fase metaestable α y el sistema B está consittuido por esa misma fase metaestable y un embrión de la nueva fase β. Para continuar la idea propuesta por Volmer y Weber, la fase α es un vapor sobreenfriado, mientras que la fase β es el líquido estable. Con la presentación de los personajes de nuestra película sólo queda empezar a narrar la historia del cálculo de la barrera de nucleación, ΔG.

Lo primero que haremos será determinar la energía interna del sistema A, U_α^A:

$$U_\alpha^A = T^A S^A - p^A V + \mu^A N, \tag{4.1}$$

donde T es la temperatura, S la entropía, p la presión, V el volumen, μ el potencial químico y N el número total de partículas del sistema. Podemos calcular la misma magnitud para el otro sistema B, $U_{\alpha+\beta}^B$

$$U_{\alpha+\beta}^B = T^B S^B - p_\alpha^B V_\alpha^B - p_\beta^B V_\beta^B + A\gamma + \mu_\alpha^B N_\alpha + \mu_\beta^B N_\beta, \tag{4.2}$$

en esta ocasión debemos de tener en cuenta la aparición de la nueva fase β y por consiguiente el trabajo que tenemos que realizar para crear la interfase que las separa, la cual viene determinada por el área de la propia interfase, A y por la energía libre interfacial, γ. Como la transformación se produce a presión y temperatura constante, podemos suponer que $p_\alpha^A = p_\alpha^B = p$, $T^A = T^B$, además $N = N_\alpha + N_\beta$ y suponer que los volumenes son aditivos nos ayuda a simplificar el cálculo, así, $V = V_\alpha + V_\beta$,

$$U_{\alpha+\beta}^B = T^B S^B - p_\alpha^B V - (p_\beta^B - p_\alpha^B) V_\beta^B + A\gamma + \mu_\alpha^B N + (\mu_\beta^B - \mu_\alpha^B) N_\beta. \tag{4.3}$$

Si las fases α y β están en equilibrio termodinámico, esto implica que $\mu_\alpha^B = \mu_\beta^B$; y si el núcleo de β es muy pequeño frente a la fase metaestable α, $N_\alpha > N_\beta$. Con todas estas aproximaciones se puede utilizar la formulación de Gibbs para un trabajo reversible aplicado al crecimento del núcleo de β en la fase metaestable α. De este modo si calculamos G_α^A y $G_{\alpha+\beta}^B$, la determinación de ΔG es inmediata.

$$\Delta G = \Delta U + p\Delta V - T\Delta S, \tag{4.4}$$

en combinación con la ecuación (4.1) y la (4.3), la última relación expuesta queda modificada de la siguiente manera,

$$\Delta G = G_{\alpha+\beta}^B - G_\alpha^A = (p - p_\beta^B) V_\beta^B + A\gamma + (\mu_\beta^B - \mu_\alpha^B) N_\beta^B. \tag{4.5}$$

En este punto es donde la Teoría Clásica de nucleación hace tres aproximaciones para determinar la barrera de nucleación.

1. Las características de crecimiento de la nueva fase vienen determinadas por las propiedades de *bulk* de la misma fase, por ejemplo, $\mu_\beta^B(p_\beta^B)$.

2. La energía interfacial, γ, es calculada como la tensión superficial de una esfera de radio infinito, o una superficie plana, γ_∞.

3. Por último, el núcleo será incompresible, por lo que su densidad permanecerá constante cumpliendose la relación termodinámica, $\partial\mu/\partial p = 1/\rho$ y podemos entonces reescribir el potencial químico de función la presión de la fase β como,

$$\mu_\beta^B(p_\beta^B) = \mu_\beta^B(p_\alpha^B) + \frac{p_\beta^B - p_\alpha^B}{\rho_\beta} \tag{4.6}$$

Sustituyendo la Ec. (4.6) en la Ec. (4.5), podemos llegar a

$$\Delta G(N_\beta) = A(N_\beta)\gamma_\infty + \left[\mu_\beta^B(p_\alpha^B) - \mu_\alpha^B(p_\alpha^B)\right] N_\beta \tag{4.7}$$

$$\Delta G(N_\beta) = A(N_\beta)\gamma_\infty + |\Delta\mu|\, N_\beta. \tag{4.8}$$

Así hemos encontrado una función de ΔG dependiente del número de partículas que forman parte de la nueva fase estable β, de la diferencia de potenciales químicos entre las fases y de la energía libre interfacial γ. Si el núcleo de la fase β tiene la forma esférica, podemos escribir ΔG en función del radio de este núcleo. Si tomamos como $A(N_\beta) = 4\pi R^2$, área de una esfera y N_β el número de partículas de esa esfera de volumen, $V = (4/3)\pi R^3$, la barrera en la Ec. (4.7) queda:

$$\Delta G(R) = 4\pi R^2\gamma_\infty + |\Delta\mu|\, \rho_\beta (4/3)\pi R^3. \tag{4.9}$$

ΔG en ambas expresiones (4.8) y (4.9) tiene dos términos:

- El primer término está determinado por la tensión superficial y tiene en cuenta el trabajo necesario para crear la interfase entre la nueva fase β y la metaestable α.

- El otro es un término de *bulk* que depende del grado de metaestabilidad de la fase α con respecto a la fase termodinamicamente estable β. Al contrario del otro término, éste es negativo y favorece al proceso de nucleación.

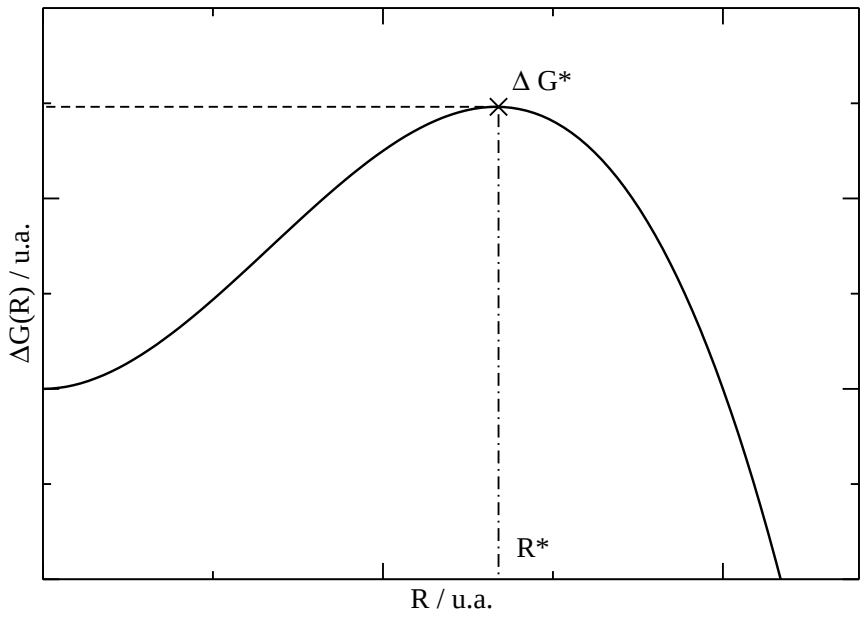

Figura 4.2: Representación esquemática de la barrera de energía libre del proceso de nucleación. El aspa negro marca el máximo de la barrera, ΔG^*, donde el cual corresponde al valor del radio crítico, R^*.

Si representamos cualquiera de las dos ecuaciones 4.8 y 4.9, aunque en esta memoria nos centraremos en la segunda, observaremos un máximo en la función ΔG.

Este punto, se conoce como *top de la barrera*. Está caracterizado por el valor de un radio concreto, **radio crítico** y por el valor máximo de la energía libre del proceso activado de nucleación, ΔG^*. El núcleo que nos encontramos en este punto de la función se denomina **núcleo crítico** y se define como el *cluster* que tiene una probabilidad del 50 % de continuar creciendo irremediablemente hasta que la transformación hacia la fase estable es completa y el otro 50 % de probabilidad de volverse a disolver en la fase metaestable α. El radio crítico es:

$$R^* = \frac{2\gamma_\infty}{\rho_\beta \left|\Delta\mu\right|}, \tag{4.10}$$

y el top de la barrera:

$$\Delta G^* = \frac{16\pi\gamma_\infty^3}{3(\rho_\beta\,|\Delta\mu|)^2}. \tag{4.11}$$

La diferencia de presiones entre las dos fases (el nucleo termodinámicamente estable rodeado por el *bulk* termodinámicamente metaestable) implicadas en función del radio crítico y de la energia libre interfacial,

$$\Delta p = \frac{2\gamma_\infty}{R^*}, \tag{4.12}$$

es la *presión de Laplace*. En el ejemplo que estamos considerando, una gota líquida que crece en un vapor sobresaturado, podemos utilizar la presión de Laplace para determinar la sobresaturación del sistema.

El trabajo de formación de un núcleo de la fase estabe de tamaño n en una fase metaestable se puede también calcular teniendo en cuenta la Termodinámica Estadística. Con los mismos sistemas A y B calculamos la energía libre asociada a la formación de la nueva fase, β. Determinamos el potencial químico del sistema B a través de la expresión,

$$\mu_n(p) = A\gamma + n\mu_\beta(p), \tag{4.13}$$

donde n ($n = N_\beta$) es el número de partículas que forman el núcleo de area A, γ es la energía libre interfacial y p es la presión de la fase metaestable β. Esta expresión nos ofrece un valor general del potencial químico que depende de las propiedades macroscópicas. Pero como vimos en la sección (1.3), si elegimos el colectivo correcto, seremos capaces de determinar las magnitudes mascroscópicas a través de las funciones de distribución de probabilidad de los microestados. En nuestro caso trabajamos con el colectivo NpT. Además trataremos al sistema como una mezcla ideal de núcleos, de distintos tamaños que no interaccionan entre sí y están caracterizados por una presión parcial, p_n. Partiendo de la relación termodinámica $\mathrm{d}\mu/\mathrm{d}p = 1/\rho$ y la definición de presión de un gas ideal, $p = \rho k_B T$ calculamos el potencial químico de estos núcleos de tamaño n,

$$\mu_n(p_n) = \mu_n(p) + k_B T \ln\left(\frac{p_n}{p}\right). \tag{4.14}$$

Si sustituimos en la Ec. (4.8) las relaciones (4.12) y (4.13) obtendremos la expresion de ΔG para el proceso de nucleación.

$$\Delta G = \mu_n(p_n) - n\mu_\alpha(p) - k_B T \ln\left(\frac{p_n}{p}\right), \tag{4.15}$$

como los núcleos de distintos tamaño n estan en equilibrio termodinámico con la fase metaestable α. Se cumple que $\mu_n(p_n) = n\mu_\alpha(p)$, por lo tanto la expresión anterior se simplifica a

$$\Delta G = -k_B T \ln\left(\frac{p_n}{p}\right). \tag{4.16}$$

El calculo de la presiones parciales de los núcleos es complicado. Pero si aplicamos la Ley de Raoult que dice que $p_n/p \simeq N_n/N$ (donde p es la presion total del sistema y N el numero total de moleculas). La Ec. (4.16) se transforma en la ecuación general del cálculo de ΔG en procesos de equilibrio.

$$\Delta G = -k_B T \ln\left(\frac{N_n}{N}\right) = -k_B T \ln P(n), \tag{4.17}$$

donde $P(n)$ es la probabilidad de encontrar un núcleo de n partículas en equilibrio con la fase metaestable que lo rodea.

Después de las anteriores fórmulas y disgresiones, hemos obtenido las principales relaciones para el cálculo de la energía libre asociada al proceso de nucleación. A continuación pasaremos a estudiar la tasa de nucleación y cómo ha sido abordado su resolución por la CNT.

4.4. La tasa de nucleación según la CNT

Otro aspecto del proceso de nucleación abordado por la CNT es el cálculo de la tasa de nucleación. Por definición la tasa de nucleación es el número de núcleos críticos formados por unidad de volumen y de tiempo. Esta magnitud se representa por la letra J y en el trabajo de Volmer y Weber se determina a partir del crecimiento y la desaparición del núcleo crítico como una ecuación cinética. La condición inicial de este planteamiento es que el proceso de crecimento y redisolución del embrión será por medio de añadir y eliminar del núcleo critico monómeros de la nueva fase. En la formulación original los autores estudiaron la condensación de un líquido (nueva fase) a partir de un vapor metaestable. Para ello se tiene que cumplir que la población de monómeros sea predominante frente a dímeros, trímeros... y que no haya colisiones entre núcleos. Con estas premisas podemos escribir las siguientes reacciones de formación y desaparición del núcleo.

$$\beta_{n-1} + \beta_1 \underset{k_{-,n}}{\overset{k_{+,n+1}}{\rightleftharpoons}} \beta_n \tag{4.18}$$

$$\beta_n + \beta_1 \underset{k_{-,n+1}}{\overset{k_{+,n}}{\rightleftharpoons}} \beta_{n+1} \tag{4.19}$$

donde β_1 es el monómero de la fase β, $n-1$, n y $n+1$ los índices del número de partículas que forman el núcleo y $k_{+,n}$, $k_{-,n}$, $k_{+,n+1}$ y $k_{-,n+1}$ las tasas de crecimiento $(+)$ y de desaparición $(-)$ de los embriones implicados. Podemos calcular la dependencia con el tiempo de la distribución de núcleos $N_n(t)$ resolviendo la ecuación general

$$\frac{\mathrm{d}N_n(t)}{\mathrm{d}t} = N_{n-1}(t)k_{+,n-1} + N_{n+1}(t)k_{-,n+1} - [N_n(t)k_{-,n} + N_n(t)k_{+,n}] \quad (4.20)$$

Ahora, si queremos calcular la tasa neta de nucleación, es decir la tasa de crecimiento y desaparición del cluster β_n podemos escribirlo como sigue,

$$J(n,t) = N_n(t)k_{+,n} - N_{n+1}(t)k_{-,n+1}, \quad (4.21)$$

que corresponde al flujo (dependiente del tiempo) de núcleos que alcanzan un tamaño n. Para calcular la Ec. (4.21) Volmer y Weber hicieron la suposición de que el flujo de retorno de un núcleo más grande que el núcleo crítico desde este tipo de embrión es cero, es decir, $N_n(t) = 0$, para $n > n^*$. Además para $n < n^*$, podemos tomar como $N_n(t)$ independiente del tiempo si representa a la distribución de núcleos en equilibrio, convirtiendose en N_n. Si utilizamos la Ec. (4.17) podemos definir N_n en función de la energía libre del sistema en combinación con la definición de ΔG quedando la Ec. (4.21) como sigue,

$$J(n) = N_n k_{+,n^*} = N_1 k_{+,n^*} e^{-\beta \Delta G(n^*)}, \quad (4.22)$$

siendo k_{+,n^*} y $\Delta G(n^*)$ la tasa de crecimiento y la energía libre del núcleo crítico, respectivamente.

Esta tasa de nucleación calculada por Volmer y Weber es dependiente del número de partículas del embrión y este hecho puede ser dificil de evaluar. Los encargados de eliminar esta dependencia fueron Becker y Döring[37]. Proponen utilizar en la Ec. (4.21) la distribución del estado estacionario N_n^{ss}, quedando

$$J = N_n^{ss} k_{+,n} - N_{n+1}^{ss} k_{-,n+1}. \quad (4.23)$$

A partir de esta expresión y teniendo en cuenta que para los estados estacionarios el flujo es el mismo, se llega a la definición siguiente[43]

$$J = N_1 \left[\prod_{i=1}^{\infty} \frac{1}{k_{+,n} K_n} \right]^{-1}, \quad (4.24)$$

donde $K_n = \prod_{j=1}^{n-1} \frac{k_{+,n}}{k_{-,n+1}}$ siendo $n > 1$. Lo que se plantea con la utilización de la constante englobadora K_n es aproximar las semi-reacciones a una reacción global de formación del núcleo N_n.

$$nN_1 \overset{K_n}{\rightleftharpoons} N_n. \quad (4.25)$$

Utilizando la relación entre K_n y la Ec. (4.17), $\left(\frac{N_n}{N_1}\right) = K_n = e^{-\beta\Delta G}$, que nos permite obtener la expresión general de la tasa de nucleación independiente de n:

$$J = N_1 \left[\prod_{i=1}^{\infty} \frac{1}{k_{+,n} e^{-\beta\Delta G}}\right]^{-1}. \tag{4.26}$$

Al igual que hicieron Volmer y Weber, Becker y Döring simplificaron esta expresión (4.26) con el fin de obtener una relación con solución abordable por experimentos. Si se realiza el cáculo de J en la región del top de la barrera, y además si el límite de cálculo es el tamaño del núcleo crítico, n^*, podemos reescribir la ecuación como,

$$J = N_1 k_{+,n^*} \left(\frac{|\Delta G''(n)|_{n^*}}{2\pi k_B T}\right)^{1/2} e^{-\beta\Delta G(n^*)}, \tag{4.27}$$

siendo $|\Delta G''(n)|_{n^*}$ la segunda derivada de la energía libre de Gibbs en función de n, calculado en el núcleo crítico. El término entre paréntesis se denomina *factor de Zeldovich*[38], Z, y teniendo en cuenta la Ec. (4.11) podemos simplificar la expresión anterior a

$$J = N_1 k_{+,n^*} \left(\frac{|\Delta\mu|}{6\pi k_B T n^*}\right)^{1/2} e^{-\beta\Delta G(n^*)}. \tag{4.28}$$

Utilizando la definición de *prefactor cinético* de Becker y Döring[37], κ, podemos escribir la tasa de nucleación de la Ec. (4.27) como

$$J = \kappa e^{-\beta\Delta G(n^*)} \tag{4.29}$$

$$\kappa = N_1 k_{+,n^*} Z \tag{4.30}$$

Utilizando las ecuaciones arriba expuestas, Turnbull y Fischer[39] proponen una expresión mejorada del prefactor cinético para el estudio de los sistemas condensados.

$$J = \kappa_{TF} e^{-\beta\Delta G(n^*)} \tag{4.31}$$

$$\kappa_{TF} = N_1 \frac{24 D_s (n^*)^{2/3}}{\lambda^2} Z \tag{4.32}$$

Donde D_s es el coeficiente de difusión, N_1 es la concentración de monóneros, Z es el prefactor de Zeldovitch, λ es la distancia de salto atómico, la cual es necesaria para definir la frecuencia de crecimiento/desaparición de una partícula simple en el núcleo. El término $(n^*)^{2/3}$ es el número de átomos/moléculas que se encuentran en la superficie del núcleo crítico suponiendo que es una esfera.

Después de esta descripción de la Teoría Clasica de Nucleación sólo queda explicar cómo aborda el estudio de este fenómeno la Simulación Molecular. En la siguiente sección se detallarán los principales métodos de análisis de procesos de nucleación.

4.5. Técnicas de simulación del proceso de nucleación

La Simulación Molecular es una herramienta muy útil para el estudio de este tipo de fenómenos. Es capaz de explicar procesos macroscópicos describiendo los mecanismos microscópicos que los generan. Como se ha comentado en las secciones anteriores a través de la simulación obtenemos configuraciones representativas de nuestro sistema en determinadas condiciones termodinámicas, aunque el sistema no esté en equilibrio y se encuentre en estados metaestables, como en el caso de la nucleación. Este evento, la nucleación, es un proceso activado, en el que el sistema necesida cruzar una barrera de energía libre para transformarse en la fase termodinamicamente estable. Como hemos explicado anteriormente un factor que determina la nucleación es el grado de sobresaturación, $|\Delta\mu|$, o lejanía respecto a la binodal del estado termodinámico. La altura de la barrera es inversamente proporcional a $|\Delta\mu|$, por lo tanto ésta es mayor cuanto más nos acercamos a la binodal y viceversa. Alejandonos de la binodal, nos acercamos a su vez a la espinodal, alcanzada la cual la barrera de nucleación desaparece y el sistema se separa espontáneamente en dos fases a través de un mecanismo de descomposición espinodal.

Además, la nucleación es un *evento raro* que depende tanto de la altura de la barrera de nucleación como de la cinética de crecimiento de los núcleos críticos. Este comportamiento se puede observar si evaluamos el tiempo necesario para que se produzca la nucleación. Cuando tenemos una sobresaturación elevada el tiempo requerido para la transición es muy pequeño. Pero cuando la sobresaturación es muy baja este tiempo se hace mucho más grande. Esta diferencia de tiempos hace que desde el punto de vista de la simulación exista un límite en el cual podemos marcas la frontera entre los procesos de nucleación *espontáneos* y los *no espontáneos*. Un evento de nucleación suele aparecer de manera espontánea en las simulaciones, si su barrera de nucleación tiene el máximo en torno a un valor de 14-15 k_BT[21]. Mientras que un evento de nucleación no suele aparecer espontáneamente si su barrera de nucleación es más alta que 15 k_BT. Los dos casos son ciertos bajo la suposición de que la cinética del sistema de interés sea favorable, como podría

pasar al agua sobrecalentada en una transición líquido-vapor, pero no ocurre al agua sobrenfriada en una transición líquido-sólido.

Otro aspecto muy importante a tener en cuenta antes de describir las técnicas de analásis de nucleación es la definición de **parámetro de orden de nucleación** que caracteriza cada transición de fase de primer orden, y en función del cual podemos representar la barrera de nucleación. El parámetro de orden suele ser una función de las coordenadas de todas las partículas del sistema, y tiene las siguentes propiedades:

1. Nos permite caracterizar de manera inequívoca tanto el estado metaestable inicial del sistema como el estado final, termodinámicamente estable.

2. Es una función monótona y creciente, desde el estado inicial hasta el estado final.

Una clasificación de los parámetros de orden podría ser la siguente: si estudiamos la transición desde un punto de vista general, analizamos cambios en propiedades macroscópicas tales como la densidad o la energía interna y definimos a estas magnitudes como nuestros *parámetros de orden global.* En cambio, si nos centramos en aspectos moleculares, como por ejemplo, el número de partículas que forman el núcleo más grande que está cristalizando en un líquido sobreenfriado o el tamaño de la burbuja más grande que esta creciendo en un líquido sobrecalentado, estaremos utilizando un *parámetro de orden local.* Con respecto a la Sección anterior, el tamaño del núcleo más grande n puede ser utilizado como parámetro de orden para el cálculo de la barrera de nucleación, ΔG. En general, los parámetros de orden global son sencillos de calcular y seguir durante la transformación pero no ofrecen ninguna información sobre el mecanismo microscópico de nucleación. Por otro lado, los parámetros de orden locales sí que son capaces de describir este mecanismo pero la elección y definición como tal no es tan secilla.

Para facilitar la conexión entre esta parte de la memoria y los resultados presentados hemos cambiado la nomenclatura tradicional por una más acorde con los datos y el método utilizado durante el estudio de doctorado. Así, el número de partículas n que forman el núcleo crítico por el volumen del núcleo más grande v como parámetro de orden local. Además y sólo para distinguir entre volumen total del sistema V y el volumen del núcleo más grande v, se utiliza la letra v. En el caso del proceso de condensación la conversión de un parámetro a otro (de n a v) es inmediato a través de la densidad del líquido. Pero en nuestro caso hemos trabajado en el proceso de nucleación de burbujas por lo que la relación no es tan inmediata como se puede ver en el Capítulo (6) de resultados, pero se llegan a las mismas conclusiones

y es totalmente aceptable la formulación que se presentará en líneas sucesivas.

4.5.1. *Mean First Passage Time* (MFPT)

Volviendo a la clasificación de los procesos de nucleación y su estudio por medio de la simulación molecular, en el caso de la nucleación espontánea con una "simple" simulación de DM o de MC se puede observar la transición de fase. Pero el fenómeno es estocástico y muy rápido, por lo tanto, se necesita simular la nucleación un número muy grande de veces para obtener resultados significativos con simulaciones de *fuerza bruta*, como normalmente se las conocen. Para solventar este problema, Regera *te al.*[44,45,46] desarrollaron un método por el cual se llega a un análisis riguroso de la nucleación espontánea. Este método se denomina *Mean First Passage Time* (MFPT) y está basado en la monitorización de un parámetro de orden en función del tiempo. Lo que los autores proponen es evaluar la primera vez que el parámetro de orden alcanza un determinado valor, y promediar este tiempo sobre un número muy elevado de trayectorias de nucleación para disminuir el efecto de la estocasticidad del proceso, aumentando la estadística del análisis. Se puede describir este método en pocas palabras de la siguiente manera: Primero se realiza una serie de trayectorias independientes de nucleación, las cuales parten de un estado metaestable y acaban cuando el sistema se ha completamente transformado en la fase termodinamica estable. Seguidamente se anota el tiempo al que aparece el parametro de orden por primera vez y en el momento en el que éste crece se anota el nuevo tiempo. Para aclarar este punto utilizaremos el siguiente ejemplo basado en la Tabla (4.1), donde se expone como ejemplo el seguimiento normal del volumen del núcleo de vapor más grande de la fase termodinamicamente estable durante los primeros 5 *ps* de una simulación de un sistema en una fase líquida metaestable.

$v/\text{Å}^3$	20	22	26	22	25
Tiempo/ps	1.0	2.0	3.0	4.0	5.0

Tabla 4.1: Monitorización del volumen del núcleo más grande de la fase termodinámicamente estable del sistema durante los primeros 5 ps.

Según el método MFPT la relación de este volumen con su primer tiempo de aparición se muestra en la siguiente tabla, Tabla (4.2). Según el método MFPT se tienen encuenta todos los volúmenes posibles del núcleo y se les asigna el primer tiempo de aparición. Así al volúmen 22 Å^3 le corresponde

un tiempos de 2 ps, ya que ese es el primer momento en el cual aparece un núcleo con ese volumen. Este procedimiento implica asignar tiempos a ciertos volúmenes que o no aparecen explícitamente en la trayectoria o aparecen después de que se hayan generado *clusters* mayor que ellos. Un claro ejemplo es el volumen de 21 Å^3, el cual no aparece en la trayectoria, (Tabla 4.1) pero se le asigna el tiempo de 2 ps, el mismo tiempo que el *cluster* más grande y más cercano, núcleo de 22 Å^3. El error cometido en este prodecimiento se minimiza con el análisis de un gran número de trayectorias.

v/Å^3	20	21	22	23	24	25	26
Tiempo/ps	1.0	2.0	2.0	3.0	3.0	3.0	3.0

Tabla 4.2: Nueva distribución de volúmenes respecto del primer tiempo de aparición del nucléo más grande.

Cuando hemos realizado esta reorganización de los tiempos de aparición para todas las trayectorias calculamos la media de estos tiempos para cada uno de los volúmenes, $\tau(v)$ y así obtenemos una función que sigue la expresión matemática:

$$\tau(v) = \frac{\tau_J}{2}\left(1 + erf[c(v - v^*)]\right) \tag{4.33}$$

donde τ_J es el tiempo de nucleación, c es una constante proporcional al factor de Zeldovich $Z = c(\pi)^{-1/2}$ y ofrece información sobre la curvatura de la barrera de nucleacion y v^* es el volumen crítico. A través de los términos de esta función podemos obtener tanto la tasa de nucleación como la barrera de nucleación, J y ΔG, respectivamente.

La tasa de nucleación está directamente relacionada con el tiempo de nucleación, τ_J, según la ecuación:

$$J = \frac{1}{\tau_J \langle V \rangle} \tag{4.34}$$

siendo $\langle V \rangle$ el volumen medio del sistema en la fase metaestable.

La barrera de nucleación, ΔG, como se explica en la referencia[45], se calcula por medio de la Ec. (4.35) y la Ec. (4.36), donde es necesario determinar las variables:

$\tau(v)$: Media de los tiempos para cada uno de los volúmenes, como se explicó en la Tabla (4.2).

$B(v)$: Función de distribución de volúmenes del núcleo más grande.

D: Constante que depende del parámetro de orden que se utilice.

$$\beta\Delta G(v) = \ln B(v) - \int_{v_{min}}^{v_{max}} \frac{dv'}{B(v')} + D \tag{4.35}$$

$$B(v) = -\frac{1}{P(v)}\left(\int_{v_{min}}^{v_{max}} P(v')dv' - \frac{\tau_J - \tau(v)}{\tau(v)}\right) \tag{4.36}$$

los límites de integración de las integrales son finitos y se utiliza como límite superior v_{max}, un volumen suficientemente grande para estar seguros de que el proceso de nucleación ha terminado. El límite inferior de las integrales, v_{min} es el volúmen mínimo que se puede determinar para un núcleo de vapor. En el caso de utilizar el número de partículas que contiene el núcleo más grande como parámetro de orden, el límite inferior sería la unidad.

En términos generales, podemos decir que la técnica MFPT en combinación con un parámetro de orden nos ofrece la posibilidad de calcular las tres variables de caracterizan el proceso de nucleación: J, ΔG y v^*, la tasa, la barrera de nucleación y el tamaño del núcleo crítico. Aunque tanto la altura de la barrera como el tamaño del núcleo crítico tiene una fuerte dependencia con el parámetro de orden que se use para estudiar la transición. El MFPT es la técnica que hemos utilizado para los estudios de nucleación espontánea, que se presentarán en los capítulos de resultados de esta memoria.

4.5.2. Técnicas de simulación para eventos raros. Método Bennett-Chandler

Por otro lado cuando nos enfrentamos a la caracterización y análisis de los procesos de nucleación no espontáneos, las simulaciones de *fuerza bruta* no son útiles. Tanto la técnica de MC como la DM generarán información sólo del estado metaestable y los tiempos que se pueden llegar a simular podrían ser inferiores a los tiempos que se necesitan para que ocurra el propio proceso de nucleación. Por estas razones necesitamos técnicas específicas para estudiar la nucleación no espontánea, llamados procesos de *eventos raros*, ya que desde el punto de vista de la nucleación se producen sólo eventualmente. Para caracterizar este tipo de eventos se calcula la tasa de nucleación.

Basándonos en la definición de tasa de nucleación que se extrae de la Teoría del Estado de Transición[47,48,49], y que es similar a la presentada en la Sección (4.4), podemos escribir la tasa de nucleación en función del tamaño del núcleo más grande como se ha hecho en líneas anteriores:

$$J = \kappa(v^*)P(v^*) = \kappa(v^*)e^{-\beta\Delta G(v^*)}, \tag{4.37}$$

donde $\kappa(v^*)$ es el prefactor cinético y $P(v^*)$ es la probabilidad de encontrar el núcleo más grande con volumen crítico en equilibrio con la fase metaestable que lo rodea como se demostró en la Ec. (4.17).

Nos queremos centrar en una técnica que nos permite calcular la tasa de nucleación de este tipo de eventos, el **Método Bennett-Chandler**[48,49]. Este método y más concretamente el segundo paso ha sido remarcado dentro de otras técnicas de simulación de *eventos raros* por que ha sido esta técnica la utilizada en el trabajo de tesis del candidato para el cálculo de varios resultados que se expondrán en los capítulos siguientes. A continuación se explicará brevemente. El método está divido en dos pasos: por un lado se calcula el prefactor cinético, $\kappa(v^*)$ y por el otro se determina el top de la barrera, $\Delta G(v^*)$, que nos permite calcular la probabilidad de que se forme el núcleo crítico.

Para el **primer paso** se simulan una serie de trayectorias a partir del *cluster* crítico, normalmente en el colectivo NVT, y se analiza el parámetro $\langle(\Delta v^*(t))^2\rangle$ en cada trayectoria. Siendo $\Delta v^*(t) = v^*(t) - v^*(0)$ es la variación del tamaño del núcleo crítico en el tiempo con respecto al tamaño inicial $v^*(0)$. Esta média cuadrática nos permite calcular las tasa de crecimiento presentada en la Ec. 4.28 proviene de la siguiente relación, la cual reproduce el prefactor cinético

$$k_{+,v^*} = \lim_{t\to\infty} \frac{1}{2}\frac{\langle(\Delta v^*(t))^2\rangle}{t}, \tag{4.38}$$

donde k_{+,v^*} es la tasa de crecimiento desde núcleo crítico, Una vez calculada la tasa de crecimiento, siguendo la Ec. (4.28), el producto de k_{+,v^*} por el prefactor de Zeldovich y por la densidad de estado de partida nos permite obtener el factor cinético. Para mayor detalle se aconseja ver la referencia[50], donde se aplica este método al cálculo de la tasa de nucleación en el proceso de cristalización de coloides cargados.

Para explicar el **segundo paso** nos ayudaremos del trabajo de van Duijneveldt y Frenkel[51], los cuales propusieron aplicar la formulación para el *Umbrella Sampling*[52,21] (ver Sec. 2.5) para calcular el top de la barrera en los procesos de nucleación. De la misma forma que van Duijneveldt y Frenkel partimos de un colectivo NpT y con la ayuda de un parámetro de orden adecuado Q (n o v), se muestrea la transición entre los sistemas A y B y se calcula la barrera de nucleación. Obtendremos entonces una función de probabilidad de distribuciones con una correcta estadística para evaluar el evento. Pero antes, definamos la función de distribución en equilibrio, $P(Q_0)$, y averigüemos porqué no se puede utilizar. Si analizamos las fluctuaciones del parámetro de orden, Q, alrededor del parametro de orden en equilibrio

Q_0, obtendremos la función de disribución como

$$P(Q_0) = \frac{\int e^{-\beta U + pV} \delta(Q - Q_0) d\Gamma}{\int e^{-\beta U + pV} d\Gamma} = \langle \delta(Q - Q_0) \rangle_{NpT} \,, \tag{4.39}$$

donde $d\Gamma$ define la integral en el espacio de fase. Esta función de distribución no muestrea bien el colectivo ya que el sistema raramente llega a completar la transición por la penalización energética que conlleva tener una barrera de energía tan alta. Para aumentar la estadística del parámetro de orden en este tipo de condiciones se obtienen configuraciones de forma que no siguen el factor riguroso de Boltzmann, del que se ha hablado en la Sección (2.3), ya que ese le añade la siguiente función

$$e^{-\beta U + pV} W(Q) \tag{4.40}$$

donde

$$W(Q) = e^{-\beta \omega(Q)} \tag{4.41}$$

siendo $W(Q)$ una función que aumenta el peso estadístico en las configuraciones que se encuentran cerca del valor del parámetro de order Q. Esto se logra gracias a un potencial "bias", $\omega(Q)$, la cual "orienta" las configuraciones hacia valores de Q. Este potencial es arbitrario pero normalmente se describe por medio de un potencial armónico, $\omega(Q) = \frac{1}{2} k (Q_i - Q)$. Descrito a su vez por una constante k que ajusta la amplitud del pozo, por el valor objetivo Q y Q_i que es el valor del parámetro de orden para una configuración i.

Por lo tanto, la nueva función de probabilidad de distribuciones, $P_W(Q_0)$, según este muestreo queda

$$P_W(Q_0) = \frac{\int e^{-\beta[(U+pV)+\omega(Q)]} \delta(Q - Q_0) d\Gamma}{\int e^{-\beta[(U+pV)+\omega(Q)]} d\Gamma}. \tag{4.42}$$

Como nos encontramos en el colectivo NpT, la forma de calcular la propiedades termodinámicas con esta nueva metodología se realiza con la relación,

$$\langle A \rangle_{NpT} = \frac{\langle A/W(Q) \rangle_W}{\langle 1/W(Q) \rangle_W}. \tag{4.43}$$

En el caso concreto del cálculo de la energía libre, $\beta \Delta G(Q)$, la formulación es la siguente. Partiendo de $\beta \Delta G(Q) = -\ln P(Q)$,

$$\begin{aligned} \beta \Delta G(Q) &= -\ln \Big[\langle \delta(Q - Q_0) \rangle_{NpT} \Big] \\ &= -\ln \left[\langle \delta(Q - Q_0)/W(Q) \rangle_W \right] + \ln \langle 1/W(Q) \rangle_W \end{aligned} \tag{4.44}$$

donde

$$\langle \delta(Q - Q_0) \rangle_{NpT} = \frac{\langle \delta(Q - Q_0)/W(Q) \rangle_W}{\langle 1/W(Q) \rangle_W}. \tag{4.45}$$

Así obtenemos la barrera de nucleación gracias al análisis de *Umbrella Sampling*.

En resumen, el método Bennett-Chandler tiene como objetivo el cálculo de la tasa de nucleación, J, según se expone en la Ec. (4.37). Através de determinar los dos parámetros necesarios: $\kappa(v^*)$ y $\Delta G(v^*)$. El primero de ellos lo obtenemos por medio de una serie de trayectorias de evolución del crecimiento/decrecimiento del núcleo completando así el método Bennett-Chandler.

4.5.3. Otras técnicas de eventos raros. TPS, TIS, FFS

Para terminar esta sección de técnicas de simulación de procesos de *eventos raros* con los que podemos calcular la tasa de nucleación, no podemos dejar de hacer una lista de otras técnicas que nos encontramos en la literatura con el mismo fin. Como por ejemplo, el método *Transition Path Sampling* (TPS)[53] que es capaz de analizar el evento de nucleación a través de un conjunto de trayectorias entre el estado inicial y el final utilizando un parámetro de orden que no tiene porque ser la coordenada de reacción más representativa. El problema del TPS es el alto coste computacional necesario para generar un numero elevado de trayectorias. A partir de esta técnica, se desarrolló en 2003 el *Transition Interphases Sampling* (TIS)[54,55,56] que calcula las probabilidad de cruzamiento de una serie de interfases definidas por el parámetro de orden y localizadas entre el estado inicial y el final del proceso. Por último, la técnica de *Forward Flux Sampling* (FFS)[57,58,59] descrita por Allen *et al.* nos permite analizar el flujo de trayectorias que pasan por unas interfases situadas entre los dos estados implicados en la nucleación. Con lo descrito en esta sección esperamos que se haya dado una vision general tanto al fenómeno de nucelación como a las técnicas utilizadas en Simulación Molecular para estudiar este evento.

Fundamento Teórico: Capítulo 5

Escenarios termodinámicos para el agua. ¿Segundo punto crítico del agua?

Ciertas propiedades termodinámicas del agua tienen valores anormalmente altos (o bajos). Además sus variaciones a lo largo de una isoterma (o isócora o isobara) muestran la presencia de un mínimo o un máximo. El ejemplo más conocido es el máximo de la densidad a presión ambiente. El agua tiene un máximo de densidad a una temperatura de 4 ^{o}C y una presión de 1 bar. Además, la estructura sólida de esta sustancia tiene menor densidad que el líquido a presión atmosférica, por lo ue el hielo flota en el agua líquida. Si además nos movemos a la zona del agua sobreenfriada el comportamiento anómalos se acentúa. Un claro ejemplo de este hecho es el incremento exacerbado de la compresiblidad isoterma y de las capacidades caloríficas. Existen otras propiedades, tales como viscosidad, conductividad eléctrica o la constante eléctrica, que también presentan un comportamiento anómalo. Para explicar estas anomalías se han propuesto diversos escenarios termidinámicos, donde se representan las principales funciones que presentan las anomalías y su interelación.

En esta memoria se entiende como **escenario termodinámico** de una sustancia como el plano p-T donde se representan los puntos críticos y triple, las líneas de transición de fase, los lugares geométricos de los máximos y mínimos de las funciones que presentan anomalías en su comportamiento. Esta sección trata sobre los cuatro escenarios termodinámicos del agua propuestos hasta ahora, (ver Fig. (5.1)). Todos ellos tienen en común las líneas de transición entre vapor, líquido y sólido, el punto crítico líquido-vapor, el punto triple, la línea espinodal líquido-vapor y la línea de los máximos de densidad (TMD o LDM, *line of density maxima*). Dependiendo del escenario se representa el segundo punto crítico líquido-líquido, la espinodal líquido-líquido y la línea de los máximos y mínimos de las funciones respuesta, C_V,

C_p, κ_T... Una **función respuesta** se define como la magnitud que nos informan sobre los cambios de una variable de estado en respuesta a un cambio de otra variable de estado bajo condiciones controladas, siendo las dos variables independientes.

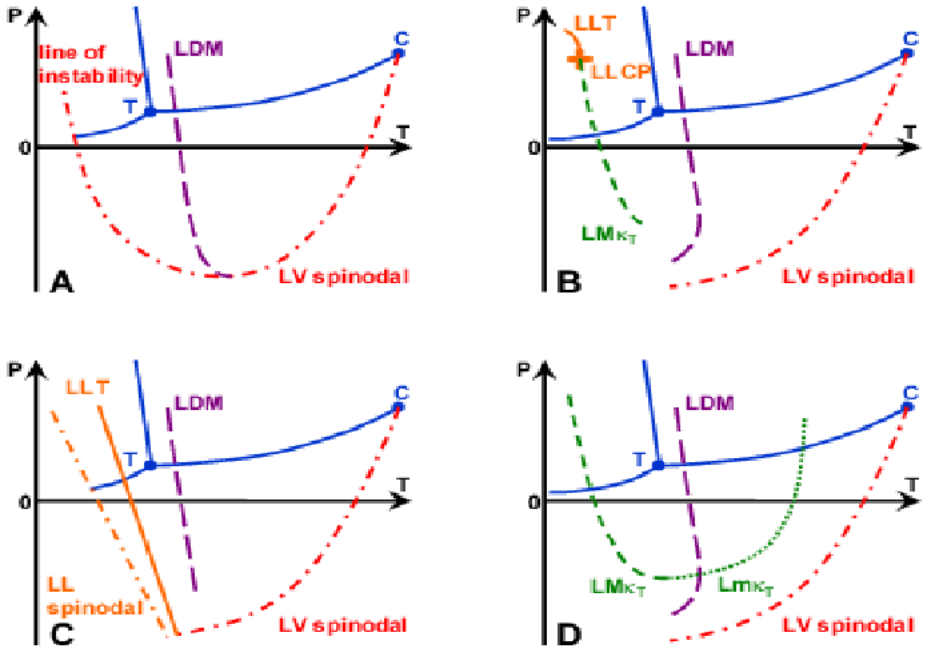

Figura 5.1: Los cuatro escenarios propuestos para explicar las anomalías del agua. En todos ellos nos encontramos con las líneas de equilibrio entre las fases sólido, líquido y vapor (líneas azules), sobre ellas estan representados el punto crítico líquido-vapor (C) y el punto triple (T) , la curva morada y discontínua corresponde a la línea de TMD o LDM, la línea roja se ha utilizado en la representación de la espinodal líquido-vapor (LV spinodal). En el escenario A[60], nos encontramos con una espinodal reentrante que aparece a presiones positivas a bajas temperaturas. El escenario B[61], añade un punto crítico líquido-líquido (LLCP) representado por una cruz naranja, la línea de transición líquido-líquid (LLT) corresponde a la línea contínua naranja, por último la línea de Widon de la compresibilidad isoterma es la curva verde dsicontínua. El tercer escenario C[62,63,64] está caracterizado por la línea continua y naraja de la transición líquido-líquid (LLT), con el mismo color pero discontínua tenemos la espinodal líquido-líquid (LL spinodal). Por último el escenario D[65] contempla una prolongación de la línea de Widom, continuando con los mínimos de κ_T, marcados con la línea de puntos.

Antes de describir los escenarios debemos definir las líneas que los componen. La **línea de máxima densidad** se construye a través del cálculo de la densidad en diferentes temperaturas a presión constante. En cada una de esas isóbaras localizamos un máximo a una temperatura concreta. Si unimos todos esos máximos de densidad obtendremos la TMD o LMD. Por otro lado todos los puntos de la **espinodal** cumplen la condición termodinámica $(\partial p/\partial V)_T = 0$ y son fácilmente calculables a través de las isotermas en un plano $p - V$. Las **líneas de los máximos y mínimos de las funciones respuesta o líneas de Widom** se calculan como cualquier extremo de una función.

El problema de todas estas propiedades es que las anomalías se presentan en la región de temperaturas bajas y presiones negativas, lo cual experimentalmente entraña problemas. Una posibilidad para resolver este problema e intentar llegar un poco más lejos que los experimentos es la extrapolación de las funciones de estado ajustadas a partir de datos experimentales. Estas fuciones tienen un gran valor predictivo dentro de los rangos para los que se ajustaron pero no son fiables cuando extraemos información de extrapolaciones de las funciones. Por estas dos razones, el límite experimental y la baja fiabilidad de las extrapolaciones de la funciones de estado, se utiliza la simulación como herramienta auxiliar para explicar el comportamiento del agua en la región sobreenfriada y de presiones negativas.

Speedy y Angell[66] en 1976 fueron los primeros que registraron las anomalías de la compresibilidad isoterma a temperaturas bajas (-45 °C), observando que los valores aumentaban significativamente según se disminuía la temperatura. Este comportamiento se puede explicar por medio de la conjetura del límite estable[60] que fue propuesta por Speedy y es nuestro primer escenario, Fig. (5.1.A). Este escenario está basado en una inestabilidad del líquido, es decir, la espinodal líquido-vapor del agua, que nace en el punto crítico líquido–vapor, tiene un mínimo y diverge hacia valores altos de presión al disminuir la temperatura, (espinodal reentrante). Esto implica que la LDM cruce con la esponidal y a partir de ese punto las dos líne tengan la misma pendiente. Este escenario esta avalado por la extrapolación de la ecuación de estado para el agua IAPWS[67].

Unos años después, se propone el escenario termodinámico obtenido a partir de datos de simulación. Está basado en la existencia de un segundo punto crítico en el agua en el cual las dos fases en exixtencia están en estado líquido[61]. Este escenario, Fig. (5.1.B),exige que la LDM sea reentrante a presiones negativas, como sucede en muchos modelos de agua. Por lo tanto la pendiente de la espinodal tiene que continuar monótona desde el punto crítico. Esta relación entre la pendiente de la LDM y la espinodal se demuestra

en el trabajo de Sastry *et. al* [65] que ambas funciones tienen el mismo signo y no pueden cruzarse. Además en el mismo artículo se explica que existe una línea de Widom de la compresibilidad isoterma, asociada al punto crítico líquido-líquido, y que cruza con la LDM. Las anomalias y divergencias de las propiedades se producen por la presencia del nuevo punto crítico. Este escenario esta apoyado por los trabajos de Sciortino *et. al*[68,69].

El tercer y el cuarto escenario surgen de ligeros cambios del segundo escenario. Estas modificaciones se basan en eliminar el punto crítico líquido-líquido o quitar además la transición líquido-líquido. El tercer escenario, Fig. (5.1.C), propuesto por Poole *et. al*[62,63,64], consiste en desplazar el punto crítico líquido-líquido fuera del plano $p - T$ pero manteniendo la línea espinodal líquido-líquido.

Por último el cuarto escenario[65], Fig. (5.1.D), es muy similar al escenario B y propaga la línea de Widom con los mínimos de compresibilidad isoterma.

En esta memoria se expondrán los resultados de simulación para el TIP4P/2005 en combinación con los primeros datos experimentales de *bulk* a presiones negativas, los cuales apoyan al escenario Fig. (5.1.B y 5.1.D

APÉNDICE A: Relación entre la distribución más probable y la entropía

Partimos[2] de un colectivo NVT (el lector podrá encontrar una definición y breve explicación sobre colectivos en la Sección 1.2). Nuestro colectivo está compuesto por una serie de microestados, con el mismo número de partículas (N), el mismo volumen (V) y se encuentran a la misma temperatura (T). Al no ser constante la energía E que existen muchos microestados con diferentes valores de esta propiedad que cumplen la condición de colectivo. También dentro del colectivo nos encontramos con microestados que tienen el mismo valor de energia, E_i, y se pueden cualtificar a través de una distribución estadística, $\Omega(n)$. Para calcular el número microestados que tiene una distribución se utiliza la formula estadística siguiente:

$$\Omega(n) = \frac{M!}{\prod_{i=1}^{n} n_i!}, \tag{5.1}$$

donde n es el número de distribuciones del sistema, M es el número de microestados totales y n_i es el número de veces que aparece el microestado i dentro de la distribución. Para simplificar los cálculos se ha utilizado $\ln \Omega(n)$ en lugar de $\Omega(n)$, ya que la distribución que da el máximo para $\Omega(n)$ es la misma que se genera para $\ln \Omega(n)$, porque $\ln f(x)$ varia de forma monótona con $f(x)$. Esta suposicion, combinada con la **aproximaxión de Stirling**

$$\ln N! \approx N \ln N - N \text{ (donde } N \text{ tiende a infinito)} \tag{5.2}$$

deja la función $\ln \Omega(n)$ como

$$\ln \Omega(n) = \left(\sum_j n_j \right) \ln \left(\sum_j n_j \right) - \sum_j n_j \ln n_j, \tag{5.3}$$

se ha hecho un cambio de variable de i a j para facilitar el cáldulo del máximo, como se verá en los parrafos siguentes.

Por otro lado, todas las distribuciones tienen que cumplir dos condiciones dentro del colectivo, para que sean aceptadas como tal.

$$\sum_i n_i = M \tag{5.4}$$

$$\sum_i n_i E_i = E_t \tag{5.5}$$

siendo E_t, la energía total del colectivo.

Para cada distribución, definimos la probabilidad de obtener un microestado con una determinada energía, E_i, como n_i/M. Pero nuestro sistema está descrito, en principio, por varias distribuciones y necesitamos evaluar la probabilidad media de encontrar un microestado con la energía, E_i, dentro del conjunto de distribuciones. Esta probabilidad media se obtiene según la relación,

$$P_i = \frac{\bar{n_i}}{M} = \frac{1}{M}\frac{\sum_n \Omega(n) n_i(n)}{\sum_n \Omega(n)}. \tag{5.6}$$

Además sabemos que cuando $M \to \infty$ también se cumple que $n_i \to \infty$ y encontramos una distribución predominante frente a todas las demás. Esta distribución la denominamos como distribución más probable, n_i^*, y averiguar su expresión es el primer paso que tenemos que dar para luego relacionarla con la entropía. Siguiendo esta premisa podemos reescribir la Ec. (5.6) como:

$$P_i = \frac{\bar{n_i}}{M} = \frac{1}{M}\frac{\Omega(n^*) n_i^*}{\Omega(n^*)} = \frac{n_i^*}{M} \tag{5.7}$$

donde n_i^* es el valor de n_i de la distribución más probable, n^*. Esta distribución, como el resto de distribuciones, cumple los dos criterios que se exponen en la Ec. (5.4) y la Ec. (5.5).

Una vez conocida la probabilidad de la distribución podemos calcular los promedios del colectivo para la energía y para la presión, aplicando el primer postulado de la termodinámica estadística. Quedando

$$\bar{E} = \sum_i P_i E_i \tag{5.8}$$

y para la presión

$$\bar{p} = \sum_i P_i p_i \tag{5.9}$$

$$p_i = -\left(\frac{\partial E_i}{\partial V}\right)_N \tag{5.10}$$

Volviendo a lo que nos ocupa en este apéndice, ya tenemos las herramientas necesarias para calcular la distribución más probable, es decir, determinar el máximo de la Ec. (5.3) que además cumple las dos condiciones: la Ec. (5.4) y la Ec. (5.5).

El método utilizado para calcular este máximo es el denominado **Método de multiplicadores indeterminados**, que se explica en el Apéndice III de la Ref. [2]. La idea de este método es encontrar una relación entre la función que tiene el máximo y las dos condiciones matemáticas que tiene que cumplir ese máximo, en nuestro caso (5.4) y (5.5). Esta conexión matemática se lleva a cabo por medio de los multipicadores indeterminados, α y β, como se muestra en la siguiente exprexión:

$$\frac{\partial}{\partial n_i}\left[\ln\Omega(n) - \alpha\sum_j n_j - \beta\sum_j n_j E_j\right] = 0, \qquad i = 1, 2, 3, ... \quad (5.11)$$

siendo el primer término la función donde se encuentra el máximo, el segundo y tercer término son, respectivamente, las expresiones de la primera y segunda condición que tiene que cumplir la distribución en el máximo. Si derivamos la expresión anterior obtenemos como solución:

$$\ln\left(\sum_j n_j\right) - \ln n_i^* - \alpha - \beta E_i = 0, \qquad i = 1, 2, 3, ... \quad (5.12)$$

también se puede reescribir como

$$n_i^* = Me^{-\alpha}e^{-\beta E_i}, \qquad i = 1, 2, 3, ... \quad (5.13)$$

de este modo tenemos la distribución más probable en función de α y β. Si queremos calcular estos términos, el método de multiplicadores indeterminados nos dice que debemos sustituir la expresión obtenida, Ec. (5.13), en las condiciones que debe cumplir la distribución y si además tenemos en cuenta que $E_t = M\bar{E}$, encontraremos las soluciones a α y a β:

$$e^{\alpha} = \sum_i e^{-\beta E_i}, \quad (5.14)$$

$$\bar{E} = \frac{\sum_i E_i e^{-\beta E_i}}{\sum_i e^{-\beta E_i}}, \quad (5.15)$$

notese que β tiene que ser función de N y V, ya que se expresa como función de $\bar{E}$ la cual también lo es. Utilizando la Ec. (5.13) podemos obtener la probabilidad P_i fácilmente en función de β,

$$P_i = \frac{n_i^*}{M} = \frac{e^{-\beta E_i(N,V)}}{\sum_j e^{-\beta E_j(N,V)}} = \frac{e^{-\beta E_i(N,V)}}{Q(N,V,T)} \qquad i = 1, 2, 3, ... \quad (5.16)$$

Aunque todavía no hemos demostrado el valor de β ni su relación con T, vamos a adelantar que el denominador de esta ecuación es la función de partición del colectivo NVT, $Q(N,V,T)$, ya que utilizaremos el término $Q(N,V,T)$ para faciliar la comprensión de los desarrollos La relación entre β y la temperatura es una consecuencia lógica del siguiente desarrollo que nos llevará a la relación entre P_i y la entropía, S.

El siguiente paso que debemos dar es encontrar el punto de partida entre las ecuaciones macroscópicas y las ecuaciones basadas en eventos microscópicos que acabamos de deducir. Para ello derivamos la Energía promedio del colectivo que hemos definido en la Ec. (5.8) y recordemos que esta relación proviene del primer postulado, el cual está en relación con P_i.

$$d\bar{E} = \sum_i E_i dP_i + \sum_i P_i dE_i. \tag{5.17}$$

Ahora sustituimos la Ec. (5.16) en el primer término y teniendo en cuenta que la energía E_i depende de V y de N, la derivada de la Energía promedio queda de la siguiente manera,

$$\begin{aligned} d\bar{E} &= -\frac{1}{\beta}\sum_i (\ln P_i + \ln Q(N,V,T))dP_i + \sum_i P_i \left(\frac{\partial E_i}{\partial V}\right)_N dV, \qquad (5.18)\\ &= -\frac{1}{\beta}\left(\sum_i \ln P_i dP_i + \sum_i \ln Q(N,V,T)dP_i\right) + \sum_i P_i \left(\frac{\partial E_i}{\partial V}\right)_N dV,\\ &= -\frac{1}{\beta}\left(d\sum_i P_i \ln P_i + \ln Q(N,V,T)\sum_i dP_i\right) - \bar{p}dV,\\ &= -\frac{1}{\beta}\left(d\sum_i P_i \ln P_i\right) - \bar{p}dV.\\ d\bar{E} + \bar{p}dV &= -\frac{1}{\beta}\left(d\sum_i P_i \ln P_i\right). \qquad (5.19) \end{aligned}$$

Para llegar a la Ec. (5.19) desde la Ec. (5.18) se ha utilizado la definición de presión promedio que se da en la Ec. (5.9) y además las siguientes consideraciones:

$$\sum_i P_i = 1, \tag{5.20}$$

$$\sum_i dP_i = 0, \tag{5.21}$$

$$\sum_i \ln P_i dP_i = d\sum_i P_i \ln P_i. \tag{5.22}$$

Si comparamos la última ecuación (5.19) con la relación termodinámica $TdS = dE + pdV$, son inmediatas las relaciones entre términos que se deducen.

$$TdS \quad \leftrightarrow \quad -\frac{1}{\beta}\left(d\sum_i P_i \ln P_i\right), \tag{5.23}$$

$$dS \quad \leftrightarrow \quad -\frac{1}{\beta T}\left(d\sum_i P_i \ln P_i\right). \tag{5.24}$$

Como en la Ec. (5.24) dS es una direfencial exacta, el otro miembro de la relación también tiene que ser una diferencial exacta, que llámaremos $df(G)$.

$$dS \leftrightarrow \frac{1}{\beta T} dG \leftrightarrow df(G) \tag{5.25}$$

Por lo tanto,

$$df(G) = \frac{1}{\beta T} dG, \tag{5.26}$$

donde

$$G = -\sum_i P_i \ln P_i, \tag{5.27}$$

la condicion de que dS sea una diferencial exacta se cumple sólo si también $df(G)$ lo es: esto es verdad si $1/\beta T$ es una función cualquiera de $G(phi(G))$. La expresión $\phi(G)$ será

$$\phi(G) = \frac{df(G)}{dG}. \tag{5.28}$$

Entonces,

$$dS \leftrightarrow \phi(G) dG. \tag{5.29}$$

Si integramos en los dos lados de la Ec. (5.29) obtendremos que la relación entre S y $f(G)$ es directa $S \leftrightarrow f(G)$, pero seguimos sin conocer la identidad de la función $f(G)$. Si estudiamos un sistema que está constituido por dos subsistemas A y B a la misma temperatura, la misma propiedad termodinámica su entropía será, $S_{AB} = S_A + S_B$. Entonces, volviendo al caso del cálculo de la propiedad G_{AB}, se demuestra que se cumple la misma relación porque G también es aditivo. Entonces se cumple que

$$f(G_{AB}) = f(G_A) + f(G_B) = f(G_A + G_B). \tag{5.30}$$

Si diferenciamos esta última expresión respecto de G_A y G_B, tenemos la relación siguiente

$$\frac{df(G_A)}{dG_A} = \frac{df(G_B)}{dG_B}. \tag{5.31}$$

Sólo existe una función $f(G)$ que cumple la igualdad anterior y es:

$$f(G) = kG + cte. \tag{5.32}$$

La constante se iguala a cero para que se cumpla la condicón de aditividad y finalmente se llega a la expresión de la función $f(G)$, $f(G) = kG$. Gracias a conocer la $f(G)$ podemos convertir la relación (5.24) en la igualdad siguiente:

$$S = -k \sum_i P_i \ln P_i. \tag{5.33}$$

donde el multiplicador indeterminado tiene el valor de $\beta = 1/kT$. Esta expresión final nos relaciona la entropía, S, con la probabilidad de la distribución más probable. Para terminar aplicaremos la Ec. (5.33) en el colectivo NVE, donde P_i es $1/\Omega$.

$$S = -k \sum_i P_i \ln P_i = -k\Omega \left(\frac{1}{\Omega} \ln \frac{1}{\Omega} \right) \tag{5.34}$$

$$= k \ln \Omega. \tag{5.35}$$

Para cerrar este apéndice de una forma redonda y no dejar cabos sueltos en el desarrollo podemos redefinir la probabilidad de ocupación de un microestado en una determinada energía, E_i y también redefinir la función de partición del colectivo. Se hace necesario la redefinición porque hasta ahora no se había puesto estas magnitudes en función de la T, ya que no sabíamos el valor del término β, $\beta = 1/kT$. Por lo tanto, se redefinirá de la siguiente forma

$$P_i(N,V,T) = \frac{e^{-E_i(N,V)/kT}}{\sum_i e^{-E_i(N,V)/kT}} \tag{5.36}$$

$$Q(N,V,T) = \sum_i e^{-E_i(N,V)/kT}. \tag{5.37}$$

donde k es la constante de Boltzmann, la cual es una constante universal designada como k_B y con un valor aproximado de $1{,}3806488(13) \cdot 10^{-23}$ JK^{-1}

El mismo desarrollo se puede hacer para los distintos colectivos teniendo en cuenta las peculiaridades de cada uno de ellos.

APÉNDICE B: Cálculo de la compresibilidad isoterma por fluctuaciones

La compresibilidad se define como el cambio relativo de volumen frente a una variación de la presión[3]. La magnitud de la compresibilidad depende de las condiciones de trabajo, por que se puede producir una variación el volumen respecto de la presión a entropía constante, *compresibilidad adiabática*, κ_S o a temperatura constante, *compresibilidad isotérmica*, κ_T.

$$\kappa_T = -\frac{1}{V}\left(\frac{\partial V}{\partial p}\right)_T \tag{5.38}$$

$$\kappa_S = -\frac{1}{V}\left(\frac{\partial V}{\partial p}\right)_S = -\frac{C_V}{C_p}\frac{1}{V}\left(\frac{\partial V}{\partial p}\right)_T \tag{5.39}$$

$$\kappa_S = \frac{C_V}{C_p}\kappa_T \tag{5.40}$$

También se puede definir la compresibilidad isoterma como la variación relativa de densidad respecto de la presión a temperatura constante. Este cambio de variable es matemáticamente y conceptualmente correcto y se demuestra facilmente sólo teniendo en cuenta la definición de densidad. Se podría determinar esta propiedad a través de la definición, siguiendo la propia definición (5.38), o por medio de la teoría de las fluctuaciones. Este último tiene en cuenta las variaciones de volumen en el sistema cuando los demás parámetros se encuentran totalmente constantes. A continuación se expondrá brevemente el desarrollo matemático[3] para el cálculo por fluctuaciones:

$$\sigma^2(V) = \langle \delta V^2 \rangle_{NpT} = \langle V^2 \rangle - \langle V \rangle^2 = \sum_i V_i^2 P_i - \langle V \rangle^2 = X - \langle V \rangle^2, \tag{5.41}$$

donde V es el volumen del sistema, X es un sumatorio que lo hemos denominado de esta manera para que los siguientes pasos sean mucho más claros

y P_i es el peso estadístico o la probabilidad de que el sistema se encuentre en el estado i.

$$P_i = \frac{e^{(-\beta E_i)} e^{(-\beta pV)}}{Q(NpT)}. \tag{5.42}$$

Si sustituimos (5.42), donde $\beta = 1/kT$, en el sumatorio de la ecuación (5.41), lo cual implica desarrollar matemáticamente sólo ese término de la ecuacion que hemos llamado X, podremos llegar a una expresión con la que podamos trabajar comodamente.

$$X = \sum_i V_i^2 P_i = \frac{1}{Q(NpT)} \sum_i V_i^2 exp(-\beta E_i) exp(-\beta pV). \tag{5.43}$$

De forma independiente calculamos la derivada parcial de $exp(-\beta pV)$ respecto del tiempo para poder generar un término dependiente de V_i,

$$\frac{\partial}{\partial p} exp(-\beta pV) = -\beta V exp(-\beta pV), \tag{5.44}$$

el cual se sustituye en la expresión (5.43) de la siguiente forma

$$\frac{1}{\beta Q(NpT)} X = -\frac{\partial}{\partial p} \sum_i V_i exp(-\beta E_i) exp(-\beta pV). \tag{5.45}$$

La función de partición en este colectivo se escribe como:

$$Q(NpT) = \sum_i exp(-\beta E_i) exp(-\beta pV). \tag{5.46}$$

Si sustituimos (5.46) en (5.45) queda

$$X = -\frac{1}{\beta Q(NpT)} \frac{\partial}{\partial p} (\langle V \rangle Q(NpT)) \tag{5.47}$$

$$X = -\frac{1}{\beta} \frac{\partial \langle V \rangle}{\partial p} - \frac{\langle V \rangle}{\beta Q(NpT)} \frac{\partial (Q(NpT))}{\partial p} \tag{5.48}$$

$$X = -\frac{1}{\beta} \frac{\partial \langle V \rangle}{\partial p} - \frac{\langle V \rangle}{\beta} \frac{\partial Ln(Q(NpT))}{\partial p} \tag{5.49}$$

$$X = -kT \frac{\partial \langle V \rangle}{\partial p} - \langle V \rangle kT \frac{\partial Ln(Q(NpT))}{\partial p}. \tag{5.50}$$

Por definición el volumen en este colectivo es[3]:

$$\langle V \rangle = -kT \frac{\partial Ln(Q(NpT))}{\partial p}. \tag{5.51}$$

Entonces

$$X = -kT\frac{\partial\langle V\rangle}{\partial p} + \langle V\rangle\langle V\rangle \tag{5.52}$$

$$X = -kT\frac{\partial\langle V\rangle}{\partial p} + \langle V\rangle^2, \tag{5.53}$$

sustituyendo (5.53) en la equación (5.41) y teniendo en cuenta la definición de compresibilidad isoterma (5.38) llegamos a la expresión final:

$$\sigma^2(V) = -kT\frac{\partial\langle V\rangle}{\partial p} + \langle V\rangle^2 - \langle V\rangle^2 \tag{5.54}$$

$$\sigma^2(V) = \langle V\rangle kT\kappa_T. \tag{5.55}$$

A partir de aqui es muy sencillo encontrar la ecuación que define la compresibilidad isoterma dentro de la teoría de fluctuaciones.

$$\sigma^2(V) = \langle V^2\rangle - \langle V\rangle^2 = \langle V\rangle kT\kappa_T \tag{5.56}$$

$$\kappa_T = \frac{\langle V^2\rangle - \langle V\rangle^2}{\langle V\rangle kT}. \tag{5.57}$$

El otro método utilizado para calcular κ_T se basa en la definición termodinámica (5.38), por lo cual es necesario encontrar varios puntos que se ajusten a la funcion de estado del sistema y con una simple derivada respecto de la presión y dividida por el volumen obtenemos el valor de la compresibilidad isoterma a la presión y temperatura requerida. Todo los valores que se han calculado en esta memoria han sido obtenidos por medio del método de fluctuaciones.

Bibliografía

1. Tuñón, I. & Silla, E., *Química molecular estadística* (Editorial Sintesis, Vallehermoso, 34 - 28015 MADRID, 2009).

2. Hill, T. L., *An Introduction to Statistical Thermodynamics* (Dover Publications Inc., New York, 1986), second edn.

3. McQuarrie, D. A., *Statistical Mechanics* (University Science Books, 55D Gate FIve Road Sausalito, CA 94965, 2000).

4. Allen, M. P. & Tildesley, D. J., *Computer Simulation of Liquids* (Oxford University Press, Oxford, 1987).

5. Rahman, A., Correlations in motion of atoms in liquid argon. *Phys. Review A-General Phys.* **136**, A405 (1964).

6. Metropolis, N., Rosenbluth, A. W., Rosenbluth, M. N., Teller, A. H. & Teller, E., Equation of state calculations by fast computing machines. *J. Chem. Phys.* **21**, 1087 (1953).

7. Alder, B. J. & Wainwright, T. E., Studies in molecular dynamics 1. general method. *J. Chem. Phys.* **31**, 459 (1959).

8. Frenkel, D. & Smit, B., *Understanding Molecular Simulation* (Academic Press, London, 2002).

9. Ewald, P., Die berechnung optischer und electrostatischer gitterpotentiale. *Ann. Physik* **64**, 253 (1921).

10. Frenkel, D. & Smit, B., *Understanding Molecular Simulation*, chap. 12.1 (Academic Press, 2002).

11. de Leeuw, S., Perram, J. & Smith, E., Simulation of electrostatic systems in periodic boundary conditions. I. Lattice sums and dielectric constants. *Proc. R. Soc. London A* **373**, 27 (1980).

12. de Leeuw, S., Perram, J. & Smith, E., Simulation of electrostatic systems in periodic boundary conditions. II. Equivalence of boundary conditions. *Proc. R. Soc. London A* **373**, 56 (1980).

13. Darden, T., York, D. & Pedersen, L., Particle mesh ewald - an n.log(n) method for ewald sums in large systems. *J. Chem. Phys.* **98**, 10089–10092 (1993).

14. Essmann, U., Perera, L., Berkowitz, M. L., Darden, T., Lee, H. & Pedersen, L. G., A smooth particle mesh ewald method. *J. Chem. Phys.* **103**, 8577–8593 (1995).

15. Verlet, L., Computer experiments on classical fluids. i. thermodynamical properties of Lennard-Jones molecules. *Phys. Rev.* **159**, 98 (1967).

16. Berendsen, H. J. C. & van Gusteren, W. F., Molecular dynamics simulations: Techniques and approaches, in *Molecular Liquids-Dynamics and Interactions*, Proceedings of the NATO Advanced Study Institute on Molecular Liquids, 475–500 (Reidel Dordretch, 1984).

17. Duane, S., Kennedy, A., Pendleton, B. J. & Roweth, D., Hybrid monte carlo **195**, 216 – 222 (1987).

18. Mehlig, B., Heermann, D. W. & Forrest, B. M., Hybrid monte-carlo method for condensed-matter systems. *Phys. Rev. B* **45**, 679–685 (1992).

19. Gonzalez, M. A., Sanz, E., McBride, C., Abascal, J., Vega, C. & Valeriani, C., Nucleation free-energy barriers using hybrid monte-carlo/umbrella sampling. *In preparation* (2014).

20. Limmer, D. T. & Chandler, D., The putative liquid-liquid transition is a liquid-solid transition in atomistic models of water. *J. Chem. Phys.* **135**, 134503 (2011).

21. Chandler, D., *Introduction to modern statistical mechanics* (Oxford university press, New York, Oxford, 1987).

22. Wang, L.-P., Head-Gordon, T., Ponder, J. W., Ren, P., Chodera, J. D., Eastman, P. K., Martinez, T. J. & Pande, V. S., Systematic improvement of a classical molecular model of water. *J. Phys. Chem. B* **117**, 9956–9972 (2013).

23. Jorgensen, W. L., Chandrasekhar, J., Madura, J. D., Impey, R. W. & Klein, M. L., Comparison of simple potential functions for simulating liquid water. *J. Chem. Phys.* **79**, 926–935 (1983).

24. Berendsen, H. J. C., Grigera, J. R. & Straatsma, T. P., The missing term in effective pair potentials. *J. Phys. Chem.* **91**, 6269–6271 (1987).

25. Mahoney, M. W. & Jorgensen, W. L., A five-site model for liquid water and the reproduction of the density anomaly by rigid, nonpolarizable potential functions. *J. Chem. Phys.* **112**, 8910–8922 (2000).

26. Stillinger, F. H. & Rahman, A., Improved simulation of liquid water by molecular dynamics. *J. Chem. Phys.* **60**, 1545 (1974).

27. Abascal, J. L. F. & Vega, C., A general purpose model for the condensed phases of water: Tip4p/2005. *J. Chem. Phys.* **123**, 234505 (2005).

28. Abascal, J. L. F., Sanz, E., García Fernández, R. & Vega, C., A potential model for the study of ices and amorphous water: Tip4p/ice. *J. Chem. Phys.* **122**, 234511 (2005).

29. Horn, H. W., Swope, W. C., Pitera, J. W., Madura, J. D., Dick, T. J., Hura, G. L. & Head-Gordon, T., Development of an improved four-site water model for biomolecular simulations: TIP4P-Ew. *J. Chem. Phys.* **120**, 9665 (2004).

30. Molinero, V. & Moore, E. B., Water modeled as an intermediate element between carbon and silicon. *J. Phys. Chem. B* **113**, 4008–4016 (2009).

31. Franzese, G., Differences between discontinuous and continuous soft-core attractive potentials: The appearance of density anomaly. *J. Molec. Liq.* **136**, 267–273 (2007).

32. de Oliveira, A. B., Franzese, G., Netz, P. A. & Barbosa, M. C., Waterlike hierarchy of anomalies in a continuous spherical shouldered potential. *J. Chem. Phys.* **128**, 064901 (2008).

33. Franzese, G. & Stanley, H., Liquid-liquid critical point in a hamiltonian model for water: analytic solution. *J. Phys. Condens. Matter* **14**, 2201–2209 (2002).

34. Moore, E. B. & Molinero, V., Structural transformation in supercooled water controls the crystallization rate of ice. *Nature* **479**, 506–U226 (2011).

35. Stokely, K., Mazza, M. G., Stanley, H. E. & Franzese, G., Effect of hydrogen bond cooperativity on the behavior of water. *Proc. Nat. Acad. Sci.* **107**, 1301–1306 (2010).

36. Volmer, M. & Weber, A., Germ-formation in oversaturated figures. *Zeitschrift Physik. chemie–stochiometrie und verwandtschaftslehre* **119**, 277–301 (1926).

37. Becker, R. & Doring, W., Kinetic treatment of germ formation in supersaturated vapour. *Ann. Physik* **24**, 719–752 (1935).

38. Zeldovich, J., On the theory of new phase formation, cavitation. *Acta Physicochimica URSS* **18**, 1–22 (1943).

39. Turnbull, D. & Fisher, J. C., Rate of nucleation in condensed systems. *J. Chem. Phys.* **17**, 71–73 (1949).

40. Cahn, J. & Hilliard, J., Free energy of a nonuniform system .1. interfacial free energy. *J. Chem. Phys.* **28**, 258–267 (1958).

41. Oxtoby, D. & Evans, R., nonclassical nucleation theory for the gas-liquid transition. *J. Chem. Phys.* **89**, 7521–7530 (1988).

42. Debenedetti, P. G., *Metaestable liquids* (Princeton University Press, Princeton, New Jersey, 1996).

43. Oxtoby, D., Homogeneous nucleation - theory and experiment. *J. Phys. Condens. Matter* **4**, 7627–7650 (1992).

44. Wedekind, J., Strey, R. & Reguera, D., New method to analyze simulations of activated processes. *J. Chem. Phys.* **126**, 134103 (2007).

45. Wedekind, J., Chkonia, G., Woelk, J., Strey, R. & Reguera, D., Crossover from nucleation to spinodal decomposition in a condensing vapor. *J. Chem. Phys.* **131**, 114506 (2009).

46. Chkonia, G., Woelk, J., Strey, R., Wedekind, J. & Reguera, D., Evaluating nucleation rates in direct simulations. *J. Chem. Phys.* **130** (2009).

47. Anderson, J., Statistical-theories of chemical reactions - distributions in transition region. *J. Chem. Phys.* **58**, 4684–4692 (1973).

48. Bennett, C. H., *Molecular Dynamics and Transition State Theory: The Simulation of Infrequent Events*, chap. 5, 63–97 (Am. Chem. Soc., Washington, D. C., 1977).

49. Chandler, D., Statistical-mechanics of isomerization dynamics in liquids and transition-state approximation. *J. Chem. Phys.* **68**, 2959–2970 (1978).

50. Auer, S. & Frenkel, D., Crystallization of weakly charged colloidal spheres: a numerical study. *J. Phys. Condens. Matter* **14**, 7667–7680 (2002).

51. Vanduijneveldt, J. & Frenkel, D., Computer-simulation study of free-energy barriers in crystal nucleation. *J. Chem. Phys.* **96**, 4655–4668 (1992).

52. Torrie, G. & Valleau, J., Monte-carlo free-energy estimates using non-boltzmann sampling - application to subcritical lennard-jones fluid. *Chem. Phys. Lett.* **28**, 578–581 (1974).

53. Bolhuis, P., Chandler, D., Dellago, C. & Geissler, P., Transition path sampling: Throwing ropes over rough mountain passes, in the dark. *Ann. Rev. Phys. Chem.* **53**, 291–318 (2002).

54. van Erp, T., Moroni, D. & Bolhuis, P., A novel path sampling method for the calculation of rate constants. *J. Chem. Phys.* **118**, 7762–7774 (2003).

55. Moroni, D., van Erp, T. & Bolhuis, P., Investigating rare events by transition interface sampling. *Physica A-statistical Mechanics and its Applications* **340**, 395–401 (2004).

56. van Erp, T. & Bolhuis, P., Elaborating transition interface sampling methods. *J. Comput. Phys.* **205**, 157–181 (2005).

57. Allen, R. J., Warren, P. B. & ten Wolde, P. R., Sampling rare switching events in biochemical networks. *Phys. Rev. Lett.* **94**, 018104 (2005).

58. Allen, R. J., Frenkel, D. & ten Wolde, P. R., Simulating rare events in equilibrium or nonequilibrium stochastic systems. *J. Chem. Phys.* **124**, 024102 (2006).

59. Allen, R. J., Frenkel, D. & ten Wolde, P. R., Forward flux sampling-type schemes for simulating rare events: Efficiency analysis. *J. Chem. Phys.* **124**, 194111 (2006).

60. Speedy, R., A simple equilibrium statistical mechanical theory of dense hard-sphere fluid mixtures-comment. *J. Chem. Phys.* **77**, 2702–2703 (1982).

61. Poole, P., Sciortino, F., Essmann, U. & Stanley, H., Phase-behavior of metastable water. *Nature* **360**, 324–328 (1992).

62. Poole, P., Sciortino, F., Grande, T., Stanley, H. & Angell, C., Effect of hydrogen-bonds on the thermodynamic behavior of liquid water. *Phys. Rev. Lett.* **73**, 1632–1635 (1994).

63. Zheng, Q., Green, J., Kieffer, J., Poole, P., Shao, J., Wolf, G. & Angell, C., Limiting tensions for liquids and glasses from laboratory and md studies, in A. Imre, H. Maris & P. Williams, eds., *Liquids Under Negative Pressure*, vol. 84 of *NATO Science series, Series II: Mathematics, Phys. and Chem.*, 33–46 (NATO, 2002).

64. Angell, C. A., Insights into phases of liquid water from study of its unusual glass-forming properties. *Science* **319**, 582–587 (2008).

65. Sastry, S., Debenedetti, P. G., Sciortino, F. & Stanley, H. E., Singularity-free interpretation of the thermodynamics of supercooled water. *Phys. Rev. E* **53**, 6144–6154 (1996).

66. Speedy, R. J. & Angell, C. A., Isothermal compressibility of supercooled water and evidence for a thermodynamic singularity at -45 degrees c. *J. Chem. Phys.* **65**, 851–858 (1976).

67. Wagner, W. & Pruss, A., The iapws formulation 1995 for the thermodynamic properties of ordinarywater substance for general and scientific use. *J. Phys. Chem. Ref. Data* **31**, 395 (2002).

68. Sciortino, F., Poole, P. H., Essmann, U. & Stanley, H. E., Line of compressibility maxima in the phase diagram of supercooled water. *Phys. Rev. E* **55**, 727–737 (1997).

69. Xu, L. M., Kumar, P., Buldyrev, S. V., Chen, S. H., Poole, P. H., Sciortino, F. & Stanley, H. E., Relation between the widom line and the dynamic crossover in systems with a liquid-liquid phase transition. *Proc. Nat. Acad. Sci.* **102**, 16558–16562 (2005).

Parte II

Results

Results: Chapter 1

Anomalies in water as obtained from computer simulations of the TIP4P/2005 model: density maxima, and density, isothermal compressibility and heat capacity minima

Helena L. Pi, Juan L. Aragones, Carlos Vega, Eva G. Noya, Jose L. F. Abascal, **Miguel A. Gonzalez** *and Carl McBride*

Departamento de Química Física, Facultad de Ciencias Químicas, Universidad Complutense de Madrid, 28040 Madrid, Spain

1.1. Abstract

The so-called thermodynamic anomalies of water form an integral part of the peculiar behaviour of this both important and ubiquitous molecule. In this paper our aim is to establish whether the recently proposed TIP4P/2005 model is capable of reproducing a number of these anomalies. Using molecular dynamics simulations we investigate both the maximum in density and the minimum in the isothermal compressibility along a number of isobars. It is shown that the model correctly describes the decrease in the temperature of the density maximum with increasing pressure. At atmospheric pressure the model exhibits an additional minimum in density at a temperature of about 200K, in good agreement with recent experimental work on super-

cooled confined water. The model also presents a minimum in the isothermal compressibility close to 310K. We have also investigated the atmospheric pressure isobar for three other water models; the SPC/E and TIP4P models also present a minimum in the isothermal compressibility, although at a considerably lower temperature than the experimental one. For the temperature range considered no such minimum is found for the TIP5P model.

1.2. Introduction

The study of polar fluids has long been a topic of interest, even moreso since the development of perturbation theories and computer simulation techniques[1,2]. Amongst the many polar molecules, water stands out in particular. Water is a fascinating molecule, both from a practical and from a fundamental point of view. In the liquid phase water presents a number of anomalies when compared to other liquids[3,4,5,6,7], whilst the solid phase exhibits a highly complex phase diagram, having at least fifteen different crystalline structures[3,8]. Due to its importance and its complexity, understanding the properties of water from a molecular point of view is of considerable interest and presents a veritable challenge.

Computer simulations of water started with the pioneering papers by Watts and Barker[9] and by Rahman and Stillinger[10] about forty years ago. However, a key issue that still exists when performing simulations of water is the choice of model for the pair potential that is used to describe the interaction between molecules[11,12,13,14,15]. The SPC[16], SPC/E[17], TIP3P[18], TIP4P[18] and TIP5P[19] models have become highly popular among the large community of people simulating water or water solutions. Each of the aforementioned models are rigid and non-polarisable, but naturally, real water is both flexible and can be polarised. It is almost needless to say that these models represent a very simplified version of the true interactions between real water molecules. Water also exhibits important quantum nuclear effects, so a realistic description of water should also take this into account[20]. That said, it is of interest at this stage to analyse how far it is possible to go in describing real water using these simple models.

In recent years the inexorable increase in computing power has permitted the calculation of properties that were previously inaccessible to simulations. These properties can be used as new 'target quantities'when fitting the parameters for any new potential. More importantly, some of these properties have provided stringent tests for the existing water models. In particular, some of the authors have recently determined the phase diagram for different

water models and have found that the performance of the models can vary significantly[21,22,23,24,25]. For example, it has been found that TIP4P provides a qualitatively correct description of the global phase diagram of water, whereas the SPC, SPC/E, and TIP5P models do not.[26] For the SPC and SPC/E models the melting temperature and the maximum in density of water occur at temperatures far below the experimental values. Taking this into account some of the authors proposed a new rigid non-polarisable model with the following constraints: that it should be based on the TIP4P model, since this model provides a reasonable description of the phase diagram of water. It should also reproduce the maximum in density of liquid water (notice that most of models fail when it comes to predicting the location of the density maximum[27]). Finally, the model should account for the vaporisation enthalpy of real water, but only after incorporating the self-polarisation energy correction proposed by Berendsen *et al.* for the SPC/E model[17]. It was from these considerations that the TIP4P/2005 model of water arose.[25] In the paper in which the model was presented it was shown that TIP4P/2005 correctly describes the global phase diagram of water, the diffusion coefficient at atmospheric pressure and temperature, the maximum in density along the atmospheric pressure isobar, the density of the ice polymorphs, and the equation of state of liquid water at high pressures. Afterwards, additional studies have shown that the model is also able to provide a good description of the vapour-liquid equilibria[28] and the surface tension[29]. Further information concerning the performance of TIP4P/2005 and its comparison with other water models can be found elsewhere[26]. The overall results indicate that TIP4P/2005 is probably close to being the best rigid non-polarisable model that can be achieved; any significant improvement would require the introduction of 'new'physics, i.e., flexibility, polarisability and nuclear quantum effects.

In this paper we are interested in the thermodynamic response functions in the region where water exhibits 'anomalous'behaviour. In particular, these are the expansion coefficient (which vanishes at temperatures close to the melting point, resulting in the well known maximum of density at about 4°C at atmospheric pressure) and the isothermal compressibility[30] (κ_T) which shows a minimum at 46.5°C at p=1 bar. Moreover, we shall investigate whether the model is able to describe the pressure dependence of these thermodynamic properties, namely, the decrease in the temperature of the density maximum and the shift towards slightly higher temperatures of the minimum in κ_T as the pressure increases. It will be shown that the model is indeed able to describe these two features quite well, which provides further evidence of the robust behaviour of the model even when estimating properties that were not taken into account in the original fitting process.

1.3. Methodology

The interaction between water molecules will be described by the TIP4P/2005 model.[25] In this model, a Lennard-Jones centre is located on the oxygen atom, positive charges are placed on the hydrogen atoms and a negative charge is located at the site M situated along the H-O-H bisector. For the simulations we have used the molecular dynamics package GROMACS (version 3.3).[31] The Lennard-Jones potential has been truncated at 9.0 Å. Long range corrections were applied to the Lennard-Jones part of the potential (for both the energy and pressure). Ewald summations were used to deal with electrostatic contributions. The real part of the Coulombic potential was truncated at 9.0 Å. The Fourier component of the Ewald sums was evaluated by using the Particle Mesh Ewald (PME) method of Essmann *et al.*[32] The width of the mesh was 1 Å and a fourth degree polynomial was used. The simulation box was cubic throughout the whole simulation and the geometry of the water molecules was enforced using constraints.[33,34] The temperature was set by using a Nosé-Hoover[35,36] thermostat with a relaxation time of 2 ps. To maintain constant pressure an isotropic Parrinello-Rahman barostat[37,38] with a relaxation time of 2 ps was used. As a check, at two pressures, p=1 bar and p=400 bar, Monte Carlo simulations were performed using a bespoke program. The Monte Carlo densities were in complete agreement with those obtained from molecular dynamics using GROMACS.

To determine the maximum in density, molecular dynamics simulations have been performed along the isobars p=1, 400, 1000, and 1500 bar. The number of molecules used in the simulations was 256. Long runs are required to determine the maximum in density; for each thermodynamic state twenty million time-steps were performed. Since the time step was 2 fs, the results presented here are an average of the properties of the system obtained from runs of 40 ns. The simulations were started at high temperatures, and the final configuration of a particular run was used as the initial configuration for a lower temperature simulation. Typically about 6 to 8 different temperatures were studied along each isobar. The isothermal compressibility is defined as:

$$\kappa_T = -\frac{1}{V}\left(\frac{\partial V}{\partial p}\right)_T. \tag{1.1}$$

The literature for the isothermal compressibility of water models is rather scant[39,40]. The computational overhead required for a study of the variation of κ_T with temperature with sufficient accuracy has, until now, been prohibitive. Here we have evaluated the isothermal compressibility for the following water models: SPC/E[17], TIP4P[18], TIP4P/2005[25] and TIP5P[19] along the atmospheric pressure isobar. The isothermal compressibility has been evaluated

using the well known fluctuation formula

$$\kappa_T = \frac{\langle V^2 \rangle - \langle V \rangle^2}{kT \langle V \rangle}. \tag{1.2}$$

The volume fluctuations were typically averaged over 20 ns using a time-step of 1 fs. Preliminary results for TIP4P/2005 model were sufficiently close to the experimental value as to warrant a more precise calculation. Thus, for this model, the isothermal compressibility has been determined via two different procedures using, in both cases, a time-step of 0.5 fs and a sample size of 500 molecules. The first method is the application of the volume fluctuation formula, typically over 40 million molecular dynamics time-steps, for a total simulation length of about 20ns. The relative uncertainty of the calculated compressibilities is about $\pm 3\,\%$. The second route is the numerical evaluation of the derivative appearing in the definition of κ_T (Eq. 1.1). To this end, the results for the equation of state of five different state points (at different pressures but at the same temperature) were fitted to a second degree polynomial. In addition to the state point of interest, for which the volume is already known from the runs used to calculate κ_T via the fluctuation route, four additional runs are required: two runs at the same temperature but at pressures of 200 and 400 bar higher, and another two runs at pressures 200 and 400 bar lower. The simulation length of these additional runs was 6.5 ns , so in the end the computational cost of both routes is almost the same. We have also computed the heat capacity at constant pressure C_p for the TIP4P/2005 model. C_p is defined as :

$$C_p = \left(\frac{\partial H}{\partial T} \right)_p. \tag{1.3}$$

Thus in order to compute C_p the enthalpy at each temperature was first calculated. These values for the enthalpy were then fitted to a polynomial and this fit was then differentiated with respect to temperature to obtain $C_p(T)$.

1.4. Results

The simulation results for the densities are reported in Tables 1.1, 1.2, 1.3 and 1.4 for p=1, 400, 1000 and 1500 isobars, respectively. For the four isobars considered a clear maximum in density has been found. The results for p=1 bar and p =400 bar, along with experimental measurements, are plotted in Fig. 1.1. It can be seen that the model is able to reproduce the experimental

data quite nicely. The density maximum for each isobar was obtained by fitting the densities around the maximum (typically 5 or 6 densities were used in the fit) to a second or a third degree polynomial.

Table 1.1: Molecular dynamics results for the TIP4P/2005 model of water along the $p = 1$ bar isobar. Only the residual part of the internal energy is given.

T/K	p/bar	ρ/(g/cm^3)	U/(kJ/mol)
150.0	1	0.9379	-57.05
156.0	1	0.9370	-56.87
162.4	1	0.9359	-56.68
169.0	1	0.9347	-56.47
176.0	1	0.9341	-56.25
183.3	1	0.9331	-55.99
191.0	1	0.9341	-55.74
199.0	1	0.9339	-55.51
207.3	1	0.9432	-54.81
215.8	1	0.9559	-54.04
224.6	1	0.9659	-53.27
233.5	1	0.9787	-52.47
242.7	1	0.9890	-51.70
252.1	1	0.9953	-50.98
261.9	1	0.9991	-50.28
272.2	1	1.0008	-49.57
283.0	1	1.0002	-48.84
294.4	1	0.9987	-48.10
300.0	1	0.9972	-47.73

The values of the maximum are reported in Table 1.5. In Fig. 1.2 the temperatures at which the maxima appear (TMD) are compared to the experimental values[41]. As can be seen, the agreement is rather good. The model correctly predicts a decrease of about 33 K in the temperature of the maximum when going from atmospheric pressure to a pressure of about 1500 bar. In other words, 45 bar are required to induce a decrease in the TMD of about one degree. For D_2O Angell and Kanno found a similar lowering of the TMD with pressure.[42] For the TIP4P/2005 not only does the TMD decrease with pressure but the melting temperature does too. In Fig.1.2 the melting curve of ice I_h (taken from our previous work[25,43,44]) is plotted along the TMD curve determined in this work. As can be seen, both curves have a negative slope. Notice also that at room pressure the distance between the melting

Table 1.2: Molecular dynamics results for the TIP4P/2005 model of water along the p=400 bar isobar. Only the residual part of the internal energy is given.

T/K	p/bar	ρ/(g/cm^3)	U/(kJ/mol)
215.8	400	0.9766	-53.39
224.6	400	0.9963	-52.92
233.5	400	1.0051	-52.27
242.7	400	1.0125	-51.57
252.1	400	1.0171	-50.90
261.9	400	1.0192	-50.24
272.2	400	1.0200	-49.55
283.0	400	1.0190	-48.85
294.4	400	1.0164	-48.14

curve of ice I_h and the TMD is about 25K, which is in contrast with the 4K of difference found experimentally. The impossibility of reproducing simultaneously both the TMD and the melting temperature in models having three charges has been discussed previously[27,26].

Another interesting issue is the behaviour of the density along the atmospheric pressure isotherm at very low temperatures. Experimentally, it is not possible to obtain the density of water at temperatures below 233 K (the homogeneous stability limit of water at atmospheric pressure[45]) due to spontaneous nucleation and freezing. However, recently, it has been possible to avoid the formation of ice by confining water in pores a few nanometers

Table 1.3: Molecular dynamics results for the TIP4P/2005 model of water along the p=1000 bar isobar. Only the residual part of the internal energy is given.

T/K	p/bar	ρ/(g/cm^3)	U/(kJ/mol)
215.8	1000	1.0308	-53.25
224.6	1000	1.0397	-52.62
233.5	1000	1.0438	-52.04
242.7	1000	1.0463	-51.43
252.1	1000	1.0476	-50.82
261.9	1000	1.0475	-50.19
272.2	1000	1.0462	-49.55
283.0	1000	1.0441	-48.89
294.4	1000	1.0407	-48.20

Table 1.4: Molecular dynamics results for the TIP4P/2005 model of water along the p=1500 bar isobar. Only the residual part of the internal energy is given.

T/K	p/bar	ρ/(g/cm^3)	U/(kJ/mol)
199.0	1500	1.0472	-54.25
207.3	1500	1.0617	-53.61
215.8	1500	1.0667	-53.06
224.6	1500	1.0678	-52.52
233.5	1500	1.0702	-51.94
242.7	1500	1.0701	-51.37
252.1	1500	1.0700	-50.78
261.9	1500	1.0682	-50.18
272.2	1500	1.0662	-49.56
283.0	1500	1.0631	-48.91
294.4	1500	1.0593	-48.24

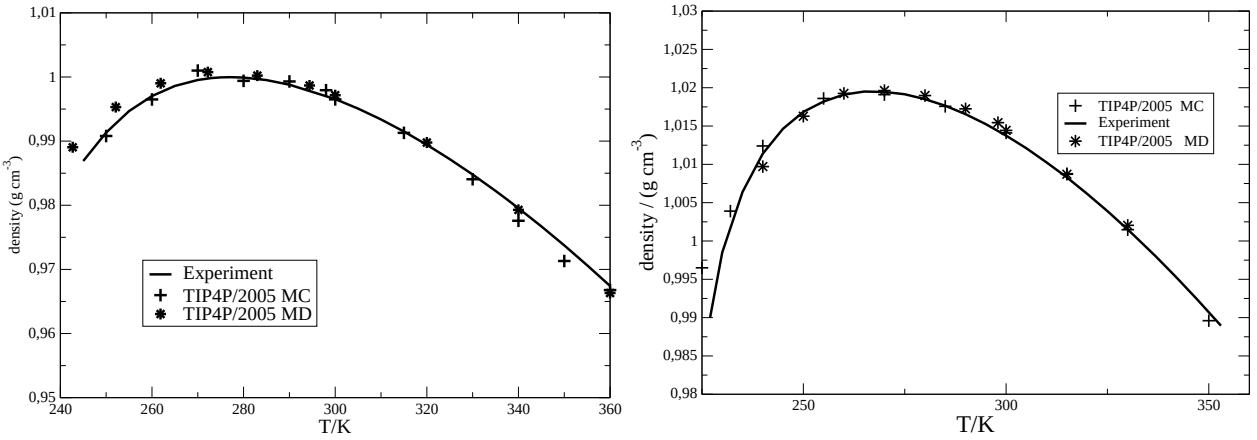

Figure 1.1: Density of liquid water at p = 1 bar (upper panel) and p=400 bar (lower panel) as obtained from Monte Carlo and molecular dynamics simulations with the TIP4P/2005 model. The experimental results were taken from Ref.[54]

in diameter (most probably because of the decrease in the freezing point of water due to confinement as described qualitatively by the Gibbs-Thomson approach[46]). Thanks to this the density of deuterated water has recently been determined for the first time[47] for temperatures as low as 160 K, reporting the existence of a minimum in the density at a temperature of about 200 K. A similar study (for water instead of deuterated water) was performed by Mallamace *et al.*[48]. By using infra-red (IR) spectroscopy, it was possible to determine the density of liquid water in the super-cooled regime down to 150 K. In Fig. 1.3 the reported experimental densities (from IR spectroscopy of a sample within a 1.5 nm pore) for liquid water along the atmospheric pressure isobar are compared to those obtained in this work from molecular dynamics simulations of the TIP4P/2005 water model. The agreement is surprisingly good, and the location of the minimum around 200 K is described properly by TIP4P/2005. Such a minimum in density has also been found[49,50] in computer simulations of the TIP5P and ST2 models of water, but the agreement with experiment was not as good as that exhibited by TIP4P/2005. For temperatures below this minimum the density increases as

Table 1.5: Temperature of maximum density at different pressures. The TMD has been obtained by fitting the data in the proximity of the maximum to a quadratic or a cubic polynomial. The temperature ranges used in the fit were 260-300 K for p=1 bar, 242-295 K for p=400 bar, 233-283 K for p=1000 bar, and 207-272 K for p=1500 bar.

p/bar	1	400	1000	1500
TMD/K	277(3)	270(3)	256(3)	244(3)

the temperature decreases (as in a normal fluid). In Fig. 1.4 we compare the equation of state of supercooled water to the equation of state of ice I_h for the TIP4P/2005 model along the room pressure isobar.[51] The minimum in density of supercooled water occurs just when the density is approaching that of the ice I_h. However, we did not succeed in obtaining ice I_h by cooling water; the radial distribution functions of the supercooled water (at room pressure) below 200K are clearly different from those of ice I_h. Rather the minimum in density corresponds to the formation of a glassy state.

Note that the existence of such a minimum is not only restricted to water but is also present in materials such as tellurium[52]. Interestingly the melting curve for tellurium exhibits re-entrance . Such re-entrant behaviour was also found in our studies of the phase diagram of water models[21].

We have also computed the self-diffusion coefficient at p =1 bar and p=1000 bar. The results, presented in Fig. 1.5, show that the diffusion coef-

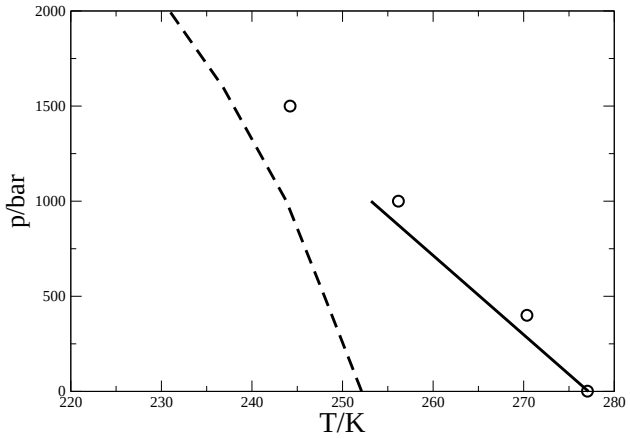

Figure 1.2: Dependence of the TMD with pressure for the TIP4P/2005 model (open circles). Experimental data for the TMD (solid line) taken from Fig.8 of Ref.[41]. The dashed line is the melting curve of ice I_h for the TIP4P/2005 model.

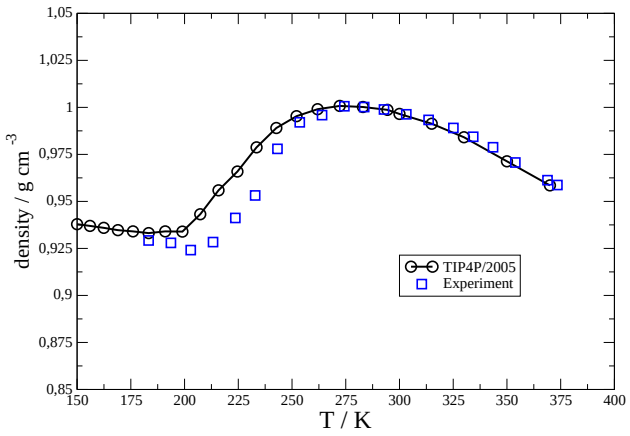

Figure 1.3: Density of liquid water at atmospheric pressure as obtained from molecular dynamics simulations with the TIP4P/2005 model. For comparison, experimental data of water confined in narrow pores are also given[48].

ficient drops significantly as the temperature decreases. The decay is less pronounced at higher pressures. At low temperatures the diffusion coefficient increases significantly with pressure (this behaviour is anomalous[30] since, for most fluids, it decreases with increasing pressure). One can imagine that the application of pressure somehow breaks the hydrogen bond network, thus aiding diffusion processes. Some indirect evidence of the decrease in hydrogen bonding with pressure can be obtained from the analysis of the different contributions (Lennard-Jones and Coulombic) to the residual internal energy. In Table 1.6 the different contributions to the residual internal energy obtained

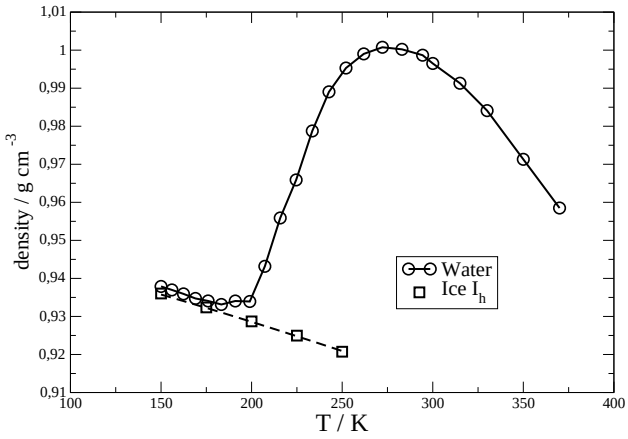

Figure 1.4: Density of liquid water at atmospheric pressure as obtained from molecular dynamics simulations with the TIP4P/2005 model (solid line and open circles). Density of ice I_h at atmospheric pressure as obtained from molecular dynamics simulations with the TIP4P/2005 model (dashed line and open squares).

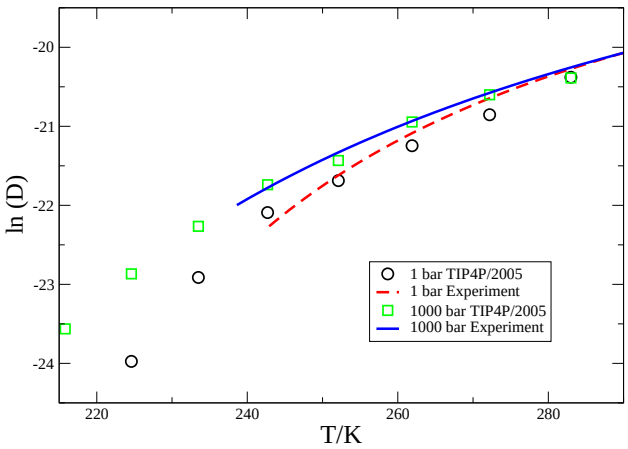

Figure 1.5: Self-diffusion coefficient (in cm^2/s) of the TIP4P/2005 model at p=1 bar and p=1000 bar compared to the experimental results (taken from Ref.[53]).

from molecular dynamics of the TIP4P/2005 model along the T=224.6K isotherm (at different pressures) are given. Notice the large decrease (in absolute value) of the Coulombic energy with pressure, clearly pointing to a reduction of hydrogen bonding with pressure. The Lennard-Jones contribution is more repulsive at low pressures (even though the density is lower) as a consequence of the stronger hydrogen bond found at lower pressures. At temperatures above 280 K the diffusion coefficients at the two pressures considered become virtually identical as the differences fall to within the statistical uncertainty.

Table 1.6: Different contributions to the residual internal energy of water along the $T = 224{,}6K$ isotherm. Results were obtained from molecular dynamics simulations of the TIP4P/2005 model of water. The Lennard-Jones contribution $U_{\text{Lennard-Jones}}$, the Coulombic contribution $U_{\text{Coulombic}}$ and the total residual energy U are reported. All energies are given in kJ/mol.

p/bar	$U_{\text{Lennard-Jones}}$	$U_{\text{Coulombic}}$	U
1	11.34	-64.61	-53.27
400	11.08	-64.00	-52.92
1000	10.78	-63.40	-52.62
1500	10.66	-63.18	-52.52

The agreement with the experimental values of the diffusion coefficient[53] is quite good.

Let us now focus on another of the 'anomalous'properties of water, the isothermal compressibility. The experimental measurements[55,56,54,57]

Table 1.7: Isothermal compressibility κ_T for $p = 1$ bar as obtained in this work for the TIP4P, SPC/E and TIP5P models of water. Reported values correspond to $(\kappa_T/\text{ bar}^{-1}) \times 10^6$.

T/K	TIP4P	SPC/E	TIP5P	Experiment
260	51.8	45.1	46.5	57.8
298.15	52.8	46.1	57	45.3
360	67.2	57.7	84	47.0

show that, at atmospheric pressure, κ_T drops as the temperature increases from the melting temperature up to 46.5°. Above this temperature water behaves as a normal liquid and the isothermal compressibility increases with temperature. It is also well established from experiment that the temperature for which κ_T is minimal shifts slightly towards higher values as the pressure increases. Contrary to the maximum in density, the ability of the water models to account for the compressibility minimum has not yet been established. As mentioned in the previous section, simulation studies of the isothermal compressibility are few and far between[39,40]. Moreover, the computational resources available did not allow the extended simulations needed to calculate κ_T with the precision required to determine whether the most common water models predict the compressibility minimum. For this reason we have calculated the compressibility for a select few 'popular'water models.

Table 1.8: Isothermal compressibility κ_T for $p = 1$ bar and $p = 1000$ bar as obtained in this work for the TIP4P/2005 model of water. Reported values correspond to $(\kappa_T/\ \mathrm{bar}^{-1})\ \times 10^6$.

T/K	p/bar	TIP4P/2005	Experiment
260	1	51.4	57.8
280	1	48.7	48.6
298	1	46.3	45.3
320	1	46.2	44.2
340	1	47.8	44.9
360	1	50.9	47.0
370	1	52.3	48.5
260	1000	42.4	42.3
280	1000	38.5	37.7
298	1000	37.2	35.7
320	1000	36.7	34.9
340	1000	36.6	35.1
360	1000	38.2	36.0
370	1000	39.2	36.7

The results are presented in Table 1.7 for the SPC/E, TIP4P and TIP5P models and in Table 1.8 for TIP4P/2005. The calculations for SPC/E, TIP4P and TIP5P were performed at atmospheric pressure for three different temperatures, namely 260 K, 300 K and 360 K. Fig. 1.6a shows that the temperature dependence of the isothermal compressibility for TIP5P does not follow the experimental pattern since, for this model, κ_T is a monotonously increasing function along the whole experimental liquid range. Despite the fact that the slope of the TIP5P curve is opposite to the experimental one, the values of κ_T are coincident in a narrow range of temperatures because the simulation and the experimental curves cross at a temperature close to the freezing point of liquid water. For temperatures near the boiling point the TIP5P model fails completely, where the predicted compressibility at 360 K is almost twice the experimental value.

As for the performance of the SPC/E and TIP4P models, both provide fairly similar results. In fact their curves are parallel, showing a more or less defined minimum around 270 K (more computations would be needed to determine the precise location of the minima). The results of SPC/E are somewhat shifted to higher temperatures with respect to those of TIP4P, which results in a slightly better agreement with the experimental data. At

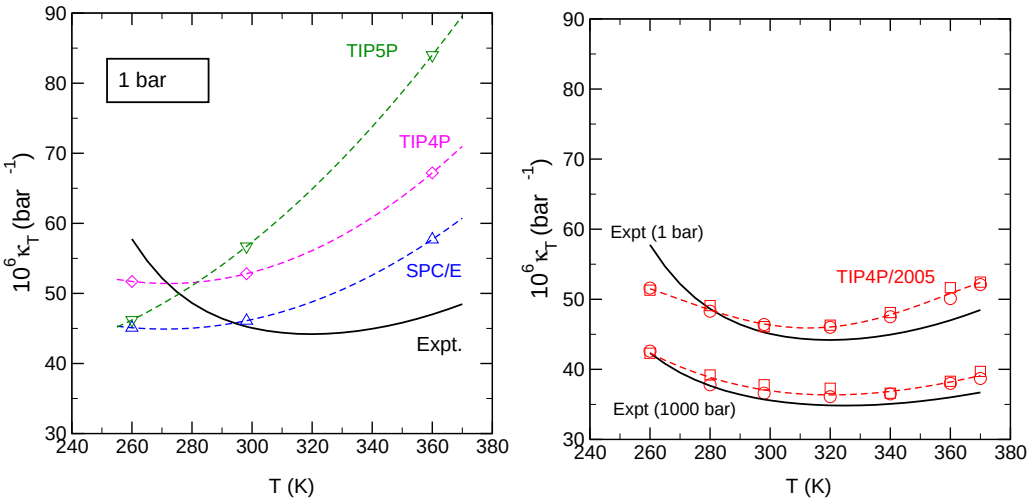

Figure 1.6: Isothermal compressibility calculated from molecular dynamics simulations. Left: Results for SPC/E, TIP4P and TIP5P at p=1 bar using the fluctuation formula (Eq. 1.2). Right: Results for TIP4P/2005 using the fluctuation equation (squares) and the derivative route (Eq. 1.1, circles); upper results are for 1 bar and lower curves are for 1000 bar. Notice that we have deliberately used the same scale in both panels. For comparison, experimental data[54] (full lines) are also plotted.

high temperatures, the differences between simulation and experiment are quite noticeable for both SPC/E and TIP4P (though less dramatic than in the TIP5P case).

As can be seen in Fig. 1.6b, the TIP4P/2005 model provides an excellent description of the isothermal compressibility of water. The compressibilities obtained from the two routes (differenciation of the equation of state and fluctuation formula) were found to be mutually consistent. The departures of the calculated compressibilities with respect to the experimental values[55,56,54,57] are in general smaller than 7 %. By fitting the TIP4P/2005 compressibilities at atmospheric pressure to a third degree polynomial, a minimum in the isothermal compressibility is found for a temperature of about 37°C which is in good agreement with the experimental value (46.5°C). Thus the model is able to accurately reproduce not only the isothermal compressibility along the whole liquid range at atmospheric pressure but also the compressibility minimum. This assertion is particularly true when one compares the TIP4P/2005 predictions with those of the other models, shown in Fig 1.6 (notice that we have plotted both panels using the same scale). In Fig 1.6, we also present the compressibility results at a higher pressure (1000 bar). TIP4P/2005 predictions for this isobar are slightly better than those for at-

mospheric pressure. A compressibility minimum is also found at 1000 bar, and, in accordance with the experiment, the minimum appears at an slightly higher temperature than it does at atmospheric pressure[54].

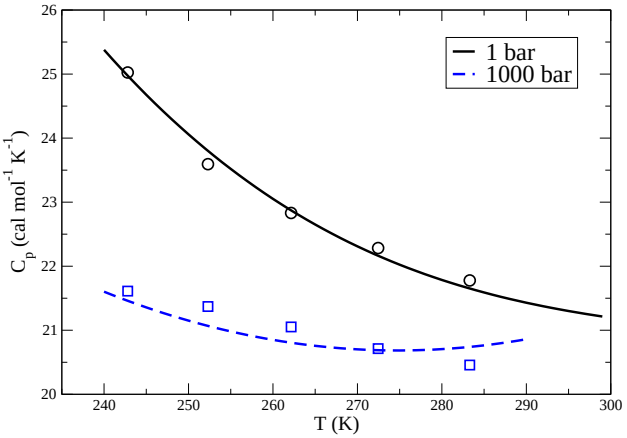

Figure 1.7: Heat capacity of water at constant pressure (C_p) as obtained from simulation results of the TIP4P/2005 for $p = 1$ bar (solid line/circles) and for $p =$ 1000 bar (dashed line/squares). The symbols represent the results of a first degree finite difference calculation for equation (3), and the curves were obtained from the results of a third degree polynomial fit (p=1000 bar) and fourth degree (p=1 bar) for the enthalpy.

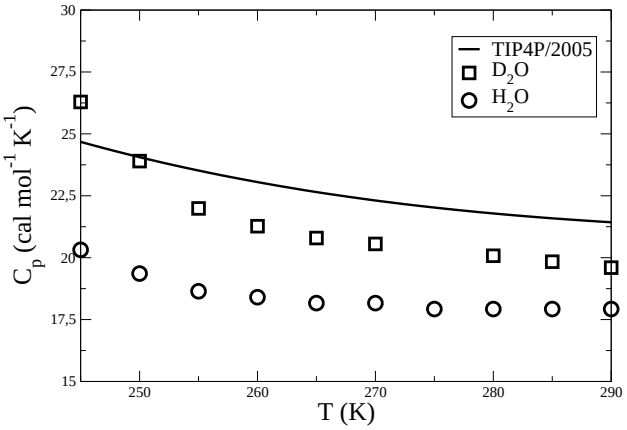

Figure 1.8: Heat capacity of water at constant pressure (C_p) as obtained from simulation results of the TIP4P/2005 for $p = 1$ bar. Experimental results for D_2O and for H_2O taken from Angell,Oguni and Sichina[58] are also presented.

Finally we have examined the behaviour of the heat capacity at constant pressure for two isobars, namely, $p = 1$ bar and $p = 1000$ bar. The results

are presented in figure 1.7. As can be seen, the model hints at the existence of minima in the heat capacity for both of these isobars. The location of the minimum seems to move to lower temperatures as the pressure increases, in concordance with experiment (see fig.7 of Ref.[41]).

In figure 1.8 the values of C_p from the simulations are compared to the experimental[58] values for water and D_2O. As one can see, the model overestimates the experimental values of the heat capacity of water at constant pressure. The large difference in the experimental values of the heat capacity of H_2O and D_2O demonstrate the importance of nuclear quantum effects in the description of the heat capacity of water. Not surprisingly, the values of TIP4P/2005 which were obtained through classical simulations lie closer to the experimental values of D_2O, probably reflecting the somewhat more classical behaviour of D_2O with respect to H_2O.

Taking into account the success of $TIP4P/2005$ in describing most of the properties of water, the failure in the quantitative description of C_p (along with the important differences in the experimental values of D_2O and H_2O) points out the necessity of incorporating nuclear quantum effects for a quantitative description of this property. Although one could incorporate quantum corrections empirically[59,25], quantum simulations (for example, via path integrals) are probably the only way to correctly describe the heat capacity of water[60,61].

1.5. Conclusions

In this work molecular dynamics simulations have been undertaken for liquid water along several isobars. The TIP4P/2005 model has been used to describe the interaction between water molecules. The results obtained in relatively long runs (i.e., 40 ns) indicate that a maximum in density is found for the isobars considered in this work (i.e., p=1, 400, 1000 and 1500 bar). The TMD decreases by about 1 K for each 45 bar of applied pressure. Thus, the TIP4P/2005 model, designed to reproduce the TMD at atmospheric pressure, is also able to predict the dependence of the TMD with pressure. Motivated by recent experimental work the behaviour of the density at low temperatures along the atmospheric pressure isobar was also studied, resulting in a density minimum at temperatures around 200 K. The location and density at the minimum of the model are in very nice agreement with recent experimental work on the equation state of water at very low temperatures (obtained by confining water in narrow pores in order to prevent the nucleation of ice). Also in agreement with experimental measurements we have found a significant increase of the diffusion coefficient of super-cooled water with pressure.

Finally, we have also computed the isothermal compressibility along the atmospheric pressure isobar for several water models and, once again, the results for TIP4P/2005 are those closest to experimental values. A minimum in the isothermal compressibility was found for temperatures around 37°C, once again in good agreement with the location of the minimum found in experiments (46.5°C) . Not only is the location of the minimum well described by the model, but the value at the minimum as well. Finally, we have calculated κ_T at several temperatures at a higher pressure (1000 bar) observing that TIP4P/2005 also exhibits a compressibility minimum. In accordance with experiment, the minimum is shifted towards slightly higher temperatures[62] when the pressure increases from 1 bar to 1000 bar.

The results of this work indicate that the TIP4P/2005 is able to reproduce almost quantitatively many of the anomalous properties of water occurring at low temperatures with the exception of the heat capacity. Therefore, the model can be used with confidence to obtain a better understanding of the behaviour of water in the super-cooled regime where the experimental determination of properties is a difficult task. It seems that for super-cooled water the performance of the TIP4P/2005 model of water supersedes the performance of other more traditional models.

Acknowledgments

This work has been funded by grants FIS2007-66079-C02-01 from the DGI (Spain), S-0505/ESP/0299 from the CAM, and 910570 from the UCM.

1. Anomalies in water as obtained from computer simulations of the TIP4P/2005 model: density maxima, and density, isothermal compressibility and heat capacity minima

Bibliografía

1. L. Verlet and J. J. Weis, Molec. Phys. **28**, 665 (1974).
2. D. Levesque and J. J. Weis, Phys. Rev. E **49**, 5131 (1994).
3. D. Eisenberg and W. Kauzmann, *The Structure and Properties of Water* (Oxford University Press, London, 1969).
4. V. F. Petrenko and R. W. Whitworth, *Physics of Ice* (Oxford University Press, 1999).
5. J. L. Finney, Phil. Trans. R. Soc. Lond. B **359**, 1145 (2004).
6. M. Chaplin, http://www.lsbu.ac.uk/water/ (2005).
7. J. L. Finney, J. Molec. Liq. **90**, 303 (2001).
8. C. G. Salzmann, P. G. Radaelli, A. Hallbrucker, E. Mayer, and J. L. Finney, Science **311**, 1758 (2006).
9. J. A. Barker and R. O. Watts, Chem. Phys. Lett. **3**, 144 (1969).
10. A. Rahman and F. H. Stillinger, J. Chem. Phys. **55**, 3336 (1971).
11. R. M. Lynden-Bell, J. C. Rasaiah, and J. P. Noworyta, Pure Appl. Chem. **73**, 1721 (2001).
12. K. M. Åberg, A. P. Lyubartsev, S. P. Jacobsson, and A. Laaksonen, J. Chem. Phys. **120**, 3770 (2004).
13. M. Ferrario, G. Ciccotti, E. Spohr, T. Cartailler, and P.Turq, J. Chem. Phys. **117**, 4947 (2002).
14. D. Paschek, J. Chem. Phys. **120**, 6674 (2004).
15. C. R. W. Guimaraes, G. Barreiro, C. A. F. de Oliveria, and R. B. de Alencastro, Brazil. J. Phys. **34**, 126 (2004).

16. H. J. C. Berendsen, J. P. M. Postma, W. F. van Gunsteren, and J. Hermans, *Intermolecular Forces, ed. B. Pullman, page 331* (Reidel, Dordrecht, 1982).

17. H. J. C. Berendsen, J. R. Grigera, and T. P. Straatsma, J. Phys. Chem. **91**, 6269 (1987).

18. W. L. Jorgensen, J. Chandrasekhar, J. D. Madura, R. W. Impey, and M. L. Klein, J. Chem. Phys. **79**, 926 (1983).

19. M. W. Mahoney and W. L. Jorgensen, J. Chem. Phys. **112**, 8910 (2000).

20. B. Guillot, J. Molec. Liq. **101**, 219 (2002).

21. E. Sanz, C. Vega, J. L. F. Abascal, and L. G. MacDowell, Phys. Rev. Lett. **92**, 255701 (2004).

22. C. Vega, J. L. F. Abascal, E. Sanz, L. G. MacDowell, and C. McBride, J. Phys. Cond. Mat. **17**, S3283 (2005).

23. C. Vega, E. Sanz, J. L. F. Abascal, and E. G. Noya, J. Phys. Condens. Matter **20**, 153101 (2008).

24. J. L. F. Abascal, E. Sanz, R. G. Fernández, and C. Vega, J. Chem. Phys. **122**, 234511 (2005).

25. J. L. F. Abascal and C. Vega, J. Chem. Phys. **123**, 234505 (2005).

26. C. Vega, J. L. F. Abascal, M. M. Conde, and J. L. Aragones, Faraday Discussions **141**, 251 (2009).

27. C. Vega and J. L. F. Abascal, J. Chem. Phys. **123**, 144504 (2005).

28. C. Vega, J. L. F. Abascal, and I. Nezbeda, J. Chem. Phys. **125**, 034503 (2006).

29. C. Vega and E. de Miguel, J. Chem. Phys. **126**, 154707 (2007).

30. P. G. Debenedetti, J. Phys. Cond. Mat. **15**, R1669 (2003).

31. D. V. der Spoel, E. Lindahl, B. Hess, G. Groenhof, A. E. Mark, and H. J. C. Berendsen, J. Comput. Chem. **26**, 1701 (2005).

32. U. Essmann, L. Perera, M. L. Berkowitz, T. Darden, H. Lee, and L. G. Pedersen, J. Chem. Phys. **103**, 8577 (1995).

33. J. P. Ryckaert, G. Ciccotti, and H. J. C. Berendsen, J.Comp.Phys. **23**, 327 (1977).

34. H. J. C. Berendsen and W. F. van Gunsteren, in *Molecular Liquids-Dynamics and Interactions* (Reidel Dordretch, 1984), Proceedings of the NATO Advanced Study Institute on Molecular Liquids, pp. 475–500.

35. S. Nosé, Molec. Phys. **52**, 255 (1984).

36. W. G. Hoover, Phys. Rev. A **31** (1985).

37. M. Parrinello and A. Rahman, J. Appl. Phys. **52**, 7182 (1981).

38. S. Nosé and M. L. Klein, Molec. Phys. **50**, 1055 (1983).

39. K. A. Motakabbir and M. Berkowitz, J. Phys. Chem. **94**, 8359 (1990).

40. A. Glättli, X. Daura, and W. van Gunsteren, J. Chem. Phys. **116**, 9811 (2002).

41. R. A. Fine and F. J. Millero, J. Chem. Phys. **63**, 89 (1975).

42. C. A. Angell and H. Kanno, Science **193**, 1121 (1976).

43. J. L. F. Abascal, E. Sanz, and C. Vega, Phys.Chem.Chem.Phys. **11**, 556 (2009).

44. J. L. Aragones, M. M. Conde, E. G. Noya, and C. Vega, Phys.Chem.Chem.Phys. **11**, 543 (2009).

45. H. Kanno, R. J. Speedy, and C. A. Angell, Science **189**, 880 (1975).

46. S. Kittaka, S. Ishimaru, M. Kuranishi, T. Matsuda, and T. Yamaguchi, Phys. Chem. Chem. Phys. **8**, 3223 (2006).

47. D. Liu, Y. Zhang, C. C. Cheng, C. Y. Mou, P. H. Poole, and S. H. Chen, Proc. Natl. Acad. Sci. **104**, 9570 (2007).

48. F. Mallamace, C. Branca, M. Broccio, C. Corsaro, C. Y. Mou, and S. H. Chen, Proc. Natl. Acad. Sci. **104**, 18387 (2007).

49. D. Paschek, Phys.Rev.Lett. **94**, 217802 (2005).

50. P. H. Poole, I. Saika-Voivod, and F. Sciortino, J.Phys.Condens.Matter **17**, L431 (2005).

51. E. G. Noya, C. Menduina, J. L. Aragonés, and C. Vega, J. Phys. Chem. C **111**, 15877 (2007).

52. C. A. Angell, Nature Nanotechnology **2**, 396 (2007).

53. R. F.X Prielmeier, E.W.Lang and H.D.LÃn, Ber.Bunsenges.Phys.Chem **92**, 1111 (1988).

54. A. Saul and W. Wagner, J. Phys. Chem. Ref. Data **18**, 1537 (1989).

55. G. S. Kell, J. Chem. Eng. Data **20**, 97 (975).

56. R. J. Speedy and C. A. Angell, J. Chem. Phys. **65**, 851 (1976).

57. T. S. Carlton, J. Phys. Chem. B **111**, 13398 (2007).

58. C. A. Angell, M. Oguni, and W. J. Sichina, J.Phys.Chem. **86**, 998 (1982).

59. H. W. Horn, W. C. Swope, J. W. Pitera, J. D. Madura, T. J. Dick, G. L. Hura, and T. Head-Gordon, J. Chem. Phys. **120**, 9665 (2004).

60. W. Shinoda and M. Shiga, Phys. Rev. E **71**, 041204 (2005).

61. G. S. D. Buono, P. J. Rossky, and J. Schnitker, J. Chem. Phys. **95**, 3728 (1991).

62. R. A. Fine and F. J. Millero, J. Chem. Phys. **59**, 5529 (1973).

Results: Chapter 2

The shear viscosity of rigid water models

Miguel Angel González *and José L. F. Abascal*

Departamento de Química Física, Facultad de Ciencias Químicas, Universidad Complutense de Madrid, 28040 Madrid, Spain

2.1. Abstract

In this work the shear viscosity at ambient conditions of several water models (SPC/E, TIP4P, TIP5P and TIP4P/2005) is evaluated using the Green-Kubo formalism. The performance of TIP4P/2005 is excellent, that of SPC/E and TIP5P is more or less acceptable whereas TIP4P and, especially, TIP3P give a poor agreement with experiment. Further calculations have been carried out for TIP4P/2005 to provide a wider assessment of its performance. In accordance with experimental data, TIP4P/2005 predicts a minimum in the shear viscosity for the 273 K isotherm, a shift of the minimum towards lower pressures at 298 K and its disappearance at 373 K.

2.2. Introduction

Computer simulation is a useful tool which can be employed to validate models of physical systems by comparing the simulation results with experimental data. Obviously, the quality of a model should be established by its ability to predict other properties different from those used to fit the model parameters. Given the importance of water there have been a large number of computer simulation studies[1]. Among the successful water models we may

cite SPC/E[2] and TIP4P[3] proposed more than twenty years ago. Despite their simplicity (both models are rigid and non-polarizable) and the work devoted to refine the water force field, until recently there has been no clear improvement. Already in the 2000's, Mahoney and Jorgensen[4] proposed a new promising water model, TIP5P. More recently the study of the phase diagram of water[5] has triggered several reparametrizations of TIP4P.[6,7] One of these, TIP4P/2005, has an impressive performance for a wide variety of properties and thermodynamic conditions.[7,8,9,10,11] In fact, for condensed phases, the predictions of TIP4P/2005 are better than those of TIP4P for *all the properties* investigated up to now. But it is important to note that this model has not been thoroughly checked for dynamical properties. The shear viscosity of water is particularly interesting because it shows an "anomalous"behavior: its dependence with pressure exhibits a minimum below 306 K[12].

An accurate calculation of the shear viscosity requires significant computer resources. There are some reports of simulations of this property for SPC/E[13,14,15,16,17], TIP4P,[18] and TIP3P.[16] To the best of our knowledge, the viscosities of TIP5P and TIP4P/2005 have not yet been reported. Thus in this work we have undertaken the task of calculating the viscosity of SPC/E, TIP3P, TIP4P, TIP5P and TIP4P/2005 at ambient conditions. As we will see below, it turns out that the models providing a better account of the water viscosity at 298 K are SPC/E and, especially, TIP4P/2005. A deeper investigation of the performance will only be done for these models.

The Green-Kubo formula relates the shear viscosity to the autocorrelation function (ACF) of the off-diagonal components of the pressure tensor, $P_{\alpha\beta}$. Namely,

$$\eta = \frac{V}{kT}\int_0^\infty \langle P_{\alpha\beta}(t_0)P_{\alpha\beta}(t_0+t)\rangle_{t_0}dt, \tag{2.1}$$

The main contribution comes from the short time ACF but an accurate computation of the shear viscosity also requires a precise calculation of the ACF tail (for this reason alternative methods have been proposed to compute the shear viscosity, see Ref.[15] and references therein). A careful analysis for the case of SPC/E water made by Guo and Zhang[14] has shown that the Green-Kubo relation leads to reliable results using an upper limit of the order of 3 ps in the above integral. In order to obtain good statistics for the ACF at such correlations times, simulations of about 4 ns were required. In this work we follow the same methodology as in the paper by Guo and Zhang but we have extended the simulation length to improve the statistics of the ACF tail and, thus, the accuracy of the calculations. As the system is isotropic, the off-diagonal elements of the pressure tensor, P_{xy}, P_{xz}, P_{zy},

are equivalent. Besides, due to the rotational invariance of the molecule, the terms $(P_{xx} - P_{yy})/2$ and $(P_{yy} - P_{zz})/2$ are also equivalent.[14,19] In this way, in our calculations, the accuracy of the resulting ACF is enhanced by averaging over five pressure components.

2.3. The simulations

For the simulations we have used the GROMACS package.[20] The simulations have been performed in the canonical (NVT) ensemble using the Nosé-Hoover thermostat[21,22] for a sample size of 500 water molecules. The box size was fixed from the knowledge of the density of the model at the desired pressure. As a result the final pressures were slightly different from the target ones —typically by less than 1 MPa— but this has a negligible effect on the reported viscosities.

Long range electrostatic interactions have been calculated with the Ewald summation method using PME for the reciprocal part.[23] The simulated time was between 20 ns and 60 ns using a timestep of 1 fs. The ACF has been calculated from the pressure components saved on disk every 2 fs. All the configurations were used as a time origin. The upper limits in the integral were between 3 ps and 10 ps depending on the system.[24] Other details of the simulations as well as the ACF functions and the numerical values of the viscosity are given as supplementary material.[24]

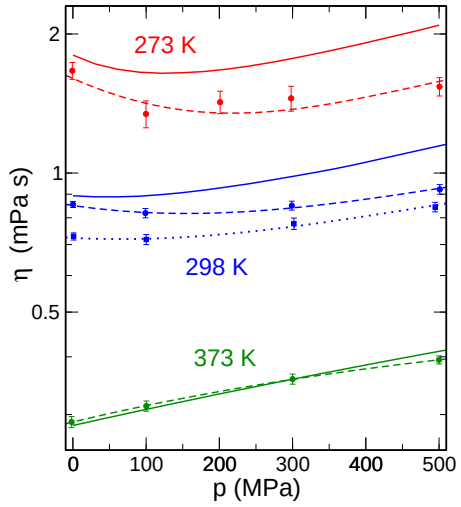

Figure 2.1: Shear viscosities, in logarithmic scale, of TIP4P/2005 (circles, dashed lines) and SPC/E (squares, dotted line). Full lines are the experimental results.

2.4. Results

The shear viscosities at ambient conditions for the water models considered in this paper are shown in Table 2.1. It is interesting to note that

Table 2.1: Shear viscosities (in mPa·s) of several rigid water models at 298 K and 1 bar.

TIP3P	TIP4P	TIP5P	SPC/E	TIP4P/2005	Expt.[25]
0.321	0.494	0.699	0.729	0.855	0.896

our results are close to those reported recently by other authors at about the same temperature: 0.31 mPa·s for TIP3P[16], 0.47 mPa·s for TIP4P[18] and 0.64,[15] 0.65,[14] 0.67,[17] and 0.72[16] mPa·s for SPC/E (the results for TIP3P and SPC/E correspond to temperatures slightly above 300 K which may explain the small departures from our values). The predictions of TIP3P and TIP4P are quite poor. The estimates from TIP5P and SPC/E are somewhat better but still far from the experimental value (around a 20 percent departure). On the contrary, TIP4P/2005 performs quite well since the deviation from experiment is slightly less than a 5 percent. This is an accordance with the excellent predictions of TIP4P/2005 at normal pressure shown in recent calculations[26].

Figure 2.3 shows the viscosities of SPC/E and TIP4P/2005 for several temperatures. Although both models systematically underestimates the viscosity at 298 K, the results for TIP4P/2005 are closer to the experimental data. Besides, the latter model predicts a minimum whereas SPC/E does not show it (or, if exists, it is a very shallow one). The minimum shifts towards lower pressures at increasing temperatures so it does not appear at 373 K. Thus, the overall behavior of TIP4P/2005 closely follows the experimental trends[12,25]. The results shown in this work together with those previously reported for the self-diffusion coefficient[11] indicate that TIP4P/2005 also gives an impressive performance for the dynamical properties. We may conclude that the model is able to account for the "anomalies" in the dynamical properties of water as well as for the static ones.[10]

This work has been funded by grants FIS2007-66079-C02-01 from the DGI (Spain), S-0505/ESP/0229 from the CAM, and 910570 from the UCM.

SUPPLEMENTAL MATERIALS for "The shear viscosity of rigid water models"

We present the supplemantal materiasl for this chapter. Where we find the figure of the normalized autocorrelation fucntion for several water models, the figure of the running values of shear viscosity, the figure with the same magnitude but for only TIP4P/2005 water model using 500 and 1000 molecules. In the end, we look at the last Table 2.2 with the values of different models at different conditions.

Autocorrelation functions

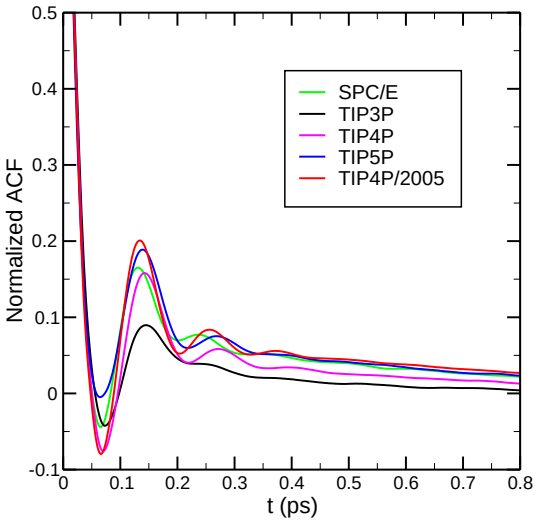

Figure 2.2: Normalized autocorrelation functions of the non-diagonal components of the pressure tensor for rigid water models at ambient conditions (298 K, 1 bar)

Running values of the viscosity

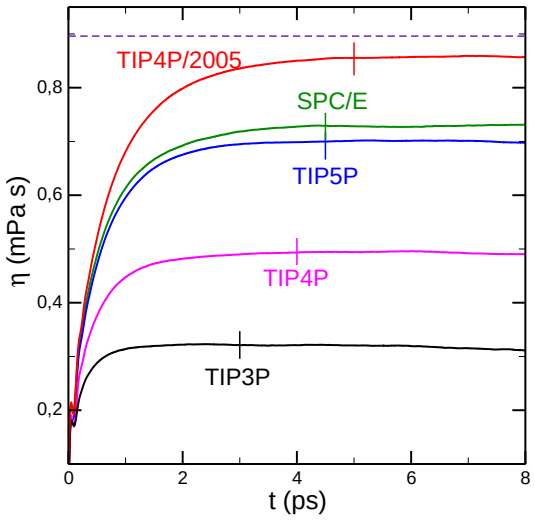

Figure 2.3: Running values of the viscosity obtained by integration of the normalized ACF displayed in Fig.1. The vertical lines indicate the upper limits used for the final results. The experimental value is displayed as a dashed line.

Effect of system size

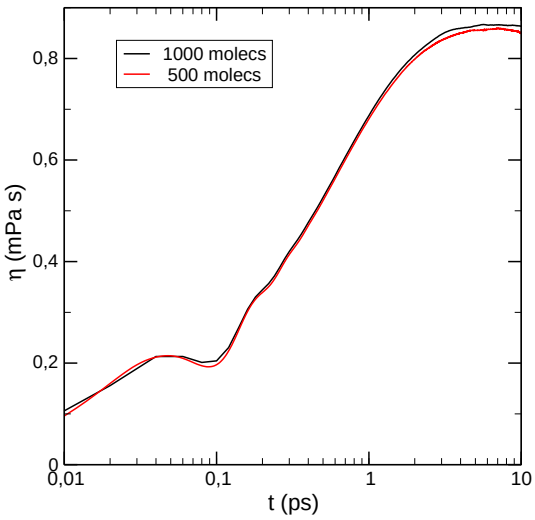

Figure 2.4: Viscosity of TIP4P/2005 at ambient conditions for two different system samples: 500 and 1000 molecules.

Numerical values of the viscosity of rigid water models

Table 2.2: Shear viscosities (in mPa·s) of rigid water models. The fifth column shows the upper limit (in ps) in the integral over the autocorrelation functions and the sixth the simulation length (in ns).

Model	T/K	p/MPa	η	t_{max}	length
TIP3P	298	-1	0.324± 0.009	4.0	18
* TIP4P	298	1	0.495± 0.013	4.5	30
* TIP5P	298	0	0.699± 0.012	4.5	40
* SPC/E	298	1	0.729± 0.012	4.5	20
SPC/E	298	100	0.718± 0.022	4.5	20
SPC/E	298	302	0.777± 0.018	4.5	20
SPC/E	298	495	0.844± 0.024	4.5	20
TIP4P/2005	373	-2	0.289± 0.008	4.0	20
TIP4P/2005	373	100	0.313± 0.008	4.0	20
TIP4P/2005	373	300	0.358± 0.009	4.0	20
TIP4P/2005	373	500	0.394± 0.008	4.0	20
TIP4P/2005	298	0	0.855± 0.013	5.0	40
TIP4P/2005	298	99	0.819± 0.019	5.0	30
TIP4P/2005	298	299	0.850± 0.019	5.0	30
TIP4P/2005	298	501	0.922± 0.022	5.0	30
TIP4P/2005	273	-1	1.66 ± 0.04	10.0	54
TIP4P/2005	273	100	1.34 ± 0.05	8.0	27
TIP4P/2005	273	201	1.42 ± 0.04	7.5	30
TIP4P/2005	273	298	1.45 ± 0.05	7.5	23
TIP4P/2005	273	501	1.54 ± 0.04	8.0	38

Bibliografía

1. B. Guillot, J. Molecular Liquids **101**, 219 (2002).
2. H. J. C. Berendsen, J. R. Grigera, and T. P. Straatsma, J. Phys. Chem. **91**, 6269 (1987).
3. W. L. Jorgensen, J. Chandrasekhar, J. D. Madura, R. W. Impey, and M. L. Klein, J. Chem. Phys. **79**, 926 (1983).
4. M. W. Mahoney and W. L. Jorgensen, J. Chem. Phys. **112**, 8910 (2000).
5. E. Sanz, C. Vega, J. L. F. Abascal, and L. G. MacDowell, Phys. Rev. Lett. **92**, 255701 (2004).
6. J. L. F. Abascal, E. Sanz, R. García Fernández, and C. Vega, J. Chem. Phys. **122**, 234511 (2005).
7. J. L. F. Abascal and C. Vega, J. Chem. Phys. **123**, 234505 (2005).
8. C. Vega, J. L. F. Abascal, and I. Nezbeda, J. Chem. Phys. **125**, 034503 (2006).
9. C. Vega and E. de Miguel, J. Chem. Phys. **126**, 154707 (2007).
10. H. L. Pi, J. L. Aragones, C. Vega, E. G. Noya, J. L. F. Abascal, M. A. Gonzalez, and C. McBride, Molecular Physics **107**, 365 (2009).
11. C. Vega, J. L. F. Abascal, M. M. Conde, and J. L. Aragones, Faraday Discuss. **141**, 251 (2009).
12. K. E. Bett and J. B. Cappi, Nature **207**, 620 (1965).
13. S. Balasubramanian, C. J. Mundy, and M. L. Klein, J. Chem. Phys. **105**, 11190 (1996).
14. G.-J. Guo and Y.-G. Zhang, Mol. Phys. **99**, 283 (2001).

15. B. Hess, J. Chem. Phys. **116**, 209 (2002).

16. Y. J. Wu, H. L. Tepper, and G. A. Voth, J. Chem. Phys. **124**, 024503 (2006).

17. T. Chen, B. Smit, and A. T. Bell, J. Chem. Phys. p. 246101 (2009).

18. E. Wensink, A. Hoffmann, P. van Maaren, and D. van der Spoel, J. Chem. Phys. **119**, 7308 (2003).

19. D. Alfè and M. J. Gillan, Phys. Rev. Lett. **81**, 5161 (1998).

20. D. van der Spoel, E. Lindahl, B. Hess, G. Groenhof, A. E. Mark, and H. J. C. Berendsen, J. Comput. Chem. **26**, 1701 (2005).

21. S. Nosé, Mol. Phys. **52**, 255 (1984).

22. W. G. Hoover, Phys. Rev. A **31**, 1695 (1985).

23. U. Essmann, L. Perera, M. L. Berkowitz, T. A. Darden, H. Lee, and L. Pedersen, J. Chem. Phys. **103** (1995).

24. See Supplementary Material Document No. — for other simulation details and numerical values of the viscosity.

25. K. R. Harris and L. A. Woolf, J. Chem. Eng. Data **49**, 1064 (2004).

26. J. Vrabec, private communication.

Results: Chapter 3

A flexible model for water based on TIP4P/2005

Miguel Angel González *and José L. F. Abascal*

Departamento de Química Física, Facultad de Ciencias Químicas, Universidad Complutense de Madrid, 28040 Madrid, Spain

3.1. Abstract

A new flexible water model, TIP4P/2005f, is developed. The idea was to add intramolecular degrees of freedom to the successful rigid model TIP4P / 2005 in order to try to improve the predictions for some properties, and to enable the calculation of new ones. The new model incorporates flexibility by means of a Morse potential for the bond stretching and a harmonic term for the angle bending. The parameters have been fitted to account for the peaks of the infrared spectrum of liquid water and to produce an averaged geometry close to that of TIP4P/2005. As for the intermolecular interactions, only a small change in the σ parameter of the Lennard-Jones potential has been introduced. The overall predictions are very close to those of TIP4P/2005. This ensures that the new model may be used with the same confidence as its predecessor in studies where a flexible model is advisable.

3.2. Introduction

Given the importance of water, it seems pertinent to understand the interaction between water molecules in the condensed phase. Several successful interaction potentials have been developed in the past. Simulation studies

show that these force fields account for many important properties of liquid water although, needless to say, there is still room for improvement.[1,2] A common feature of the most popular water models is that they are rigid, i.e., the intramolecular degrees of freedom are frozen. It may seem obvious that a step forward for the improvement of the water potential would be the addition of flexibility. However, there has been some skepticism on the past about the usefulness of flexible water models.[3,4,5,6] In fact, Tironi et al.[4] concluded that the introduction of flexibility creates more problems than it solves and does not improve upon the accuracy of rigid models. Notice that the high frequency of the bond stretching forces one to use a time step about five times smaller than that of a rigid model. In this way, the performance of flexible models may not justify its increased computational cost. It may be argued that flexible models make possible the calculation of new properties. But that must be done with care because the high frequency of the new accessible vibrational modes indicates that these are strongly quantized. In this context, a flexible model would be more justified in the case of a quantum treatment of the nuclear motion. In fact, interesting results have been obtained in quantum simulations of a flexible water model.[7]

However, rigid models do not allow to investigate certain properties, noticeably the infrared (IR) spectrum, that require the use of a flexible molecular geometry. This is important because computer simulations provide a set of instantaneous configurations of the system from which it is possible to get useful structural information that can not be directly extracted from experiment. For instance, it enables the assignment of some bands of unclear origin appearing in the Raman spectrum of liquid water. Moreover it enables a detailed analysis of the relationship between power spectrum and the hydrogen bonding network.[8,9] A flexible model is also imperative in other situations as, for example, in the empirical valence bond methodology and its multistate generalization.[10] Besides, there are a number of reports claiming that some predictions of flexible models are closer to experimental data than those of rigid potentials.[11,13,14,15,12] Yuet and Blankschtein[15] have concluded that the surface tension of water is determined by the delicate balance between intramolecular (bond stretching) and intermolecular (LJ) interactions. Raabe and Sadus[12] have shown that introducing bond flexibility significantly improves the prediction of both the dielectric constants and the equation of state of liquid water. These authors argue that adding intramolecular degrees of freedom to a rigid water model introduces in some way the effect of the local environment. This is because the changes in the molecular geometry in response to the thermodynamic state point produce variations in the dipole moment. Thus, the fluctuations in the total dipole moment of the system come not only from the variations in the relative orientation of the molecules

(as in a rigid model) but also from the changes in the dipole moment of the molecules. In this way the variation of the dielectric constant as a consequence of changes in the environment of the molecules could be better described with a flexible model than with a rigid one (notice also that the ability of a flexible model to vary in a changing environment could be, in principle, of great value in the study of interfaces.) On the other hand, flexible bonds and angles are required when dealing with systems with torsional degrees of freedom. Consequently, the force-fields employed in biomolecular simulations contain terms according with this need. Although many authors prefer to use a rigid water model in these conditions, some of them find more consistent to use also a flexible water model. In summary, despite the skepticism of several reports, there are some reasons supporting the interest in developing (or improving) flexible water models.

It seems natural that the development of flexible models will consist on the addition of flexibility to a successful rigid potential. Until recently, it has been a general feeling that two models, namely TIP4P[16] and SPC/E,[17] provided the best ratio between performance and simplicity. However, recent investigations on the phase diagram involving the solid phases of water have demonstrated[18,19,20,21] the superiority of the charge distribution of TIP4P model over that of SPC/E. For this reason, an updated version of TIP4P including intramolecular degrees of freedom could of interest for those investigating water properties that require the use of a flexible model. On the other hand, the idea behind the parametrization of SPC/E (a correction term is added to the enthalpy of vaporization) seems to be responsible for the good predictions of this model. In this way, TIP4P and SPC/E obtain similar scores in a recently reported performance analysis of water models.[2] It was evident that the water force field could be improved by merging the relevant features of both models. This is in essence the basis of the success of TIP4P/2005.[22] Since its proposal, a rather comprehensive set of properties has been evaluated for this model. It provides an excellent agreement with experiment for thermodynamic,[22,23,24] structural,[25,26] and dynamical[27,28] properties, over a wide range of temperatures from subcritical[29] to the liquid-gas critical point. Its performance has also been contrasted with experiment in the case of biomolecular systems.[30] Because of this, the goal of this work is to develop a flexible version of TIP4P/2005.

This article is organized as follows: In section II we give the details of our choice for the intramolecular interactions and present the parameters of the new model (which we term as TIP4P/2005f) as well as the averaged geometry in the liquid state. In section III we discuss the results obtained in molecular dynamics simulations of the model which are compared with experiment and with those for TIP4P/2005. Finally, conclusions are given in

Section IV.

3.3. The model

A number of computer simulations with different flexible water models have been reported[31,32,33,34,8,11] since the pioneering works of Lemberg and Stillinger[35] and Toukan and Rahman.[36] As commented in the introduction it seems convenient to develop a new flexible model based on the rigid water model TIP4P/2005. The first problem we face is the choice of the character of this flexibility, namely harmonic or anharmonic. The use of a harmonic function $V_{OH_i} = D_r\beta^2(r_{OH_i} - r_{eq})^2$ may be advised because it is computationally less expensive. Figure 3.1 compares the harmonic potential for the bond stretching with the cubic and quartic ones as well as the full Morse potential. All functions have the minimum at the same distance but the interaction differs significantly as one moves away from equilibrium. When calculating the power spectrum with the harmonic potential we observed a splitting in the OH stretching band ($\sim$3400cm^{-1}) which did not correspond with the experimental data.[37,38] In the case of using anharmonic functions, the splitting of the band disappeared and was closer to experiment. For this reason we chose an anharmonic function to represent the flexibility of the OH bond. Once the harmonic potential is ruled out, it can be seen in Fig. 3.1 that the cubic function exhibits a wiggle which can be problematic in computer simulation. The quartic and Morse functions are quite similar even at distances relatively far from equilibrium. We finally opted for the full Morse function because the calculations indicated that its use did not increase the computational cost. The intramolecular potential is then given by

$$V^{intra} = V_{OH_1}(r) + V_{OH_2}(r) + V_{HOH}(\theta), \tag{3.1}$$

$$V_{OH_i} = D_r\{1 - exp[-\beta(r_{OH_i} - r_{eq})]\}^2, \tag{3.2}$$

where r_{eq} and θ_{eq} are the values of the bond length and angle at equilibrium and r_{OH_i} is the instantaneous distance between the hydrogen atom i and the oxygen atom. D_r and β are the parameters of the Morse potential that determine the bond strength and width. For the angle bending, a harmonic function (with an associated strength constant K_θ) seems to be sufficient

$$V_{HOH}(\theta) = \frac{1}{2}K_\theta(\theta - \theta_{eq})^2. \tag{3.3}$$

The molecular geometry of our model is given by a slight modification of the TIP4P/2005 parameters. This amendment is the result of incorporating

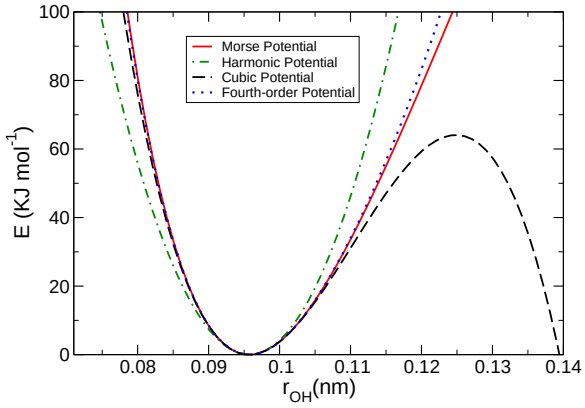

Figure 3.1: Four alternative functions to describe the bond stretching in a flexible water model.

the flexibility which produces a elongation of the OH distance and a reduction of the HOH angle. For this reason we chose a smaller bond distance at equilibrium ($r_{eq} = 0{,}9419$ Å) and a larger angle ($\theta_{eq} = 107{,}4°$) than those of TIP4P/2005 (Table I).

As for the intermolecular potential, we follow the usual choice of TIP4P-like models: a Lennard-Jones center at the position of the oxygen atom plus the electrostatic interaction given by two positive charges located at the hydrogen atoms and a compensating negative charge placed at the so-called M-site. Since the molecule is not rigid, the location of the M site is defined in terms of the positions of the hydrogen atoms:

$$d_{OM} = d_{OM}^{rel}(z_{OH_1} + z_{OH_2}), \tag{3.4}$$

where z_{OH_1} and z_{OH_2} are the distances to the oxygen of the hydrogens projections along the HOH bisector, $z_{OH_i} = d_{OH_i}\cos(\theta/2)$. We have chosen the value for d_{OM}^{rel} so as to reproduce the distance d_{OM} in the TIP4P/2005 geometry (i.e., $d_{OH} = 0{,}9572$, $\theta = 104{,}52$ and, thus, $d_{OM} = 0{,}1546$). As a result of the addition of flexibility and the changes in the average molecular geometry it produces, the intermolecular parameters may not be optimized[39] and require a further tuning. We observed that the properties more related to the interaction energy did not change significantly while those dependent on the molecular size (the orthobaric densities in particular) were slightly shifted with respect to those of the rigid model. Thus, it has been necessary to increase the parameter σ of the Lennard-Jones interaction while the rest of parameters are not altered from TIP4P/2005. The parameters of the TIP4P/2005f model are collected in Table I where we have also included for comparison the corresponding values for TIP4P/2005.

Table 3.1: Potential parameters of the TIP4P/2005f and TIP4P/2005 water models. Notice that r_{eq} and θ_{eq} define the rigid geometry of TIP4P/2005.

Parameter	TIP4P/2005f	TIP4P/2005
ϵ/k(K)	93.2	93.2
σ(Å)	3.1644	3.1589
q_H(e)	0.5564	0.5564
d_{OM}^{rel}	0.13194	0.13194
D_r(kJ/mol)	432.581	-
r_{eq}(Å)	0.9419	0.9572
β(nm^{-1})	22.87	-
θ_{eq}/deg	107.4	104.52
K_θ(kJ/ (mol rad^2))	367.810	-

Figure 3.3 shows the normalized histogram of the distribution of bond distances for a single molecule at a temperature close to 0 K (the actual value is 2 K) compared to that for bulk conditions. We have used here a small time-step, 0.1 fs, and the simulations lasted 10ps. As can be expected for a classical solution of the equation for the intramolecular motion, the bond distribution for a single molecule has two maxima coincident with the turning points of the bond stretching (at this temperature the behavior corresponds approximately to a harmonic spring). This result is completely different from that given by quantum mechanics so one could question the validity of the results for the condensed state. But the collective effect of the intermolecular interactions dramatically change the distribution, which shows a more or less Gaussian profile in the liquid, in close agreement with quantum mechanical results. It is noticed that the maximum appears at distances larger than r_{eq}. For liquid water, the position of the peak depends slightly on the thermodynamic state. At room temperature and pressure, the value r_{eq}=0.9419 Å results in a maximum at 0.966 Å (close to the fixed OH distance in TIP4P/2005).

Table 3.2 presents the average value along a simulation at ambient conditions of the parameters related to the molecular geometry, namely bond distance $\langle r_{OH}\rangle$, distance O-M $\langle r_{OM}\rangle$, angle H-O-H $\langle\theta\rangle$ and dipole moment $\langle\mu\rangle$. Also given are the corresponding values for the rigid model TIP4P/2005. It may be seen that the averaged molecular geometry of the model somewhat differs from that of the isolated molecule (cf. Table I and Fig. 3.3) but it is very close to that of TIP4P/2005.

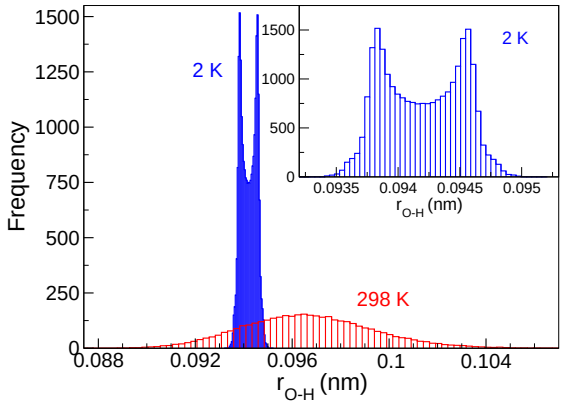

Figure 3.2: Distribution of bond distances at different conditions. The area of both histograms is normalized. The red (broader) histogram corresponds to liquid water at 1bar, 298 K while the blue one corresponds to the results for a single molecule at 2 K (zoomed at the inset).

Table 3.2: Average value of the parameters related to the molecular geometry in a simulation at T=298 K and p=1 bar. The corresponding values for TIP4P/2005 are also given for comparison.

Model	TIP4P/2005f	TIP4P/2005
$\langle r_{OH} \rangle$(Å)	0.9664	0.9572
$\langle r_{OM} \rangle$(Å)	0.1555	0.1546
$\langle \theta \rangle$(deg)	104.79	104.52
$\langle \mu \rangle$ (D)	2.319	2.305

3.4. Results

The simulations were carried out with the GROMACS 4.0 package[40,41] for a sample of 500 water molecules. When necessary we used the velocity-rescale thermostat,[42] and the barostat of Parrinello-Rahman.[43] The Lennard-Jones interactions were truncated at 8.0 Å. The particle mesh Ewald method[44] was employed to calculate the long-range electrostatics forces. For the calculation of most of the properties discussed in this article we used a time step of 0.2 fs lasting 10 ns of total simulation time. In the event that we have used other conditions for the simulation we shall describe it at the corresponding place in the manuscript.

Table 3.3 presents a summary of the properties of the TIP4P/2005f water model at T=298 K, p=1 bar compared with experimental data and with the results for TIP4P/2005. We also give there the melting point and

Table 3.3: A summary of the properties of TIP4P/2005f compared to the corresponding values for TIP4P/2005 and with experimental data. Density, ρ, isothermal compressibility, κ_T, (relative) static dielectric constant, $\varepsilon_r = \varepsilon/\varepsilon_0$, and self-diffusion coefficient, D_s, have been calculated at T=298 K, p=1 bar. The melting temperature, T_m, and the enthalpy of vaporization, $\Delta_v H$, also correspond to a pressure of 1 bar. $\Delta_v H$ include the self-polarization correction —Eq.(3.6)— while the values in parenthesis are the result of Eq.(3.5) without any further correction.

Model	TIP4P/2005f	TIP4P/2005	Expt.
ρ (g/cm^3)	0.9977	0.9979	0.9970
$10^5\kappa_T$ (MPa^{-1})	4.46	4.63	4.53
ε_r	55.3	57.3	78.4
$10^9 D_s$ (m^{2}s^{-1})	1.93	2.08	2.27
Melting temperature (K)	254	252.1	273.15
$\Delta_v H$ (KJ mol^{-1})	45.7(50.3)	45.6 (50.1)	44.05

the enthalpy of vaporization of the TIP4P/2005f model at room pressure. In what follows we describe in more detail the properties of this new flexible model.

Liquid densities at normal pressure

We have evaluated the density for the room pressure isobar at twelve different temperatures, from 250 K to 370 K. Numerical data are provided in Table IV and a plot of the results is shown in Figure 3.4 where the characteristic “anomalous"behavior of water is clearly seen. The calculated densities are in excellent agreement with the experimental data. In fact, TIP4P/2005f performs even better than TIP4P/2005 for this property. Densities for the flexible model have been adjusted to a fifth-order polynomial. The temperature of maximum density (TMD) obtained with the fit is 280.3 K, only three degrees above the experimental value. As stated in several studies,[45,2] an accurate prediction of the densities at room pressure and the TMD usually indicates that the model has an excellent performance in reproducing a wide variety of properties of liquid water.

Structure. Radial distribution function

Oxygen-oxygen radial distribution function $g_{oo}(r)$ is shown in Fig 3.4. TIP4P/2005f results are in general very close to the experimental data.[46] Similarly to TIP4P/2005, it overestimates the height of the main peak and

Table 3.4: Liquid densities (g/cm^3) at p=1 bar

T/K	TIP4P/2005f	Expt.
250	0.9906	0.9913
260	0.9959	0.9970
270	0.9984	0.9995
280	0.9997	0.9999
290	0.9993	0.9988
300	0.9971	0.9965
315	0.9927	0.9915
330	0.9862	0.9848
340	0.9808	0.9795
350	0.9748	0.9737
360	0.9684	0.9674
370	0.9615	0.9606

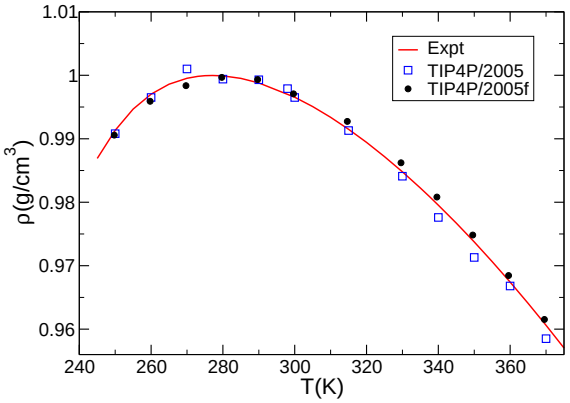

Figure 3.3: Densities of the TIP4P/2005f model (full circles) at $p = 1$ bar compared to the values of the same property of TIP4P/2005 model (open squares) and experimental data (full line).

follows closely the experiment at larger distances. Minor differences between the results of both water models are seen at the first minimum where the flexible model results are slightly lower than those for TIP4P/2005 and at the second maximum where TIP4P/2005f performs slightly better.

Enthalpy of vaporization

The difference between the gas phase enthalpy minus the enthalpy of the liquid phase is known as enthalpy of vaporization, $\Delta_v H = H_g - H_l$. At

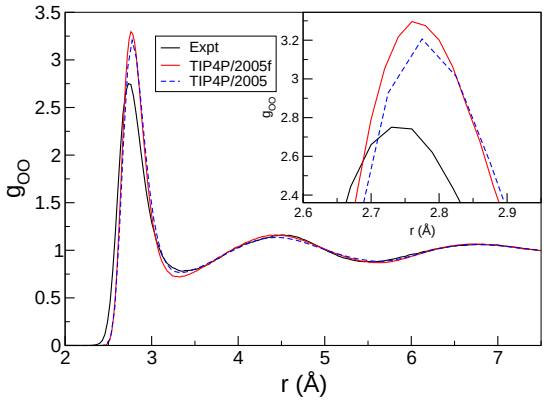

Figure 3.4: Oxygen-oxygen radial distribution function at T=298 K, p=1 bar.

low pressures the gas may be considered ideal and gives a negligible contribution to the internal energy. Besides, its volume may be calculated from the perfect gases equation. In this way, the enthalpy of vaporization may be approximated by

$$\Delta_v H = -U_l - pV_l + RT \tag{3.5}$$

The computed value for our model (Table 3.3) is, by design, larger than the experimental result. This is because it is now widely accepted[2] the need of the so-called self-energy correction proposed by Berendsen and coworkers in 1987.[17] This term should be subtracted from the enthalpy of vaporization to take into account the difference in polarization between the gas and the liquid phase. The correction depends on the difference between the dipole moment of the model μ_l and that of the gas phase μ_g and may be approximated by

$$\Delta E_{pol} = (\mu_l - \mu_g)^2/2\alpha. \tag{3.6}$$

Using the average dipole moment of the liquid at room temperature and temperature, the correction amounts to 4.6 kJ/mol. In these conditions, the enthalpy of vaporization is close to the experimental value.

Isothermal compressibility

To calculate the isothermal compressibility we make use of the fluctuations equation

$$\kappa_T = \frac{\langle V^2 \rangle - \langle V \rangle^2}{k_B T \langle V \rangle}, \tag{3.7}$$

where $\langle V \rangle$ is the average volume, k_B is the Boltzmann's constant and T is the temperature. The value of κ_T for our model is $(4{,}46 \pm 0{,}003) \cdot 10^5$ MPa

at 298 K and atmospheric pressure. This result is again similar to that for the TIP4P/2005 model but it is slightly closer to the experiment as it may be seen in Table 3.3.

Self-diffusion coefficient

The self-diffusion coefficient was calculated by means of the Einstein equation

$$6D_s t = \lim_{t\to\infty} \langle |r_i(t) - r_i(0)| \rangle^2 , \tag{3.8}$$

where $r_i(t)$ is the position of particle i at time t. The value of D_s for the flexible model is $(1{,}93 \pm 0{,}03) \cdot 10^{-9}$ m^2 s^{-1} at 298 K and ambient pressure. It is slightly lower than the experimental data $2{,}27 \cdot 10^{-9}$ m^2 s^{-1} and $2{,}23 \cdot 10^{-9}$ m^2 s^{-1} reported by Mills,[47] by Krynicki *et al.*,[48] and by Gillen *et al.*,[49] respectively.

3.4.1. Melting temperature of ice Ih

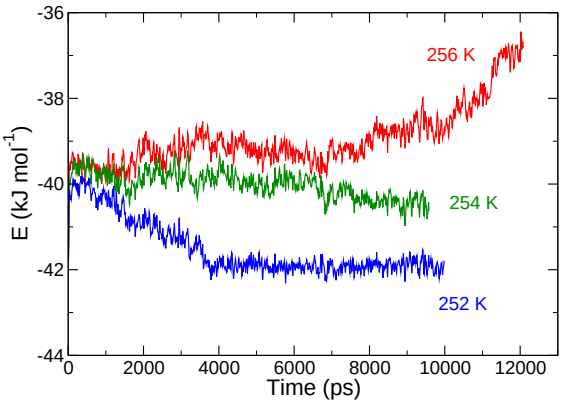

Figure 3.5: Evolution of the total energy of a system made of liquid water in contact with ice Ih. The results are averages over 20 ps simulation blocks for three NpT simulation runs at 1 bar and T=256 K, 254 K and 252 K, respectively.

To calculate this point of the phase diagram we have used the direct coexistence method.[51,52,50] The system consisted of an anisotropic simulation box containing 432 molecules with the ice Ih structure in contact with 438 molecule with a liquid arrangement. Several NpT runs are carried out in order to establish if the solid-liquid interface evolves towards the growth of the solid phase or to its disappearance. Selected runs are shown in Figure 3.4.1. In the simulation at 252 K, the energy progressively decreases because the liquid

phase is transforming into ice Ih until total crystallization. The opposite is true for the run at 256 K where the solid phase melts completely thus increasing the total energy of the system. Finally, the energy remains more or less constant in the run at 254 K indicating that the interface does not change. We thus assign this value as the melting temperature of the TIP4P/2005f water model. There is a modest improvement over the TIP4P/2005 result (the melting temperature increases 4 degrees but the result is still 19 degrees lower than the experimental value). It seems that a polarizable model is needed to get a closer agreement with experiment.

3.4.2. Relative stability of ices

It has been shown recently that the relative stability of the ice polymorphs is not correctly predicted be several rigid water models.[18,45] In particular, the stable phase at ambient conditions of three site models such as TIP3P, SPC or SPC/E is not the hexagonal ice Ih but the proton ordered ice II. The calculation of the complete phase diagram is outside the scope of this work but there is a simple alternative consisting in the calculation of the relative stabilities at 0 K.[53] Table 3.5 present the densities and energies of ices Ih, II, III and VI for the flexible models TIP4P/2005f and SPC/Fw as well as for their rigid counterparts TIP4P/2005 and SPC/E. Both TIP4P/2005 and TIP4P/2005f predict ice Ih as the more stable phase while ice II is more stable for SPC/E and SPC/Fw indicating that the flexibility has a small influence on the relative stability of ices. In this respect, it is perhaps worth to mention the slight increased stability of ice III which is marginally more stable than ice II at 0 K for TIP4P/2005f. This means that ice II would be absent from the phase diagram of this model. This is in accordance with a recent calculation for a flexible model (also based on TIP4P/2005) designed to be used in simulations explicitly accounting for the quantum nuclear motion.[54]

The fact that SPC/Fw is unable to predict the relative stabilities of ices Ih and II is a serious drawback of the model and supports our decision to develop a flexible model based on TIP4P/2005. It may be argued that the properties of water in the solid state are not important because these models are intended to be used for the liquid state. But this is a simplification because it is now well documented that the relative stability of ice II with respect to the other proton disordered polymorphs (Ih, III, V and VI) is related to the ratio between the magnitudes of the dipole and quadrupole moments of the model.[20,21] Thus, the failure of SPC/Fw in accounting for the relative stability of ices Ih and II is not a simple inadequacy for the study of ices but it has deeper roots with consequences also for the liquid state.

Table 3.5: Properties of several ice polymorphs at T=0 K and p=0 bar for flexible water models and their rigid counterparts. The results marked in bold correspond to the more stable phase.

Ice	TIP4P/2005	TIP4P/2005f	SPC/E	SPC/Fw
		U(kcal/mol)		
Ih	**-15.06**	**-14.76**	-14.69	-14.64
II	-14.85	-14.49	**-14.85**	**-14.80**
III	-14.74	-14.52	-14.35	-14.26
VI	-14.51	-14.20	-13.95	-13.85
		ρ(g/cm^3)		
Ih	0.954	0.961	0.981	0.996
II	1.230	1.232	1.279	1.295
III	1.184	1.189	1.181	1.214
VI	1.385	1.390	1.413	1.434

Table 3.6: Dielectric constant at different thermodynamics states.

T/K	p/bar	TIP4P/2005	TIP4P/2005f	Expt
298	1	57.2	55.3	78.4
298	2000	62.2	63.1	84.9
473	2000	31.8	33.0	41.3
673	2000	16.6	16.7	19.4

3.4.3. Static dielectric constant

The static dielectric constant is one of the few properties for which the TIP4P/2005 model does not provide a satisfactory result. The appropriate equation for its computation in a simulation using Ewald sums with conducting boundary conditions reads[55]

$$\varepsilon_r = 1 + \frac{4\pi}{3k_BTV}\left(\langle M^2\rangle - \langle M\rangle^2\right). \tag{3.9}$$

In order to compute the dielectric constant we have performed several simulation in the NVE ensemble lasting 15 ns. It seems interesting to check not only the values of the dielectric constant but also how the model is able to predict its change for different thermodynamic states. Table 3.6 presents the dielectric constant for several points along the 298 K isotherm and the 1000 bar isobar. The results for the flexible model follow the same trends as the experimental values but the error is considerable. Besides the dielectric

constants of the flexible model are quite similar to those of the rigid one; except for the point at ambient conditions there is a marginal improvement associated to the addition of flexibility.

3.4.4. Power spectrum

There are several methods to calculate the infrared (IR) spectrum. We used a method based on the computation of the density of states or the power spectra[56]. This involves the Fourier transform of the velocity autocorrelation function (VAC) for the relative velocities of a hydrogen atom with respect to the oxygen atom,[57,58,56]

$$I(\omega) \propto \int_0^\infty dt \exp(-i\omega t) \langle v(0)v(t)\rangle \,, \tag{3.10}$$

where $\langle v(0)v(t)\rangle$ is the velocity autocorrelation function and ω is the frequency. This method allows one to obtain the values of the maximum of the bands at a much lower computational cost than the traditional method based on the dipole moment of the system. This is sufficient to verify the validity of the model but if one wants to improve the calculation of the infrared spectrum, quantum corrections[33] or, better, advanced methods based on quantum calculations[59,60,61,62,63] are required. To obtain this information of the system, we have used specific simulation conditions. The required simulation time is quite short, only 10 ps, because of the rapid decay of the VAC but a small time-step, 0.1 fs, is needed to define precisely the VAC at very short times. Besides this, a larger system (4000 molecules) is necessary to eliminate noise and to obtain accurate values for $I(\omega)$.

Figure 3.4.4 displays the profile of the spectrum of densities of states of water. We have also included in the plot the positions of the peaks of the experimental bands. As expected, the frequency at the maximum for the angle bending and the bond stretching are more or less coincident with the experimental values. The bands corresponding to the librational motion with symmetries A2, B2 are merged together in a single band whose maximum appears approximately at the middle point of the experimental peaks.[65] The intramolecular stretch is somewhat shifted towards higher frequencies. It is to be noticed that the band at about 50 cm^{-1} appears clearly resolved in our model and that is maximum is coincident with the experimental value. The peaks of the bands of the power spectrum are collected in Table 3.7 where we compare it with experimental measurements.[64,65,37]

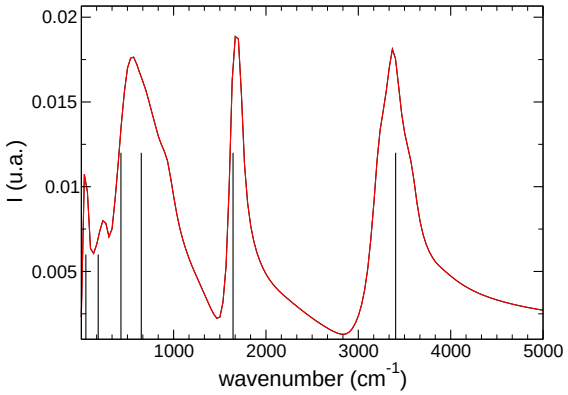

Figure 3.6: Spectrum of densities of state of water. Vertical lines signal the position of the peaks in the experimental spectra of liquid water.

Table 3.7: Wavenumbers (in cm^{-1}) at the peak of the bands of the power spectrum for the TIP4P/2005f model and liquid water. Experimental results have been taken from Refs.[64,65,37] and[66]

	TIP4P/2005f	Expt
Cage vibrations[9]	50	50
Intermolecular stretch	230	183.4
Librations A2, B2	570	430, 650
Bending (H-O-H)	1670	1643.5
Stretching (O-H)	3370	3404.0

3.5. Conclusions

In this work we have developed a flexible water model, TIP4P/2005f, based on the rigid potential TIP4P/2005. A number of structural, thermodynamic and dynamic properties have been evaluated for the new model. Most of the results are in excellent agreement with experiment in line with as those of its rigid predecessor. Taking into account the excellent performance of TIP4P/2005 for other properties not evaluated in this work, this seems to ensure that TIP4P/2005f is a very accurate flexible model. The model slightly improves the melting point and there are also marginal improvements in other properties. On the negative side, although the results for the dielectric constant follow similar trends as the experimental ones, they are still considerably different from experiment. In summary, the flexible TIP4P/2005f

seems to inherit the excellent performance of TIP4P/2005 but it does not improve it substantially. We must conclude that adding flexibility does not improve the performance for those properties for which the predictions of TIP4P/2005 are not quantitative.

The reasoning of the preceding paragraph seem to be in contradiction with several reports claiming that some predictions of flexible models are closer to experimental data than those of rigid potentials.[15,12] It seems that the flexibility has more influence on the final results (at least for a few number of properties) when the model is based on SPC/E than for a model based on TIP4P/2005. The reasons of this different behavior are unclear to us but this might be simply because the TIP4P/2005 results are already very good so its improvement is not an easy task. It was not the objective of this work to compare the results of TIP4P/2005f to those of other flexible models. We have calculated the relative stability of ices just to confirm that our choice on using a TIP4P topology as the starting point of a flexible model was based on correct premises. We have shown that SPC/Fw predicts erroneously that ice Ih is less stable than ice II. Moreover, given the value of the expansivity reported by Wu et al.[11], it is likely that the temperature of maximum density for SPC/Fw is far from the experimental value (following the behavior of SPC/E for which the maximum density is reached at 241 K, 36 degrees below the experimental value). TIP4P/2005f is free from these drawbacks and its performance is excellent even if the addition of flexibility does not improve substantially that of TIP4P/2005. It is then a good candidate in simulations where the use of a flexible water model is advisable.

Acknowledgments

This work has been funded by grants FIS2010/16159 of the MEC, P2009/ESP-1691 of CAM and UCM-Banco de Santander GR35/10-A-910570.

Bibliografía

1. B. Guillot, J. Molecular Liquids **101**, 219 (2002).
2. C. Vega and J. L. F. Abascal, Phys. Chem. Chem. Phys. **13**, 19663 (2011).
3. D. E. Smith and A. D. J. Haymet, J. Chem. Phys. **96**, 8450 (1992).
4. I. G. Tironi, R. M. Brunne, and W. F. vanGunsteren, Chem. Phys. Lett. **250**, 19 (1996).
5. B. S. Gonzalez, E. G. Noya, C. Vega, and L. M. Sese, J. Phys. Chem. B **114**, 2484 (2010).
6. I. Kurisaki and T. Takahashi, Computational and Theoretical Chemistry **966**, 26 (2011).
7. S. Habershon, T. E. Markland, and D. E. Manolopoulos, J. Chem. Phys. **131**, 024501 (2009).
8. J. Marti, E. Guardia, and J. A. Padro, J. Chem. Phys. **101**, 10883 (1994).
9. J. Marti, J. A. Padro, and E. Guardia, J. Chem. Phys. **105**, 639 (1996).
10. U. W. Schmitt and G. A. Voth, J. Phys. Chem. B **102**, 5547 (1998).
11. Y. J. Wu, H. L. Tepper, and G. A. Voth, J. Chem. Phys. **124**, 024503 (2006).
12. G. Raabe and R. J. Sadus, J. Chem. Phys. **134**, 234501 (2011).
13. G. Raabe and R. J. Sadus, J. Chem. Phys. **126**, 044701 (2007).
14. J. Lopez-Lemus, G. A. Chapela, and J. Alejandre, J. Chem. Phys. **128**, 174703 (2008).
15. P. K. Yuet and D. Blankschtein, J. Phys. Chem. B **114**, 13786 (2010).

16. W. L. Jorgensen, J. Chandrasekhar, J. D. Madura, R. W. Impey, and M. L. Klein, J. Chem. Phys. **79**, 926 (1983).

17. H. J. C. Berendsen, J. R. Grigera, and T. P. Straatsma, J. Phys. Chem. **91**, 6269 (1987).

18. E. Sanz, C. Vega, J. L. F. Abascal, and L. G. MacDowell, Phys. Rev. Lett. **92**, 255701 (2004).

19. J. L. F. Abascal and C. Vega, Phys. Chem. Chem. Phys **9**, 2775 (2007).

20. J. L. F. Abascal and C. Vega, Phys. Rev. Lett. **98**, 237801 (2007).

21. J. L. F. Abascal and C. Vega, J. Phys. Chem. C **111**, 15811 (2007).

22. J. L. F. Abascal and C. Vega, J. Chem. Phys. **123**, 234505 (2005).

23. H. L. Pi, J. L. Aragones, C. Vega, E. G. Noya, J. L. F. Abascal, M. A. Gonzalez, and C. McBride, Molecular Physics **107**, 365 (2009).

24. C. Vega, J. L. F. Abascal, and I. Nezbeda, J. Chem. Phys. **125**, 034503 (2006).

25. L. Pusztai, O. Pizio, and S. Sokolowski, J. Chem. Phys. **129**, 184103 (2008).

26. F. Sedlmeier, D. Horinek, and R. R. Netz, J. Am. Chem. Soc **133**, 1391 (2011).

27. M. A. Gonzalez and J. L. F. Abascal, J. Chem. Phys. **132**, 096101 (2010).

28. G. Guevara-Carrion, J. Vrabec, and H. Hasse, J. Chem. Phys. **134**, 074508 (2011).

29. J. L. F. Abascal and C. Vega, J. Chem. Phys. **134**, 186101 (2011).

30. R. B. Best and J. Mittal, J. Phys. Chem. B **114**, 14916 (2010).

31. O. Teleman, B. Jonsson, and S. Engstrom, Mol. Phys. **60**, 193 (1987).

32. J. L. Barrat and I. R. McDonald, Mol. Phys. **70**, 535 (1990).

33. B. Guillot, J. Chem. Phys. **95**, 1543 (1991).

34. A. Wallqvist and O. Teleman, Mol. Phys. **74**, 515 (1991).

35. H. L. Lemberg and F. H. Stillinger, J. Chem. Phys. **62**, 1677 (1975).

36. K. Toukan and A. Rahman, Phys. Rev. B **31**, 2643 (1985).

37. J.-J. Max and C. Chapados, J. Chem. Phys. **131**, 184505 (2009).

38. J. E. Bertie and Z. D. Lan, Applied Spectroscopy **50**, 1047 (1996).

39. C. P. Lawrence and J. L. Skinner, Chem. Phys. Lett. **372**, 842 (2003).

40. B. Hess, C. Kutzner, D. van der Spoel, and E. Lindahl, J. Chem. Theory Comput. **4**, 435 (2008).

41. D. van der Spoel, E. Lindahl, B. Hess, G. Groenhof, A. E. Mark, and H. J. C. Berendsen, J. Comp. Chem. **26**, 1701 (2005).

42. G. Bussi, D. Donadio, and M. Parrinello, J. Chem. Phys. **126**, 014101 (2007).

43. M. Parrinello and A. Rahman, J. Appl. Phys. **52**, 7182 (1981).

44. U. Essmann, L. Perera, M. L. Berkowitz, T. A. Darden, H. Lee, and L. G. Pedersen, J. Chem. Phys. **103**, 8577 (1995).

45. C. Vega, J. L. F. Abascal, M. M. Conde, and J. L. Aragones, Faraday Discuss. **141**, 251 (2009).

46. A. K. Soper, Chem. Phys. **258**, 121 (2000).

47. R. Mills, J. Phys. Chem. **77**, 685 (1973).

48. K. Krynicki, C. D. Green, and D. W. Sawyer, Faraday Discuss. Chem. Soc. **66**, 199 (1978).

49. K. T. Gillen, D. C. Douglass, and M. J. R. Hoch, J. Chem. Phys. **57**, 5117 (1972).

50. R. García Fernández, J. L. F. Abascal, and C. Vega, J. Chem. Phys. **124**, 144506 (2006).

51. A. Ladd and L. Woodcock, Chem. Phys. Lett. **51**, 155 (1977).

52. J. R. Morris and X. Song, J. Chem. Phys. **116**, 9352 (2002).

53. J. L. Aragones, E. G. Noya, J. L. F. Abascal, and C. Vega, J. Chem. Phys. **127**, 154518 (2007).

54. S. Habershon and D. E. Manolopoulos, Phys. Chem. Chem. Phys. **13**, 19714 (2011).

55. M. Neumann, Mol. Phys. **50**, 841 (1983).

56. M. P. Allen and D. J. Tildesley, *Computer Simulation of Liquids* (Oxford University Press, Oxford, 1987).

57. D. A. McQuarrie, *Statistical Mechanics* (University Science Books, Sausalito, 2000).

58. S. Amira, D. Spangberg, and K. Hermansson, Chem. Phys. **303**, 327 (2004).

59. G. S. Fanourgakis and S. S. Xantheas, J. Chem. Phys. **128**, 074506 (2008).

60. J. L. Skinner, B. M. Auer, and Y.-S. Lin, Adv. Chem. Phys. **142**, 59 (2009).

61. B. M. Auer and J. L. Skinner, Chem. Phys. Lett. **470**, 13 (2009).

62. M. Yang and J. L. Skinner, Phys. Chem. Chem. Phys **12**, 982 (2010).

63. C. Zhang, D. Donadio, F. Gygi, and G. Galli, J. Chem. Theory Comput. **7**, 1443 (2011).

64. G. E. Walrafen, J. Chem. Phys. **40**, 3249 (1964).

65. D. M. Carey and G. M. Korenowski, J. Chem. Phys. **108**, 2669 (1998).

66. M. Chaplin, *http://www.lsbu.ac.uk/water*. A site about the structure, function, behavior and properties of water.

Results: Chapter 4

Thermodynamic scenario for TIP4P/2005 water model

Miguel A. González, *Jose L. F. Abascal and Chantal Valeriani*

Departamento de Química Física, Facultad de Ciencias Químicas, Universidad Complutense de Madrid, 28040 Madrid, Spain.

4.1. Introduction

Water is the most abundant liquid on Earth. It is involved in many processes, both industrial processes and biochemical or chemical reactions. Water has been studied since the beginning of science and chemistry. There are many studies about the properties of this molecule as a reaction medium, as a reagent or as a product of many chemical reactions.

The anomalous behaviour of water is well known: others liquids do not exhibit minima and/or maxima in its thermodynamics properties as it occurs with water. The most famous anomaly is the maximum in the density that appears at 4 ^{o}C. There are other properties that show anomalies: viscosity, isothermal compressibility, heat capacities,...

In the last years, efforts have been focused on studying the supercooled water region and its anomalous behaviour[1,2,3,4,5]. In 1976 Speedy and Angell, measured the isothermal compressibility, κ_T, in the supercooled liquid region[6] and found a sharp increase in this property for decreasing temperatures. Six years later, Speedy interpreted this behaviour[7] as the effect of the liquid-vapour spinodal which changes its slope increasing the value of the pressure when the temperature decreases. This scenario was called stability-limit (SF) conjecture, (see Fig. (4.1.A)).

Following this idea, the critical point free (CF) scenario[8,9,10] was propo-

sed in 1994 by Poole *et al.* supported by the works of Zheng and Angell[9,10]. The scenario is presented in Fig. (4.1.C). The authors explained in their experimental data the presence of the liquid-liquid transition (LLT) without any critical point. Since there was a liquid-liquid spinodal line associated with it, this spinodal line was the responsable of any divergence in the response functions.

Poole *et al.*[1,8,11,12], using molecular simulations, attempted to reproduce the theoretical behaviour proposed by Speedy, but they did not find the re-entrant spinodal. From the extrapolation of the simulation results, the existence of a new (liquid-liquid) critical point in water was conjectured. This could explain the behaviour of supercooled water. The name of this scenario is second critical point (CP) scenario (see Fig. (4.1.B)).

Sastry *et al.*[13] carried out several studies followed by a thermodynamic analysis which gave strong support to the critical point scenario, but in this scenario they located the critical point at 0 K keeping the rest of the lines. This singularity-free (SF) scenario is shown in Fig. (4.1.D). In fact, the few experimental data available and, especially, computer simulation studies seem to indicate that the anomalies in supercooled water are perturbations associated with the Widom line[14,15] which is the line of maximum correlation length emanating from the critical point. Related to the Widom line are the extrema observed for the response functions such as the compressibility or the expansion coefficient emanating from a critical point.

The purpose of this work is to perform a computer simulation study on the thermodynamic behaviour in the supercooled region in order to clarify which is the scenario characterizing TIP4P/2005.

4.2. Simulation details

The results presented in this work have been obtained for a rigid and non-polarizable water model, TIP4P/2005, under extreme conditions of pressure and temperature. All simulations were performed with the GROMACS 4.0 molecular dynamics software package[16,17]. The system consists of 500 molecules, although in specific thermodynamic conditions the number was increased to 4000 to avoid finite size effects. The corresponding temperature vary from 190 K to 320 K and the pressure from -3000 bar to 1500 bar. The calculation of most of the properties was carried out in the NpT ensemble, except for the case of the determination of the spinodal line, which was performed in the NVT ensemble. The Nosé-Hoover thermostat[18,19] was used to keep the temperature constant; in order to maintain the pressure constant, the Parrinello-Rahman barostat[20] was used. The time step was set to 1fs.

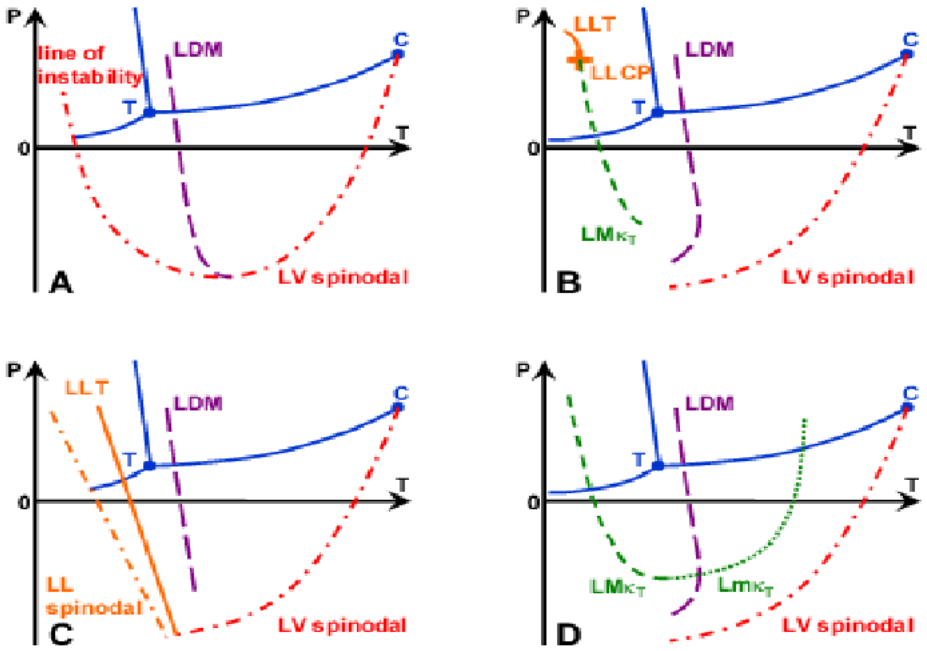

Figure 4.1: The four scenarios proposed to explain the water anomalies. In all of them we find the coexistence lines between solid, liquid and vapour phases (blue lines), the vapour-liquid critical point (C) and the triple point (T). The purple dashed curve corresponds to TMD line or LDM (line of the density maxima), and the red line represents the vapour-liquid spinodal line (LV spinodal). In scenario A[7], *stability-limit (SF) conjecture*, there is a re-entrant spinodal that appears at positive pressure at low temperatures. Panel B shows the *Second critical point (CP) scenario*[1], with the liquid-liquid critical point (LLCP) represented by an orange cross. The liquid-liquid transition (LLT) is the solid orange line. The line of isothermal compressibility maxima is the dashed green curve. The *critical point free (CF) scenario*[8,9,10] represented in panel C, is characterised by the solid orange line of the liquid-liquid transition (LLT). The dashed orange line represents the liquid-liquid spinodal line (LL spinodal). Finally, the *Singularity-free (SF) interpretation*[13], is similar to scenario B but with the critical point shifted to 0 K.

The Lennard-Jones potential had a cut-off of 8,5 Å and the long range electrostatic interactions where simulated via the Particle Mesh Ewald Method (PME)[21,22] is used.

4.3. Results

This chapter is the study of the thermodynamic scenario for the TIP4P/2005, water model. We will investigate the location of the extrema of the isothermal compressibility at positive and negative pressure. We will also evaluate the TMD line, the liquid-vapour spinodal line and the cavitation line in order to complete the scenario. Previous studies[14,15] had proposed the existence of a liquid-liqdui critical point (LLCP) for this model. A line of compressibility maxima was obtained for positive pressure. Although the existence of the LLCP for TIP4P/2005 model is still nowadays disputed in a recent paper[23]. Our study will focus on the possible re-entrant behaviour of the TMD line, involving simulations at negative pressure. This allowed us to extend the line of maxima κ_T to the negative pressure region. When performing these simulations, we eventually found several cavitation events. In order to obtain the spinodal line, we had to change the simulations to the NVT ensemble.

4.3.1. Widom line. Maxima y minima of the isothermal compressibility

The Widom line is the locus of maximum correlation length. Close to the critical point the Widom line coincides with the lines of extrema in the response functions. As we move away from the critical point the locus of extrema in the response function are not coincident any more. Thus the extrema for the isothermal compressibility κ_T, thermal expansion coefficient α_p and heat capacities C_p and C_V have a different path on the $p-T$ plane but they all emerge from the critical point. For example, in a previous study[14] the liquid-liquid critical point for the TIP4P/2005 model was extrapolated from the maxima in κ_T and the inflection point of the density of the system (which was equivalent to the maxima of α_p). For simplicity, given the similarities of the lines of maximum κ_T and α_p, we refer to as then Widom line.

We evaluate the Widom line from the locus of the maxima of the isothermal compressibility because the location of a maximum or a minimum is more accurate than the location of an inflection point, as shown to be the case if the density of the system is used (locating the maxima in α_p). On the other hand, we could also determine the maxima and minima of the heat capacity, calculating the corresponding Widom line. However, when dealing with numerical simulations to calculate C_p, quantum nuclear effect have been shown to be significant at low temperatures[24]. Since we are working with a classical model without quantum corrections, it is not possible to generate a Widom line accurate enough. Thus, we have decided to use the maxima and

minima of κ_T to calculate the Widom line.

Table (4.1) shows the numerical results for the isothermal compressibility of supercooled water in positive pressures region. These data are collected from Refs.[25] and[14].

	Pressure (bar)				
T (K)	1	400	700	1000	1200
272.2	5.0E-5	4.6E-5	4.3E-5	4.00E-5	-
261.9	5.3E-5	5.0E-5	4.6E-5	4.18E-5	-
252.1	5.7E-5	5.3E-5	4.9E-5	4.53E-5	4.23E-5
242.7	5.8E-5	5.8E-5	5.55E-5	4.99E-5	4.60E-5
233.5	6.5E-5	6.6E-5	6.4E-5	5.47E-5	5.31E-5
224.6	6.4E-5	8.6E-5	6.9E-5	6.36E-5	6.10E-5
215.8	5.5E-5	8.2E-5	9.9E-5	7.86E-5	7.54E-5
207.3	3.6E-5	5.2E-5	9.9E-5	10.7E-5	9.89E-5
203.0	2.6E-5	4.1E-5	-	11.8E-5	-
199.0	2.1E-5	3.5E-5	4.9E-5	12.8E-5	12.3E-5
195.0	2.5E-5	3.0E-5	3.1E-5	-	16.5E-5
191.0	1.4E-5	1.6E-5	2.0E-5	3.5E-5	5.78E-5
183.0	-	-	-	2.3E-5	2.91E-5

Table 4.1: Isothermal compressibility (MPa^{-1}) in the supercooled region at positive pressures for TIP4P/2005 water model from Refs.[25] and[14].

The results are also shown in Fig. (4.2). Notice that the height of the maxima strongly increase when decreasing temperatures, suggesting the vicinity of a critical point. The scale of the figure does not allow to show the κ_T minima, which were reported in a previous publication[25,14] for the 1 and 1000 bar isobars.

In this chapter, we have extended the calculations to investigate the behaviour of the model at negative pressure. The numerical results are given in Table (4.2) and displayed in Fig. (4.3).

The trend observed for the κ_T maxima in Fig. (4.2) also appears at negative pressure. Moreover, it is now possible to represent in the same plot both maxima and minima of κ_T. When decreasing pressures the distance between them decreases until they eventually collapse into an inflection point. Below this pressure (around -1000 bar) the isothermal compressibility does not exhibit a maximum or a minimum.

Fig. (4.4) represents the locus of κ_T maxima and minima in the $p-T$ plane. We have also depicted the positon of the LLCP reported in Ref.[14].

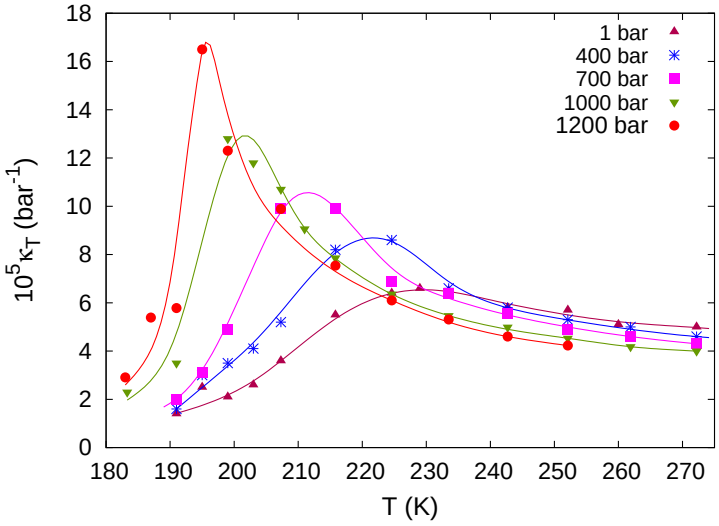

Figure 4.2: Isothermal compressibility in the supercooled region at positive pressures for TIP4P/2005 water model Ref.Refs.[25] and[14]. Notice that the y-axis has been multiplied by 10^5 and we are keeping the original paper format, thus the units are bar^{-1}.

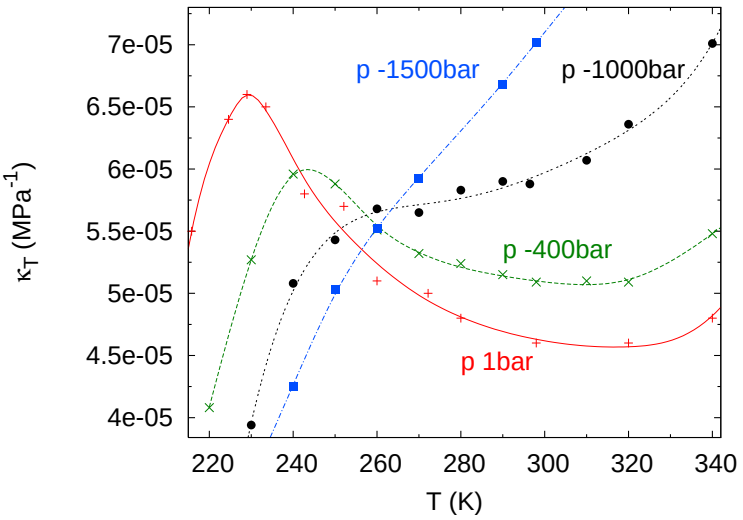

Figure 4.3: Isothermal compressibility at negative pressures for the TIP4P/2005 water model.

Notice that the region of anomalies in κ_T extends deeply into the negative pressures.

	Pressure (bar)			
T (K)	1	-400	-1000	-1500
370.0	5.2E-5	-	-	-
360.0	5.8E-5	6.01E-5	-	-
340.0	4.8E-5	5.48E-5	7.01E-5	-
320.0	4.6E-5	5.09E-5	6.36E-5	-
310.0	-	5.10E-5	6.07E-5	7.52E-5
298.0	4.6E-5	5.09E-5	5.88E-5	7.02E-5
290.0	-	5.15E-5	5.90E-5	6.684E-5
280.0	4.8E-5	5.24E-5	5.83E-5	-
272.2	5.0E-5	-	-	-
270.0	-	5.32E-5	5.65E-5	5.925E-5
261.9	5.3E-5	-	-	-
260.0	-	5.51E-5	5.68E-5	5.52E-5
252.1	5.7E-5	-	-	-
250.0	-	5.88E-5	5.43E-5	5.03E-5
242.7	5.8E-5	-	-	-
240.0	-	5.96E-5	5.08E-5	4.25E-5
233.5	6.5E-5	-	-	-
230.0	-	5.27E-5	3.94E-5	3.48E-5
224.6	6.4E-5	-	-	-
220.0	-	4.08E-5	-	2.85E-5

Table 4.2: Numerical results for the isothermal compressibility (MPa^{-1}) of TIP4P/2005 at negative pressures.

4.3.2. The line of temperatures of maximum density

For the calculation of this property, we performed simulations at constant pressure in order to obtain the density of the system for a wide range of temperatures. The simulations were carried out in the NpT ensemble with 500 molecules because the density is not significantly affected by the system size. Table (4.3) shows the numerical values of the density at different pressures and temperatures for the TIP4P/2005 water model. A visual representation of the results is given in Fig. (4.5). A fit of the densities for each isobar provides the temperature of maximum density (TMD) represented in the figure as a red triangle. The TMD is shifted to higher temperatures when the pressure is lowered. The slope increases until it becomes infinite and change its sign.

This point is as the re-entrant point of the TMD (R_{TMD}) (already

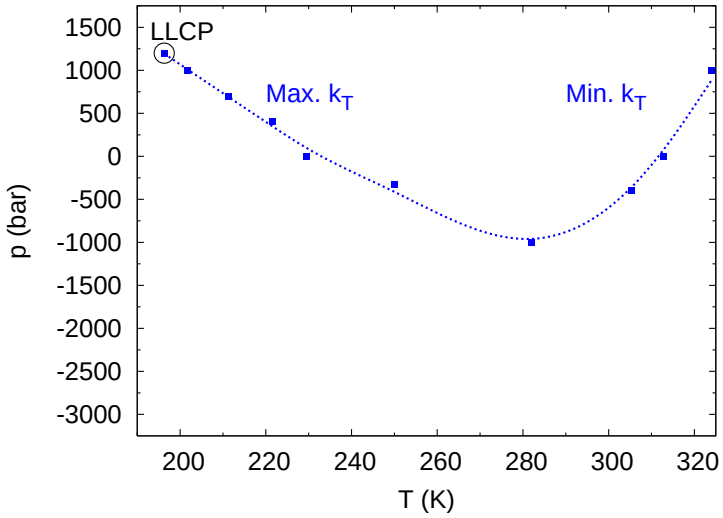

Figure 4.4: Locus of extrema in the isothermal compressibility. The minimum of this curve is the inflection point at approximately −1000 bar. The blue dotted line is a guide to the eye. The black circle indicates the location of the liquid-liquid critical point (LLCP) for the TIP4P/2005 water model.

	Pressure (bar)							
T (K)	1000	400	1	-400	-750	-1000	-1250	-1500
230	1.0416	1.0111	0.9771	0.9507	-	0.9250	-	0.9090
240	1.0452	1.0166	0.9878	0.9633	-	0.9319	-	0.9119
250	1.0469	1.0189	0.9941	0.9719	0.9527	0.9389	0.9266	0.9156
260	1.0472	1.0199	0.9986	0.9770	0.9582	0.9437	0.9316	0.9192
270	1.0464	1.0189	1.0003	0.9799	0.9612	0.9469	0.9344	0.9205
280	1.0444	1.0171	1.0006	0.9808	0.9627	0.9484	0.9352	0.9211
290	1.0418	1.0150	0.9993	0.9799	0.9620	0.9477	0.9345	0.9196
298	1.0391	1.0107	0.9974	0.9783	0.9604	0.9467	0.9326	0.9171
310	-	1.0107	0.9934	0.9746	0.9564	0.9419	0.9277	0.9117
320	1.0300	1.0066	0.9892	0.9702	0.9521	0.9370	0.9222	0.9044
340	1.0200	0.9964	0.9787	0.9590	-	0.9241	0.9070	0.8864
360	1.0085	0.9838	0.9658	0.9452	-	-	0.8871	-

Table 4.3: Equilibrated densities (g/cm^{-3}) of different isobars at positive and negative pressures.

mentioned in in previous sections). Under these conditions of strongly negative pressure it is very complicated to experimentally measure the properties

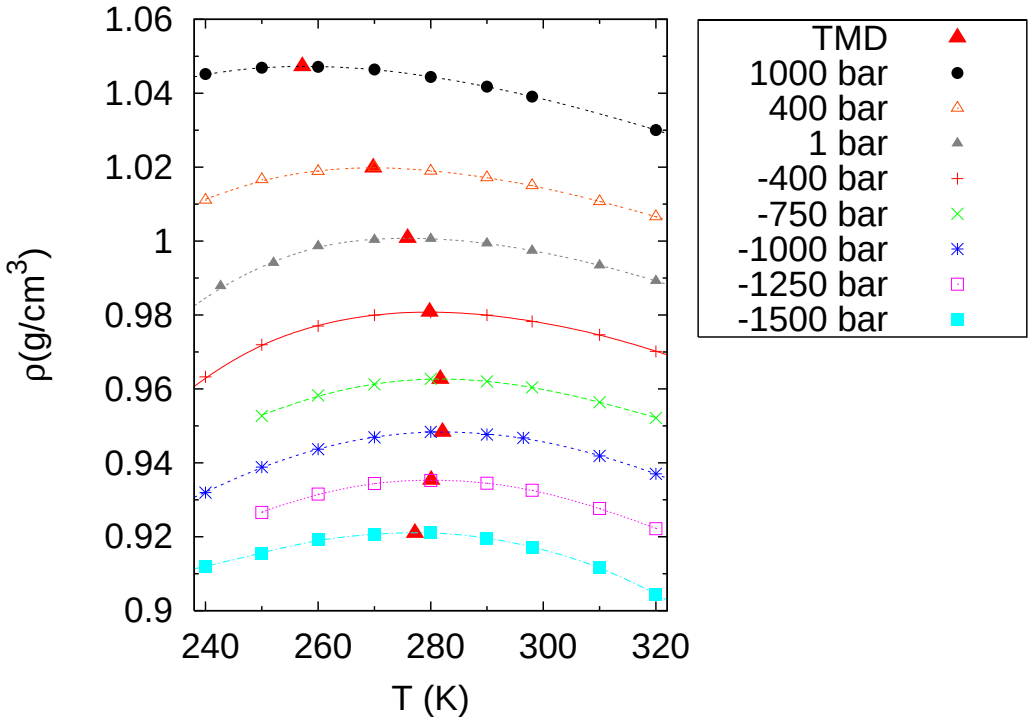

Figure 4.5: Values of density versus temperature at constant pressure. The maxima of each isobar, TMD, is marked with a red triangle.

of water. Hence, in order to validate our results and to compare them to experiments, we used a reliable equation of state calculated from experimental data, which provides reliable values of the TMD until a pressure of about -400 bar[26]. The fact that the TMD line is reentrant implies that the stability-limit conjecture is not valid for TIP4P/2005 scenario. Thermodynamic considerations[13,1] indicate that from the retracing point, the TMD line approaches but cannot cross the liquid-vapour spinodal line. Moreover, it has also been rigurousy demoustrated that the retracing point of the LDM should coincide with a point of the line of extrema in the isothermal compressibility[1]. Fig. (4.7) shows both curves. Crossing at the retracing point of the TMd line of TIP4P/2005 model, thus showing that our results are thermodinamically consistent.

4.3.3. Cavitation line

Cavitation is defined as the formation of bubbles in a metastable superheated or overstretched liquid. The nucleation rate, i.e, the rate at which

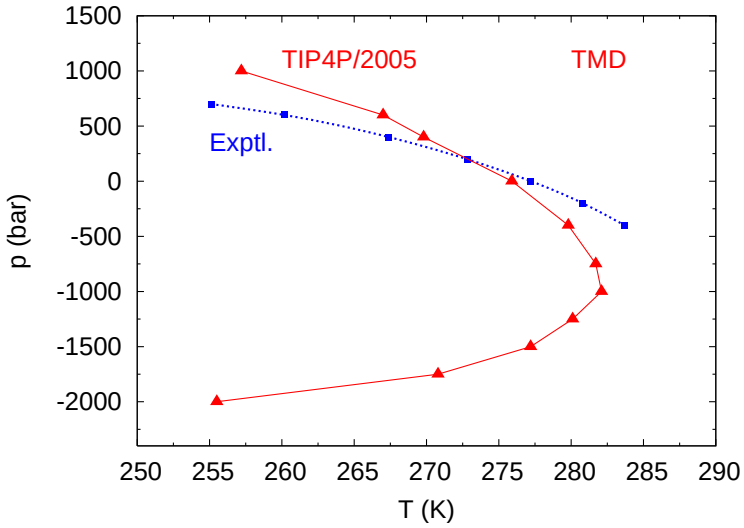

Figure 4.6: Comparison of the values of the TMD line TIP4P/2005 model with the IAPWS[26] equation of state for water.

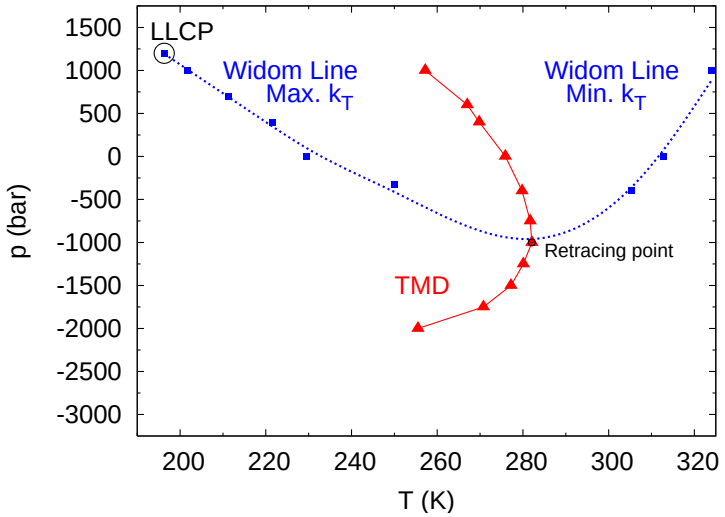

Figure 4.7: TMD line (in red) together with the line of extrema in the isothermal compressibility (in blue) for TIP4P/2005 in the $p - T$ plane. The black circle represents the location of the LLCP. Whereas the point where the TMD crosses the line of extrema of κ_T is the retracing point.

a bubble is formed depends, among other factors, on the degree of supersaturation (the distance of the metastable state from coexistence) and on the system volume. For a given volume, the deeper the supersaturation the easier

is for the system to cavitate, up to the point that we get to the spinodal line and cavitation happens spontaneously. Thus, cavitation provides an approximate idea of the position of the spinodal. Several events of spontaneous nucleation were observed in our simulations. That allowed us to calculate a "cavitation" line. By this we mean the pressure at which a fixed volume of water cavitates within a given range of time. Fig. (4.8) shows the evolution of the density for several runs, each at different pressures and $T = 280$ K. Notice that at -1500 bar the system does not cavitate for at least 10 ns, thus allowing to easily estimate the density of this metastable state. On the contrary, the runs at lower pressures exhibit at a given time a sudden drop of density corresponding to the formation of a bubble which grows very quickly. Table (4.4) and Fig. (4.9) show the cavitation pressures (within a given tem-

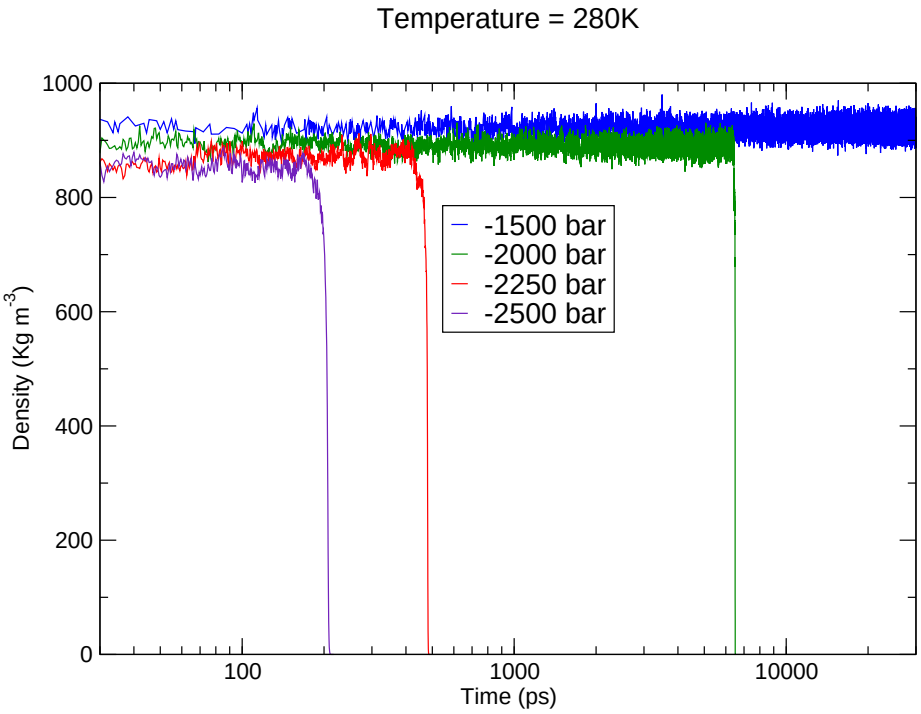

Figure 4.8: Sampling of several isobars at 280 K. The time scale is taken on a logarithmic scale.

perature range). In Fig.(4.9) we observe that the cavitation line appears to be monotonons function which increases with temperature. To ensure representative data for the TIP4P/2005 model, we set a minimum time to allow the

system to equilibrate (approximately 10 ns) and simulate a system of 4000 molecules. The cavitation line indicates the mechanical limit of the system,

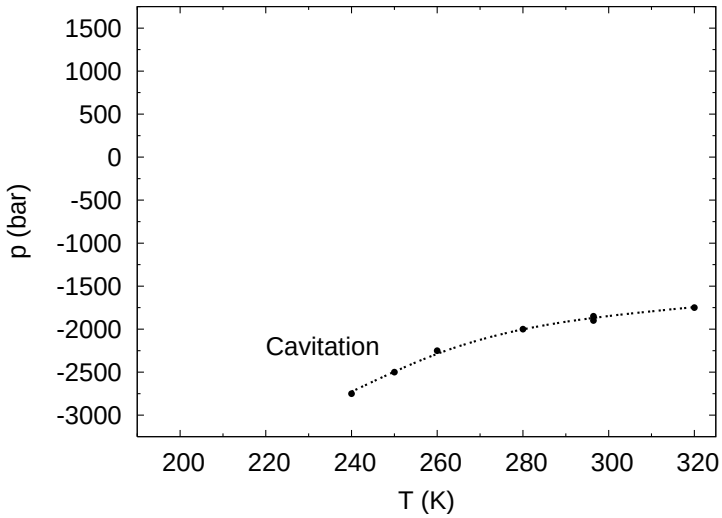

Figure 4.9: Cavitation line in the p-T plane for the TIP4P/2005 model.

given that when the system cavitates, the simulation box literally "explodes". This explosion is due to the presence of cavitation bubbles rapidly growing. If we now represent the cavitation line together with all lines presented in

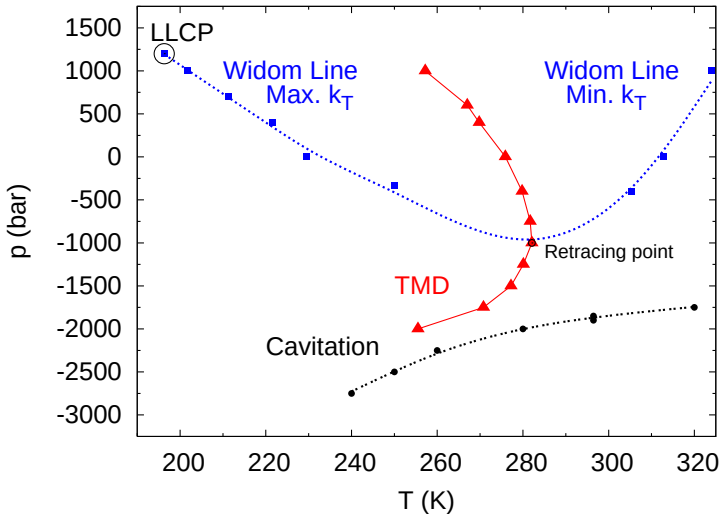

Figure 4.10: Same as Fig.(4.7) including the cavitation line in the $p-T$ plane.

Fig.(4.7) this line in the $p-T$ plane. We note that it does not cross at any

time another property Fig.(4.10). Moreover, its tendency is not to have a minimum that could change the slope of the line (thus leading to a cross with another function). To conclude, we have to calculate the spinodal line and find out if it has the retracing point as suggested by Speedy.

Temperature (K)	Pressure (bar)
240	-2750
250	-2500
260	-2250
280	-2000
296.45	-1850
320	-1750

Table 4.4: Simulation results of cavitation for TIP4P/2005.

4.3.4. Liquid-vapour spinodal line

As stated in the previous section, this property cannot be evaluated by means of simulations in the NpT ensemble because the system cavitates. Therefore, we carried out simulations in the NVT ensemble and used the same simulation conditions except for the box volume which is now fixed. In Fig. (4.11) we observe that all the isotherms exhibit a minimum at negative pressure. These minima correspond to the beginning of the so-called *Van Der Waals'loops*, which are generated in the vicinity of a phase separation and are typical in NVT simulation. In this case the spinodal point is defined as that for which the slope of $(\partial p/\partial \rho)_T$ is zero. The spinodal points are reported in Table (4.5) and represented in Fig. (4.12). As expected, the trend of this function is similar to the cavitation line. This indicates that there is no re-entrant point in the spinodal as proposed in the second critial point scenario, Fig. (4.1.B), and in the singularity-free interpretation, Fig. (4.1.D). Finally, we represent also the spinodal line to the scenario for the TIP4P/2005 model, Fig. (4.13).

4.4. Discussion and Conclusions

In this chapter we have calculated several water properties, mainly in the supercooled and negative pressure region for the TIP4P/2005 water model. This allows us to analyze which of the scenarios shown in Fig. (4.1) is

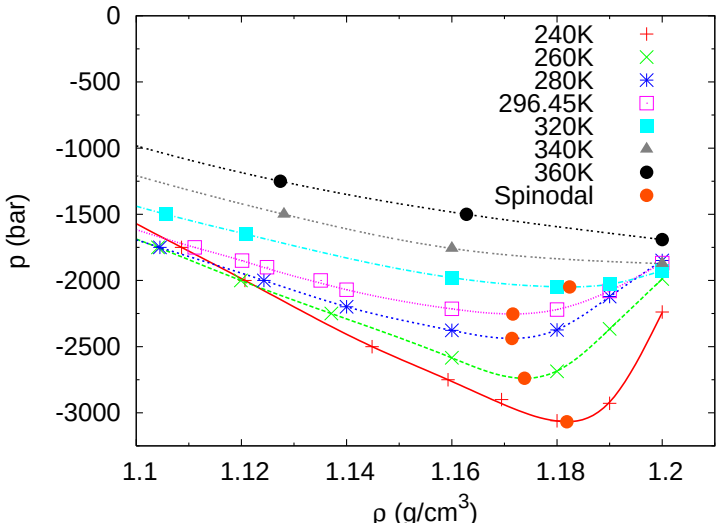

Figure 4.11: Isotherms at negative pressures. The orange circles indicate the spinodal for TIP4P/2005.

Temperature (K)	Pressure (bar)
240	-3067.68
260	-2739.34
280	-2438.08
296.45	-2253.75
320	-2048.71

Table 4.5: Liquid-vapour spinodal for TIP4P/2005 at negative pressures.

the correct one for TIP4P/2005. A summary of our calculations is shown in Fig. (4.13).

The first conclusion is that the stability limit conjecture is not valid for this model. There are several reasons for that. The main reason is that the line of density maxima is retracing and, according to thermodinamics considerations, cannot merge with the liquid-vapour (LV) spinodal. In fact, our calculations of the liquid-vapour spinodal indicate that, after the retracing pressure, the TMD line goes more or less parallel to the LV spinodal. Also, in agreement with thermodynamic consistency arguments is the fact that the TMD line retracing point also belongs to the line of isothermal compressibilty extrema. In our case this point is almost coincident with the temperature dividing the region where κ_T exhibits a maximum from that showing a minimum. Notice that below approx. -1000 bar the isothermal

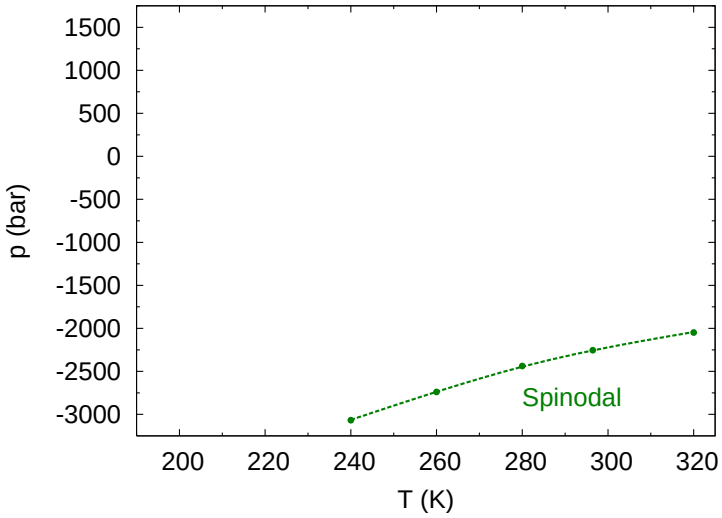

Figure 4.12: Spinodal line for the TIP4P/2005 water model in the $p-T$ plane.

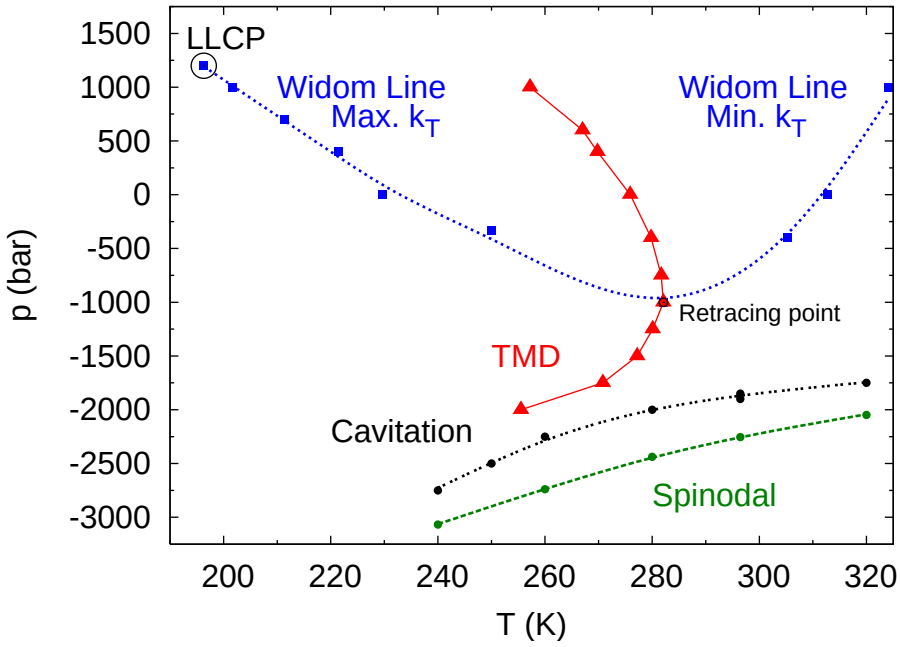

Figure 4.13: The scenario proposed for the TIP4P/2005 water model at extreme conditions and negative pressures in the $p-T$ plane.

compressibility can no longer present a maximum nor a minimum.

The results presented in this chapter are then compatible the critical

point (CP) or the singularity-free (SF) scenario. As previously commented, both scenarios may be seen as a unique one, where the CP is shifted to 0 K in the SF conjecture. However, the shape of the $p-\rho$ isotherms reported by Abascal and Vega[14] are strongly suggesting the vicinity of a critical point. Finally, it may be noted that the critical point-free (CF) scenario is not supported by our calculations because, if the spinodal of a liquid-liquid transtion is crossed, we should find a divergence but not a maximum in κ_T.

An interesting question to discuss is to which extent are the results of this work representative of the behaviour of real water. An extensive analysis of the predictions of TIP4P/2005 for a wide range of conditions and water properties[27] indicates that the model behaves very close to real water. Fig.(4.14) (taken from a paper by Absacal and Vega[15]) shows a comparison of

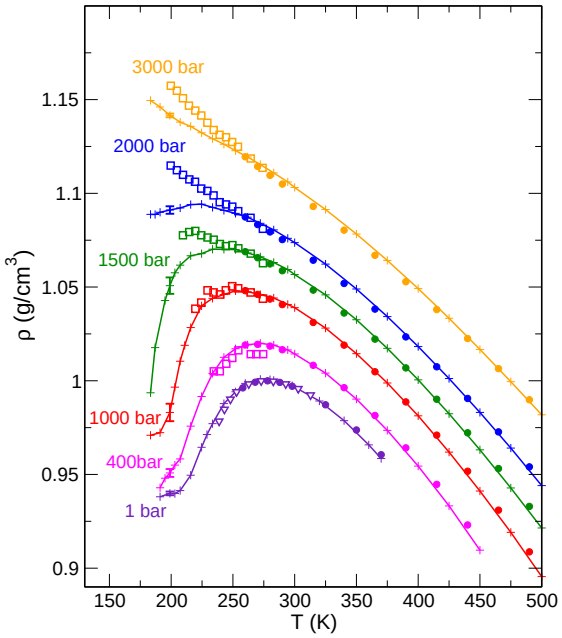

Figure 4.14: These isobars show the trend of density of the TIP4P/2005 model in a large range of temperatures. The solid lines correspond to the computational model and the empty squares to the experimental data[28].

the densities predicted by the model with experiments. Notice that the temperature interval covers essentially the whole liquid range up to pressures of 3000 bar including few points in the supercooled region. The agreement is excellent and the simulation data follow closely the experimental trend in the region of relevant to this work. Moreover, we recently had the opportunity of collaborating with an experimetal group performing measurements of the speed of sound in the deeply negative pressure region. The speed of sound is

related to the adiabatic compressibility κ_S; therefore, the maxima predicted for κ_T may be traced as minima in the speed of sound. These results for the sound velocity will be the subject of another part of this thesis, in particular Chapter 5.

The observation of cavitation events and the (approximate) calculation of the liquid-vapour spinodal open new possibilities for the study of bubble nucleation in water. This chapter shows that spontaneous bubble nucleation can be detected in simulations without the need of special simulation techniques. On the one hand, cavitation is a stochastic event: therefore, a large number of simulations is required to obtain reliables results. On the other hand, the location of small bubbles within liquid water is a non trivial problem. We will deal with these issues in Chapters 6, 7 and 8 of this thesis. While at deep supersaturation, cavitation happens spontaneously, the formation of bubbles at not too large supersaturation can be followed using special rare-events techniques, such as Umbrella Sampling (see the Theory Chapter). To conclude, besides being interested in homogeneous bubble nucleation from over-stretched water, we have started studying heterogeneous bubble nucleation of over-stretched water from a curved surface (represented by a carbon nanotube). These preliminary results will be presented in Chapter 9.

Bibliografía

1. P. Poole, F. Sciortino, U. Essmann, and H. Stanley, Nature **360**, 324 (1992).

2. P. G. Debenedetti, J. Phys. Condens. Matter **15**, R1669 (2003).

3. G. Franzese, J. Molec. Liq. **136**, 267 (2007).

4. F. Mallamace, C. Branca, M. Broccio, C. Corsaro, C.-Y. Mou, and S.-H. Chen, Proc. Nat. Acad. Sci. **104**, 18387 (2007).

5. F. Mallamace, C. Corsaro, M. Broccio, C. Branca, N. González-Segredo, J. Spooren, S.-H. Chen, and H. E. Stanley, Proc. Nat. Acad. Sci. **105**, 12725 (2008).

6. R. J. Speedy and C. A. Angell, J. Chem. Phys. **65**, 851 (1976).

7. R. Speedy, J. Chem. Phys. **77**, 2702 (1982).

8. P. Poole, F. Sciortino, T. Grande, H. Stanley, and C. Angell, Phys. Rev. Lett. **73**, 1632 (1994).

9. Q. Zheng, J. Green, J. Kieffer, P. Poole, J. Shao, G. Wolf, and C. Angell, in *Liquids Under Negative Pressure*, edited by A. Imre, H. Maris, and P. Williams (NATO, 2002), vol. 84 of *NATO Science series, Series II: Mathematics, Phys. and Chem.*, pp. 33–46.

10. C. A. Angell, Science **319**, 582 (2008).

11. H. Tanaka, Nature **380**, 328 (1996).

12. P. H. Poole, F. Sciortino, U. Essmann, and H. E. Stanley, Phys. Rev. E **48**, 3799 (1993).

13. S. Sastry, P. G. Debenedetti, F. Sciortino, and H. E. Stanley, Phys. Rev. E **53**, 6144 (1996).

14. J. L. F. Abascal and C. Vega, J. Chem. Phys. **133**, 234502 (2010).

15. J. L. F. Abascal and C. Vega, J. Chem. Phys. **134**, 186101 (2011).

16. B. Hess, C. Kutzner, D. van der Spoel, and E. Lindahl, J. Chem. Theory Comput. **4**, 435 (2008).

17. D. van der Spoel, E. Lindahl, B. Hess, G. Groenhof, A. E. Mark, and H. J. C. Berendsen, J. Comp. Chem. **26**, 1701 (2005).

18. S. Nosé, Mol. Phys. **52**, 255 (1984).

19. W. G. Hoover, Phys. Rev. A **31**, 1695 (1985).

20. A. Rahman and F. H. Stillinger, J. Chem. Phys. **55**, 3336 (1971).

21. U. Essmann, L. Perera, M. L. Berkowitz, T. Darden, H. Lee, and L. G. Pedersen, J. Chem. Phys. **103**, 8577 (1995).

22. T. Darden, D. York, and L. Pedersen, J. Chem. Phys. **98**, 10089 (1993).

23. D. T. Limmer and D. Chandler, J. Chem. Phys. **138**, 214504 (2013).

24. C. Vega, M. M. Conde, C. McBride, J. L. F. Abascal, E. G. Noya, R. Ramirez, and L. M. Sese, J. Chem. Phys. **132**, 046101 (2010).

25. H. L. Pi, J. L. Aragones, C. Vega, E. G. Noya, J. L. F. Abascal, M. A. Gonzalez, and C. McBride, Mol. Phys. **107**, 365 (2009).

26. W. Wagner and A. Pruss, J. Phys. Chem. Ref. Data **31**, 395 (2002).

27. C. Vega and J. L. F. Abascal, Phys. Chem. Chem. Phys. **13**, 19663 (2011).

28. O. Mishima, J. Chem. Phys. **133**, 144503 (2010).

Results: Chapter 5

Anomalies in bulk supercooled water at negative pressure

Gaël Pallares[1], *Mouna El Mekki Azouzi*[1], **Miguel Angel Gonzalez**[2], *Juan Luis Aragones*[2], *Jose Luis F. Abascal*[2], *Chantal Valeriani*[2] *and Frédéric Caupin*[1]

(1) Institut Lumière Matière, UMR5306 Université Lyon 1–CNRS, Université de Lyon and Institut Universitaire de France, 69622 Villeurbanne cedex, France.

(2) Departamento de QuÃmica FÃsica I, Facultad de Ciencias QuÃmicas, Universidad Complutense, 28040 Madrid, Spain.

5.1. Abstract

Water anomalies still defy explanation. In the supercooled liquid, many quantities, for example heat capacity and isothermal compressibility κ_T, show a large increase. The question arises if these quantities diverge, or if they go through a maximum. The answer is key to our understanding of water anomalies. However, it has remained elusive in experiments because crystallization always occurred before any extremum is reached. Here we report measurements of the sound velocity of water in a scarcely explored region of the phase diagram, where water is both supercooled and at negative pressure. We find several anomalies: maxima in the adiabatic compressibility and non–monotonic density dependence of the sound velocity, in contrast with a standard extrapolation of the equation of state. This is reminiscent of the behavior of supercritical fluids. To support this interpretation, we have performed simulations with the TIP4P/2005 potential. Simulations and experiments are in near quantitative agreement, suggesting the existence of a line of maxima in κ_T (LMκ_T). This LMκ_T could either be the thermodynamic

consequence of the line of density maxima of water (Sastry S., Debenedetti P. G., Sciortino F., Stanley H. E. (1996) *Phys. Rev. E* 53:6144–6154), or emanate from a critical point terminating a liquid–liquid transition (Sciortino F., Poole P. H., Essmann U., Stanley H. E. (1997) *Phys. Rev. E* 55:727–737). At positive pressure, the LMκ_T has escaped observation because it lies in the 'no man's land'beyond the homogeneous crystallization line. We propose that the LMκ_T emerges from the 'no man's landát negative pressure.

5.2. Introduction:

Water is the most familiar liquid, and arguably the most complex. Anomalies of supercooled water have been measured during decades, and competing interpretations proposed. Yet, a decisive experiment remains elusive, because of unavoidable crystallization into ice. We investigate the state of water that is both supercooled and under mechanical tension, or negative pressure. Liquids under negative pressure can be found in plants or fluid inclusions in minerals. Using such water inclusions in quartz, we report the first measurements on doubly metastable water down to −15°C and around −100 MPa. We observe sound velocity anomalies that can be reproduced quantitatively with molecular dynamics simulations. These results suggest the possibility to rule out two proposed scenarios for water anomalies, and put further constraints on the remaining ones.

Water differs in many ways from standard liquids: ice floats on water, and, upon cooling below 4°C, the liquid density decreases. In the supercooled liquid, many quantities, for example heat capacity and isothermal compressibility, show a large increase. Extrapolation of experimental data suggested a power–law divergence of these quantities at −45°C[16]. Thirty years ago, the stability–limit conjecture proposed that an instability of the liquid would cause the divergence[17] (Fig. 5.1A). This is supported by equations of state (EoSs), such as the IAPWS EoS[2], fitted on the stable liquid and extrapolated to the metastable regions. Ten years later, the second critical point interpretation, based on simulations[18], proposed that, instead of diverging, the anomalous quantities would reach a peak, near a Widom line[19,20] that emanates from a liquid–liquid critical point (LLCP) terminating a first order liquid–liquid transition (LLT) between two distinct liquid phases at low temperature (Fig. 5.1B). The two scenarios differ in the shape of the line of density maxima (LDM) of water (see Fig. 5.1A and B). A recent work[21] has added one point on this line at large negative pressure, but this was not enough to decide between the two scenarios.

It has been argued[22] that the stability–limit conjecture would imply

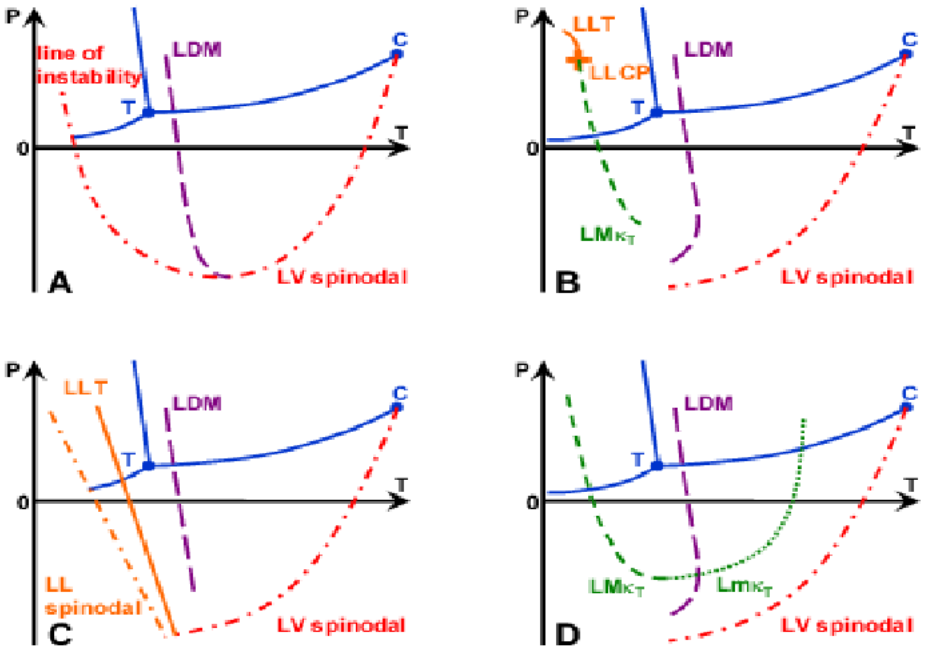

Figure 5.1: Scenarios proposed to explain water anomalies. Schematic phase diagrams for water in the pressure–temperature plane with equilibrium transitions between liquid, vapor and ice (solid blue curves); T is the triple point and C the liquid–vapor critical point. (*A*) Stability–limit conjecture[17]. If the line of density maxima (LDM, long-dashed purple curve) reaches the liquid-vapor (LV) spinodal (dash-dotted red curve) at negative pressure, the latter bends to lower tension at lower temperature. This would provide a line of instability at positive pressure on which several thermodynamic functions would diverge. (*B*) Second critical point scenario[18]. The LDM bends to lower temperatures at larger tension, and the LV spinodal remains monotonic. The anomalies of supercooled water are due to the vicinity of a liquid–liquid critical point (LLCP) terminating a liquid-liquid transition (LLT, solid orange curve). Thermodynamic functions exhibit a peak on lines emanating from the LLCP[19,20], such as the line of isothermal compressibility maxima along isobars (LMκ_T, short–dashed green curve). (*C*) Critical point free scenario[23,24,13]. The LLT extends down to the LV spinodal, so that there is no accessible LLCP. The spinodal associated with the LLT (LL spinodal, dash-dotted orange curve) would cause the divergence of several thermodynamic functions. (*D*) Singularity-free interpretation[25]. There is no LLT nor LLCP. Thermodynamic functions do not diverge, but several exhibit extrema as a consequence of the existence of a LDM. The LDM reaches its highest temperature when it crosses one of the lines of isothermal compressibility extrema along isobars; the case where it is the line of minima (Lmκ_T, dotted green curve) is displayed.

the existence of an improbable second, low temperature liquid-vapor critical point. However, it is not necessary if the line of instability at positive pressure is not a liquid-vapor spinodal, but rather a line of instability towards another phase. The critical-point free scenario[23,24,13] (Fig. 5.1C) provides such a line. There would be a LLT, but its critical-point would be absent because it lies beyond the liquid-vapor spinodal. The low-density liquid could become metastable at low temperature, but unstable on the liquid-liquid spinodal, where κ_T would diverge. Finally, the singularity-free scenario[25] (Fig. 5.1D), does not exhibit any LLT. It predicts peaks in several thermodynamic quantities instead of divergences, which would be "the thermodynamically inevitable consequences of the existence of density anomalies"[22]. It may also be seen as a second critical point interpretation, but with a LLCP at zero temperature[13,14].

In bulk water at positive pressure, despite tremendous efforts[22] decisive experiments to discriminate between the proposed scenarios have been precluded by unavoidable crystallization. To circumvent this problem, water proxies have been used: water confined in narrow pores[26], or bulk water–glycerol mixtures[27]. Although the results supported the second critical point interpretation, their relevance to bulk water is not straightforward.

Here we study bulk water samples, a few microns in diameter, in the doubly metastable region: the liquid is simultaneously supercooled and exposed to mechanical tension or negative pressure. Negative pressures occur in nature, e.g. in the sap off trees, under the tentacles of octopi, or in fluid inclusions in minerals[28,29]. The study of the largest tensions achievable in water was pioneered by the group of Angell[7]. They used a 'Berthelot tube'technique (Fig. 5.2A), based on isochoric cooling of a micrometer size inclusion of water in quartz. Tensions as large as $-140\,\mathrm{MPa}$ have been reported, and confirmed by others [21,8,30], which exceed by far the limit of other techniques[28,29]. It was already recognized in the work of Angell that the high density water inclusions that were able to survive cooling to room temperature without cavitation were also able to be supercooled below 0°C. Indeed, when the isochore crosses the line of density maxima of water, the tension is released and cavitation becomes less likely. Another study[31] using macroscopic Berthelot tubes also reached the doubly metastable region, but the tensions were around $-10\,\mathrm{MPa}$ only.

In order to reach large tensions, we use two microscopic inclusions of water in quartz (Fig. 5.2B, inset) (see *Materials and Methods*, Samples). We perform Brillouin light scattering experiments on these samples; this technique gives access to the sound velocity within the liquid. Several Brillouin light scattering studies on supercooled water at ambient pressure are available[32,33,34,35,36,37], but only one work investigated water under tension[8]: all

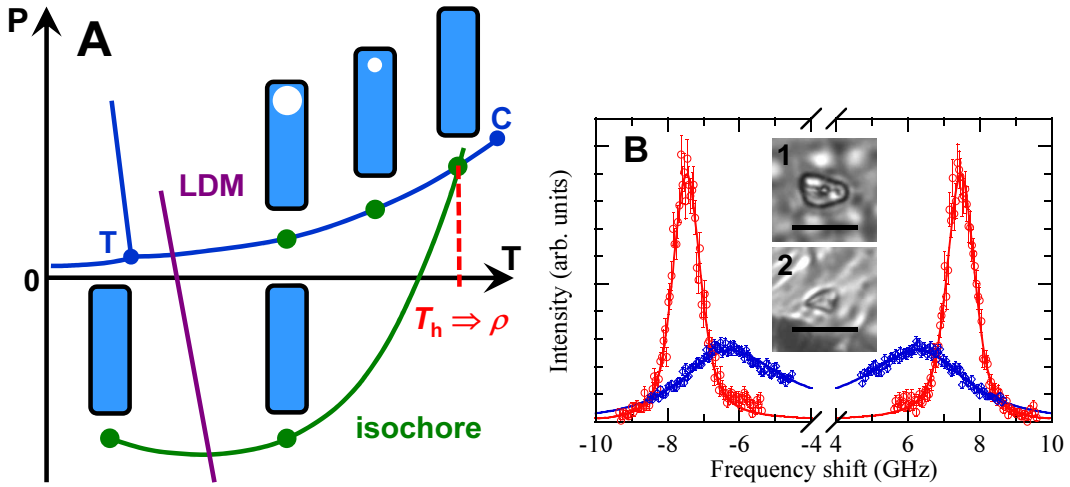

Figure 5.2: Experiments on metastable liquid water. *A*, Berthelot tube method[7,8,30,21]. A closed, rigid container with a fixed amount of water is heated until the last vapor bubble disappears at T_h. Upon cooling, the bubble does not reappear and the liquid follows an isochore (green curve) and is put under mechanical tension. If the density is high enough, cavitation does not occur and the liquid can reach the doubly metastable region, where water is both supercooled and under tension. *B*, Typical Brillouin spectra. They were obtained with the homogenized sample 1 at 140°C (red circles) and −12°C (blue diamonds). The solid curves are fits used to obtain the sound velocity (see *Appendix text*). Note that the −12°C spectrum was rescaled to the same exposure time as the 140°C spectrum for easier comparison. The samples are shown as inset (scale bars, 10 μm).

samples in that study cavitated above room temperature except one with a density close to that of our sample 1. However, measurements in Ref.[8] were reported only down to 0°C, and the direct comparison to an extrapolated EoS was not considered. Our work extends the covered range to supercooled water under tension, reporting measurements down to −15°C along two isochores at $\rho_1 = 933{,}2 \pm 0{,}4\,\mathrm{kg\,m^{-3}}$ and $\rho_2 = 952{,}5 \pm 1{,}5\,\mathrm{kg\,m^{-3}}$, and reaching pressures beyond −100 MPa (see *Appendix text*).

5.3. Results

Representative Brillouin spectra are shown in Fig. 5.2B. Such spectra are analyzed to give the zero frequency sound velocity c (see *Materials and Methods*, Brillouin light scattering). To support the experimental results, we also perform molecular dynamics simulations of c. Previous numerical studies of water at negative pressure are available, for several potentials: ST2[18], SPC/E[38], TIP5P[39]. They all find a liquid–vapor spinodal whose pressure increases monotonically with temperature, and a TMD that avoids meeting the spinodal, in contrast with the stability-limit conjecture. Here we choose to use TIP4P/2005[40] because it has demonstrated an excellent overall performance[41] and, in particular, it yields results in satisfactory agreement with the reported experimental results in the supercooled region[42]. Thus, we calculate values of c for TIP4P/2005 at the experimental thermodynamic conditions (see *Materials and Methods*, Molecular dynamics simulations).

Figure 5.3 shows the experimentally measured and the numerically computed values of c as a function of temperature at several thermodynamic conditions. Let us first describe the measurements on sample 1 after cavitation, at temperatures up to $T_{\mathrm{h},1}$: at these conditions the liquid is in equilibrium with its vapor. The measured sound velocity is in excellent agreement with the known sound velocity along the binodal and with our simulations of TIP4P/2005 water along its binodal[43]. The agreement between simulations and tabulated experimental data also illustrates the quality of the potential used to simulate water[40]. When the temperature of sample 1 reaches $T_{\mathrm{h},1}$, the last vapor bubble disappears leaving the inclusion entirely filled with liquid at density ρ_1. Upon further heating, the pressure increases along the ρ_1 isochore. Once more, the measurements agree with the sound velocity from the known EoS and from our simulations along the ρ_1 isochore. Note that the measurements leave the binodal exactly at $T_{\mathrm{h},1}$, which has been determined independently by direct observation under the microscope. This consistency further corroborates the robustness of our data.

Next, we make sample 1 metastable by cooling along the ρ_1 isochore.

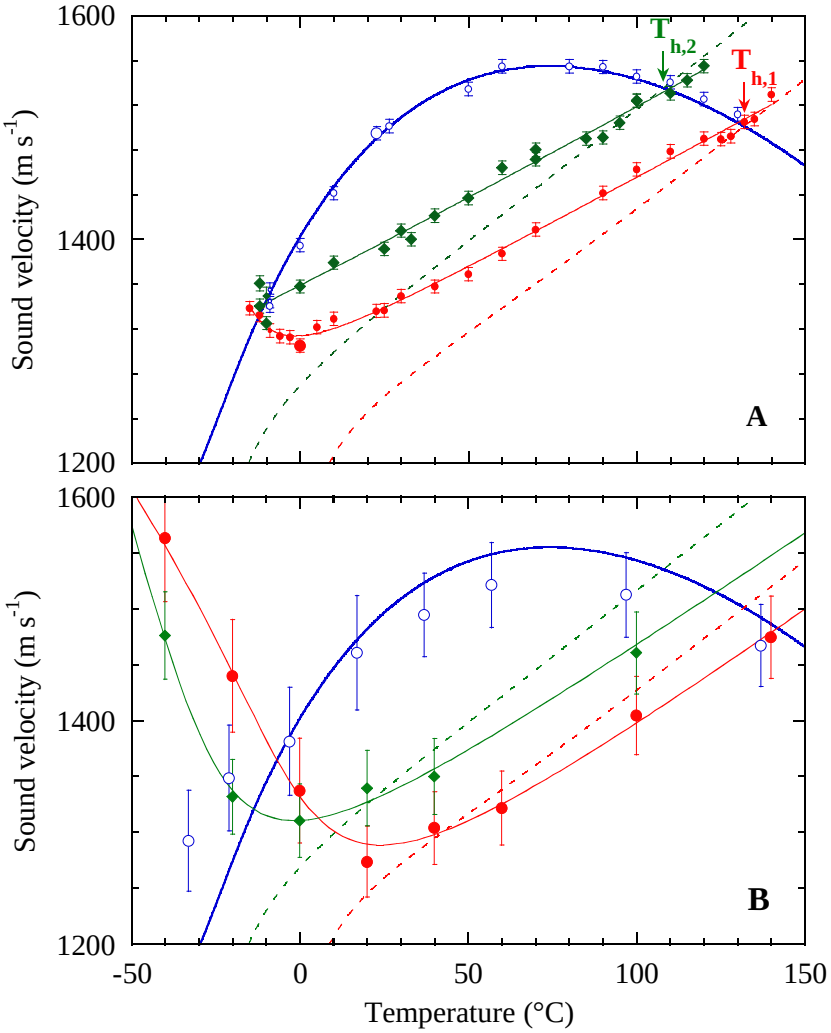

Figure 5.3: Sound velocity as a function of temperature. The IAPWS EoS is used to plot the sound velocity along the binodal (thick blue curve) and along the isochores at ρ_1 (dashed red curve) and ρ_2 (dashed green curve). **A**, comparison with experiments. The symbols show our measurements on sample 1 after cavitation (open blue circles) and on metastable samples 1 (filled red circles) and 2 (filled green diamonds). The three symbol sizes correspond to three pinhole sizes on the spectrometer. The solid red and green curves are guides to the eye. The arrows show the homogeneization temperatures of samples 1 and 2 as observed under the microscope. **B**, comparison with simulations of TIP4P/2005 water. The sound velocity was calculated along the TIP4P/2005 binodal (open blue circles), and the isochores at ρ_1 (filled red circles) and ρ_2 (filled green diamonds). The solid red and green curves are guides to the eye. Whereas the IAPWS EoS predicts a monotonic variation of c along the isochores, both experiments and simulations find that c reaches a minimum and increases above the values on the binodal at low temperature.

We observe that below $T_{\mathrm{h},1}$, the measured sound velocity starts diverging with respect to the one extrapolated using the IAPWS EoS. In contrast, it agrees with our simulations. The IAPWS EoS predicts a re–entrant liquid–vapor spinodal: in this case, one would expect the sound velocity curve to reach a small value when the isochore approaches the spinodal at low temperature (for ρ_1, the IAPWS EoS predicts that they meet at $-15°\mathrm{C}$ with $c = 697\,\mathrm{m\,s^{-1}}$). In contrast, both experiment and simulation give a sound velocity that reaches a minimum near 0°C, before increasing on further cooling. Therefore, the isochore at ρ_1 does not approach the liquid–vapor spinodal as expected from the IAPWS EoS. The sound velocity c is related to the adiabatic compressibility κ_S through $c = 1/\sqrt{\rho\kappa_S}$, where ρ is the density. Since we follow an isochore, the sound velocity minimum corresponds to a maximum in the adiabatic compressibility. Eventually, the sound velocity reaches a value *higher* than the value that one would expect along the binodal at $-15°\mathrm{C}$, even though ρ_1 lies *below* the liquid density on the binodal, $\rho_0 = 996{,}3\,\mathrm{kg\,m^{-3}}$ at $-15°\mathrm{C}$[44].

To confirm our results, we have repeated measurements and simulations on sample 2 with a higher density ρ_2. We find a similar deviation from the extrapolation of the IAPWS EoS. In the simulations, the sound velocity reaches a minimum, which is not clear in the experiments that seem to reach a plateau. This is consistent with the fact that the simulations find the minimum for ρ_2 at a temperature lower than for ρ_1, while for ρ_1 the experiment finds the minimum at a temperature lower than the simulations. Therefore it is likely that the minimum for ρ_2 lies at temperatures below the one reached in the experiment. In both experiment and simulations, while at $-12°\mathrm{C}$ ρ_2 is *between* ρ_1 and ρ_0, the corresponding sound velocity is even slightly *higher* than both. Therefore, the sound velocity must reach a minimum between ρ_2 and ρ_0 along the $-12°\mathrm{C}$ isotherm. This is more clearly seen on Fig. 5.4: the sound velocity at ρ_0, ρ_1 and ρ_2 virtually fall on a horizontal line, but the slope of $c(\rho)$ at ρ_0 necessarily implies a minimum. This observation agrees with the predictions of the simulations but contrasts those of the IAPWS EoS.

5.4. Discussion

To explain the observed anomalies, it is interesting to look for other systems with a minimum in $c(\rho)$ along an isotherm. This actually occurs in all fluids, in their supercritical phase: the sound velocity at a constant temperature above the liquid–vapor critical temperature passes through a minimum at a density close to the critical density (see for instance Fig. 8

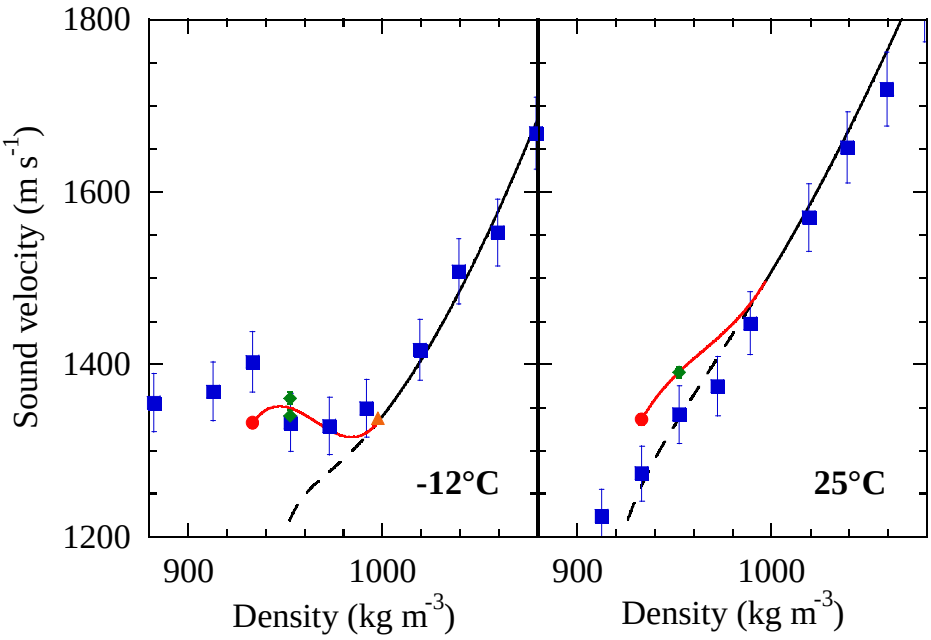

Figure 5.4: Sound velocity versus density at −12°C and 25°C. The IAPWS EoS is shown in black, as a solid curve above the binodal, and as a dashed curve for its extrapolation to lower density. Our measurements for ρ_1 and ρ_2 are shown as filled red circles and green diamonds, respectively. The red curves are guides to the eye chosen to connect the data to the IAPWS EoS above the binodal with the correct slope. Note that the IAPWS EoS reproduces accurately experimental data above the binodal for stable water (e.g. at 25°C), and data along the binodal for supercooled water (e.g. at −12°C). To illustrate the latter, we have included in the left panel the experimental value of the sound velocity at −11,2°C (orange triangle) from ref.[36] (see *Appendix text*). The solid blue squares give the results of the simulations of TIP4P/2005 water; note that the simulations in the right panel were obtained at 20°C. At high temperature, measurements and simulations agree with the IAPWS EoS, whereas at low temperature, they suggest the occurence of a minimum and maximum which are absent from the extrapolation of the IAPWS EoS.

of Ref.[45] for methanol and ethanol). Based on this observation, we propose that the anomalies of the sound velocity, observed both in experiments and in simulations, are a signature of supercritical phenomena. Here, in addition, the sound velocity reaches a maximum when the density decreases (Fig. 5.4). This is because eventually the liquid–vapor spinodal density has to be reached, and the sound velocity has then to become small. A microscopic cell model[14] is able, by tuning two parameters, to reproduce each of the possible scenarios shown in Fig. 5.1. It should be interesting to investigate the behaviour of the sound velocity within this model but this lies outside the scope of this work. It seems more convenient to use instead more realistic water models as a guide to better understand the origin of such anomalies. Several potentials predict a LLT in the supercooled region, ending at a LLCP. Based on the locus of maxima of κ_T along isobars, a LLCP for TIP4P/2005 has been proposed at $T_c = 193\,\mathrm{K}$, $P_c = 135\,\mathrm{MPa}$, and $\rho_c = 1012\,\mathrm{kg\,m^{-3}}$ [46], although the existence of a LLT for TIP4P/2005 is disputed in a recent paper[47]. The LLCP is an appealing idea because it would give a reason for which water above 193 K behaves like a supercritical fluid.

One may wonder why all previous experiments at positive pressure failed to detect a peak in thermodynamic functions. Simulations with a LLT show that specific quantities (such as isothermal compressibility κ_T or isobaric heat capacity) reach a peak on different lines, but that these lines all come close to each other near the LLCP, approaching asymptotically the locus of correlation length maxima, called the Widom line[20]. The locus of maxima for κ_T along isobars (LMκ_T) has been recently computed for TIP4P/2005 water at positive pressure[46]. We have now computed this line also at negative pressure (see *Appendix text*). The results are shown on Fig. 5.5 and compared to the isochores we studied and to the experimental line of homogeneous crystallization[48]. At positive pressure, the LMκ_T is not accessible to experiments since it lies in the so–called 'no man's land'[49], a region where bulk liquid water cannot be observed experimentally. However, at negative pressure, the slope of the LMκ_T becomes less negative than that of the line of homogeneous crystallization. Since the latter keeps the same slope, the LMκ_T line leaves the 'no man's landánd enters the doubly metastable region that we have now shown is accessible to quantitative experimentation.

Is there a way to directly observe the LLT? If it exists, it is likely to lie in the 'no man's land'. Therefore it will be hard to decide between the second critical point interpretation[18] and the singularity free scenario[25]; note however that the latter can be seen[14] as a LLT with a critical point at 0 K. What our results do show is that the liquid–vapor spinodal does not reach the location predicted by extrapolation from the IAPWS EoS, and that the measured sound velocity quantitatively agrees with the one obtained

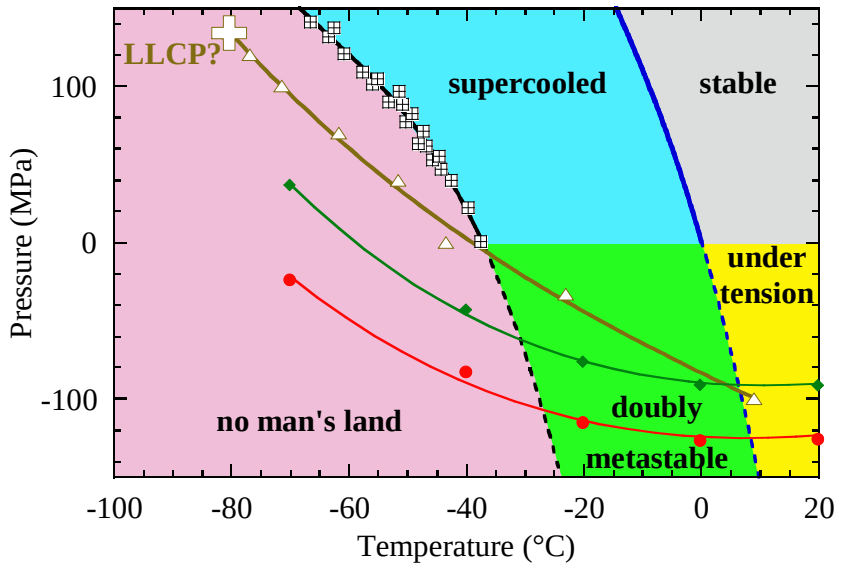

Figure 5.5: Pressure–temperature phase diagram of water. Colored areas are used to identify the different possible states for liquid water. The melting line of ice Ih is shown at positive pressure by a solid blue curve and its extrapolation to negative pressure by a dashed blue curve. The black crossed squares show the experimental supercooling limit[48]. They define the experimental homogeneous nucleation line (solid black curve), which is extrapolated here to negative pressure (dashed black curve). The ρ_1 and ρ_2 isochores of TIP4P/2005 water are shown by the red circles and curve, and green diamonds and curve, respectively. Simulations of TIP4P/2005 water are performed to find the maximum κ_T along several isobars (white triangles), defining the LMκ_T (brown curve), that might emanate from a liquid–liquid critical point (LLCP, white plus symbol). Since the predictions of TIP4P/2005 are in satisfactory agreement with the reported experimental results in the supercooled region[42], this figure seems to indicate that the LMκ_T (and other extrema in the response functions) might be accessible to experiment only in the doubly metastable region.

with simulations of TIP4P/2005 water. This suggests that the sound velocity anomalies observed in the experiment are due to a LMκ_T, a feature present in the LLCP and singularity free scenarios (Figs. 5.1B and D), but absent from the stability limit conjecture and the critical point free scenario (Figs. 5.1A and C). The doubly metastable region therefore appears like a promising experimental territory to test other predictions from the models proposed to explain water anomalies.

5.5. Materials and Methods

5.5.1. Samples

Sample 1 was prepared by hydrothermal synthesis[30]; sample 2 is a natural sample from the French Alps, filled with meteoric water (Fig. 5.2B, inset). The purity of water is estimated to be greater than 99.8 mole percent (see *Appendix text*). The samples were placed on a heating–cooling stage (Linkam THMS 600) mounted on a microscope (Zeiss Axio Imager Vario). Phase changes in the inclusions were observed with a 100× Mitutoyo plan apo infinity-corrected long working-distance objective. When a bubble is present in a sample, we observe its disappearance upon heating along the liquid-vapor equilibrium at the homogenization temperature: $T_{\mathrm{h},1} = 131{,}9 \pm 0{,}5°\mathrm{C}$ for sample 1 and $T_{\mathrm{h},2} = 107{,}9 \pm 2°\mathrm{C}$ for sample 2, where the numbers give the average and standard deviation over a series of at least 5 measurements. The known data for the binodal[3] give the densities of water after homogenization: $\rho_1 = 933{,}2 \pm 0{,}4\,\mathrm{kg\,m^{-3}}$ and $\rho_2 = 952{,}5 \pm 1{,}5\,\mathrm{kg\,m^{-3}}$, respectively.

5.5.2. Brillouin light scattering

Brillouin scattering experiments were performed in backscattering geometry through the microscope objective. The sample is illuminated with a single longitudinal monomode laser (Coherent, Verdi V6) of wavelength $\lambda = 532\,\mathrm{nm}$ focused to a $1\,\mu\mathrm{m}$ spot. The light scattered from the sample is collected on the entrance pinhole of a tandem Fabry–Perot interferometer (JRS Scientific, TFP-1). We use the recommended combination between entrance and output pinholes, and three different values for the entrance pinhole diameter: 150, 200, and $300\,\mu\mathrm{m}$. A smaller pinhole gives less signal, but more resolution. It also reduces the volume of the sample from which the scattered light is allowed to enter the spectrometer, thus decreasing the parasitic light due to elastic scattering from the quartz crystal. Figure 5.3A shows that the results are consistent for the three pinhole sizes used, indica-

ting that the resolution is sufficient and validating the assumption that the elastically scattered light can be neglected in the analysis. Consequently we have fitted the Brillouin peaks only, using a viscoelastic model described in detail in Ref.[50]. It introduces a memory function with an exponential decay:

$$m(Q,t) = ({c_\infty}^2 - c^2)\, Q^2 \exp\left[-\left(\frac{c}{c_\infty}\right)^2 \frac{t}{\tau}\right] , \tag{5.1}$$

where Q is the wavevector probed by the scattering setup, c and c_∞ the sound velocity at zero and infinite frequency respectively, and τ a structural relaxation time. $Q = 4\pi n/\lambda$ where n is the refractive index of the liquid. In their Brillouin study, Alvarenga *et al.*[8] used for each isochore a constant value of n, determined from the known value at the homogenization temperature T_h. We chose instead to use a semi–empirical formula based on the Lorentz-Lorenz relation[51]. Along the liquid-vapor equilibrium line, it reproduces accurately the literature data. Note however that the difference with Alvarenga *et al.* is minimal: in the temperature range investigated, n is almost constant along an isochore, varying from 1.31152 to 1.31456 for sample 1 and from 1.3184 to 1.321 for sample 2. The ratio between dynamic ($S(Q,\omega)$) and static ($S(Q)$) structure factor is:

$$\frac{S(Q,\omega)}{S(Q)} = \frac{1}{\pi} \frac{(c\,Q)^2\, m_\mathrm{R}(Q,\omega)}{\left[\omega^2 - (c\,Q)^2 - \omega\, m_\mathrm{I}(Q,\omega)\right]^2 + \left[\omega\, m_\mathrm{R}(Q,\omega)\right]^2} , \tag{5.2}$$

To complete the analysis, the instrumental resolution function (IRF) and the dark count of the setup are needed. The IRF was determined for each pinhole from the elastically scattered light from a $10\,\mathrm{mg\,L^{-1}}$ solution of milk in water, and well represented by a gaussian. The dark count of the photodetector was also taken into account. It was determined from spectra taken with the spectrometer entrance closed, or with no signal reaching the entrance pinhole. The background was deduced from the dark count and the duration of each spectra, and its effect on the sound velocity is less than the $6\,\mathrm{m\,s^{-1}}$ error bar on c (see *Appendix text*).

We have then analyzed the spectra as follows. We take the functional form of the viscoelastic model (Eq. 5.2), make a numerical convolution with the IRF, add the known dark count of the photomultiplier, and fit the resulting function on the raw spectra. We use 3 fitting parameters: c, τ, and an overall intensity factor K. We minimize the merit function χ^2, defined as the sum of square errors normalized by the error bars on the data points. These error bars are due to the photon noise, which goes as the square root of the number of counts. We chose a constant value for $c_\infty = 3000\,\mathrm{m\,s^{-1}}$;[52] we checked that the results are not sensitive to this choice. All fits are very

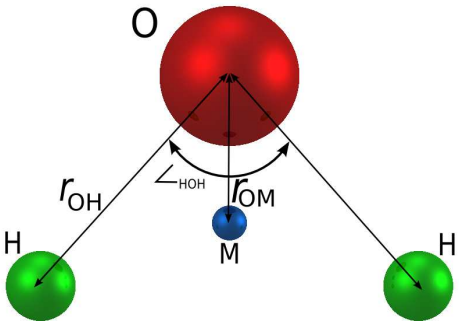

Figure 5.6: A schematic representation of the four-site model of water TIP4P/2005, consisting of a Lennard-Jones center at the oxygen atom (in red) and three charged sites: two positive charges at the hydrogen atoms and a compensating negative charge at a dummy atom (labeled as M) placed near the oxygen along the bisector of the HOH angle.

good, with a reduced χ^2 between 0.83 and 2.0, with an average of 1.28. To illustrate the quality of the fit, we show on Fig. S1 the residuals of the fits to the spectra displayed in Fig. 5.2B; they are compatible with the photon noise. The maximum value found for τ is 18 ps: our experiments are in the regime where relaxation effects are small, with $(c/c_\infty)^4(\omega\tau)^2 \ll 1$ (0.03 at most).

5.5.3. Molecular dynamics simulations

We have performed Molecular Dynamics simulations of c at the same thermodynamic conditions as the experiments. We simulate a system of 500 water molecules interacting by means of the TIP4P/2005 potential[40] with periodic boundary conditions. TIP4P/2005 represents water as a rigid and non–polarizable molecule. It consists of a Lennard-Jones site centred at the oxygen atom and a Coulomb interaction given by two partial charges placed at the hydrogen atom and a negative one placed at a point M along the bisector of the HOH angle. A schematic representation of the model is presented in Fig. S2 of the Supporting Information.

The parametrization of TIP4P/2005 has been based on a fit of the temperature of maximum density and a great variety of properties and wide range of thereof for the liquid and its polymorphs. TIP4P/2005 has been used to calculate a broad variety of thermodynamic properties of the liquid and solid phases, such as the phase diagram involving condensed phases[53,54,55], properties at melting and vaporization[43,56], dielectric constants[57], pair distribution function, and self–diffusion coefficient. These properties cover a temperature

range from 123 to 573 K and pressures up to 4000 MPa[41]. We have performed Molecular Dynamics simulations with the GROMACS 4.5 package [58,59] using the particle mesh Ewald method [60] to calculate the long–range electrostatics forces and the LINCS algorithm[61] to constrain the intramolecular degrees of freedom. We set the time step to 0,5 fs and make use of the velocity-rescaling thermostat[62] and the Parrinello-Rahman barostat,[63] with coupling constants set to 1 ps and 2 ps, respectively. The Lennard-Jones interactions are truncated at 9.5 Å. The contributions to the energy and pressure beyond this distance are approximated assuming that the molecules are uniformly distributed. In order to calculate the sound velocity of supercooled TIP4P/2005 water at negative pressure, the simulated times vary between 40 ns and 150 ns (at the lowest temperatures). The increased length of the runs at the lowest temperatures is due to the amplified density/energy fluctuations in this region for TIP4P/2005 (and other models as well[64]). This leads to an increase of the error bar associated to the calculated quantities at the lower temperatures.

The sound velocity c is defined by the Newton–Laplace formula:

$$c = \sqrt{\frac{1}{\rho \kappa_S}} = \sqrt{\frac{C_p}{C_V} \frac{1}{\rho \kappa_T}}, \tag{5.3}$$

where ρ is the density, $\kappa_S = -(1/V)(\partial V/\partial p)_S$ and $\kappa_T = -(1/V)(\partial V/\partial p)_T$ are the adiabatic and isothermal compressibility, respectively, defined in terms of the entropy S, volume V, pressure p, and temperature T of the system. C_p and C_v the heat capacity at constant pressure and volume, respectively. We calculate C_V, C_p and κ_T using the fluctuation formulas,

$$C_V = \frac{\langle U^2 \rangle - \langle U \rangle^2}{k_B T^2}, \quad C_p = \frac{\langle H^2 \rangle - \langle H \rangle^2}{k_B T^2}, \quad \kappa_T = \frac{\langle V^2 \rangle - \langle V \rangle^2}{\langle V \rangle \, k_B T}, \tag{5.4}$$

where U is the energy, H the enthalpy, and k_B the Boltzmann constant. We run numerical simulations in two different ensembles. First, by equilibrating the systems in a NVT ensemble, we compute C_V. Next, by equilibrating the system in a NpT ensemble, we compute C_p and κ_T.

We have also used an alternative method to obtain C_V, coming back to its definition:

$$C_V = \left(\frac{\delta U}{\delta T} \right)_V. \tag{5.5}$$

Thus, we compute the values of the energy along the desired isochore and calculate C_V as the derivative with respect to T. Table S1 of the Supporting Information shows the consistency between the values obtained with each route.

Table 5.1: Values of C_v for the isochore $\rho = 933{,}2\,\mathrm{kg\,m^{-3}}$ obtained with the energy fluctuations formula (Eq. 4 of the main text, second column) and the thermodynamic definition (Eq. 5 of the main text, third column). Results are given in $\mathrm{J\,K^{-1}\,mol^{-1}}$

T (K)	C_V [Eq. 4]	C_V [Eq. 5]
203	122± 6	119
233	110± 10	111
253	115± 10	105
273	114± 10	100
293	105± 5	95.0
313	93.5± 5	90.3
333	85.3± 4	85.9
373	75.3± 4	77.8
413	70.1± 3	70.7
462	63.2± 3	63.3
516	58.5± 3	57.0
570	55.0± 3	52.6
623	52.5± 3	50.1

Acknowledgments

We thank C. Austen Angell and José Teixeira for discussions; Véronique Gardien for providing us with sample 2; and Abraham D. Stroock and Carlos Vega for suggestions to improve the manuscript. The team at Lyon acknowledges funding by the ERC under the European Community's FP7 Grant Agreement 240113, and by the Agence Nationale de la Recherche ANR Grant 09–BLAN-0404-01. C.V. acknowledges financial support from a Marie Curie Integration Grant PCIG-GA-2011-303941 ANISOKINEQ and thanks the Ministerio de Educacion y Ciencia and the Universidad Complutense de Madrid for a Juan de la Cierva fellowship. The team at Madrid acknowledges funding from the MCINN Grant FIS2013-43209-P.

SUPPLEMENTAL MATERIAL for "Anomalies in bulk supercooled water at negative pressure"

Data analysis and error bars

When the experimental spectra were fitted with the function given by Eq. 2 of the main text, convoluted with the IRF and corrected for the back-

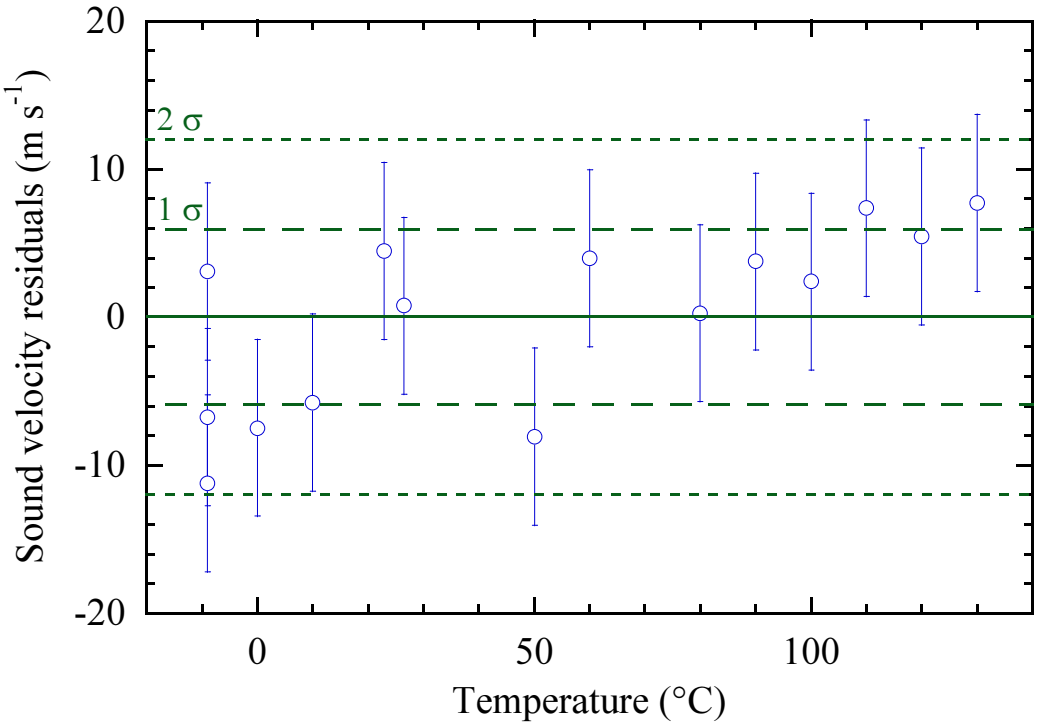

Figure 5.7: Sound velocity residuals of the data for sample 1 with a bubble present, to the reference data for liquid water in equilibrium with its vapor[1,2,3]. Their standard deviation $\sigma = 5{,}97\,\mathrm{m\,s^{-1}}$ was used to set the error bar on the sound velocity to $6\,\mathrm{m\,s^{-1}}$.

ground, the results for sample 1 with a bubble present exhibited a sound velocity value systematically lower than the reference data for liquid water in equilibrium with its vapor[1,2,3]. This is due to the uncertainty in the λ, and to the finite numerical aperture of the objective[4] (0.70). The average scattering angle 2θ is less than 180°, which lowers the value of $Q = 4\pi n \sin\theta/\lambda$. The results for the sound velocity must be corrected for this effect: a uniform factor of 1.0086 (which corresponds to $2\theta = 165°$, compatible with the numerical aperture of the objective) is sufficient to bring the data for sample 1 with a bubble present in excellent agreement with the reference data.

Fig. 5.7 shows the residuals. Their standard deviation was used to set the error bar, which gave $6\,\mathrm{m\,s^{-1}}$ (less than 0,45 %) and was applied to all data.

The guides to the eye in Fig. 3A are arbitrary fits to the data for the homogenized samples. With the $6\,\mathrm{m\,s^{-1}}$ error bar, the resulting reduced χ^2 is 0.94 and 1.98 for samples 1 and 2, respectively, showing that the data scatter is compatible with the error bar. Note that the measurements were performed

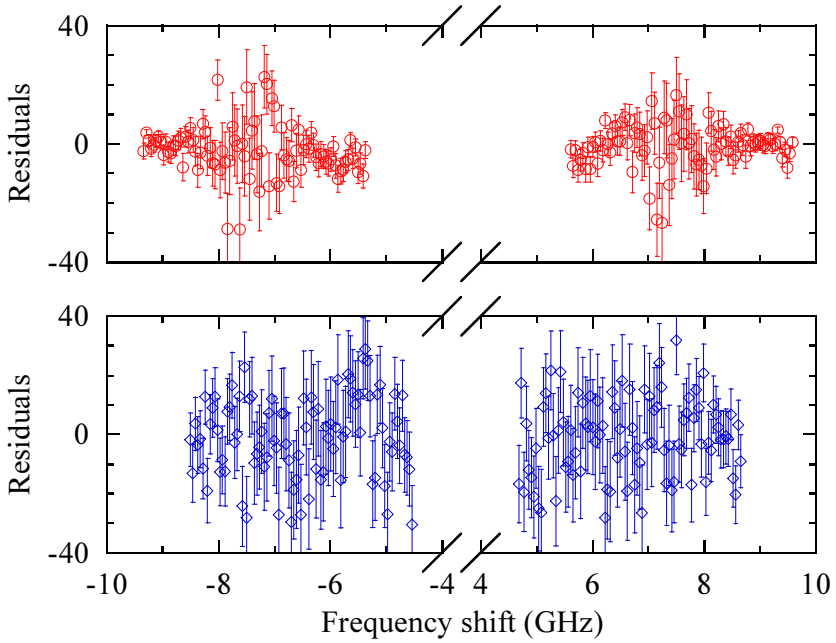

Figure 5.8: Residuals of the fits based on Eq. 2 of the main text to the experimental spectra shown in Fig. 2B of the main text for homogenized sample 1 at 140°C (top) and −12°C (bottom). The error bars are the square root of the photon counts at each frequency. The data for −12°C were not rescaled (in contrast to Fig. 2B of the main text).

over a one month period, with many thermal cycling of the samples, and also indifferently after heating or cooling. This illustrates the reproducibility of the results. We have also performed repeated measurements under the same conditions on a sample similar to sample 2, but containing salty water. We gathered 5 measurements at −10°C and 4 measurements at −15°C. The relative standard deviation of the sound velocity for each group of data is 4.6 and 3,5 $\mathrm{m\,s^{-1}}$, respectively, which is even less than the 6 $\mathrm{m\,s^{-1}}$ used for the error bar. The uncertainty given by the non-linear fitting procedure on the sound velocity is also always less than 6 $\mathrm{m\,s^{-1}}$, except for three of the four lower temperature points for sample 2. These exceptions comes from a low number of photon counts in the corresponding spectra, due in particular to the extremely small size of sample 2. For these points (for which the reduced χ^2 of the fit remains less than 2), the 6 $\mathrm{m\,s^{-1}}$ error bar was replaced by the uncertainty on the fit parameter, which amounted to at most 7,8 $\mathrm{m\,s^{-1}}$.

Finally, we discuss the statistical confidence we can have about the minimum in sound velocity versus temperature along the isochore at ρ_1. The data points at the six lowest temperatures are in an order such that the

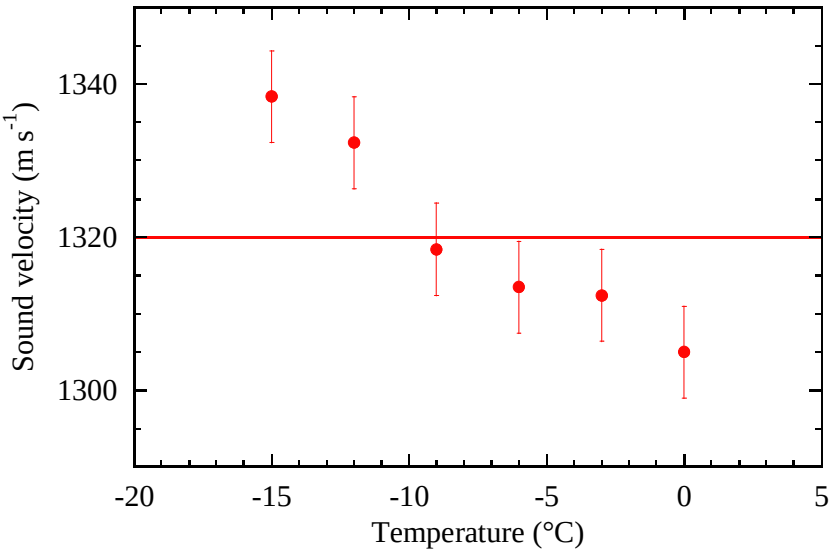

Figure 5.9: Sound velocity at low temperature for the homogenized sample 1. The red line is an attempt to fit the data with a constant. It yields $c = 1320\,\mathrm{m\,s^{-1}}$, but an unreasonably high reduced $\chi^2 = 4{,}55$.

sound velocity decreases with increasing temperature. At higher temperature it clearly increases with temperature. Can this be due to a statistical fluctuations of the measured values? The limiting case would be that the sound velocity reaches a plateau. Hence an attempt was made to fit the data at the six lowest temperatures with a constant (Fig. 5.9).

The fit gives $1320\,\mathrm{m\,s^{-1}}$, but an unreasonably high reduced $\chi^2 = 4{,}55$. To check the significance of this value, we have simulated $2^{20} = 1048576$ series of 6 points, picked up from a Gaussian distribution with mean value $1320\,\mathrm{m\,s^{-1}}$ and standard deviation $6\,\mathrm{m\,s^{-1}}$. Only in 453 occurrences (0,043 %) does the reduced χ^2 exceed 4,5. Only in 1450 occurrences (0,14 %) are the 6 data in descending order, and among these, only 1 has a reduced χ^2 above 4,5. We conclude that the minimum in sound velocity versus temperature along the isochore at ρ_1 is observed with more than 99,8 % confidence.

IAPWS equation of state

The International Association for the Properties of Water and Steam (IAPWS) provides useful releases on the properties of water for general and scientific use. The equation of state (EoS) is given by a multi-parameter formulation for the Helmholtz free energy[1,2]. The Helmholtz free energy is separated in two parts, an ideal-gas part and a residual part. The latter

is fitted to a comprehensive set of experimental data (thermal properties of the single-phase region and of the vapor-liquid phase boundary, specific isochoric heat capacity, specific isobaric heat capacity, speed of sound, differences in the specific enthalpy and in the specific internal energy, Joule-Thomson coefficient, and isothermal throttling coefficient). It is stated that this formulation is 'valid in the entire stable fluid region of H_2O from the melting-pressure curve to 1273 K at pressures up to 1000 MPa', and that it 'represents the currently available experimental data of the subcooled liquid (solid-liquid metastable region) and of the superheated liquid (liquid-gas metastable region) to within the experimental uncertainty'. The sound velocity can be computed using appropriate derivatives. A comparison showing the agreement between the calculated sound velocity and experimental data on supercooled water at ambient pressure is given in Fig. 7 of Ref.[5]. The saturation properties of water, including the density along the liquid-vapor binodal, are also available[3].

Water purity

Water in natural and synthetic fluid inclusions may contain salt[6,7], although Raman scattering studies show that fluid inclusions can be synthesized with a negligible salt content[7,8]. Dissolved salts will lower the melting point of the frozen samples. It has been shown[6] that the measurement of the melting point depression gives a value for the salt content consistent with the value obtained using Raman scattering from the liquid. Water in samples 1 and 2 melt at 0,1 and 0,3°C, respectively, which is consistent with pure water given the uncertainty of the stage (0,15°C) and the difficulty to detect changes of phase in sample 2 due to its small size. We also note that water in our simulations is pure, and give results consistent with our measurements; it would be surprising that this is the case if samples 1 and 2 contained impure water. As a further test of water purity, we have measured the sound velocity in fluid inclusions as a function of temperature when a bubble is present. Figure 5.10 compares the results with our measurements on a simple ultrapure (Millipore Direct Q3 UV) free water droplet and with literature data. All results agree within the error bars. Figure 5.10 also displays the sound velocity along the binodal for several aqueous NaCl solutions. They are clearly higher than the measured values. Taking the error bars into account, we conclude that water in the inclusions studied has a purity greater than 99.8 mole percent, even higher than the samples studied in Ref.[7].

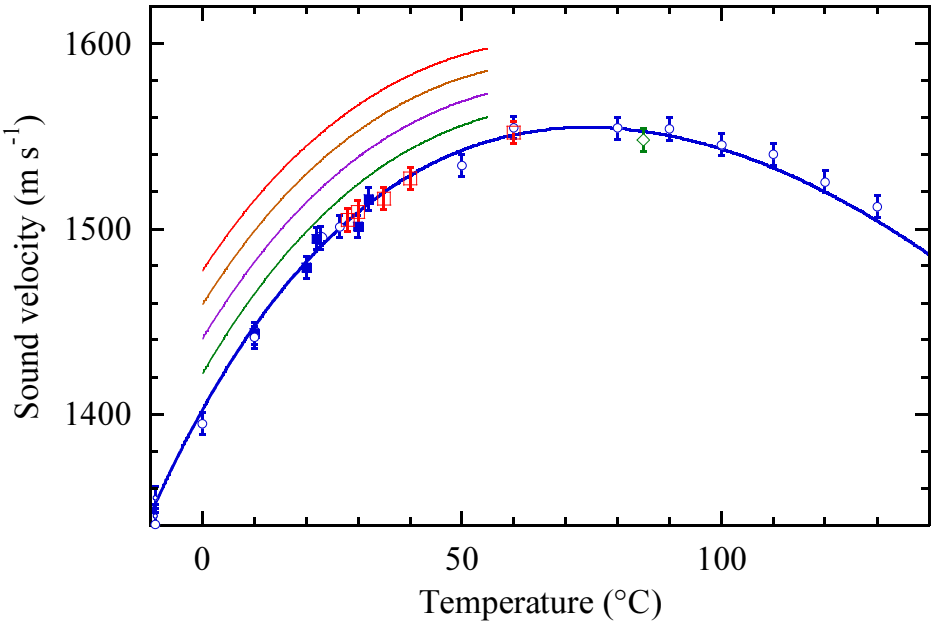

Figure 5.10: Sound velocity versus temperature along the liquid-vapor equilibrium. The symbols show our Brillouin measurements for sample 1 (open blue circles), sample 2 (open green diamond), another fluid inclusion from the same quartz crystal as sample 2 (open red squares), and an ultrapure (Millipore Direct Q3 UV) water droplet deposited on glass slide (filled blue squares). The three symbol sizes correspond to three pinhole sizes on the spectrometer. The blue curve is the literature value for pure water[1,2,3], and the other curves illustrate the shift in sound velocity due to dissolved NaCl, measured at 0,1 MPa (ref.[15]). The salt molality increases from bottom to top: 0.25 (green), 0.5 (purple), 0.75 (brown), and 1 (red).

Discussion of possible artefacts

In this section, we consider other possible explanations of the experimental results.

First, we question the validity of the isochoric assumption. In platelet-like inclusions, Alvarenga *et al.*[8] have shown that the inclusion walls could collapse when submitted to large tensions, thus increasing the density in comparison to the isochore. However, our inclusions are not platelet-like and a simple density effect could not explain the values of sound velocity above the binodal observed at low temperature. Indeed, the density cannot become higher than the binodal, because the inclusion would then experience positive pressures, and any deformation would yield densities lower than the isochore density.

One could also argue that a phase transition occurs inside the inclusion. If the new phase had a low density, the density of the liquid in equilibrium would increase, thus yielding a sound velocity larger than expected. At the given thermodynamics conditions, the most natural candidate for the new phase would be hexagonal ice. But at $-12°C$, the ice-liquid equilibrium occurs at $+128\,MPa$ and the sound velocity of the liquid would be around $1575\,m\,s^{-1}$[2]), much higher than the largest measured value, $1414\,m\,s^{-1}$ for sample 2. To get a lower sound velocity for the liquid, one should think of a new phase having higher density than hexagonal ice. This also excludes cubic ice, the only other crystal that could be found in this region of the phase diagram. Therefore, one could recur to another liquid phase, which would appear if we had actually crossed a liquid-liquid transition (LLT). This would require the LLT to be at negative pressure, which has been already found in a few simulations[9,10,11] (see however Ref.[12]) and proposed for some models[13,14]. However, in our experimental measurements, we did not see the two other Brillouin peaks that would come from the low density liquid, and we did not find any hysteresis between measurements taken after heating or cooling. A possibility remains that the Brillouin shifts of the two liquids are too close to be seen with the resolution of our setup. But another difficulty arises: to explain why the sound velocity in both samples rises above the binodal, one would require the LLT to lie at positive pressure at $-12°C$. Undoubtedly, this should have been seen in the numerous experiments performed in this region. Therefore, the hypothesis suggesting that a phase transition occurred has also to be discarded.

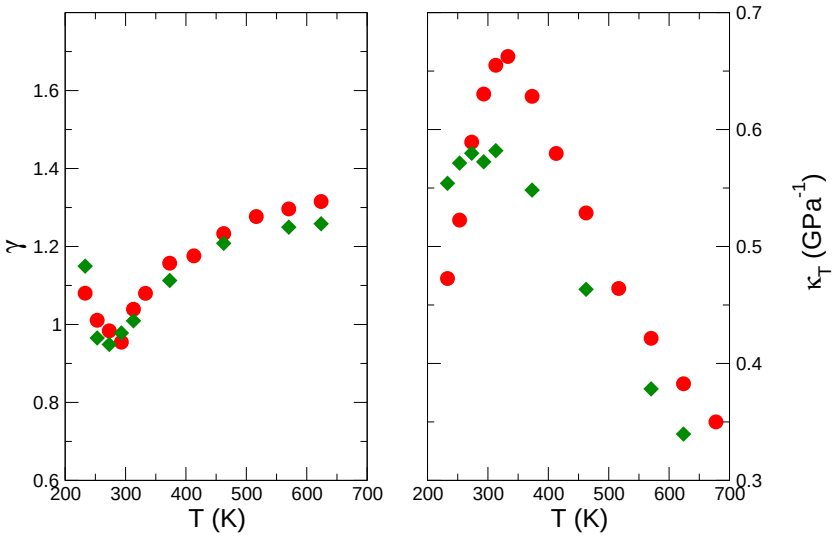

Figure 5.11: Contributions of the adiabatic index (left panel) and the isothermal compressibility (right panel) to the sound velocity along the isochores at $\rho_1 = 933{,}2\,\mathrm{kg\,m^{-3}}$ (red circles) and $\rho_2 = 952{,}5\,\mathrm{kg\,m^{-3}}$ (green diamonds).

On the origin of a minimum in the sound velocity

The simulations enable a detailed analysis of the appearance of a minimum in the sound velocity. In Figure 5.11 we represent the values of the adiabatic index γ and of the isothermal compressibility κ_T.

Both quantities show an extremum, a minimum for γ and a maximum for κ_T. Since the sound velocity depends inversely on the latter (Eq. 3 of the main text), both γ and κ_T justify the minimum in the sound velocity. However, the relative variation of the isothermal compressibility along the isochores is sensibly larger than that of the adiabatic index. Thus, κ_T mostly determines the appearance of the minimum in c. Note that, however, below $\simeq -100\,\mathrm{MPa}$, κ_T becomes monotonic along isobars. A minimum is still seen in the temperature variation of the sound velocity for sample 1 because the variation is taken along an isochore (see Fig. 5.11).

Calculation of the pressure

To compute the pressure, we equilibrate the systems in a NVT ensemble, and use the virial expression. Because our TIP4P/2005 simulations and our sound velocity measurements agree well for both isochores studied, the pressure calculated in the simulations gives a reasonable estimate of the actual pressure reached in the samples. Figure 5.12 shows the pressure as a

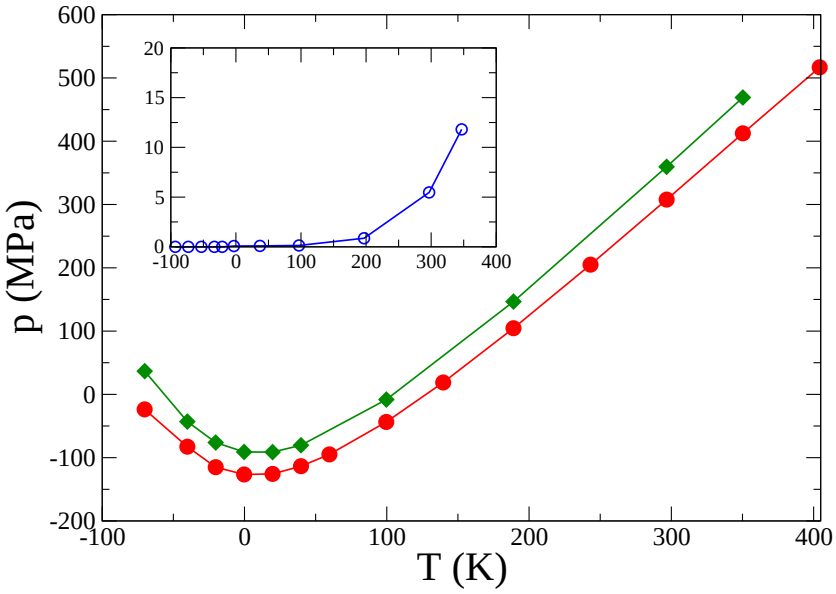

Figure 5.12: Pressure versus temperature for the isochores at ρ_1 (red circles) and ρ_2 (green diamonds) and the binodal (open blue circles, inset).

function of temperature along the two isochores ρ_1 and ρ_2 and the binodal.

The values of the pressure and temperature along isochore ρ_1 are represented in Table S2 and along isochore ρ_2 in Table S3.

Table 5.2: Pressure versus temperature for the isochore ρ_1

T (K)	Pressure (MPa)	T (K)	Pressure (MPa)
202.99	-23.6878	372.82	-43.548
232.99	-82.688	412.82	18.840
252.90	-115.014	462.19	104.560
272.90	-126.520	516.37	205.019
292.87	-125.604	569.85	307.850
312.87	-113.452	623.41	412.515
332.85	-94.878	677.41	516.803

Table 5.3: Pressure versus temperature for the isochore ρ_2

T (K)	Pressure (MPa)	T (K)	Pressure (MPa)
203.01	36.719	312.88	-80.366
233.01	-42.996	372.85	-8.192
252.91	-76.043	462.19	146.632
272.90	-90.980	569.84	359.583
292.89	-91.243	623.41	469.163

Bibliografía

1. Wagner, W. (2002) The IAPWS formulation 1995 for the thermodynamic properties of ordinary water substance for general and scientific use. *Journal of Physical and Chemical Reference Data* **31**, 387–535.

2. The International Association for the Properties of Water and Steam. (2009) Revised release on the IAPWS formulation 1995 for the thermodynamic properties of ordinary water substance for general and scientific use.

3. The International Association for the Properties of Water and Steam. (1992) Revised supplementary release: saturation properties of ordinary water substance, september 1992.

4. Bencivenga, F, Battistoni, A, Fioretto, D, Gessini, A, Sandercock, J. R, & Masciovecchio, C. (2012) A high resolution ultraviolet brillouin scattering set-up. *Review of Scientific Instruments* **83**, 103102.

5. Holten, V, Bertrand, C. E, Anisimov, M. A, & Sengers, J. V. (2012) Thermodynamics of supercooled water. *The Journal of Chemical Physics* **136**, 094507–094507–18.

6. Green, J. L, Durben, D. J, Wolf, G. H, & Angell, C. A. (1990) Water and solutions at negative pressure: Raman spectroscopic study to -80 megapascals. *Science* **249**, 649–652.

7. Zheng, Q, Durben, D. J, Wolf, G. H, & Angell, C. A. (1991) Liquids at large negative pressures: water at the homogeneous nucleation limit. *Science* **254**, 829–832.

8. Alvarenga, A. D, Grimsditch, M, & Bodnar, R. J. (1993) Elastic properties of water under negative pressures. *J. Chem. Phys.* **98**, 8392–8396.

9. Tanaka, H. (1996) Phase behaviors of supercooled water: Reconciling a critical point of amorphous ices with spinodal instability. *J. Chem. Phys.* **105**, 5099–5111.

10. Brovchenko, I, Geiger, A, & Oleinikova, A. (2005) Liquid-liquid phase transitions in supercooled water studied by computer simulations of various water models. *J. Chem. Phys.* **123**, 044515.

11. Brovchenko, I & Oleinikova, A. (2008) Multiple phases of liquid water. *ChemPhysChem* **9**, 2660–2675.

12. Liu, Y, Panagiotopoulos, A. Z, & Debenedetti, P. G. (2009) Low-temperature fluid-phase behavior of ST2 water. *The Journal of Chemical Physics* **131**, 104508.

13. Angell, C. A. (2008) Insights into phases of liquid water from study of its unusual glass-forming properties. *Science* **319**, 582–587.

14. Stokely, K, Mazza, M. G, Stanley, H. E, & Franzese, G. (2010) Effect of hydrogen bond cooperativity on the behavior of water. *Proceedings of the National Academy of Sciences* **107**, 1301–1306.

15. Chen, C.-T, Chen, L.-S, & Millero, F. J. (1978) Speed of sound in NaCl, $MgCl_2$, Na_2SO_4, and $MgSO_4$ aqueous solutions as functions of concentration, temperature, and pressure. *The Journal of the Acoustical Society of America* **63**, 1795–1800.

16. Speedy, R. J & Angell, C. A. (1976) Isothermal compressibility of supercooled water and evidence for a thermodynamic singularity at -45°C. *J. Chem. Phys.* **65**, 851–858.

17. Speedy, R. J. (1982) Stability-limit conjecture. an interpretation of the properties of water. *J. Phys. Chem.* **86**, 982–991.

18. Poole, P. H, Sciortino, F, Essmann, U, & Stanley, H. E. (1992) Phase behaviour of metastable water. *Nature* **360**, 324–328.

19. Sciortino, F, Poole, P. H, Essmann, U, & Stanley, H. E. (1997) Line of compressibility maxima in the phase diagram of supercooled water. *Phys. Rev. E* **55**, 727–737.

20. Xu, L, Kumar, P, Buldyrev, S. V, Chen, S. H, Poole, P. H, Sciortino, F, & Stanley, H. E. (2005) Relation between the widom line and the dynamic crossover in systems with a liquid–liquid phase transition. *Proceedings of*

the National Academy of Sciences of the United States of America **102**, 16558-16562.

21. El Mekki Azouzi, M, Ramboz, C, Lenain, J.-F, & Caupin, F. (2013) A coherent picture of water at extreme negative pressure. *Nat Phys* **9**, 38–41.

22. Debenedetti, P. G. (2003) Supercooled and glassy water. *Journal of Physics: Condensed Matter* **15**, R1669–R1726.

23. Poole, P, Sciortino, F, Grande, T, Stanley, H, & Angell, C. (1994) Effect of hydrogen bonds on the thermodynamic behavior of liquid water. *Phys. Rev. Lett.* **73**, 1632–1635.

24. Zheng, Q, Green, J, Kieffer, J, Poole, P. H, Shao, J, Wolf, G. H, & Austen Angell, C. (2002) in *Liquids Under Negative Pressure*, NATO Science Series, eds. Imre, A. R, Maris, H. J, & Williams, P. R. (Springer Netherlands) Vol. 84, pp. 33–46.

25. Sastry, S, Debenedetti, P. G, Sciortino, F, & Stanley, H. E. (1996) Singularity–free interpretation of the thermodynamics of supercooled water. *Physical Review E* **53**, 6144-6154.

26. Liu, D, Zhang, Y, Chen, C.-C, Mou, C.-Y, Poole, P. H, & Chen, S.-H. (2007) Observation of the density minimum in deeply supercooled confined water. *Proceedings of the National Academy of Sciences* **104**, 9570–9574.

27. Murata, K.-I & Tanaka, H. (2012) Liquid-liquid transition without macroscopic phase separation in a water-glycerol mixture. *Nature Materials* **11**, 436–443.

28. Caupin, F & Herbert, E. (2006) Cavitation in water: a review. *Comptes Rendus Physique* **7**, 1000–1017.

29. Caupin, F & Stroock, A. D. (2013) in *Liquid polymorphism*, Advances in Chemical Physics, eds. Stanley, H. E & Rice, S. (Wiley, New York) No. 152.

30. Shmulovich, K. I, Mercury, L, ThiÃ©ry, R, Ramboz, C, & El Mekki, M. (2009) Experimental superheating of water and aqueous solutions. *Geochimica et Cosmochimica Acta* **73**, 2457–2470.

31. Henderson, S & Speedy, R. (1980) A berthelot–bourdon tube method for studying water under tension. *Journal of Physics E: Scientific Instruments* **13**, 778.

32. Teixeira, J & Leblond, J. (1978) Brillouin scattering from supercooled water. *J. Phyique Lett.* **39**, 83–85.

33. Conde, O, Leblond, J, & Teixeira, J. (1980) Analysis of the dispersion of the sound velocity in supercooled water. *Journal de Physique* **41**, 997–1000.

34. Conde, O, Teixeira, J, & Papon, P. (1982) Analysis of sound velocity in supercooled H2O, D2O, and water–ethanol mixtures. *The Journal of Chemical Physics* **76**, 3747–3753.

35. Maisano, G, Migliardo, P, Aliotta, F, Vasi, C, Wanderlingh, F, & Dárrigo, G. (1984) Evidence of anomalous acoustic behavior from brillouin scattering in supercooled water. *Physical Review Letters* **52**, 1025–1028.

36. Magazu, S, Maisano, G, Majolino, D, Mallamace, F, Migliardo, P, Aliotta, F, & Vasi, C. (1989) Relaxation process in deeply supercooled water by mandelstam–brillouin scattering. *The Journal of Physical Chemistry* **93**, 942–947.

37. Cunsolo, A & Nardone, M. (1996) Velocity dispersion and viscous relaxation in supercooled water. *The Journal of Chemical Physics* **105**, 3911.

38. Netz, P. A, Starr, F. W, Stanley, H. E, & Barbosa, M. C. (2001) Static and dynamic properties of stretched water. *The Journal of Chemical Physics* **115**, 344.

39. Yamada, M, Mossa, S, Stanley, H. E, & Sciortino, F. (2002) Interplay between time–temperature transformation and the liquid–liquid phase transition in water. *Phys. Rev. Lett.* **88**, 195701.

40. Abascal, J. L. F & Vega, C. (2005) A general purpose model for the condensed phases of water: TIP4P/2005. *The Journal of Chemical Physics* **123**, 234505.

41. Vega, C & Abascal, J. L. F. (2011) Simulating water with rigid non–polarizable models: a general perspective. *Physical Chemistry Chemical Physics* **13**, 19663–19688.

42. Abascal, J. L. F & Vega, C. (2011) Note: Equation of state and compressibility of supercooled water: Simulations and experiment. *The Journal of Chemical Physics* **134**, 186101.

43. Vega, C, Abascal, J. L. F, & Nezbeda, I. (2006) Vapor–liquid equilibria from the triple point up to the critical point for the new generation of TIP4P–like models: TIP4P/Ew, TIP4P/2005, and TIP4P/ice. *The Journal of Chemical Physics* **125**, 034503.

44. Hare, D. E & Sorensen, C. M. (1987) The density of supercooled water. II. bulk samples cooled to the homogeneous nucleation limit. *The Journal of Chemical Physics* **87**, 4840–4845.

45. Ohmori, T, Kimura, Y, Hirota, N, & Terazima, M. (2001) Thermal diffusivities and sound velocities of supercritical methanol and ethanol measured by the transient grating method. *Physical Chemistry Chemical Physics* **3**, 3994–4000.

46. Abascal, J. L. F & Vega, C. (2010) Widom line and the liquid-liquid critical point for the TIP4P/2005 water model. *The Journal of Chemical Physics* **133**, 234502.

47. Limmer, D. T & Chandler, D. (2013) The putative liquid–liquid transition is a liquid-solid transition in atomistic models of water. II. *The Journal of Chemical Physics* **138**, 214504.

48. Kanno, H, Speedy, R. J, & Angell, C. A. (1975) Supercooling of water to -92°C under pressure. *Science* **189**, 880–881.

49. Mishima, O & Stanley, H. E. (1998) The relationship between liquid, supercooled and glassy water. *Nature* **396**, 329–335.

50. Boon, J. P & Yip, S. (1980) *Molecular Hydrodynamics*. (Courier Dover Publications).

51. The International Association for the Properties of Water and Steam. (1997) Release on the refractive index of ordinary water substance as a function of wavelength, temperature and pressure.

52. Bencivenga, F, Cimatoribus, A, Gessini, A, Izzo, M. G, & Masciovecchio, C. (2009) Temperature and density dependence of the structural relaxation time in water by inelastic ultraviolet scattering. *The Journal of Chemical Physics* **131**, 144502.

53. Aragones, J. L & Vega, C. (2009) Plastic crystal phases of simple water models. *The Journal of chemical physics* **130**, 244504.

54. Conde, M. M, Vega, C, Tribello, G. A, & Slater, B. (2009) The phase diagram of water at negative pressures: Virtual ices. *The Journal of chemical physics* **131**, 034510.

55. Aragones, J. (2011) Phase diagram of water under an applied electric field. *Phys. Rev. Lett.* **107**.

56. Vega, C, Abascal, J. L. F, Conde, M. M, & Aragones, J. L. (2008) What ice can teach us about water interactions: a critical comparison of the performance of different water models. *Faraday Discuss.* **141**, 251–276.

57. Aragones, J. L, MacDowell, L. G, & Vega, C. (2011) Dielectric constant of ices and water: A lesson about water interactions. *Journal of Physical Chemistry A* **115**, 5745.

58. Hess, B, Kutzner, C, van der Spoel, D, & Lindahl, E. (2008) GROMACS 4: Algorithms for highly efficient, load–balanced, and scalable molecular simulation. *J. Chem. Theory Comput.* **4**, 435–447.

59. Van Der Spoel, D, Lindahl, E, Hess, B, Groenhof, G, Mark, A. E, & Berendsen, H. J. C. (2005) GROMACS: fast, flexible, and free. *Journal of Computational Chemistry* **26**, 1701–1718.

60. Essmann, U, Perera, L, Berkowitz, M. L, Darden, T, Lee, H, & Pedersen, L. G. (1995) A smooth particle mesh ewald method. *The Journal of Chemical Physics* **103**, 8577–8593.

61. Hess, B. (2008) P–LINCS: a parallel linear constraint solver for molecular simulation. *J. Chem. Theory Comput.* **4**, 116–122.

62. Bussi, G, Donadio, D, & Parrinello, M. (2007) Canonical sampling through velocity rescaling. *The Journal of Chemical Physics* **126**, 014101.

63. Parrinello, M & Rahman, A. (1981) Polymorphic transitions in single crystals: A new molecular dynamics method. *Journal of Applied Physics* **52**, 7182–7190.

64. Shevchuk, R & Rao, F. (2012) Note: Microsecond long atomistic simulation of supercooled water. *The Journal of Chemical Physics* **137**, 036101.

Results: Chapter 6

Homogeneous bubble nucleation in water at negative pressure: A Voronoi polyhedra analysis

Jose L. F. Abascal, **Miguel A. González**, *Juan L. Aragones and C. Valeriani*

Departamento de Química Física, Facultad de Ciencias Químicas, Universidad Complutense de Madrid, 28040 Madrid, Spain.

6.1. Abstract

We investigate vapor bubble nucleation in metastable TIP4P/2005 water at negative pressure via the Mean First Passage Time (MFPT) method using the volume of the largest bubble as a local order parameter. We identify the bubbles in the system by means of a Voronoi-based analysis of the Molecular Dynamics trajectories. By comparing the features of the tessellation of liquid water at ambient conditions to those of the same system with an empty cavity we are able to discriminate vapor (or interfacial) molecules from the bulk ones. This information is used to follow the time evolution of the largest bubble until the system cavitates at 280 K above and below the spinodal line. At the pressure above the spinodal line, the MFPT curve shows the expected shape for a moderately metastable liquid from which we estimate the bubble nucleation rate and the size of the critical cluster. The nucleation rate estimated using Classical Nucleation Theory turns out to be about 8 order of magnitude lower than the one we compute by means of MFPT. The behavior at the pressure below the spinodal line, where the liquid is thermodynamically unstable, is remarkably different, the MFPT curve being a monotonous function without any inflection point.

6.2. Introduction

Bubble nucleation is a widespread phenomenon in our daily life, relevant to processes such as explosive boiling[1] and sonochemistry[2]. Despite its technological relevance, the mechanism of nucleation of vapor bubbles from homogeneous metastable liquids is still not entirely understood. Classical Nucleation Theory (CNT) is usually employed to predict the nucleation rate, both in bubble nucleation and in vapor condensation experiments. Early measurements of vapor condensation estimated nucleation rates consistent with the CNT predictions.[3] Regarding bubble nucleation, measurements on different materials[4,5,6,7,8,9,10,11] have shown that, even though Classical Nucleation Theory correctly predicts the temperature dependence of the bubble nucleation rate, it yields nucleation rates that are too low at the lowest temperatures. Delale et al.,[12] using a phenomenological estimate of the minimum work of bubble formation, computed the steady-state bubble nucleation rate and found that, as with the CNT estimates, there was a large discrepancy between the computed and measured bubble-nucleation rates. Recently, El Mekki Azouzi et al.[13], performing experiments of liquid water under large mechanical tension, used the cavitation statistics to get the free-energy barrier. The authors observed that both the free energy and the volume of the critical bubble were well described by CNT whereas the surface tension was reduced.

From a theoretical and numerical point of view, Zeng and Oxtoby[14] used Density Functional Theory to estimate the bubble nucleation rate in a super-heated Lennard Jones system and concluded that CNT underestimated the nucleation rate by more than 15 orders of magnitude. One reason for it was that CNT neglects curvature corrections to the surface free-energy of the bubble[15]. By means of a DFT constrained method and molecular simulations, Uline and coworkers studied bubble nucleation in a super-heated Lennard-Jones liquid[16,17] and found that cavities play an important role in the initial stages of the liquid-to-vapor transition: when cavities are small, the superheated liquid is thermodynamically stable whereas when cavities becomes too large, the liquid is unstable. The locus of instabilities is the free-energy surface of bubble formation represented as a function of the number of particles inside a bubble of a given volume. In 1999, Shen and Debenedetti[18] performed a computer simulation study of bubble nucleation from a metastable super-heated Lennard Jones system. Using the vapor density as a global order parameter, they found that the critical nucleus was a large system-spanning cavity, in contrast to the spherical cluster predicted with CNT. Later on, Wang et al[19] reported a Molecular Dynamic study of homo-

geneous bubble nucleation for the same Lennard-Jones fluid. Using Forward Flux Sampling and the volume of the largest bubble as a local order parameter, they computed the bubble nucleation rate at a given super-heating and obtained $10^{-22}\sigma^{-3}\tau^{-1}$. At the same conditions, the CNT estimate could vary from $10^{-22}\sigma^{-3}\tau^{-1}$ to $10^{-36}\sigma^{-3}\tau^{-1}$, depending on the value of the interfacial tension (whether obtained from MD or DFT calculations) used to estimate the free-energy barrier height. The authors also observed that local temperature fluctuations correlated strongly with bubble formation (mechanism not taken into account in CNT) and that, contrary to Ref.[18], cavitation started from compact bubbles. Recently, Meadley and Escobedo[20] studied the same Lennard Jones metastable fluid, undergoing not only super-heating but also over-stretching (negative pressure). The authors used several rare-event numerical techniques and both a local (the volume of the largest bubble) and a global order parameter (the global vapor density) to follow the liquid to vapor phase transition and estimated the nucleation rate and the free-energy barrier. They found that the free-energy barrier was higher when projected over the bubble volume rather than over the vapor density and concluded that the former was a more ideal reaction coordinate. When analyzing the shape of the growing vapor bubble, they observed bubbles with non-spherical shapes and irregular and undulating surfaces.

In contrast to the work done to unravel the bubble nucleation mechanism in simple fluids (such as Lennard Jones), little effort has been made so far to understand the mechanism behind the liquid to vapor transition in molecular liquids such as water. The goal of the present manuscript is to study bubble nucleation in numerical simulations of TIP4P/2005 water at negative pressures using the size of the largest bubble as a local order parameter. The bubble volume is obtained by means of a Voronoi-based algorithm. Knowing the location of the spinodal line for TIP4P/2005 water at negative pressures,[21] we study bubble nucleation for two state points located, respectively, slightly above and below the spinodal. In both cases the system cavitated spontaneously. Therefore, the *Mean First Passage Time* (MFPT) method[22,23] seemed to be adequate to compute the bubble nucleation rate and to estimate the volume of the critical bubble. MFPT has been successfully applied to study liquid condensation from metastable vapor in a Lennard-Jones system[24,25] and from metastable TIP4P/2005 water[26]. The application of the MFPT technique to bubble nucleation ultimately relies in the investigation of the time evolution of the bubble growth. The detection of bubbles in computer generated configurations of a metastable liquid is more complex than it may appear at first. A number of procedures have been proposed to distinguish liquid-like from vapor-like particles.[27,28,29] A bubble is a region of vapor within the liquid and since the vapor is much less dense

than the liquid (except in the vicinity of the critical point), in principle, one might think of a bubble as a “voidregion. Given the small size of the bubble, it is difficult to know to what extent the interface affects the structure of the vapor molecules. The problem is more complex for a network forming liquid such as water whose structure is not determined exclusively by packing effects since the hydrogen bond network is a structure with many voids. Because of this, the fixed cutoff criterion of Ref.[30] which has been successfully employed in the analysis of the condensation of a metastable Lennard-Jones vapor might not work in the case of water. We thus face a challenging geometrical problem.

The procedure to tag the molecules as either liquid or vapor may be performed in three steps: *1)* A partition of the space between the molecules into regions, *2)* An assignment of each region as belonging to a "vapor"(or interfacial) or a liquid molecule, and *3)* A clustering of the vapor molecules into bubbles. To solve the first step, the Voronoi (also known as Dirichlet) tessellation is a natural choice leading to an unambiguous partition of the system. The Voronoi construction is a partition of the space based on the distance to a set of points. Each region contains exactly one generating point and every point in a given region is closer to its generating point than to any other. The Voronoi tessellation has been found useful in many scientific and technical applications.[31,32,33,34] When the space is Euclidean and the set of points are physical or chemical particles, it allows to univocally assign a given region to every particle —a polygon in 2D and a polyhedron in 3D— thus providing structural information of the system. To our knowledge, the first application of the tessellation to elucidate the structure of a chemical-physics system was done by Bernal in 1964.[35] Since then a number of studies have used the Voronoi tessellation to investigate the structure of fluids, glasses and solids.[36,37,38,39,40,41,42,43,44,45,46,47] Other typical examples of the utility of the Voronoi construction are the analysis of solvation shells,[48,49,50,51] clustering and chemical association.[38,52,53,54] The Voronoi construction has also been employed to define the interface between two systems[55,56,57] and to obtain structural information of pure water.[58,59,60,61,62,52,63,64] and water solutions[38,65,66,67,68,69,70,71] More closely related with the goals of this work is its application to detect different types of cavities such as pores, pockets, clefts, channels and docking sites.[72,73,74,52,75,76,77,78,79,80,81] In fact, Fern *et al.*[82] have already used the Voronoi tessellation as a tool for distinguishing whether a particle belongs to a condensed or vapor phase in two-phase simulations of ethanol.

The Voronoi tessellation can be performed trivially in crystalline systems but it becomes increasingly complex in disordered systems.[37,38,83,84,79] In fact, when the system is strongly heterogeneous (as is the case of bub-

bles within a metastable liquid) many algorithms fail. In this work we use an algorithm especially designed to deal with inhomogeneous fluids which has been successfully applied to interpret the structure of quenched liquids[37] and electrolyte solutions.[38] Once the tessellation is done, the properties of the Voronoi polyhedra (VP) associated to each particle can be used to distinguish between liquid and vapor molecules. The choice of the parameters that denote a molecule as belonging to the vapor phase is somewhat arbitrary. Therefore, as a test case, we have investigated the properties of a system consisting of liquid water with an artificially created spherical cavity. Once the vapor molecules are identified with the Voronoi construction, it is a trivial task to cluster them into one or more bubbles because the Voronoi tessellation directly provides the list of neighbors of each molecule. We then use the volume of the largest bubble as the order parameter and apply the MFPT technique to study the spontaneous bubble nucleation.[22] The analysis of the evolution of the volume of the largest bubble provides the desired relevant features of the nucleation, in particular the nucleation rate and the size (volume) of the critical bubble. In this work we will show that the overall procedure is quite robust and yields a consistent description of the bubble nucleation.

The main drawback of the overall method is that the Voronoi tessellation is far from trivial for highly inhomogeneous systems. We have thus dedicated a section to describe the algorithm used for the tessellation and another one to investigate what are the relevant parameters of the tessellation that enable us to track down the bubble growth. The paper is organized as follows. Section II describes some methodological issues, in particular, the algorithm employed for the Voronoi construction and a brief description of the simulations. Section III analyzes which are the relevant parameters of the Voronoi Polyhedra that allow to detect a bubble within metastable liquid water. Finally, section IV reports the application of the MFPT technique to two state points, one above and the other below the liquid- vapor spinodal line of TIP4P/2005 water.

6.3. Methods

6.3.1. Algorithm used for the Voronoi tessellation

The Voronoi tessellation involves the calculation of the intersection of the planes normal to the line joining a given particle with the remaining ones. Usually, in simple liquids, the number of Voronoi neighbors is less than twenty. It is then a waste of resources evaluating the normal planes for all

particles in the system. Thus, it is customary to perform the calculations for a reduced set of particles, the so called çandidate neighbors".

The list of candidate neighbors of each particle is usually obtained using a cutoff radius. This procedure works well for common liquids but fails for inhomogeneous systems[37,38] because some actual Voronoi neighbors are relatively distant from the reference particle. In the case of a bubble some Voronoi neighbors may be found at distances of the order of the bubble diameter so the number of candidate neighbors may well exceed a hundred particles. Thus, it is important to devise a different way to obtain a reliable list of candidate neighbors without the computational cost associated to a very large cutoff. As in Ref.[37], the procedure we follow can be described in few steps.

Step1: First, we obtain a first approximation of each particle's list of Voronoi candidate neighbors. This is done by dividing the system in boxes with the use of a grid, each box being assigned to its closest particle. Therefore, two particles are nearest candidate neighbors if at least two boxes (each box belonging to a particle) are adjacent. Rigorously, this stage of the algorithm only works in the limit of zero thickness grid. Thus, we need to improve this initial list of candidates.

Step 2: To amend the calculated set of candidate neighbors, the atoms sharing a certain number of common neighbors with a given one are recursively added to its list of candidates (see Fig. 6.1). At the end of this stage, we have generated a set of candidates for each particle that hopefully includes all the actual Voronoi neighbors.

Step 3: Having the list of candidate neighbors for all the particles, we proceed with the tessellation using any standard algorithm.[85,86,87,88] For this final third step we choose to use a variation of the Finney's algorithm[86] in order to increase its efficiency (see Ref.[37] for details and a forthcoming paper[89]).

The main advantage of the algorithm is its robustness. However, the large inhomogeneities of our systems have forced us to use it choosing parameters in a conservative way. We have used a 200x200x200 grid and performed the neighbor expansion with a reduced number (6) of common neighbors. In these conditions, the number of actual Voronoi neighbors can be sometimes close to 40. With these parameters, we have been able to analyze all the generated configurations (about $8{\cdot}10^5$ in total) before the system cavitates.

6.3.2. Molecular dynamics simulations

We have carried out 200 independent Molecular Dynamics simulation runs for each of the state points of liquid water at 280 K. One of them, at p=-2250 bar, is above the spinodal line and the other one, at p=-2630 bar,

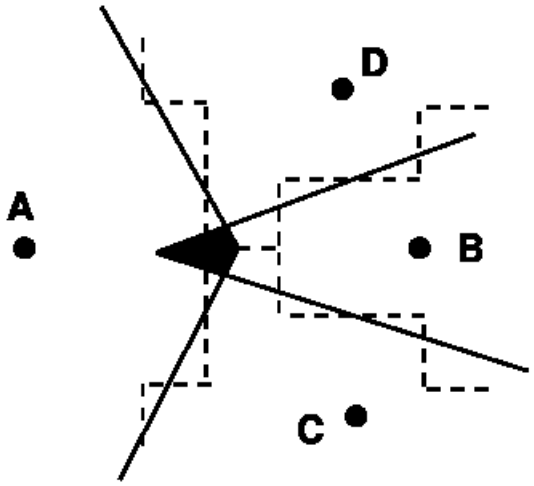

Figure 6.1: Particles A and B have not been identified by the grid as Voronoi neighbours. As a consequence the filled region would be ascribed to both particles (and it would be counted twice). Since A and B have C and D as common neighbors, the expansion of the initial list for A and B to include particles with a given number of common neighbors (see step 2 in the text) would allow to divide the filled volume among A and B.

is below it (recently, a first approach to the spinodal line at low temperatures has been reported for this model[21]). Choosing to simulate the system slightly above the spinodal line corresponds to study homogenous nucleation at thermodynamic conditions where the size of the critical cluster is expected to be relatively small. Given that we need to simulate a system such that the box can easily accommodate the critical bubble, we estimate that, at the chosen supersaturation, this condition is already satisfied when the system consists of 500 molecules. Our choice of a system size of 500 molecules is also supported by Ref.[90], where the authors show that choosing a small system leads to a deviation in the nucleation rate of less than a 10 % (thus saving CPU time).

All simulations have been performed for 500 water molecules in the isothermal-isobaric NpT ensemble using the Molecular Dynamics package GROMACS[91] with a 1 fs timestep. Long range electrostatic interactions have been evaluated with the smooth Particle Mesh Ewald method.[92] The geometry of the water molecules has been enforced using *ad hoc* constraints, in particular, the SHAKE algorithm.[93] Temperature has been set to the desired value with a velocity rescaling thermostat[94] and, to keep the pressure constant, an isotropic Parrinello-Rahman barostat has been applied.[95]

In a preliminary study (data not shown), we have tested that our results are not affected neither by the chosen thermostat (velocity rescaling[94] versus Nose Hoover[97,98]), as previously demonstrated by Ref.[99], nor by the chosen barostat (Parrinello-Rahman[95] versus Berendsen[96]).

The choice of water force field is an important one for comparison with experiment due to the vapour/liquid coexistence and the fact that most water models are parametrized to describe liquid phases better than the vapor phases (the electric dipole moment is enhanced with respect to that of the vapor). We have used the TIP4P/2005 model[100] to describe the interactions between water molecules. This model provides a quantitative account of many water properties,[101,102] including not only the well known thermodynamic anomalies,[103] but also the dynamical ones.[104] Of particular relevance for the purposes of this work is the high quality of the predictions for the vapor-liquid equilibria.[105] It is finally to be mentioned that the TIP4P/2005 model has been successfully used to study the nucleation of liquid droplets within a metastable vapor.[26]

6.4. Voronoi tessellation as a tool for detecting bubbles

6.4.1. Test case: Liquid water with an empty cavity

Our goal is to detect the formation and growth of one or more bubbles within metastable liquid water. Therefore, we need a criterion to distinguish between vapor and liquid particles. Given the density difference between vapor and liquid, a bubble will contain few vapor molecules surrounded by liquid ones. Thus, to a first approximation, a bubble appears as a "void" in the liquid. It is then probably simpler to detect the bubble using the location of the interfacial molecules. To better characterize the interfacial molecules, we analyst the differences between the Voronoi Polyhedra (VP) obtained for a given number of configurations of bulk water at 298 K and 1 bar and the VP computed for the same configurations where we have artificially created an empty spherical cavity by removing 30 water molecules (this approximately corresponds to a 0.6 nm cavity radius and a 0.90-0.95nm^3 volume). Using the Voronoi tessellation, we compute properties such as the VP volume and the non-sphericity parameter (i.e., a measure of the deviation of the Voronoi Polyhedra from a spherical shape). The differences between these properties have to be attributed to the interfacial molecules around the cavity since the remaining particles have exactly the same environment. We may then find what are the VP properties that allow to discriminate interfacial particles

(only present in the system with a cavity) from the bulk ones (common to both systems). We note that the Voronoi tessellations have been done using only the positions of the oxygen atoms.

Figure 6.2 compares the normalized distribution of the VP volumes for a 500 molecules system (470 in the system with the cavity). Clearly, the volume distributions are identical (taken into account the different number of particles in each system) up to a VP volume of about 0.032 nm^3. Larger volumes in the system with the cavity outnumber the corresponding ones in the bulk due to the fact that the tessellation assigns the empty space to the "interfacial"particles. This increase is progressive but, for volumes between 0.032 nm^3 and 0.04 nm^3, it is difficult to label the molecules as either bulk or interfacial based only on this criterion since these volumes appear in more or less similar proportions in both systems. Molecules with VP volumes larger than 0.04 nm^3 are almost inexistent in the bulk system while they represent a small but significant part of the total molecules in the system with a cavity. In order to better distinguish bulk from interfacial

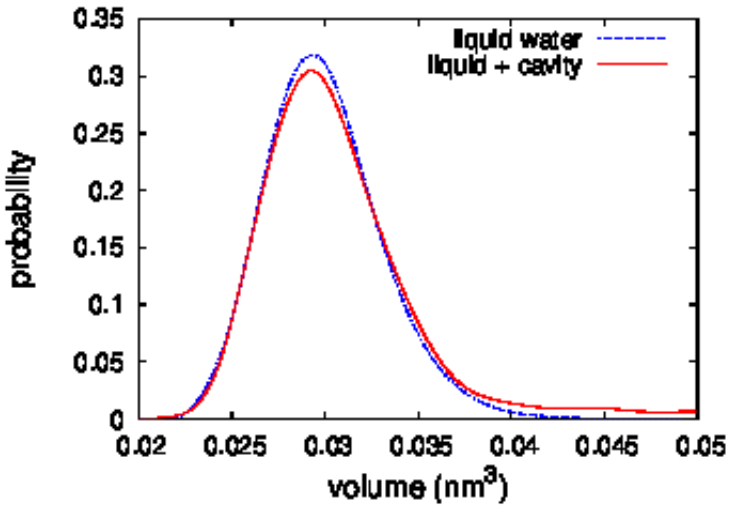

Figure 6.2: Distribution of VP volumes for TIP4P/2005 water at 298 K, 1 bar. The difference between the systems is that in one of them an empty spherical cavity of 30 molecules has been created.

molecules, it seems necessary to use another parameter obtained from the VP tessellation. The non-sphericity (or asphericity) parameter has been widely used for that purpose.[59,62,106,34,107,108,52,64] Sometimes the definition of the Voronoi Polyhedra anisotropy is made in terms of the VP surface and volume but a more rigorous definition should also involve the mean curvature radius.

Thus, we define the nonsphericity parameter, or anisotropic factor α, with the usual expression valid for convex bodies, namely

$$\alpha = RS/3V \tag{6.1}$$

where S and V are the surface and volume of the convex body, respectively, and R the mean curvature radius. In some cases, the geometry of the convex body makes difficult the evaluation of R. This is not the case of a convex polyhedron for which a simple expression allows the calculation of R:

$$R = \frac{1}{8\pi}\Sigma l_i \phi_i \,, \tag{6.2}$$

where the sum extends over polyhedron edges of length l_i and ϕ_i is the angle between the normal vectors to the intersecting faces. These magnitudes are trivially evaluated in the VP tessellation, so a rigorous calculation of α is numerically possible. As a reference, the nonsphericity parameter of a sphere is 1 and the distribution of α for a representative Lennard-Jones liquid has a maximum at about 1.3.[37] The nonsphericity factors of the VP for the

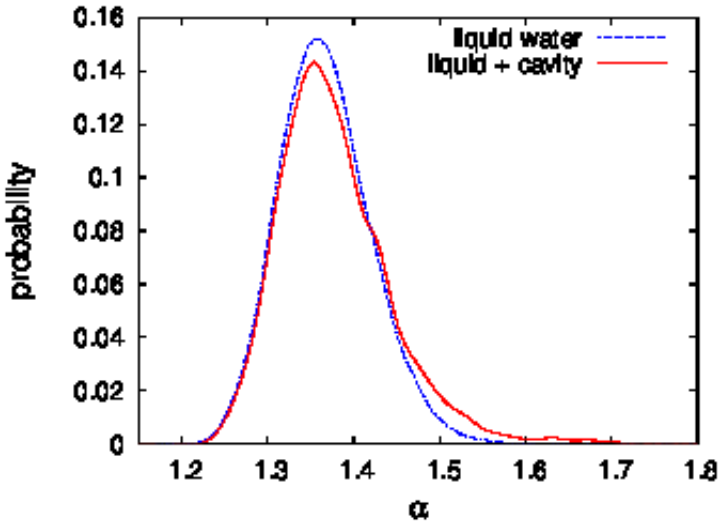

Figure 6.3: Distribution of VP nonsphericity factors for the systems of Fig. 1

liquid and the liquid with a cavity systems are shown in Figure 6.3. The larger anisotropy of the interfacial molecules around the cavity gives rise to a hump in the distribution function. But, similarly to the case of the volume distribution, there is a range of anisotropies (approximately $1{,}4 < \alpha < 1{,}5$) which may correspond to either bulk or interfacial molecules making difficult

to distinguish between them. Only when $\alpha > 1{,}5$ one may be reasonably confident that the nonsphericity parameter represents interfacial molecules.

Therefore, both the VP volume and anisotropy allow to unambiguously characterize only a part of the interfacial molecules, *i.e.,* those with $V > 0{,}40$ nm^3 or $\alpha > 1{,}5$. Thus, we need additional parameters in order to improve the particlesássignment (whether liquid or vapor-like). The VP number of faces has been sometimes proposed as a relevant structural parameter. However this seems not to be the case for water. Figure 6.4 shows that the distribution of faces is quite similar in both systems and does not provide any additional information. It is worth comment that, in liquid water, a non-negligible number of Voronoi Polyhedra has more than 20 faces and this number is over 30 for some interfacial molecules, which explains the difficulties in designing a robust algorithm for the Voronoi tessellation.

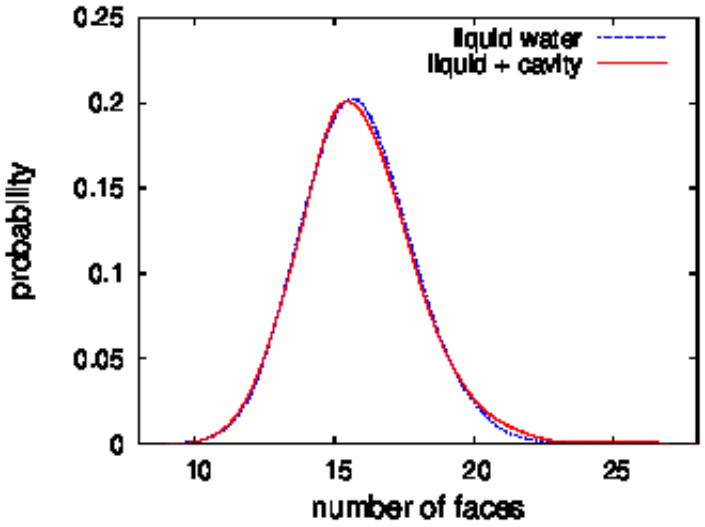

Figure 6.4: Distribution of VP number of faces for the systems of Fig. 1

Since the use of a single parameter, either V or α, does not allow an unequivocal assignment of the interfacial molecules, we suggest to use a correlation of both parameters in order to enhance the ability to detect them. Figure 6.5 represents the values of α for 11 randomly selected configurations plotted against their corresponding volumes. Notice that the points for the liquid system (without cavity) are grouped in a relatively small "pear-shaped-egion of the α-V plane. Most of these points overlap with those of the system with a cavity because they correspond to the common (bulk) molecules. On the right side of the figure appear only points coming from the system with

a cavity. These must be ascribed to the molecules surrounding the cavity (interfacial molecules) because their environments are different in both systems. Therefore, the parameters useful to identify the interfacial molecules

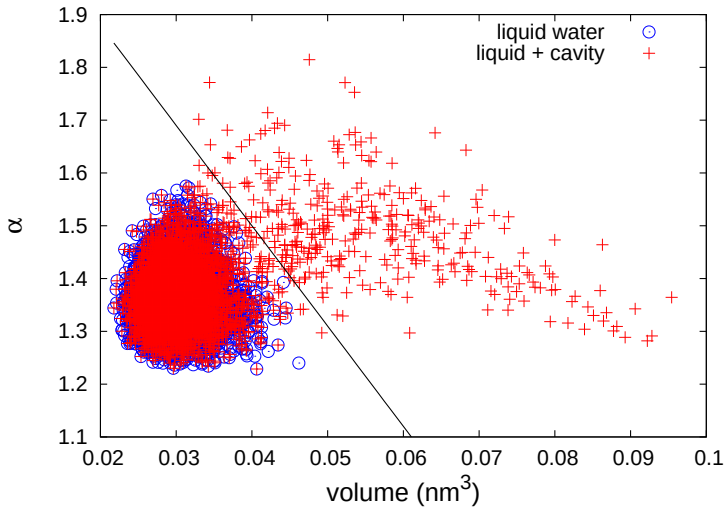

Figure 6.5: Anisotropic factor α as a function of volume for the systems of Fig. 1. The black line $\alpha = 1{,}5 - 19 * (V - 0{,}04)$ separates bulk molecules from interfacial molecules.

are clearly visible in this plot. In the figure we have also traced a straight line ($\alpha = 1{,}5 - 19 * (V - 0{,}04)$) separating two regions: all the liquid-like (bulk) particles lie to the left of the line while most of the points specific of the system with a cavity (interfacial molecules) are on the right side of the line. One could argue that the position of the line could be shifted slightly to the left but we opted for a conservative approach. In fact, the line pivots around the point ($v = 0{,}04$ nm^3, $\alpha = 1{,}5$) which was previously shown to clearly indicate that a particle is interfacial. We also stress that the sample used for the figure is relatively small (only 11 configurations out of about 500 molecules for each system). Plotting a larger number of configurations would imply the appearance of a larger number of molecules with parameters in the right side of the distribution tails (with large values of both volumes and anisotropies), and some among them in the interfacial region. In summary, we recommend a linear combination of the VP volume and anisotropy α to ensure that no bulk particles are tagged as interfacial even if it slightly underestimates the number of the latter. As shown, the use of this parameter is highly discriminating and allows to safely detect most of the interfacial molecules.

The advantage of the analysis of this system is that it allows us to compare the predictions of the Voronoi tessellation with the actual data for the cavity. The calculated average volume of the cavity is 1.70 nm^3, sensibly higher than the cavity volume which is 0.93 nm^3. But the volume of the bubble, as computed with the Voronoi tessellation, also includes the volume occupied by the interfacial molecules which was not taken into account for the cavity's volume. Therefore we must subtract the interfacial volume, that consists of the number of interfacial molecules times the average volume per molecule multiplied by an unknown factor whose value is between from 1/2 and 1. This factor comes from considering two limiting cases. In the former case (1/2), the centers of the interfacial molecules are assumed to be located at the cavity boundary whereas in the latter one (1), the interfacial molecules are tangent to the cavity boundary. If we assume an intermediate factor (3/4) the volume of the cavity calculated using the Voronoi tessellation is 0.98 nm^3, very close to the actual volume of the artificial cavity.

6.4.2. Metastable and unstable water

In this section we analyze the Voronoi tessellation of water in conditions far from the thermodynamic stability. This is performed at two state points at 280 K, one above (-2250 bar) and the other below (-2630 bar) the liquid-vapor spinodal line corresponding to the metastable and unstable regions, respectively. In both cases the system cavitated spontaneously. Figure 6.6 represents the average volume of the system for two independent runs at T=280 K, p=-2250 bar. Notice that the density fluctuations before cavitation takes place are very similar in both runs and that the average volume is essentially constant along the simulations (before cavitation). The resulting average volume per molecule for this state is $\bar{V}$=17.1nm^3. Figure 6.6 also shows that cavitation happens stochastically: although the density fluctuations are akin in both runs, the cavitation times are sensibly different.

Our main goal is to study bubble nucleation from metastable and unstable liquid water using a local order parameter (the volume of the largest bubble) whose construction is based on the Voronoi tessellation. Therefore, as previously shown, we need to define the proper parameters of the Voronoi Polyhedra. This problem differs from that commented in the previous section (detection of a cavity in a liquid) in several aspects. First, the created cavity was static, *i.e.*, the molecules in the liquid configurations had exactly the same positions as those in the system with the cavity. Thus, the VP properties of the molecules far away from the cavity were exactly the same in both systems. This allowed an unequivocal assignment of bulk and interfa-

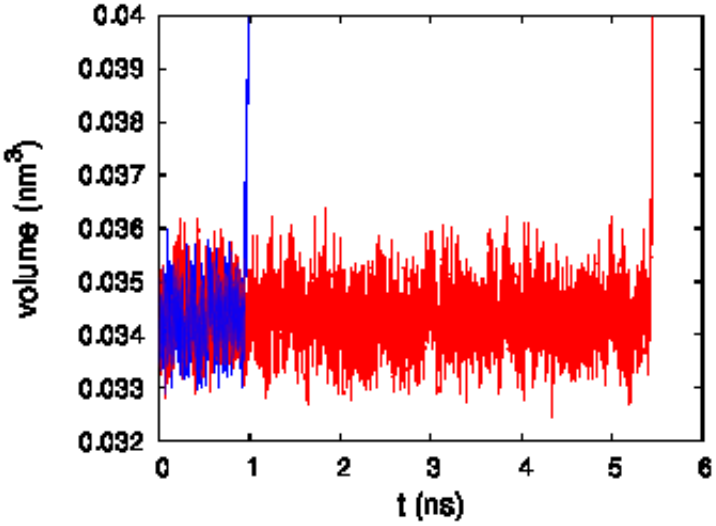

Figure 6.6: Time evolution of the average volume per molecule for two runs of a point in the metastable region (T=280 K, p=-2250 bar). The sharp increase of the volume at the end of the simulations correspond to cavitation events.

cial molecules and enabled us to safely investigate the features of the Voronoi Polyhedra for the latter particles. Bubbles forming in a metastable liquid are not static: they grow (and disappear) until, eventually, the system cavitates. A bubble may differ from an empty cavity because some reconstruction must take place at the interface, and also because of the presence of a small number of vapor molecules inside the bubble (the "cavityïs not empty now). However these vapor molecules should have, by definition, large VP volumes so the conditions imposed to tag a molecule as interfacial will also detect the vapor ones. Despite these differences, we may use the information obtained for the liquid with a cavity in order to interpret the results for metastable water.

A closer look at the differences between the properties of the Voronoi tessellations of liquid water with a cavity and metastable water is shown in Figure 6.7 where we present the distribution of VP volumes. Since the density is different, it seems important to scale the volumes using the average volume of the liquid molecules. In practice, we have applied a factor so that the maximum of the distributions appears at $V/V_0 = 1$. The curves for both systems show minor differences. Firstly, the distribution of volumes is wider for metastable water. Besides, there is a minor but significant difference in the large volumes region: the distribution in metastable water is smooth whereas the cavity gives rise to the appearance of wiggles. This seems to indicate that

the abrupt inhomogeneity of the artificially created cavity is not present in the bubbles whose interface is somewhat blurred. Figure 6.7 illustrates that the analysis made in the previous section may also be acceptable for the detection of bubbles. We only need to scale the parameters in order to account for the differences in the average volume per molecule and the sharpness of the distribution.

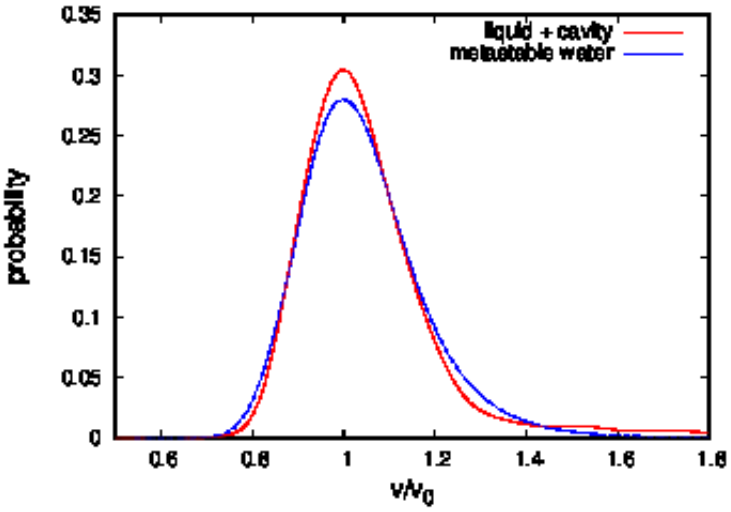

Figure 6.7: Distribution of the reduced VP volumes for metastable water (T=280 K, p=-2250 bar) compared to that of liquid water at ambient conditions with a cavity

In analogy to Fig. 6.5, Figure 6.8 shows the anisotropy of the Voronoi Polyhedra as a function of their volumes for 11 randomly selected configurations of metastable water. For comparison we have also plotted the data for liquid water already shown in Fig. 6.5 but scaled so that the mapping of the distributions is maximized. In accordance, we have also scaled the line separating the interfacial molecules from the liquid molecules obtained for liquid water with a cavity. The line contains the point (V=0.048 nm^3, $\alpha = 1{,}5$) and its slope is 18 nm^{-3}. It can be seen that the region to the left of the straight line for metastable water is very similar to that for liquid water with scaled parameters. This indicates that an analogous criterion (now the straight line $\alpha = 1{,}5 - 18 * (V - 0{,}048)$ shown in Fig. 6.8) may be used in both systems to distinguish the liquid molecules from the interfacial (vapor) ones.

The corresponding plot for water at a pressure (p=-2630 bar) below the spinodal line (unstable water) is shown in Figure 6.9. We have also included the data for liquid water using the same scaling as in Figure 6.8. The bulk

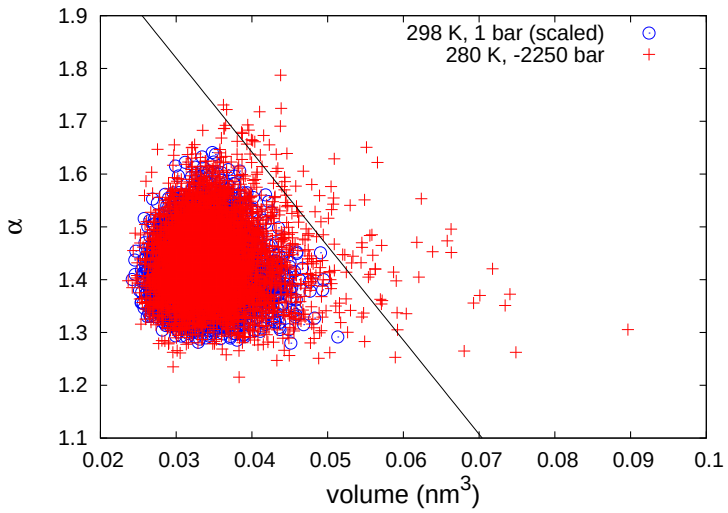

Figure 6.8: Anisotropic factor as a function of volume for metastable water (red crosses) compared to that of liquid water (empty blue circles). The black line $\alpha = 1{,}5 - 18 * (V - 0{,}048)$ separates liquid-like molecules from vapor (interfacial) molecules.

region is again quite similar in both systems but the number of interfacial molecules is much higher for unstable water. Besides, in this case, the high VP volume of some molecules (up to 0.4 nm^3) seem to indicate that the latter are actually vapor molecules (not shown in the figure because, in order to compare with the previous ones, we use the same axes scales in all of the α-V plots).

6.5. Mean first-passage times and nucleation rates

Recently, Wedekind et al.[22] proposed a formalism-the mean first-passage time (MFPT) method-to analyze the kinetics of activated processes (rare events), such as nucleation. In this work we have applied the method to investigate the nucleation rate of bubble formation in metastable water using the volume of the largest bubble as the local order parameter. Bubbles are obtained by clustering together the molecules tagged as vapor (or interfacial following the criteria established in the previous section) that share a common face. Their volumes are the sum of the VP volumes of the particles belonging to a given cluster. Only the largest bubble, *i. e.*, the cluster with

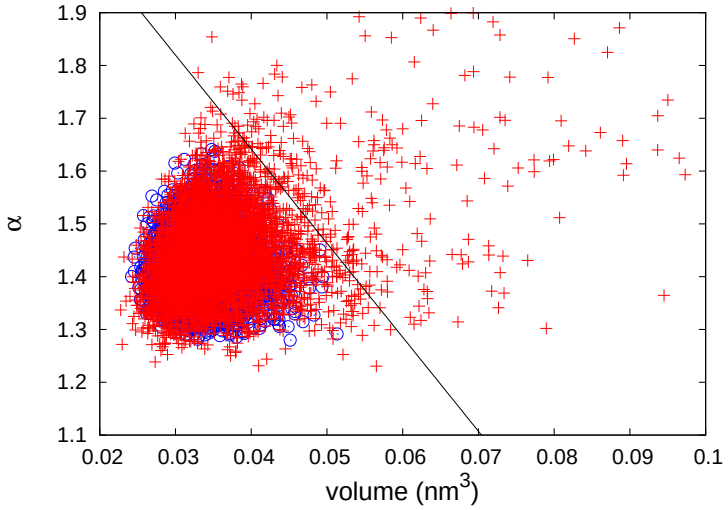

Figure 6.9: Anisotropic factor as a function of volume for unstable water (T=280 K, p=-2630 bar) compared to that of liquid water with a cavity (scaled)

the largest volume, is required in the MFPT formalism. For each trajectory, we evaluate the time it takes to reach a given volume for the first time. Being nucleation a stochastic event, the cavitation time varies significantly from one run to another, as shown in Figure 6.10 for the system at p=-2250 bar. Moreover, Figure 6.10 also shows that at p=-2250 bar the time required to form a critical bubble is much larger than the time the system takes to cavitate. Once a bubble reaches a critical size it grows very quickly and destabilizes the system that cavitates. This indicates that nucleation and growth are not coupled. A comparison of this plot with Figure 6.6 shows that the volume fluctuations are independent of the size of the largest bubble except when the bubble size exceeds the critical one. In the latter case, the largest bubble grows very quickly and becomes a significant part of the total volume (notice that the divergences in both figures occur at the same time), and the system cavitates.

Fluctuations in Fig. 6.10 already enable us to have a rough idea of the size of the critical cluster (around 1.5 nm^3). However, for a precise estimate it is necessary to average the first passage times over a large number of trajectories for a given thermodynamic state. In this way we get a smooth MFPT curve from which it is possible to extract the rate and the size of the critical cluster. In particular, the MFPT reported in this work is the outcome of 200 independent simulation runs.

Figure 6.11 shows the comparison between the MFPT curve for me-

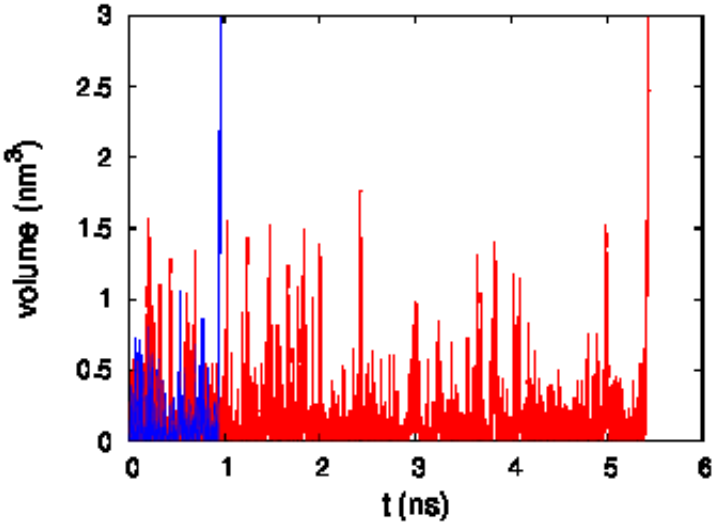

Figure 6.10: Time evolution of the volume of the largest bubble for the runs of Fig. 6.6

tastable water (above the spinodal) with that of unstable water (below the spinodal). Notice that a different time scale is used for each of the curves. The nucleation behavior is quite different for these thermodynamic states. MFPT for metastable water shows a typical sigmoidal shape which can be fitted to a function of the form

$$\tau(V) = (\tau_J/2)\{1 + erf[c(V - V^*)]\}, \tag{6.3}$$

where $erf(x)$ is the error function. Wedekind *et al.*[22] have shown that the parameters of this equation provide relevant physical information. In particular, c corresponds to the local curvature around the top of the barrier and is proportional to the Zeldovich's factor Z ($Z = c/\sqrt{\pi}$), V^* is the size of the critical cluster (location of the transition state) and τ_J is the nucleation time which is related to the nucleation rate J by

$$J = \frac{1}{\tau_J V_s}, \tag{6.4}$$

where V_s is the system volume. Applying Eq. 6.3 to the system at p=-2250 bar, we obtain τ_J = 1,88 ns, V^* = 1,52 nm^3 and c = 1,26. From τ_J and V^* it is immediate to evaluate the nucleation rate and the radius of the critical cluster for which we obtain $J = 0{,}031$ ns^{-1}nm^{-3} and $r_{crit} = 0{,}71$ nm (assuming the critical cluster to be spherical). If we subtract the volume of

the interfacial molecules, the volume of the critical cluster becomes 0.82 nm^3, corresponding to a critical radius of 0.59 nm. A visual inspection of the critical and postcritical bubbles show that they are usually empty, i.e. no actual vapor molecules are within the bubble which is essentially made only of interfacial molecules.

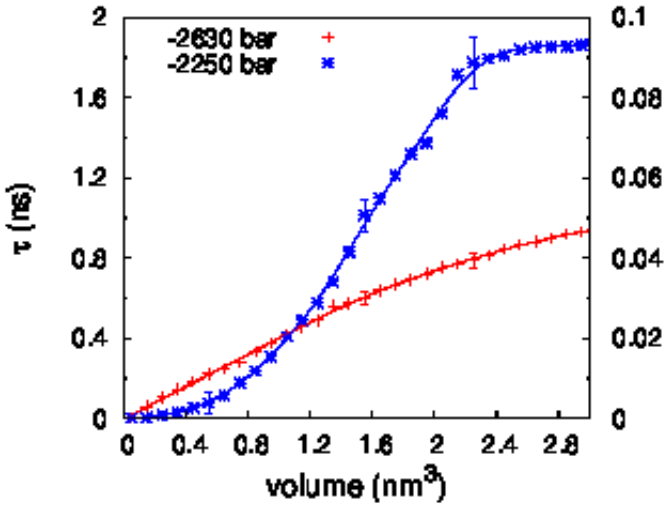

Figure 6.11: Comparison of the MFPT obtained for metastable and unstable TIP4P/2005 water at 280 K. Since the trajectories change very little from one configuration to the next one, we only analyze them every 0.5ps. Notice that a different scale is used for each of the curves, metastable liquid on the left axis and unstable on the right axis. Standard deviations of τ have been computed in each curve for three point at low, medium and large volumes.

Our results may be compared to those coming from the Classical Nucleation Theory[3] (CNT)

$$r_{crit}^{CNT} = \frac{2\gamma}{p_{sat} - p}, \tag{6.5}$$

$$J_{CNT} = \rho_N \left(\frac{2\gamma}{\pi m B} \right)^{1/2} e^{-\Delta G^{CNT}/kT}, \tag{6.6}$$

where γ is the interfacial tension, p_{sat} the coexistence pressure, m the mass of a molecule, ρ_N the number density of the liquid and B takes into account the mechanical equilibrium of the bubble (in cavitation experiments B=1), and $\Delta G^{CNT} = W(r_{crit}^{CNT}) = (16\pi/3)(\gamma^3/(p_{sat} - p)^2$. Assuming $\gamma \approx 73$ mN/m[109], we obtain $r_{crit}^{CNT} \approx 0.67$ nm, and $J_{CNT} = 1{,}7 \times 10^{-10}$ $ns^{-1}nm^{-3}$. Thus, the prediction of the CNT for the critical radius is quite accurate whereas the

differences in the nucleation rates are about eight orders of magnitude. This is in agreement with the observations made for the Lennard-Jones system.[14].

A snapshot of two bubbles, one slightly below the critical size and the other one larger than the critical bubble, are shown if Fig 6.12.

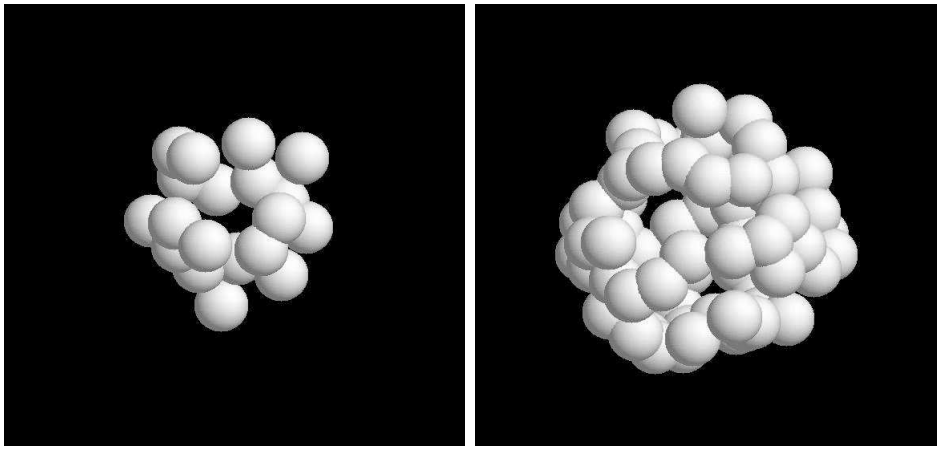

Figure 6.12: A snapshot of the growth of a bubble. The image on the left corresponds to a precritical bubble and the image on the right corresponds to a postcritical one along the same trajectory (the configurations are separated by 0.02ps).

On the contrary, the MFPT curve for unstable water is a monotonous function without an inflection point nor a plateau indicating that, in this case, nucleation and growth are coupled. A number of bubbles are quickly formed. When these bubbles grow, some of them eventually merge together giving rise to larger bubbles and the growth-coalescence process continues until cavitation (spinodal decomposition). This means that there is no nucleation free-energy barrier which is consistent with the fact that the system's pressure is below the spinodal.

We now study how the choice of parameters affect the final results. Figure 6.13 shows the MFPT using two different criteria to distinguish liquid from vapor molecules. In both cases, we tag a molecule as vapor if its VP anisotropy, α, is above a straight line defined in terms of a pivotal point and a slope in the α-V plane. One of the curves correspond to the parameters provided by the study made in the previous section, $\alpha > 1{,}5-18*(V-0{,}048)$, and the other one has been obtained with $\alpha > 1{,}5-18*(V-0{,}052)$, a quite restrictive condition (see Fig. 6.8). A more restricted choice implies a smaller number of molecules fulfilling the condition and, as a result, the MFPT curve is shifted toward lower volumes. The size of the critical bubble is then slightly

dependent on the choice of parameters. Interestingly, the value of τ_J (and, thus, the nucleation rate) does not depend at all on the definition of the order parameter. This is clear a demonstration of the robustness of the MFPT technique. Since the trajectories changes very little from one configuration

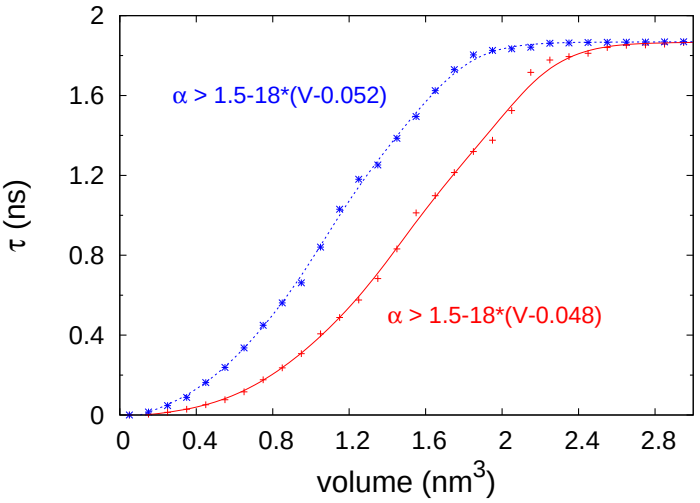

Figure 6.13: MFPT for metastable water using two different VP parameters to distinguish liquid from " vapor"molecules.

to the next one, we only analyze them every Δt ps. Figure 6.14 shows the effect of modifying the sampling time Δt. Notice that sampling times sensibly larger than the simulation timestep can be used. In fact, an increase by a factor of four in Δt has a little effect on the size of the critical cluster and a null influence on the nucleation rate.

6.6. Discussion and conclusions

In this work we set up a Voronoi-based tessellation procedure to determine the volume of the largest vapor bubble that allows us to study bubble nucleation in an over-stretched TIP4P/2005 metastable water. The parameters of the Voronoi polyhedra that allow to distinguish bulk (liquid) particles from interfacial (or vapor) ones have been obtained from the investigation of liquid configurations in which a cavity has been artificially created. It has been shown that best choice of parameters involves a combination of the Voronoi Polyhedra volume and nonsphericity factor α. The study allows to reduce to a minimum the intrinsic arbitrariness in fixing the parameters required to

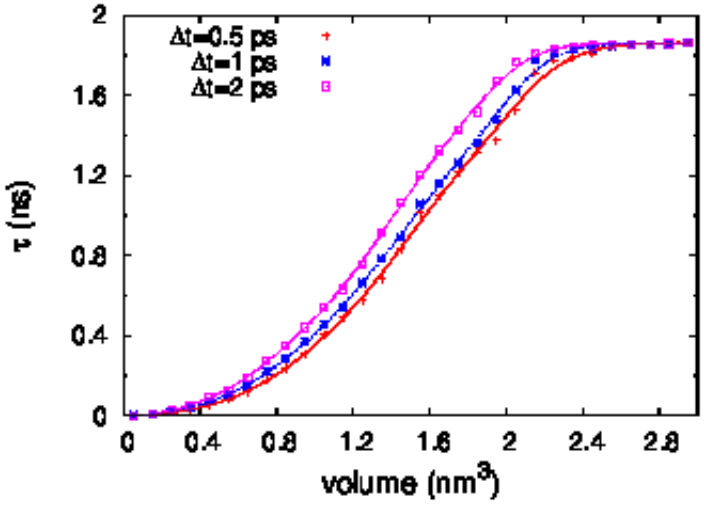

Figure 6.14: MFPT for metastable water for two different sampling times (configurations are analyzed every Δt ps).

detect the growth of bubbles in the metastable liquid. As a consequence the nucleation rate is completely independent on the parameters chosen to define the local order and the critical cluster size is only moderately dependent on them (the MFPT technique also contributes to this achievement).

One important open question is the effect of the finite-size. It has been pointed that the MFPT analysis is less sensitive to finite size effects than other approaches because it only requires a box large enough to contain several times the critical cluster.[26] Since our calculated volume of the critical cluster for metastable TIP4P/2005 water is 1.5 nm^3 and the average system volume is about 17 nm^3, we conclude that our chosen system fulfils the required condition and we can neglect (at least, at this stage) finite-size effects.

As in simple fluids, the bubble nucleation rate estimated with Classical Nucleation Theory turns out to be much lower (8 orders of magnitude) than the one computed using MFPT. This could be due to the fact that CNT neglects curvature corrections to the surface free-energy of the bubble. When analyzing the mechanism of bubble formation above and below the spinodal, we observe clear differences. In the simulations of the liquid above the spinodal line, one bubble grows larger than all others in a fairly compact shape whereas, for the liquid below the spinodal line, we detect the formation of few bubbles which, eventually, merge to form larger ones (spinodal decomposition). However, above the spinodal we have also detected bubbles with different topologies, proving that small bubbles are strongly fluctuating ob-

jects. In the coming future, we plan to attempt a systematic characterization of the topology of the bubbles, as we believe it might play an important role in the cavitation process.

In general, the Voronoi tessellation is a relatively CPU-time consuming method. For a deeper investigation of the bubble nucleation mechanism it seems interesting to devise alternative ways of partitioning and calculating the bubble volume. Therefore, the results presented in this work can be seen as a benchmark for further bubble nucleation studies.

Acknowledgments

This work has been funded by grants FIS2010/16159 of the MEC, P2009/ESP-1691 of CAM and the Marie Curie Integration Grant PCIG-GA-2011-303941 (ANISOKINEQ) C.V. also acknowledges financial support from a Juan de La Cierva Fellowship. We acknowledge Carlos Vega for helpful discussions and a critical reading of the manuscript.

Bibliografía

1. M. Shusser and D. Weihs, Int. J. Multiphase Flow **25**, 1561 (1999).
2. K. S. Suslick, SCIENCE **247**, 1439 (1990).
3. M. Blander and J. L. Katz, AICHE J. **21**, 833 (1975).
4. Y. Viisanen and R. Strey, J. Chem. Phys. **101**, 7835 (1994).
5. P. E. Wagner and R. Strey, J. Chem. Phys. **80**, 5266 (1984).
6. M. M. Rudek, J. L. Katz, I. V. Vidensky, V. Zdimal, and J. Smolik, J. Chem. Phys. **111**, 3623 (1999).
7. H. Lihavainen, Y. Viisanen, and M. Kulmala, J. Chem. Phys. **114**, 10031 (2001).
8. Y. J. Kim, B. E. Wyslouzil, G. Wilemski, J. Wolk, and R. Strey, J. Phys. Chem. A **108**, 4365 (2004).
9. M. Gharibeh, Y. Kim, U. Dieregsweiler, B. E. Wyslouzil, D. Ghosh, and R. Strey, J. Chem. Phys. **122**, 094512 (2005).
10. E. Herbert, S. Balibar, and F. Caupin, Phys. Rev. E **74**, 041603 (2006).
11. F. Caupin, Phys. Rev. E **71**, 051605 (2005).
12. C. F. Delale, J. Hruby, and F. Marsik, J. Chem. Phys. **118**, 792 (2003).
13. M. E. M. Azouzi, C. Ramboz, J.-F. Lenain, and F. Caupin, Nature Physics **advance online publication**, 1 (2012).
14. X. C. Zeng and D. W. Oxtoby, J. Chem. Phys. **94**, 4472 (1991).
15. V. Talanquer and D. Oxtoby, Journal of Chemical Physics **102**, 2156 (1995).

16. M.J. Uline and D.S. Corti, Physical Review Letter **99**, 076102 (2007).

17. M.J. Uline, K. Torani and D.S. Corti, Journal of Chemical Physics **133**, 174511 (2010).

18. V. K. Shen and P. G. Debenedetti, J. Chem. Phys. **111**, 3581 (1999).

19. Z.-J. Wang, C. Valeriani, and D. Frenkel, Journal of Physical Chemistry B **113**, 3776 (2009).

20. S. L. Meadley and F. A. Escobedo, J. Chem. Phys. **137**, 074109 (2012).

21. M. A. Gonzalez, Master's thesis, Fac. Ciencias Quimicas, Univ. Complutense, Madrid (2011).

22. J. Wedekind, R. Strey, and D. Reguera, J. Chem. Phys. **126**, 134103 (2007).

23. G. Chkonia, J. Woelk, R. Strey, J. Wedekind, and D. Reguera, Journal of Chemical Physics **130** (2009).

24. J. Wedekind, G. Chkonia, J. Woelk, R. Strey, and D. Reguera, J. Chem. Phys. **131**, 114506 (2009).

25. J. Wedekind, J. Woelk, D. Reguera, and R. Strey, J. Chem. Phys. **127**, 154515 (2007).

26. A. Perez and A. Rubio, J. Chem. Phys. **135**, 244505 (2011).

27. B. Senger, P. Schaaf, D. S. Corti, R. Bowles, J. C. Voegel, and H. Reiss, J. Chem. Phys. **110**, 6421 (1999).

28. J. Wedekind and D. Reguera, J. Chem. Phys. **127**, 154516 (2007).

29. J. A. van Meel, L. Filion, C. Valeriani, and D. Frenkel, J. Chem. Phys. **136**, 234107 (2012).

30. P. R. ten Wolde and D. Frenkel, J. Chem. Phys. **109**, 9901 (1998).

31. A. Okabe, B. Boots, K. Sugihara, and S. N. Chiu, *Spatial Tessellations: Concepts and Applications of Voronoi Diagrams* (Wiley, New York, 2000).

32. D. Eppstein, *http://www.ics.uci.edu/ eppstein/gina/voronoi.html.*

33. *http://www.voronoi.com/wiki/index.php?title=Voronoi_Applications.*

34. R. Karch, F. Neumann, M. Neumann, P. Szawlowski, and W. Schreiner, Ann. Biomed. Engin. **31**, 548 (2003).

35. J. D. Bernal, Proc. R. Soc. London A **280**, 299 (1964).

36. J. N. Cape, J. L. Finney, and L. V. Woodcock, J. Chem. Phys. **75**, 2366 (1981).

37. J. C. Gil Montoro and J. L. F. Abascal, J. Phys. Chem. **97**, 4211 (1993).

38. J. C. Gil Montoro, F. Bresme, and J. L. F. Abascal, J. Chem. Phys. **101**, 10892 (1994).

39. R. Y. Yang, R. P. Zou, and A. B. Yu, Phys. Rev. E **65**, 041302 (2002).

40. O. Gedeon and M. Liska, J. Non-Crystalline Solids **303**, 246 (2002).

41. P. Jedlovszky, N. N. Medvedev, and M. Mezei, J. Phys. Chem. B **108**, 465 (2004).

42. J. Q. Xu, R. P. Zou, and A. B. Yu, Granular Matt. **9**, 455 (2007).

43. M. Canales, Phys. Rev. E **79**, 051802 (2009).

44. O. Gedeon, M. Liska, and J. Machacek, J. Non-crystalline solids **357**, 1574 (2011).

45. J. Skvor and I. Nezbeda, Mol. Phys. **109**, 133 (2011).

46. A. Idrissi, I. Vyalov, M. Kiselev, M. V. Fedorov, and P. Jedlovszky, J. Phys. Chem. B **115**, 9646 (2011).

47. M. Swart and P. T. Van Duijnen, Int. J. Quantum Chem. **111**, 1763 (2011).

48. E. E. David and C. W. David, J. Chem. Phys. **76**, 4611 (1982).

49. G. Neumayr, T. Rudas, and O. Steinhauser, J. Chem. Phys. **133**, 084108 (2010).

50. V. P. Voloshin, N. N. Medvedev, M. N. Andrews, R. R. Burri, R. Winter, and A. Geiger, J. Phys. Chem. B **115**, 14217 (2011).

51. M. Haberler, C. Schroeder, and O. Steinhauser, Phys. Chem. Chem. Phys **13**, 6924 (2011).

52. P. Jedlovszky, J. Chem. Phys. **113**, 9113 (2000).

53. P. Gomez-Alvarez, A. Dopazo-Paz, L. Romani, and D. Gonzalez-Salgado, J. Chem. Phys. **134**, 014512 (2011).

54. I. Hoedl, J. Hoedl, A. Worman, G. Singer, K. Besemer, and T. J. Battin, PLOS ONE **6**, e26368 (2011).

55. F. B. Usabiaga and D. Duque, Phys. Rev. E **79**, 046709 (2009).

56. B. Bouvier, R. Gruenberg, M. Nilges, and F. Cazals, Proteins - Struct. Funct. Bioinformat. **76**, 677 (2009).

57. R. E. Isele-Holder, B. D. Rabideau, and A. E. Ismail, J. Phys. Chem. A **116**, 4657 (2012).

58. A. Geiger, N. N. Medvedev, and Y. I. Naberukhin, J. Struct. Chem. **33**, 226 (1992).

59. J. P. Shih, S. Y. Sheu, and C. Y. Mou, J. Chem. Phys. **100**, 2202 (1994).

60. Y. I. Jhon, K. T. No, and M. S. Jhon, Fluid Phase Equilibria **244**, 160 (2006).

61. G. G. Malenkov, J. Struct. Chem. **48**, 723 (2007).

62. Y. L. Yeh and C. Y. Mou, J. Phys. Chem. B **103**, 3699 (1999).

63. P. Jedlovszky, L. B. Partay, A. P. Bartok, V. P. Voloshin, N. N. Medvedev, G. Garberoglio, and R. Vallauri, J. Chem. Phys. **128**, 244503 (2008).

64. G. Stirnemann and D. Laage, J. Chem. Phys. **137**, 031101 (2012).

65. I. I. Vaisman, F. K. Brown, and A. Tropsha, J. Phys. Chem. **98**, 5559 (1994).

66. P. Jedlovszky, J. Chem. Phys. **111**, 5975 (1999).

67. M. Zapalowski and W. M. Bartczak, Computers & Chem. **24**, 459 (2000).

68. M. Zapalowski and W. M. Bartczak, Res. Chem. Intermed. **27**, 855 (2001).

69. A. Idrissi, P. Damay, K. Yukichi, and P. Jedlovszky, J. Chem. Phys. **129**, 164512 (2008).

70. G. Neumayr, C. Schroeder, and O. Steinhauser, J. Chem. Phys. **131**, 174509 (2009).

71. C. Schroeder, G. Neumayr, and O. Steinhauser, J. Chem. Phys. **130**, 194503 (2009).

72. C. W. David, Computers & Mathematics with Appl. **12**, 763 (1986).

73. C. W. David, Computers and Chemistry **12**, 207 (1988).

74. R. A. Lewis, J. Comp.-Aided Molec. Design **3**, 133 (1989).

75. M. G. Alinchenko, V. P. Voloshin, N. N. Medvedev, M. Mezei, L. Partay, and P. Jedlovszky, J. Phys. Chem. B **109**, 16490 (2005).

76. D.-S. Kim, C.-H. Cho, D. Kim, and Y. Cho, Computer-Aided Design **38**, 431 (2006).

77. M. Petrek, P. Kosinova, J. Koca, and M. Otyepka, Structure **15**, 1357 (2007).

78. D. Kim, C.-H. Cho, Y. Cho, J. Ryu, J. Bhak, and D.-S. Kim, J. Molec. Graph. & Model. **26**, 1104 (2008).

79. S. Sonavane and P. Chakrabarti, PLOS Comput. Biol. **4**, e1000188 (2008).

80. D. Chakraborty and A. Chandra, J. Molec. Liq. **163**, 1 (2011).

81. L. Wang and T. Ueda, Ocean Engin. **38**, 519 (2011).

82. J. T. Fern, D. J. Keffer, and W. V. Steele, J. Phys. Chem. B **111**, 13278 (2007).

83. D. S. Kim, Y. Cho, and D. Kim, Computer-Aided Design **37**, 1412 (2005).

84. D. Kim and D.-S. Kim, Computer-Aided Design **38**, 417 (2006).

85. W. Brostow, J. P. Dussault, and B. L. Fox, J. Comput. Phys. **29**, 81 (1978).

86. J. L. Finney, J. Comput. Phys. **32**, 137 (1979).

87. M. Tanemura, T. Ogawa, and N. Ogita, J. Comput. Phys. **51**, 191 (1983).

88. N. N. Medvedev, J. Comput. Phys. **67**, 223 (1986).

89. J. L. F. Abascal and J. C. G. Montoro, to be published.

90. J. Wedekind, D. Reguera and R. Strey , J. Chem. Phys. **125**, 214505 (2006).

91. B. Hess, C. Kutzner, D. van der Spoel, and E. Lindahl, J. Chem. Theory Comput. **4**, 435 (2008).

92. U. Essmann, L. Perera, M. L. Berkowitz, T. Darden, H. Lee, and L. G. Pedersen, J. Chem. Phys. **103**, 8577 (1995).

93. J. P. Ryckaert, G. Ciccotti, and H. J. C. Berendsen, J. Comput. Phys. **23**, 327 (1977).

94. G. Bussi, D. Donadio, and M. Parrinello, J. Chem. Phys. **126**, 014101 (2007).

95. M. Parrinello and A. Rahman, J. Appl. Phys. **52**, 7182 (1981).

96. H.J.C. Berendsen, J. Chem. Phys. **81**, 3684 (1984).

97. S. Nose, J. Chem. Phys. **81**, 511 (1984).

98. W.G. Hoover, Phys.Rev.A **31**, 1695 (1985).

99. J. Wedekind, D. Reguera and R. Strey, J. Chem. Phys. **127**, 064501 (2007).

100. J. L. F. Abascal and C. Vega, J. Chem. Phys. **123**, 234505 (2005).

101. C. Vega, J. L. F. Abascal, M. M. Conde, and J. L. Aragones, Faraday Discuss. **141**, 251 (2009).

102. C. Vega and J. L. F. Abascal, Phys. Chem. Chem. Phys **13**, 19663 (2011).

103. H. L. Pi, J. L. Aragones, C. Vega, E. G. Noya, J. L. F. Abascal, M. A. Gonzalez, and C. McBride, Molecular Physics **107**, 365 (2009).

104. M. A. Gonzalez and J. L. F. Abascal, J. Chem. Phys. **132**, 096101 (2010).

105. C. Vega, J. L. F. Abascal, and I. Nezbeda, J. Chem. Phys. **125**, 034503 (2006).

106. Y. C. Liao, D. J. Lee, and P. J. He, Powder Tech. **123**, 1 (2002).

107. O. Gedeon, J. Non-Crystalline Solids **351**, 1139 (2005).

108. A. Idrissi, I. Vyalov, P. Damay, M. Kiselev, Y. P. Puhovski, and P. Jedlovszky, J. Molec. Liq. **153**, 20 (2010).

109. C. Vega and E. de Miguel, J. Chem. Phys. **126**, 154707 (2007).

Results: Chapter 7

Detecting bubbles in water at negative pressure

Miguel A. González[1,*], *Georg Menzl*[2,*], *Juan L. Aragones*[1], *Philipp Geiger*[2], *Gael Pallares*[3], *Mouna El Mekki Azouzi*[3], *Frederic Caupin*[3], *Jose L. F. Abascal*[1], *Christoph Dellago*[2] *and Chantal Valeriani*[1]

(1) Departamento de Química Física, Facultad de Ciencias Químicas, Universidad Complutense de Madrid, 28040 Madrid, Spain.

(2) Faculty of Physics and Center for Computational Materials Science, University of Vienna, Boltzmanngasse 5, 1090 Vienna, Austria.

(3) Laboratoire de Physique de la Matiere Condensee et Nanostructures, Universite Claude Bernard, Lyon 1 et CNRS, Institut Universitaire de France, 43 boulevard du 11 novembre 1918, 69100, Villeurbanne, France.

(*) These authors contributed equally to this work.

7.1. Abstract

The investigation of cavitation in liquids under tension with molecular simulations requires an appropriate definition of the volume of the vapour bubble forming within the metastable liquid phase. Commonly used approaches for bubble detection exhibit two significant flaws: first, when applied to water they often lead to a false detection of small bubbles (natural cavities of the system) and, second, they lack thermodynamic consistency resulting, for instance, in a violation of the nucleation theorem. Here, we present two grid-based methods, the M-method and the V-method, to detect bubbles in metastable water specifically designed to address these shortcomings. The

M-method incorporates information about neighbouring grid cells to distinguish between liquid- and vapour-like cells, leading to a much lower frequency of false bubble detections in the metastable liquid. The V-method is calibrated such that its estimates for the bubble volume are compatible with the nucleation theorem which allows for comparison to experimental data. Both methods are computationally inexpensive such that they can be used in molecular dynamics and Monte Carlo simulations of cavitation.

7.2. Introduction

By overheating a liquid beyond the liquid-vapour coexistence temperature or reducing its pressure below the saturated vapour pressure, the liquid becomes metastable and eventually transforms into the thermodynamically stable vapour phase via a bubble nucleation mechanism. Remarkably, in the case of water, strongly negative pressures can be reached experimentally before the liquid "breaks" under the mechanical tension and cavitation occurs, which has important implications for biological processes like water transport in trees[1,2,3] and the sonocrystallization of ice.[4,5] Since bubble nucleation takes place at the nanoscale, observing it directly in experiments is very difficult. Thus, apart from the nucleation rate, little information can be obtained from experiments. Numerical simulations provide a complementary technique to investigate the microscopic details of bubble nucleation such as the size and shape of the critical bubble and the structure of the liquid around it.

In order to describe the nucleation process, one requires an adequate order parameter to track the phase transition mechanism, i.e., to detect the formation and growth of a bubble. Homogeneous bubble nucleation (or cavitation) from an over-heated fluid has been recently studied in simple liquids (Lennard-Jones) using either the volume of the largest bubble as a local order parameter[6,7,8] or the density as a global one.[9] In recent work, Meadley and Escobedo[10] demonstrated that when comparing the nucleation free energy barrier obtained with the volume of the largest bubble to the one computed using the global density, the largest bubble volume is a better reaction coordinate than the density; it correlates more strongly with committor probabilities. Even though there is a one-to-one relation between the two order parameters, the authors showed that using a global order parameter can introduce finite size effects as one observes the formation of multiple bubbles instead of capturing the formation of one single critical nucleus.

In general, detecting vapour bubbles in a metastable liquid is a challenging problem, since the vapour phase consists both of "vapour-like" molecules and of "void"spaces. Thus, to compute the volume of the largest bubble and

use it as a local order parameter, one needs to be able to identify vapour regions in the metastable liquid, compute their volumes and select the largest one as the order parameter. This procedure has been applied in Ref.[6], where homogeneous bubble nucleation in a super-heated Lennard-Jones fluid was studied using forward flux sampling, and the largest connected low-density region was used as a local order parameter. The low-density region was defined by means of a "grid-based" procedure: 1) liquid and vapour-like particles were classified using the first-neighbours distribution and, 2) a three-dimensional grid was superimposed on the system and, 3) a cluster analysis was performed on the void space, identifying the bubble with the largest volume as the local order parameter.

When studying bubble nucleation from over-stretched water, some of us have recently shown that a valid alternative to a grid-based procedure consists in employing a Voronoi-based analysis to detect the largest bubble.[11] However, the main drawback of this approach is that performing a Voronoi tessellation is a CPU-time consuming task. In addition, most of the available open-source Voronoi packages, as far as we have experienced, are not tailored to target the task of detecting bubbles since the topological distance involves a different set of neighbours than the geometrical one.

In general, an order parameter to detect bubbles in water should meet the following criteria. 1) The order parameter should be local. When studying a nucleation process, the use of a local order parameter allows to detect and follow the growing nucleus instead of the variation of a global property of the system. This is a prerequisite when studying nucleation in a large system, where fluctuations can overshadow the signature of the nucleus when observables are averaged over the entire system, and it allows to obtain structural information about the nucleus and the surrounding liquid. 2) The order parameter should not impose a specific shape on the detected bubble, which is of particular importance when the order parameter is used in a free energy computation method such as umbrella sampling, where the measured free energy barrier height would be altered by excluding certain cluster shapes from the sampling. 3) The order parameter should measure the "true" volume of a bubble. In the same way we can measure the volume of macroscopic objects by the amount of liquid they displace when immersed in a liquid, the volume of a bubble detected by a local order parameter should be equivalent to the average change in volume of the system between the metastable liquid and a system containing such a bubble. An order parameter calibrated in this fashion is also consistent with the nucleation theorem[12], which allows for direct comparison to experimental data. 4) The order parameter should not detect voids in liquid water at ambient conditions. 5) Since the order parameter has to be evaluated hundreds of thousands of times during a typical

simulation run, it should be computationally inexpensive.

In what follows, building on the method introduced in Ref.[6], we propose two novel grid-based methods tailored to work for a network-forming liquid such as water. We will analyze these order parameters with respect to the criteria listed above and present physical features of the nucleation process, in particular the size of the critical cluster and the free energy barrier height for different degrees of metastability.

The rest of the paper is organized as follows. After giving simulation details in Section II, we describe the techniques we used to study spontaneous nucleation and the case when nucleation cannot happen spontaneously on timescales accessible to computer simulation because the free energy barrier is too high. In Section III we present the two different grid-based methods to identify the volume of the largest bubble in metastable water: the V-method and the M-method. To conclude, in Section IV we report a quantitative comparison of the results obtained when computing the order parameter with both methods in the study of spontaneous as well as non-spontaneous nucleation. We discuss our results in Section V.

7.3. Simulation details

7.3.1. Molecular Dynamics

We simulate metastable water using the rigid non-polarizable TIP4P/2005 model[13] which has been shown to predict a number of water properties with great accuracy.[14] Relevant to this work are the accurate predictions for the vapour–liquid equilibrium[15,16] and the liquid–vapour surface tension.[17] We perform NpT molecular dynamics (MD) simulations either using an in-house code, based on the code previously used in Ref.[18], or GROMACS[19].

When using the home-made code, we simulate a system of $N = 2000$ water molecules. We integrate the equations of motion with a time step of 2 fs using a time-reversible quaternion-based integrator that maintains the rigid geometry of water molecules. In particular, we carry out NpT-MD using a slightly modified version of the Verlet integrator proposed by Kamberaj *et al.*[20], based on the Trotter decomposition schemes applied by Miller *et al.*[21] and Martyna *et al.*[22]. In this algorithm, the coupling to the surrounding heat bath is implemented through thermostat chains based on the Nosé–Hoover[23,24] approach with an inverse frequency of 1 ps. Constant pressure is ensured by coupling a barostat based on the Andersen approach[25] to the heat bath with a relaxation time of 3 ps, which is approximately equal to the

time a sound wave takes to transverse the simulation box.[26] [1] Long-range interactions are treated with Ewald summation.

When using the GROMACS package, we simulate a system of $N = 500$ (when nucleation is spontaneous) or $N = 4000$ (when nucleation is not spontaneous) water molecules in an NpT ensemble with a time step of 1 fs. The temperature is kept fixed using the velocity rescaling thermostat[27] with 1 ps (spontaneous nucleation) or 0,2 ps (non-spontaneous nucleation) relaxation time and the pressure is set with the isotropic Parrinello–Rahman barostat[28] with a relaxation time of 2 ps (spontaneous nucleation) or 0,2 ps (non-spontaneous nucleation). We constrain the geometry of the water molecules with the SHAKE algorithm.[29] Long range electrostatic interactions are treated using the smooth particle mesh–Ewald method.[30]

7.3.2. Nucleation rates and barriers

When we over-stretch liquid water, bubbles start appearing and disappearing at random in the system. Only when one of them overcomes a critical threshold, the entire system can cavitate. This corresponds to the system having to cross a nucleation free energy barrier, whose height depends on the supersaturation (or amount of over-streching). For low barriers, i.e., high supersaturation, cavitation can be observed spontaneously on the time-scales accessible to molecular dynamics simulations. For high barriers, i.e., low supersaturation, the time until cavitation occurs spontaneously is prohibitively long and thus one has to resort to rare event sampling techniques such as umbrella sampling.

When nucleation is spontaneous at the simulation timescale

In order to determine nucleation rates we apply the mean first passage time (MFPT) analysis[31] using the volume of the largest bubble as a local order parameter. If the barrier is high enough to guarantee separation of timescales between relaxation in the metastable basin and the barrier crossing event, the average time $\tau(V_{\text{bubble}})$ it takes until the largest bubble has a volume of V_{bubble} for the first time, is[31]

$$\tau(V_{\text{bubble}}) = (\tau_J/2)\{1 + \text{erf}[c(V_{\text{bubble}} - V^*_{\text{bubble}})]\}\,. \tag{7.1}$$

Here, $\text{erf}(x)$ is the error function, V^*_{bubble} is the size of the critical bubble, c is a constant derived from the local curvature around the top of the free

[1] The relaxation time of the barostat $\nu^{-1} = 3$ ps is chosen to approximate the length of the simulation box divided by the speed of sound $c = \sqrt{K/\rho}$, where $K = \rho\,\partial P/\partial\rho \approx 2$ GPa is the bulk modulus of TIP4P/2005 water in the studied pressure range.

energy barrier and proportional to the Zeldovich factor $Z = c\pi^{-1/2}$, and τ_J is the nucleation time. The average time τ_J the system takes to leave the metastable state and reach the point where the transition to the vapour phase is committed to proceed, is related to the nucleation rate J via

$$J = \frac{1}{\tau_J \langle V \rangle}, \tag{7.2}$$

where $\langle V \rangle$ is the average volume of the system in the metastable liquid state.

The MFPT analysis is performed in the following fashion: by averaging over 200 independent MD trajectories which start from the metastable liquid and subsequently transform into the vapour phase, we compute the average time $\tau(V_{\text{bubble}})$ it takes until the bubble reaches a volume V_{bubble} for the first time. We then fit Equ. (7.1) to the data to obtain the nucleation rate J, the Zeldovich factor Z and the size of the critical bubble V^*_{bubble}.

As in Ref.[11], we study nucleation from metastable liquid water above the spinodal line, at 280 K and $p = -2250$ bar (the spinodal at negative pressure has been calculated in Ref.[32] and corresponds to $p_{\text{sp}} \approx -2440$ bar at $T = 280$ K). It has been shown in Ref.[11] that, at these thermodynamic conditions, the volume of the critical cluster is smaller than 1 nm^3 so that a system size of $N = 500$ molecules can easily accommodate a critical bubble.

When nucleation is not spontaneous at the simulation timescale

In order to compute the nucleation free energy barrier as a function of the largest bubble volume we use two rare-events numerical techniques: 1) umbrella sampling[33] with a hybrid Monte Carlo (HMC) scheme[34,35], or 2) a novel molecular dynamics umbrella sampling (HMC-NpT) scheme. In the latter technique, the system is propagated via a series of short NpT molecular dynamics trajectories where the resulting configurations are fed to a standard umbrella sampling scheme More details on this method will be given elsewhere.[36]

7.4. Numerical methods

To study homogeneous bubble nucleation from over-stretched metastable water we use the volume of the largest bubble, V_{bubble}, as a local order parameter. We propose to detect the largest bubble choosing one of two approaches: the V-method or the M-method. Both methods, inspired by the grid-based analysis of Ref.[6], are tailored to successfully work in a network-forming liquid such as water. In what follows, we will describe them step by step.

7.4.1. V-method for the volume of the largest bubble

Step 1: We *assign all water molecules to be in either the liquid or vapour phase:* a water molecule is defined as vapour-like if it has no neighbours within its Stillinger radius r_S, which is chosen close to the first minimum of the radial distribution function of the metastable liquid at strongly negative pressures.

Step 2: We *divide the entire simulation box into small cubes of equal size* by superimposing a three-dimensional grid on the system. Since the total volume fluctuates in a simulation at constant pressure, the cube volume varies with the size of the simulation box. In order to determine "occupied" cubes we assume that each liquid water molecule occupies a sphere with radius r_S around its centre of mass. Then we iterate over all cubes in the box and any cube whose center is inside the sphere of a liquid-like water molecule is considered to be occupied, hence, it is not part of a bubble.

Step 3: We *assign unoccupied cubes to clusters* such that a cube and all its face-sharing neighbours are part of the same cluster, and use the volume v of the largest cluster as an order parameter for the size of the largest bubble. Even though the method introduces some lattice discretisation errors by construction, we assume these errors to be negligible in view of the approximation of water molecules as spheres and the high spatial resolution of the grid.

Step 4: Even though a method incorporating only the first three steps can be used to describe bubble formation in the metastable liquid, the definition of the bubble volume is somewhat arbitrary as it depends on the choice of the grid mesh and the Stillinger radius r_S, which largely determines the "volume" of the water molecules forming the interface. Since the volume of the critical bubble V^*_{bubble} is a property of great interest, which is related to the height of the free energy barrier via the nucleation theorem[12] and thus provides a connection to experimental data[37], our aim is to develop an order parameter whose estimate of the bubble volume depends as little as possible on the choice of arbitrary properties like r_S or the grid resolution.

In analogy to the macroscopic realm, a reasonable definition of the volume of a nanoscale object[38] is to equate its volume to the volume of the liquid it displaces, i.e., we *equate the volume of a bubble to the increase in system volume* it causes. While for a macroscopic object the effect of density fluctuations of the liquid on such a volume estimate is negligible, for small systems density fluctuations can influence the estimated volume considerably. However, one can still require from the definition of the bubble volume that it corresponds to the increase in system volume on the *average*. In the following we explain how to calibrate the bubble volume such that this requirement is

obeyed.

The effect of the bubble on the volume V of the simulation box is evaluated by subtracting the average volume of the metastable liquid $\langle V \rangle$ (at the given thermodynamic state point) from the average volume $\langle V \rangle_v$ of the system containing a largest bubble of size v:

$$V^{\mathrm{V}}_{\mathrm{bubble}}(v) = \langle V \rangle_v - \langle V \rangle. \tag{7.3}$$

Here, the thermodynamic average $\langle V \rangle$ is taken over the metastable liquid, i.e., excluding the stable vapour phase, and $\langle V \rangle_v$ is given by

$$\langle V \rangle_v = Q^{-1} \int V e^{-\beta\left[H(\mathbf{r}^N)+pV\right]} \delta\left[v(\mathbf{r}^N) - v\right] \mathrm{d}\mathbf{r}^N \mathrm{d}V, \tag{7.4}$$

where $Q = \int e^{-\beta\left[H(\mathbf{r}^N)+pV\right]} \delta\left[v(\mathbf{r}^N) - v\right] \mathrm{d}\mathbf{r}^N \mathrm{d}V$ is the reduced partition function. In Equ. (7.3) the superscript "V" refers to the V-method.

Figure 7.1 shows $V^{\mathrm{V}}_{\mathrm{bubble}}$ as a function of v, where we include data obtained from two different regimes: first, the small bubbles which form spontaneously in the metastable liquid over the course of a simulation and, second, the large bubbles obtained by driving the system along the order parameter v using umbrella sampling.

The data in the inset of Fig. 7.1 show the effect of very small bubbles, which appear spontaneously in the metastable liquid, on the system volume. These volume estimates were obtained by averaging the system volume V as a function of the number of clusters of a given size v in an unbiased molecular dynamics simulation. The average system volume $\langle V \rangle$ depends linearly on the number of bubbles of a given size and each data point depicted in the inset of Fig. 7.1 is the slope of this line, i.e., the increase in system volume due to the presence of one bubble of size v. The data for larger bubble volumes (starting with the data point of largest size $v \approx 0{,}027$ nm^3 shown in the inset), where it is exceedingly unlikely to observe more than one such cluster at the same time in system sizes feasible in simulations at these conditions, were obtained by averaging the system volume V as a function of the volume v of the largest cluster within each window of a HMC umbrella sampling calculation.

In order to calibrate the V-method such that the grid-based estimate for the volume v of the largest bubble is mapped onto the average change in system volume $V^{\mathrm{V}}_{\mathrm{bubble}} = \langle V \rangle_v - \langle V \rangle$ caused by a bubble of volume v, we use a fit to the data shown in Fig. 7.1. Note that the functional form of the fit is arbitrary and does not assume that the bubble has a particular geometrical shape; in cases where one finds no suitable functional form, simple numerical

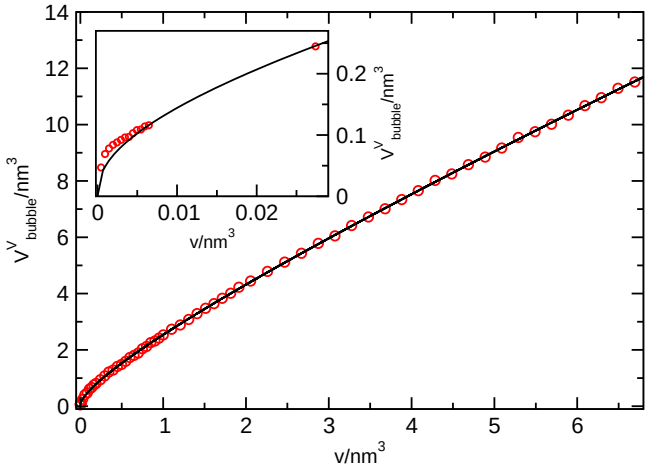

Figure 7.1: Average change in system volume $V^{\mathrm{V}}_{\mathrm{bubble}}$ as a function of the volume v of vapour-like cubes constituting the largest cluster on the grid. The inset magnifies the data for very small bubbles, which form spontaneously at these conditions (see main text). The data points in the main figure are each an average over a window, defined as a range of v-values, in an umbrella sampling simulation. All data were obtained from simulations in the isobaric-isothermal ensemble at $T = 325{,}0\,\mathrm{K}$ and $p = -1500\,\mathrm{bar}$. The black line represents the fit to the data according to Equ. (7.5).

interpolation of the data could be used. Here, we find that a fitting function of the form

$$V^{\mathrm{V}}_{\mathrm{bubble}}(v) \approx v + k_1 v^{2/3} + k_2 v^{1/3}, \tag{7.5}$$

where $k_1 \approx 1{,}17$ nm and $k_2 \approx 0{,}37$ nm^2 at $T = 325{,}0$ K and $p = -1500$ bar, works very well (indicated by the black line in the figure). This fitting function can be viewed as depending on the cluster "surface" (proportional to $v^{2/3}$) and on a term that takes into account the average "curvature" of the cluster (proportional to $v^{1/3}$).

We use this fit to calibrate our order parameter by mapping the volume v, measured directly in simulation by summing over the largest cluster of unoccupied cubes, onto the corresponding average change in system volume $V^{\mathrm{V}}_{\mathrm{bubble}}$ caused by a bubble of size v. Although this order parameter has its roots in the average change of the total system volume due to the presence of the bubble, we stress that it is still a local order parameter which does not impose any particular shape on the bubble, thus fulfilling the requirements 1 and 2 stated in the Introduction. Moreover, due to the calibration used to approximate the average change in system volume created by the bubble, the V-method is also compatible with requirement 3 and, consequently, its volu-

me estimates obey the nucleation theorem. The V-method is computationally inexpensive (thus obeying requirement 5) and we will analyze its detection of voids in the stable liquid in section IV A.

When using the V-method, in order to achieve high spatial resolution, we ensure that the volume of each cube on the grid is less than 0,5 Å^3 for the metastable liquid leading to the choice of 52^3 cubes for a system of $N = 2000$ water molecules. We choose a Stillinger radius of $r_S = 3{,}35$ Å, which is a compromise between the ability to detect the formation of small bubbles and minimising the occurrence of misassigned liquid-like cubes in the metastable liquid.

7.4.2. M-method for the volume of the largest bubble

Step 1: We first *classify the molecules as liquid or vapour-like.* This first step can be performed according to different criteria such as the ten Wolde–Frenkel (WF) criterion[39], the hydrogen bonding (HB) criterion of Ref.[40] or the tetrahedal order parameter q of Refs.[41] and 42. In the following, we will compare these criteria in order to select the best approach to distinguish liquid from vapour molecules. The WF criterion has been used by Wang *et al.*[6] to study cavitation in an over-heated Lennard-Jones fluid; it consists of identifying each particle's nearest neighbours using the first minimum of the radial distribution function (RDF) as a fixed cutoff distance (for water, we will only deal with the oxygen–oxygen RDF). The HB criterion is based on the number of donor hydrogen-bonds per molecule.[40]

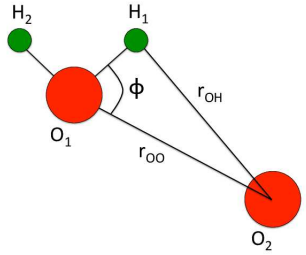

Figure 7.2: Sketch of the hydrogen bond criterium from Ref.[40].

According to Ref.[40] (see Fig. 7.2), water molecule 1 donates a hydrogen bond to molecule 2 if 1) the oxygen$_1$–oxygen$_2$ distance (r_{OO}) is smaller than the first minimum of the oxygen–oxygen RDF, 2) the hydrogen$_1$–oxygen$_2$ distance (r_{OH}) between the closest hydrogen of the "donor" molecule and the oxygen of the "acceptor" molecule is smaller than the first minimum of the oxygen–hydrogen RDF, and 3) the angle ϕ between the oxygen$_1$–hydrogen$_1$

vector and the oxygen$_1$–oxygen$_2$ vector is smaller than 30 degrees.[43] Only if all three geometrical conditions are fulfilled, we consider molecule 1 as donating a hydrogen bond to molecule 2.

The q criterion, proposed in Ref.[42], consists of computing for every molecule i the quantity q_i=$1 - \frac{3}{8}\sum_{j=1}^{3}\sum_{k=j+1}^{4}\left[cos(\theta_{ijk}) + \frac{1}{3}\right]^2$, where θ_{ijk} is the angle formed by the oxygens of molecules i and two of its four nearest neighbours j and k (the molecule i being at the vertex of the angle). The q-parameter takes a value of 1 when the four nearest neighbours are in a perfect tetrahedral arrangement around the central one.

We now compute the WF, HB or q distributions for the liquid and the vapour phase and present our results in Fig. 7.3, the conditions at which we have performed these analysis are noted in Ref. [2].

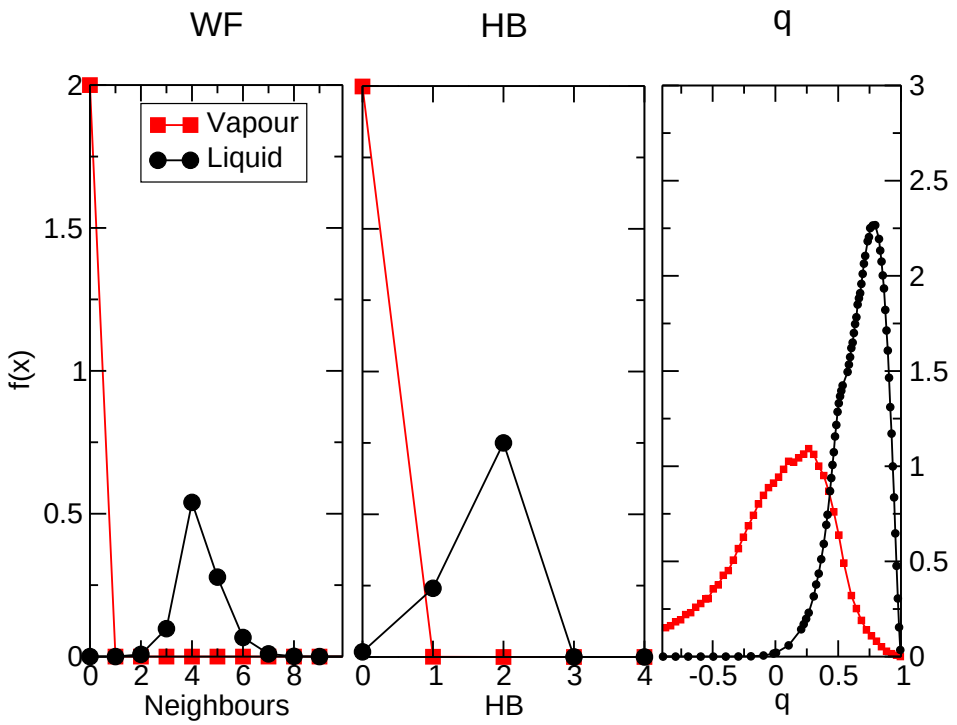

Figure 7.3: First-neighbours distribution (computed with WF), distribution of H-bonded molecules (HB) and distribution of the tetrahedal order parameter q for a system consisting of liquid water (black) or vapour (red).

[2]The liquid, with a density of ρ = 0,979 g/cm^3, has been equilibrated at T = 298 K and p = 1 bar and the vapour, with a density of ρ = 0,821 g/cm^3, at T = 578 K and p = 0,67 bar

Using the WF criterion, from the nearest neighbours distribution of the liquid and vapour system, we can identify as liquid-like all particles having a number of neighbours equal to or larger than one and vapour-like otherwise (see Fig. 7.3WF). From the distribution of H-bonded molecules in the liquid and vapour system, we can identify as liquid-like all particles that donate at least one hydrogen bond and vapour-like otherwise (see Fig. 7.3HB). In both cases, there is practically no overlap between the liquid and vapour distributions: every vapour molecule lacks hydrogen bonds, whereas most of the liquid molecules have two donor hydrogen bonds, as expected for stable water. In the q case (see Fig. 7.3q), computing the distribution of tetrahedrally ordered molecules in a vapour and a liquid, we observe that the probability distributions overlap considerably.

Given that the distributions are not overlapping, both the HB and the WF criterion are equally well suited to distinguish between vapour and liquid-like molecules, whereas the q criterion seems not to be the best choice due to the clear overlap. For our purposes, we decide to use the HB criterion and, thus, vapour molecules are detected by their lack of *donor* hydrogen bonds.

Step 2: As in the V-method and in Ref.[6], we *superimpose a three-dimensional grid* on our system and assign each cell on the grid to be either *vapour or liquid-like* depending on the molecules occupying the cell. To do this, we consider the oxygen's Lennard-Jones diameter $\sigma = 3{,}1589$ [13] to be each molecule's exclusion sphere: If the center of a cell is under an exclusion sphere, it will be labeled as either liquid- or vapour-like, according to the type of the molecule. When a cell contains more than one type of molecules, for instance a liquid- and a vapour-like molecule, it will be labelled as *liquid*-like.

Once we have classified all cells touched by molecules, we are left with labelling cells which do not clearly belong to any molecule: so called "empty cells". These appear when the size of the grid cells is comparable to the particle's diameter (see Appendix B). To classify the empty cells as liquid or vapour-like, we analyse both their first and second neighbour cells. If the number of face-sharing empty/vapour first neighbour cells is at least 7, then we analyze the number of face-sharing empty/vapour second neighbour cells: if they also are at least 7, the empty cell is identified as vapour-like. This procedure allows to avoid considering the typical small çavitiesçharacterizing a network-forming liquid as vapour-like cells.

Care should be taken when choosing the mesh size of the grid, which is defined as $\Delta = L/\delta$, where L is the box edge and δ the number of cells per edge. δ is a constant, therefore the volume Δ^3 of the grid cells fluctuates with the simulation box in a simulation at constant pressure. For all system sizes studied here, we set Δ to be about half of the oxygen diameter, which

is significantly smaller than the value of about $1{,}5\sigma$ chosen in Ref.[6]. When choosing the proper value of Δ, we aim to get a good balance between determining the volume of the bubble with good accuracy and avoiding to create small cells not easily assignable as liquid or vapour-like (See Appendix A and C): in our study, we set $\Delta = L/19$.

Step 3: Once we have allocated all cells of the grid, *we cluster vapour-like cells into bubbles and identify the bubble with the largest volume as the local order parameter,* $V^{\mathrm{M}}_{\mathrm{bubble}}$. A typical bubble obtained with the M-method is represented in Figure 7.4. By construction, the M-method satisfies the requirements 1, 2, 4 and 5 stated above. Concerning the third point, we should stress that the "true"volume of the bubble is affected by the volume discretisation we are using.

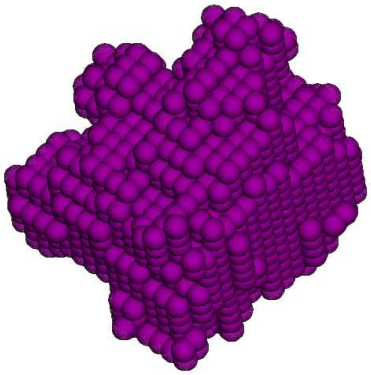

Figure 7.4: Typical bubble obtained with the M-method.

7.5. Results

In this section, we first use the two methods introduced to determine the volume of the largest bubble ($V^{\mathrm{V}}_{\mathrm{bubble}}$ and $V^{\mathrm{M}}_{\mathrm{bubble}}$) as an order parameter to analyze trajectories of water at ambient conditions. Then, we study trajectories where spontaneous cavitation occurs and compare the estimates for the volume of the largest bubble obtained using both methods. For this case, we compute the nucleation rate and elucidate nucleation properties using the MFPT-formalism. After that, we choose a thermodynamic state where nucleation is a rare event and compute the nucleation free energy barrier as a

function of the largest bubble evaluated with both the V- and the M-method and correlate both nucleation free energy barriers.

7.5.1. Water at ambient conditions

In order to assess how prone the two order parameters are to wrongly detect bubbles (and thus how well they perform according to criterion 4 given in the Introduction), we analyze molecular dynamics trajectories of liquid water at ambient conditions, where ideally no such bubbles should be detected at any time. In principle, this can be achieved easily by tuning the parameters of the respective order parameters, namely the mesh point density and the radius of the exclusion spheres, such that the detection of vapour in the liquid phase becomes extremely unlikely. However, this comes at the price of a decreased spatial resolution (including a significant increase in the size of the smallest bubble that can be detected by the order parameter) and as such our choices for the parameters represent a compromise between minimizing the erroneous detection of bubbles and obtaining good spatial resolution.

The average frequency of occurrence $\langle n(V_{\text{bubble}})\rangle/\langle V\rangle$ (shown in Fig. 7.5) is the average number of times a bubble with a volume between V_{bubble} and $V_{\text{bubble}} + \mathrm{d}V$ occurs per configuration per unit volume over the course of a trajectory.

While the false detection of bubbles does occasionally occur, analysis of the frequency of bubble occurence reveals that the detected bubbles are both rare and of very small size. If one divided the systems into parts with a volume of $1\,\mathrm{nm}^3$ each, at ambient conditions one would find a bubble roughly in one of 180 such cubes when using the M-method (due to its very accurate classification of vapour and liquid-like cells) and in one of 50 cubes when using the V-method. The typical volume of the smallest bubble detected is $0{,}0025\,\mathrm{nm}^3$ for the M-method and $0{,}035\,\mathrm{nm}^3$ for the V-method [3], comparable to the average volume occupied by a water molecule at ambient conditions ($\sim 0{,}03\,\mathrm{nm}^3$).

[3] Note that we used the V-method in the parametrisation obtained from the fit shown in Fig. 7.1, which was computed at negative pressures. Calibrating the V-method at ambient conditions would result in a (likely small) change in the volume of the detected bubbles but would not affect their frequency of appearence.

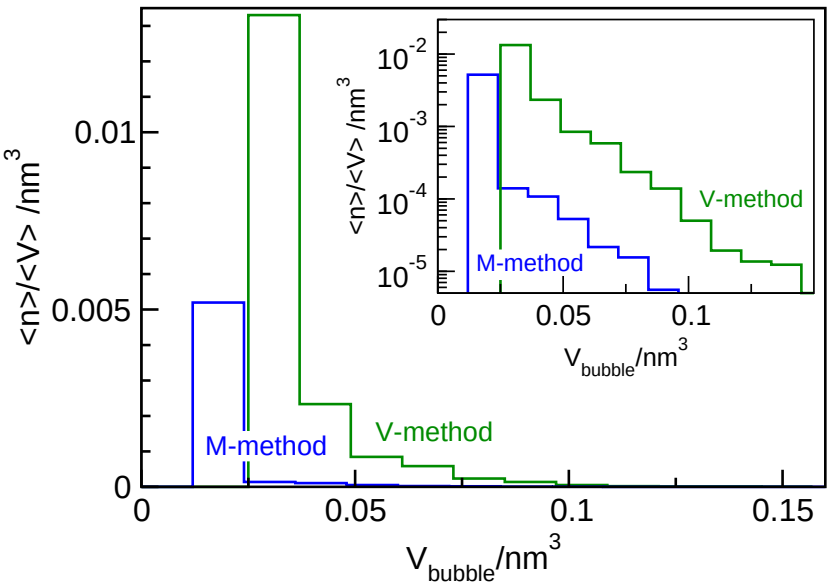

Figure 7.5: Frequency of occurrence $\langle n(V_{\text{bubble}})\rangle/\langle V\rangle$ of bubbles of volume V_{bubble} at ambient conditions. The width of each histogram bin is $\mathrm{d}V = 0{,}012\,\mathrm{nm}^3$. The inset shows $\langle n(V_{\text{bubble}})\rangle/\langle V\rangle$ on a logarithmic scale. The histograms were obtained from an unbiased molecular dynamics simulation at 298 K and 1 bar.

7.5.2. Comparing the V- and M-methods to detect the volume of the largest bubble

We now consider 200 independent trajectories of spontaneous nucleation in over-stretched water at $T = 280$ K and $p = -2250$ bar and evaluate the volume of the largest bubble with both the V- and M-method. In Figure 7.6 we show $V^{\mathrm{M}}_{\text{bubble}}$ versus $V^{\mathrm{V}}_{\text{bubble}}$.

When comparing the M-method with the V-method, we can distinguish two regimes connected by a crossover region. When the largest bubble is small ($\leq 0{,}3$ nm^3), the volume estimates obtained with the two methods are quite different. This is because, by construction, the M-method avoids labelling minute voids in the metastable liquid as bubbles whereas the V-method detects small bubbles with a comparatively higher frequency.

When the volume of the largest bubble exceeds this regime, the two methods give more similar results, even though the V-method yields larger volumes than the M-method on average. The mean value of $V^{\mathrm{M}}_{\text{bubble}}$ at a given value of $V^{\mathrm{V}}_{\text{bubble}}$ (shown as the dotted line in Fig. 7.6) does not change its shape when passing the critical regime (indicated by the change from green to pink dots) which implies that bubbles on both sides of the free energy

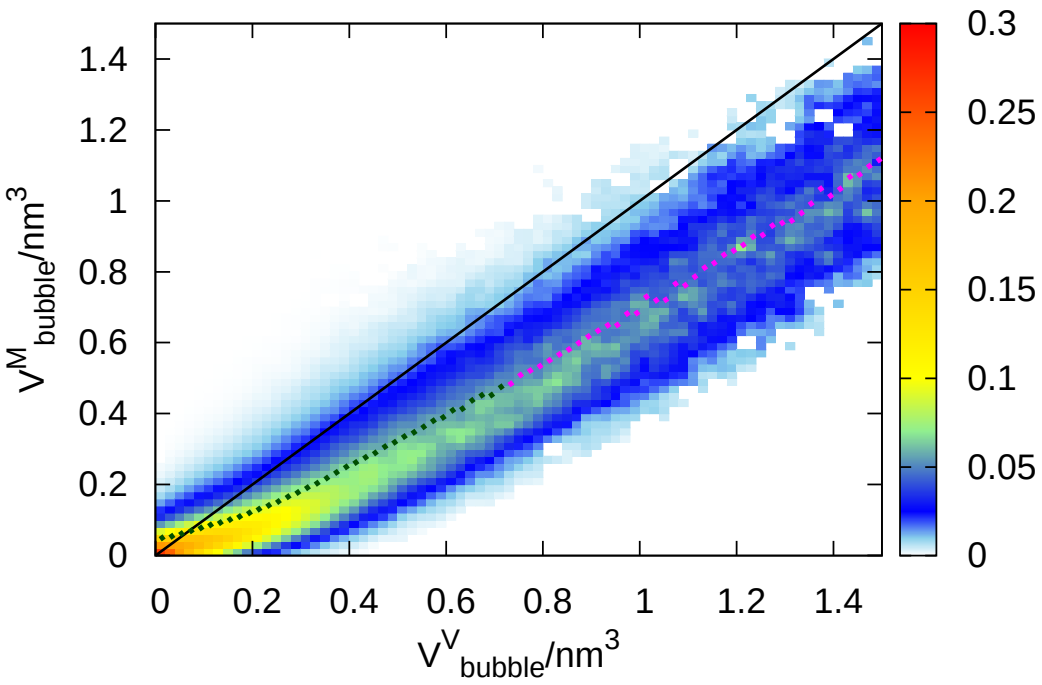

Figure 7.6: Largest bubble volume estimates using the M-method (on the y-axis) and the V-method (on the x-axis). The color of each point encodes the probability $P(V^{\mathrm{M}}_{\mathrm{bubble}}|V^{\mathrm{V}}_{\mathrm{bubble}})$ of finding $V^{\mathrm{M}}_{\mathrm{bubble}} \pm 0{,}01\,\mathrm{nm}^3$ given a value of $V^{\mathrm{V}}_{\mathrm{bubble}} \pm 0{,}01\,\mathrm{nm}^3$. The dotted line shows the average volume estimate $\langle V^{\mathrm{M}}_{\mathrm{bubble}}(V^{\mathrm{V}}_{\mathrm{bubble}})\rangle$, where green/pink dots correspond to precritical/postcritical bubble volumes (with a critical volume of $\sim 0{,}7\,\mathrm{nm}^3$, see Table I). The solid black line has a slope of one and is a guide to the eye. The fit parameters for the V-method are $k_1 \approx 0{,}99\,\mathrm{nm}$ and $k_2 \approx 0{,}37\,\mathrm{nm}^2$ at these conditions (see Equ. (7.5)).

barrier have similar structural properties.

For large bubbles ($V^{\mathrm{V}}_{\mathrm{bubble}} \geq 3\,\mathrm{nm}^3$), the ratio between the average volume estimates obtained by the two methods approaches $\langle V^{\mathrm{M}}_{\mathrm{bubble}}\rangle / V^{\mathrm{V}}_{\mathrm{bubble}} \simeq 0{,}8$, which allows for an easy conversion between the volume estimates of both methods for large bubbles.

In Fig. 7.7 we now focus on the time evolution of the volume of the largest bubble during a cavitation trajectory (one of those shown in Fig. 7.6). While the overall shape of the curves is similar, the volume estimate given by the M-method exhibits fluctuations with a higher frequency than the V-method. As shown in the inset of Fig. 7.7, both methods are able to detect "almost-critical"V_{bubble} fluctuations, i.e., the growth and shrinking of the largest bubble around its critical size of $\sim 0{,}7\,\mathrm{nm}^3$ (Table I). In what follows

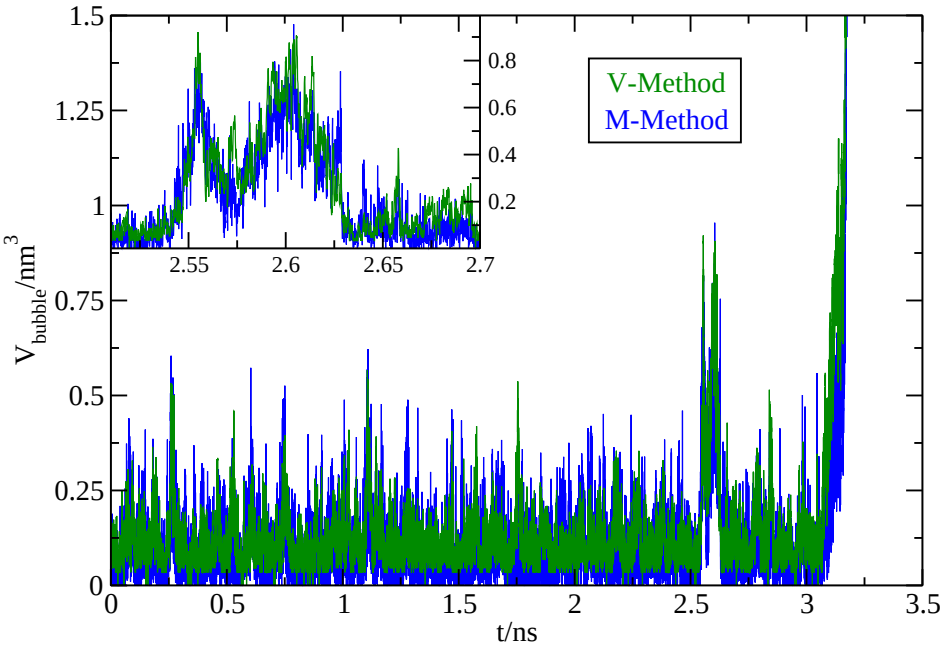

Figure 7.7: Comparing the time evolution of the volume of the largest bubble computed with either the M-method (blue) or the V-method (green) for the same cavitating trajectory. The inset shows a zoom around t $\sim$ 2,60 ns. Notice that the y-axis of the inset is on the right-hand side and the units are the same as the main figure.

we will study the effect of the two order parameters on the obtained values of nucleation properties.

7.5.3. Spontaneous bubble nucleation in over-stretched water

We first study over-stretched water at thermodynamic conditions where bubble nucleation happens spontaneously in the simulation. In particular, we investigate water bubble nucleation at $T = 280$ K and $p = -2250$ bar as in Ref.[11]. For 200 MD trajectories, along which spontaneous cavitation occurs, we compute the volume of the largest bubble and use it as a local order parameter to follow the nucleation mechanism. By means of the MFPT-formalism we compute the nucleation rate, J, and the critical volume, V^*_{bubble}. In order to determine the volume of the largest bubble, we use several approaches: the M- and V-methods proposed in this work as well as the approaches used in Ref.[6] (which uses the WF criterion to distinguish between liquid/vapour molecules) and Ref.[11] (based on the Voronoi tessellation). In the latter al-

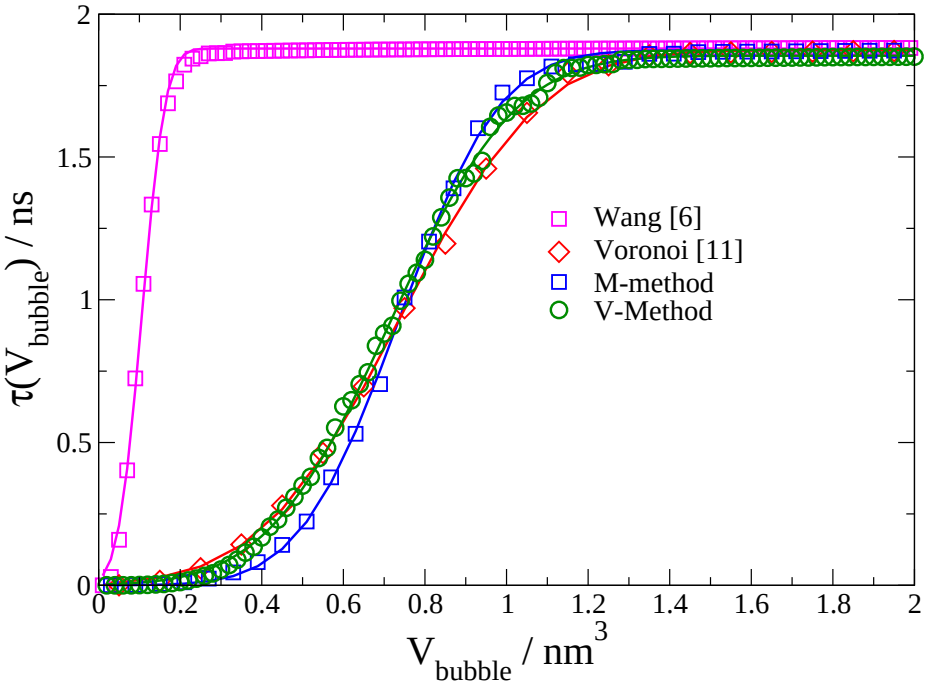

Figure 7.8: Mean first-passage time of the largest bubble at $T = 280$ K and $p = -2250$ bar using the order parameters indicated in the legend. The symbols are simulation data and the lines are fits to Equ. (7.1).

gorithm, the bubbles were detected by tracking down interfacial molecules; therefore the volume of those molecules was implicitly included in the final volume of the bubble. Since neither the M-method nor the V-method, by construction, include the interfacial molecules of the largest bubble as a part of the bubble, when representing the results from Ref.[11] we have re-computed the MFPT removing the volume of the interfacial molecules.

The calculated values for $\tau(V_{\text{bubble}})$ are presented in Fig. 7.8. The steepest MFPT curve is obtained with the method of Ref.[6]. This method fails to detect small bubbles and severely underestimates the volume of bubbles before the system cavitates, thus underestimating the size of the critical volume. Interestingly, the MFPT curves obtained with the M-method, the Voronoi-based method of Ref.[11] (removing the interfacial molecules) and the V-method have very similar shapes. These three methods allow to identify very small bubbles (as shown by their smooth MFPT curve) and show the inflection points and plateaus at essentially the same values. From the MFPT curves in Fig. 7.8 we calculate nucleation properties such as τ_J, J, Z and V^*_{bubble}[31,44] (see Equ. (7.1)), as reported in Table 7.1.

Notice that the nucleation times τ_J are independent of the method used to identify the largest bubble. Since the nucleation rate only depends on τ_J, the nucleation rate is independent of the method chosen to evaluate the size of the largest bubble.

However, when comparing the Zeldovich factors and the critical bubble volumes V^*_{bubble} provided by the algorithms, we observe some differences because both quantities are sensitive to the method used to evaluate the largest bubble volume. The smallest value of V^*_{bubble} is detected with the method used in Ref.[6], which also gives the largest value for the Zeldovich factor: this implies that the curvature of the free energy barrier is larger than in the other cases. In contrast, the Voronoi-based method from Ref.[11] (removing the interfacial molecules), the M-method and the V-method give very similar values of V^*_{bubble} [4] and Z. This means that not only are the methods able to detect the critical bubble with essentially the same volume, but also that the curvature of the computed free energy barrier is quite similar.

Method	τ_J	Z	V^*_{bubble}	J
WF[6]	1.88	4.93	0.11	3.09
Voronoi[11]	1.87	1.48	0.74	3.10
M-method	1.87	1.23	0.74	3.10
V-method	1.85	1.66	0.72	3.13

Table 7.1: Nucleation time τ_J (ns), Zeldovich factor Z (nm^{-3}), critical volume V^* (nm^3) and nucleation rate J (10^{28} cm^{-3} s^{-1}) at $T = 280$ K and $p = -2250$ bar using different methods to identify the largest bubble. The average volume of the metastable liquid is $\langle V \rangle = 17{,}23\,\text{nm}^3$.

[4] The very similar estimates for V^*_{bubble} appear to be at odds with the data presented in Fig. 7.6, which show that the V-method gives larger volume estimates than the M-methods on average. However, since the MFPT-analysis is based on the dynamics of the system, the obtained estimate depends not only on the mean of the order parameter used to track bubble nucleation but also on its fluctuations. In particular, a higher frequency of fluctuations in the order parameter leads to a higher estimate for V^*_{bubble}. As Fig. 7.7 shows, estimates obtained with the M-method exhibit larger fluctuations than estimates by the V-method, which, when V^*_{bubble} is computed from MFPT analysis, cancels the difference in the average bubble volume detected by the two methods, leading to a virtually identical estimate for V^*_{bubble}.

7.5.4. Non-spontaneous bubble nucleation in over-stretched water

We now study over-stretched water at thermodynamic conditions ($T = 325$ K and $p = -1500$ bar) where bubble nucleation does not happen spontaneously within the time scales accessible to straight-forward molecular dynamics simulation. On the one side, we identify the largest bubble volume with the V-method and use umbrella sampling combined with hybrid Monte Carlo to compute the bubble nucleation free energy barrier. On the other side, we identify the largest bubble volume with the M-method and compute the bubble nucleation free energy barrier using HMC-NpT[36].

To compute the free energy as a function of the volume V_{bubble} we proceed in the following way. First we carry out a straightforward molecular dynamics simulation at negative pressure and compute $\langle n(V_{\text{bubble}})\rangle$, the average number of bubbles with volume in a narrow interval $[V_{\text{bubble}}, V_{\text{bubble}} + \Delta V_{\text{bubble}}]$. This simulation will yield $\langle n(V_{\text{bubble}})\rangle$ in the range of volumes that are accessible on the time scale of the simulation. To compute the average bubble number $\langle n(V_{\text{bubble}})\rangle$ for larger volumes V_{bubble}, we carry out umbrella sampling simulations with a bias on the volume of the largest bubble. The average bubble numbers obtained in such biased simulations are then conjoined with the result of the straightforward molecular dynamics simulation, yielding the average bubble number $\langle n(V_{\text{bubble}})\rangle$ over a wide range of bubble volumes extending beyond the critical volume.

For large bubble volumes, the probability to find more than one bubble of a given volume at the same time becomes negligible. Accordingly, in this regime, the probability $P(V_{\text{bubble}})\,\Delta V_{\text{bubble}}$ to find a bubble with volume in the interval $[V_{\text{bubble}}, V_{\text{bubble}} + \Delta V_{\text{bubble}}]$ is given by $P(V_{\text{bubble}})\,\Delta V_{\text{bubble}} = \langle n(V_{\text{bubble}})\rangle$. Note that the probability density $P(V_{\text{bubble}})$ defined in this way is independent of the interval width ΔV_{bubble} used for the calculation of the average bubble number $\langle n(V_{\text{bubble}})\rangle$. At negative pressures, the probability density $P(V_{\text{bubble}})$ has a minimum at V^*_{bubble}, the critical bubble volume. According to classical nucleation theory, the rate at which cavitation occurs in a system of total volume V is proportional to the probability density $P(V^*_{\text{bubble}})$ of finding a bubble of critical volume V^*_{bubble} in the system. Hence, the nucleation rate, which quantifies the number of nucleation events per unit time and unit volume, is proportional to $P(V^*_{\text{bubble}})/V$. It makes therefore sense to define the free energy

$$F(V_{\text{bubble}}) = -k_{\text{B}}T \ln\left[\frac{\langle n(V_{\text{bubble}})\rangle}{V\,\Delta V_{\text{bubble}}}\right], \tag{7.6}$$

which is independent of system size. Then, $F(V^*_{\text{bubble}})$ corresponds to the

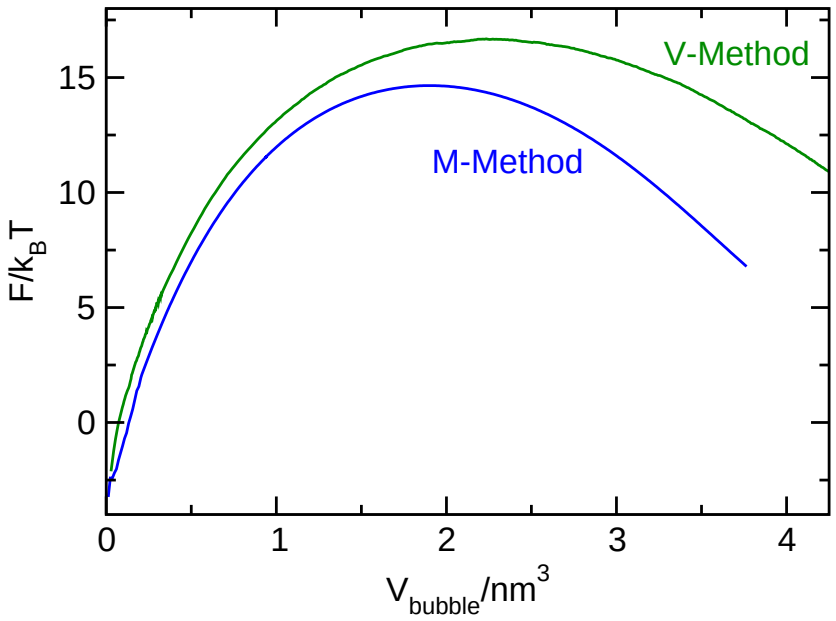

Figure 7.9: Free energy F as a function of the bubble volume for the V- and M-methods at $T = 325\,\mathrm{K}$ and $p = -1500\,\mathrm{bar}$.

nucleation barrier that needs to be crossed in order to form bubbles of supercritical size[45]. Note that this definition of the nucleation free energy ensures that the nucleation barrier $F(V^*_{\mathrm{bubble}})$ reflects the probability of critical bubbles and does not depend on the probability distribution of small bubbles, which should not affect the nucleation rate. The free energy $F(V_{\mathrm{bubble}})$ obtained using the M-method and the V-method is shown in Fig. 7.5.

The estimates for the free energy barrier heights obtained using the M-method and the V-method, respectively, differ by about $2\,k_{\mathrm{B}}T$, which constitutes reasonable agreement. At the same time, the estimates for the critical volume at the top of the barrier differ as one would expect: the critical volume obtained using the V-method is $0{,}36\,\mathrm{nm}^3(19\,\%)$ larger than the volume yielded by the M-method. These results are consistent with our findings in the case of lower barriers, namely, that on average the V-method gives higher estimates for the bubble volumes than the M-method (see Fig. 7.6).

7.6. Discussion and conclusions

In this manuscript we present two accurate and efficient grid-based methods to identify bubbles in a network-forming liquid: the M-method and the V-method. While both methods were built upon the grid-based approach

in Ref.[6], they strive to improve different aspects of the detection of bubbles in water.

The M-method introduces an accurate approach to identify vapour-like cells in the liquid. In this method, cells are labeled as either liquid- or vapour-like using information about nearest- and next-nearest neighbour cells in an effort to minimize the incorrect detection of small voids always present in network-forming liquids. This implies that the method, by taking into account additional neighbour shells, can be tuned to achieve spatial resolutions that are not accessible to straightforward grid-based approaches without wrongly detecting percolation of voids in the metastable liquid.

The V-method, on the other hand, is focused on obtaining a physically transparent volume estimate that is independent of arbitrary parameter choices such as mesh resolution or the radius of exclusion spheres. This is achieved by a calibration procedure that maps the bubble volume detected in the simulation onto the average change in system volume caused by bubbles of that size. Due to this calibration, the estimated bubble volume is compatible with the nucleation theorem and pV_{bubble} corresponds to the mechanical work associated with the formation of the bubble. This calibration procedure can also be used to improve other local order parameters when studying nucleation.

Both the M-method and the V-method yield the volume of the largest bubble, which can be used as a local order parameter. This allows one to directly track the evolution of bubbles and analyze their properties in large systems where a global order parameter would not be able to distinguish the emergence of bubbles from fluctuations in the metastable liquid. These order parameters achieve the goal of detecting the volume and shape of bubbles in the liquid with high spatial resolution without constraining the evolving bubbles to a particular shape and are computationally inexpensive.

When simulating water at ambient conditions, both methods detect bubbles only rarely. Comparing the two methods, owing to the M-method's extremely accurate detection of vapour-like cells, the bubbles detected using the M-method are even less frequent and the volume estimates for these bubbles is lower than in case of the V-method.

When comparing the nucleation properties obtained by using either method, we find that both yield similar results. Under conditions where cavitation occurs spontaneously in a straightforward molecular dynamics simulation, the estimates obtained for the volume of the critical cluster are in excellent agreement between the two methods (see Table 7.1). Under these conditions, the estimates obtained by the methods also agree very well with a Voronoi polyhedra analysis, which is a very precise but computationally expensive method for bubble detection.[11]

Closer to coexistence, when cavitation is extremely unlikely on timescales accessible in simulation, we use umbrella sampling to obtain an estimate for the free energy $-\ln \rho(V_{\text{bubble}})$ as a function of the volume of the largest bubble. Here, the estimate for the size of the critical bubble obtained by using the V-method yields, due to the volume calibration procedure, a larger value for the critical cluster and a smaller curvature of the free energy barrier than the M-method. However, the estimate for the height of the free energy barrier, which largely determines the experimentally accessible cavitation rate, obtained by the two methods is in good agreement. In the near future, we plan to use the methods introduced here to study the cavitation of water at negative pressures.

Acknowledgements

The work of M.A.G., J.L.A., J.L.F.A. and C.V. was funded by grants FIS2013/43209-P of the MEC and the Marie Curie Integration Grant PCIG-GA-2011-303941 (ANISOKINEQ). C.V. also acknowledges financial support from a Juan de La Cierva Fellowship. The work of G.M., P.G. and C.D. was supported by the Austrian Science Foundation (FWF) under grant P24681-N20. P.G. also acknowledges financial support from FWF grant P22087-N16. Calculations performed at the University of Vienna were carried out on the Vienna Scientific Cluster (VSC). We acknowledge Carlos Vega for helpful discussions and a critical reading of the manuscript. We thank Michael Grünwald and Jaffar Hasnain for useful discussions.

SUPPLEMENTAL MATERIAL for "Detecting bubbles in water at negative pressure"

M-method: assigning empty cells to be liquid or vapour-like: Initial labelling of the cells

In order to label each cell we proceed as follows. To start with, we label as liquid-like the cells beneath liquid particles and vapour-like the ones beneath vapour particles. Therefore, depending on the grid mesh L/δ (where L is the simulation box edge), we are left with a number of cells that do not clearly belong either to the liquid or to the vapour. At this initial stage, we make the assumption that empty cells are liquid-like. In what follows, we describe an algorithm to properly label them and correct for the initial guess.

The best choice for the threshold of the number of empty/vapour neighbours in the first and second cell

In our study, to identify an empty cell as vapour-like, we check that not only at least 7 of its *first neighbours* are neighbours to each other and vapour-like *but also* 7 of its *second neighbours*. In general, in order to choose the threshold for the first and second neighbour cell, we want to make sure that we avoid identifying empty cells in thermodynamically stable water.

Figure 7.10 represents the distribution of having the largest bubble of a given volume in the case of thermodynamically stable liquid water at 1 bar and 298 K. The largest bubble has been detected with the HB-criterion, assuming $\delta = 19$, and different values of the threshold for the number of first and second neighbours N_{nb} (we are always assuming that these two thresholds are the same).

As shown in the figure, all distributions are peaked around 0.017 nm^3, comparable to the volume of a water molecule ($\sim 0{,}030\,nm^3$) at these conditions: this means that with the largest probability the largest vapour bubble has the size of a water molecule. However, decreasing the threshold value of N_{nb}, the largest bubble can reach much larger volumes: this corresponds to detecting voids characteristic of the network-forming liquid as vapour bubbles (for instance, in the case N_{nb}=6). Therefore, the best choice for N_{nb} corresponds to the minimum value needed not to observe a distribution of large bubbles (larger than one water molecule in a liquid) in thermodynamically stable water. In our study, this condition is met by the choice of having at least 7 empty cells that are neighbours in the first cell together with 7 that are neighbours in the second one.

The best choice for L/δ

As stated in Step 2 of the M-method, when setting the optimal value of the grid's mesh size (L/δ) one has to satisfy two conditions. On the one side, the size of the cell grid must be as small as possible in order to reduce the error coming from the discretization of the bubble's volume. On the other side, the size of the cell grid must be as large as possible to avoid to label the "holes"which exist (even in its thermodynamically stable state) in a network-forming liquid such as water, as vapour cells. Figure 7.11 represents a two-dimensional sketch of the grid of liquid water molecules (represented by their oxygens) in three possible scenarios characterised by a different grid

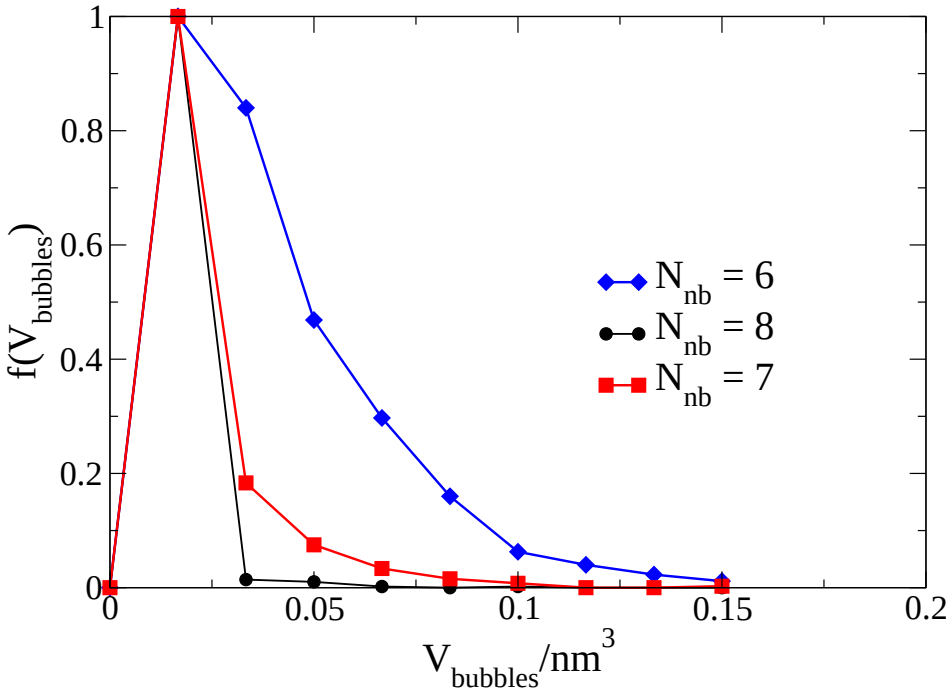

Figure 7.10: Distribution of the size of the largest bubble in a thermodynamically stable liquid at 1 bar and 298 K for different numbers of N_{nb} and $\delta = 19$.

mesh L/δ: a) $0{,}5\sigma < L/\delta$; b) $0{,}33\sigma < L/\delta < 0{,}5\sigma$; and c) $L/\delta < 0{,}33\sigma$. The distance between the molecules is slightly larger than σ (corresponding to the first minimum of the oxygen–oxygen pair distribution function).

To explain the criteria for the choice of the threshold of the number of first and second neighbours in Fig. 7.11 (2D grid), 3 was been used as the minimum number of empty/vapour-like neighbours. When we evaluate one empty cell, we check if this cell has at least 3 first empty/vapour neighbours that are also neighbours to each other and 3 or more second neighbours of the same type. Thus, we can label this cell as vapour-like under first and second neighbour criteria.

As in Ref.[6], in case a) we determine whether empty cells are liquid- or vapour-like. In this case, it is not necessary to apply our neighbour criteria because the grid size is large enough to allow to define every cell as vapour or liquid cells (there are no empty cells). However, if we find empty cells, we label all cells using only the first neighbour criterion. As shown in the figure, when

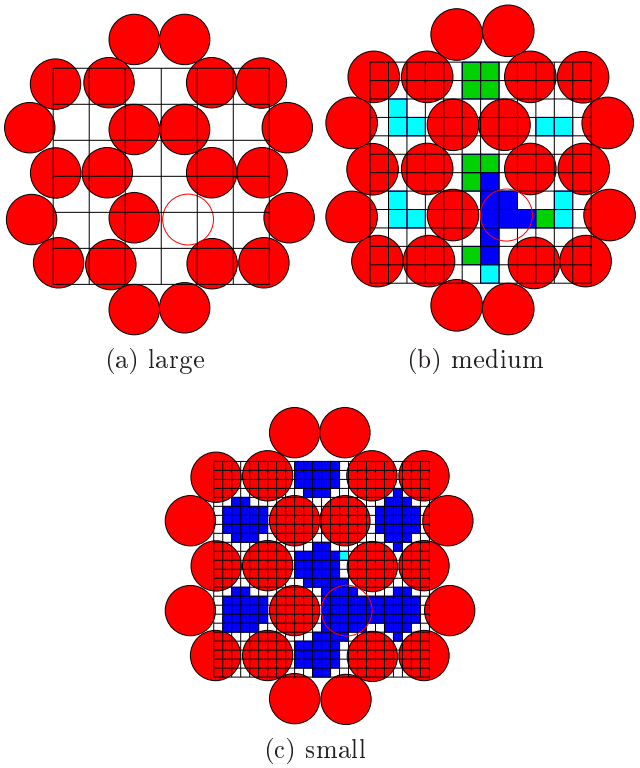

(a) large (b) medium

(c) small

Figure 7.11: Two-dimensional grid with usual liquid water-like structure. Solid red circles are oxygens and the empty red circle is one removed particle. (a) $0{,}5\sigma < L/\delta$; (b) $0{,}33\sigma < L/\delta < 0{,}5\sigma$; and (c) $L/\delta < 0{,}33\sigma$. Blue cells are the final bubble cells, cyan cells and green cells are the empty transformed into liquid cells after applying the first neighbours criteria and second neighbours criteria, respectively.

a void as large as one particle appears in the system, it is difficult to evaluate the bubble volume because we cannot detect empty cells. The drawback is that this choice strongly penalises interfacial molecules, i.e., molecules with a small number of vapour neighbours.

Case b) allows to better resolve the volume of the bubble. In this case, to assign empty cells we need to recur not only to the first neighbours, but also to the second ones. If we consider only the first-neighbour cells, we will label the empty cells between liquid particles as vapour-like (given that most of their first neighbours are empty or vapour-like). Whereas, considering also the second neighbour cells, we will label the empty cells as liquid-like (given that their second neighbours are not vapour-like).

Compared to the previous cases, the grid in case c) is the smallest. This situation can give more accurate estimates for the volume, but one would need to recur to the third neighbour cells in order to determine the nature of each empty cell. Even though in this way we improve the accuracy of the definition of the bubble's volume, this method is CPU-time consuming.

Therefore, we conclude that the best compromise in terms of CPU-time and precision in determining the bubbles'volume is case b). Labelling empty cells corrects for the initial guess that empty cells are liquid-like unless when the cells are under the bubble. This allows us to find the real bubble not the natural voids always present in a network-forming liquid. Moreover, having properly detected all empty cells has also the advantage to be able to clearly distinguish between two neighbouring bubbles (without detecting them as a merged single bubble[6]).

Bibliografía

1. H. Cochard, C. R. Phys. **7**, 1018 (2006).
2. T. D. Wheeler and A. D. Stroock, Nature **455**, 208 (2008).
3. O. Vincent, P. Marmottant, P. A. Quinto-Su, and C.-D. Ohl, Phys. Rev. Lett. **108**, 184502 (2012).
4. K. Ohsaka and E. H. Trinh, Appl. Phys. Lett. **73**, 129 (1998).
5. D. Yu, B. Liu, and B. Wang, Ultrason. Sonochem. **19**, 459 (2012).
6. Z.-J. Wang, C. Valeriani, and D. Frenkel, J. Phys. Chem. B **113**, 3776 (2009).
7. K. Torabi and D. S. Corti, J. Phys. Chem. B **117**, 12479 (2013).
8. K. Torabi and D. S. Corti, J. Phys. Chem. B **117**, 12491 (2013).
9. V. K. Shen and P. G. Debenedetti, J. Chem. Phys. **111**, 3581 (1999).
10. S. L. Meadley and F. A. Escobedo, J. Chem. Phys. **137**, 074109 (2012).
11. J. L. F. Abascal, M. A. Gonzalez, J. L. Aragones, and C. Valeriani, J. Chem. Phys. **138**, 084508 (2013).
12. D. Kashchiev, J. Chem. Phys. **76**, 5098 (1982).
13. J. L. F. Abascal and C. Vega, J. Chem. Phys. **123**, 234505 (2005).
14. C. Vega and J. L. F. Abascal, Phys. Chem. Chem. Phys. **13**, 19663 (2011).
15. C. Vega, J. L. F. Abascal, and I. Nezbeda, J. Chem. Phys. **125**, 034503 (2006).

16. J. L. Aragones, L. G. MacDowell, I. J. Siepmann, and C. Vega, Phys. Rev. Lett. **107**, 155702 (2011).

17. C. Vega and E. de Miguel, J. Chem. Phys. **126**, 154707 (2007).

18. P. Geiger and C. Dellago, J. Chem. Phys. **139** (2013).

19. D. Van Der Spoel, E. Lindahl, B. Hess, G. Groenhof, A. E. Mark, and H. J. C. Berendsen, J. Comput. Chem. **26**, 1701 (2005).

20. H. Kamberaj, R. J. Low, and M. P. Neal, J. Chem. Phys. **122**, 224114 (2005).

21. T. F. Miller, M. Eleftheriou, P. Pattnaik, A. Ndirango, D. Newns, and G. J. Martyna, J. Chem. Phys. **116**, 8649 (2002).

22. G. J. Martyna, M. E. Tuckerman, D. J. Tobias, and M. L. Klein, Mol. Phys. **87**, 1117 (1996).

23. S. Nosé, J. Chem. Phys. **81**, 511 (1984).

24. W. J. Hoover, Phys. Rev. A **31**, 1695 (1985).

25. H. Andersen, J. Comput. Phys. **52**, 24 (1983).

26. H. C. Andersen, J. Chem. Phys. **72**, 2384 (1980).

27. G. Bussi, D. Donadio, and M. Parrinello, J. Chem. Phys. **126**, 014101 (2007).

28. M. Parrinello and A. Rahman, J. Appl. Phys. **52**, 7182 (1981).

29. J. P. Ryckaert, G. Ciccotti, and H. J. C. Berendsen, J. Comput. Phys. **23**, 327 (1977).

30. U. Essmann, L. Perera, M. L. Berkowitz, T. Darden, H. Lee, and L. G. Pedersen, J. Chem. Phys. **103**, 8577 (1995).

31. J. Wedekind, R. Strey, and D. Reguera, J. Chem. Phys. **126**, 134103 (2007).

32. M. A. Gonzalez, Master's thesis, Fac. Ciencias Quimicas, Univ. Complutense, Madrid (2011).

33. G. M. Torrie and J. P. Valleau, J. Comput. Phys. **23**, 187 (1977).

34. S. Duane, A. D. Kennedy, B. J. Pendleton, and D. Roweth, Phys. Lett. B **195**, 216 (1987).

35. B. Mehlig, D. W. Heermann, and B. M. Forrest, Phys. Rev. B **45**, 679 (1992).

36. M. A. Gonzalez, E. Sanz, C. McBride, J. Abascal, C. Vega, and C. Valeriani, In preparation (2014).

37. M. E. M. Azouzi, C. Ramboz, J.-F. Lenain, and F. Caupin, Nat. Phys. **9**, 38 (2013).

38. M. Grünwald and C. Dellago, J. Chem. Phys. **131**, 164116 (2009).

39. P. R. ten Wolde and D. Frenkel, J. Chem. Phys. **109**, 9901 (1998).

40. A. Luzar and D. Chandler, J. Chem. Phys. **98**, 8160 (1999).

41. P. L. Chau and A. J. Hardwick, Mol. Phys. **93**, 511 (1998).

42. J. R. Errington and P. G. Debenedetti, Nature **409**, 318 (2001).

43. E. Guàrdia, J. Martí, L. García-Tarrés, and D. Laria, J. Mol. Liq. **117**, 63 (2005).

44. J. Wedekind, G. Chkonia, J. Wölk, R. Strey, and D. Reguera, J. Chem. Phys. **131**, 114506 (2009).

45. L. Maibaum, Phys. Rev. Lett. **101**, 019601 (2008).

Results: Chapter 8

Spontaneous bubble nucleation in simple and molecular liquids studied with the largest spherical cavity

Miguel A. González[1,2], *Jose L. F. Abascal*[1], *C. Valeriani*[1] *and F. Bresme*[2,3]

(1) Departamento de Química Física, Facultad de Ciencias Químicas, Universidad Complutense de Madrid, 28040 Madrid, Spain.

(2) Chemical Physics Section, Department of Chemistry, Imperial College London, London SW7 2AZ.

(3) Department of Chemistry, Norwegian University of Science and Technology, Trondheim, Norway.

8.1. Abstract

We investigate homogeneous spontaneous vapour nucleation from two very different over-stretched liquids: a simple liquid (such as Lennard-Jones) and a molecular one (such as water). To detect the bubbles forming in the system, we make use of an order parameter based on the identification of the largest spherical cavity in the metastable liquid. This allows us to follow the nucleation mechanism and to numerically evaluate the bubble nucleation free-energy using the mean first passage time technique. For the Lennard-Jones, we obtain a free-energy barrier height of ~ 11 k_BT, in good agreement with Ref.[1] at the same thermodynamic conditions. For water, we predict a free-

energy barrier height of ~ 11 k_BT, in good agreement with Ref.[2] at the same thermodynamic conditions. Therefore, we conclude that the largest spherical cavity can be used to study bubble nucleation not only when dealing with a simple fluid but also in a molecular liquid (such as water) at negative pressures.

8.2. Introduction

The nucleation free-energy barrier is a key quantity to estimate nucleation rates in crystal, droplet or vapor nucleation (also called cavitation). The top of the free-energy barrier (ΔG^*) determines the probability to form the critical nucleus of the stable phase within the thermodynamically metastable phase. Classical Nucleation Theory[3] (CNT) is a phenomenological theory widely used to describe the nucleation phenomenon: under given assumptions, it allows to estimate the top of the free-energy barrier (thus the size of the critical nucleus), and the steady-state nucleation rate, even though predictions of nucleation rates can differ from experimental estimates by several orders of magnitude[4,5,6,7,8] Besides CNT, statistical mechanics theories[6] have been developed to study nucleation phenomena and quantify free-energy barriers and nucleation rates, together with atomistic computational approaches[9,10,11,12,13,14,15], that also allow to investigate the microsocopic mechanism of nucleation, visualizing the formation of the critical nucleus and examining its structure (see e.g.[12,11,16]).

In this work, we study cavitation under negative pressure and determine the vapor nucleation free-energy barrier in two very different liquids: a molecular liquid (such as water) and a simple liquid (such as Lennard-Jones). Vapour nucleation is a relevant mechanism in sonochemistry[17] or erosion induced by cavitation[18]. In the last decades, there have been a number of theoretical and numerical studies that provided insights of vapour nucleation from a metastable super-heated simple liquid. In their numerical work, Shen and Debedenetti[12] used a global order parameter (function of the total vapor density) together with the umbrella sampling technique to investigate bubble nucleation in a simple liquid under superheated conditions. They observed that the critical nucleus significantly departed from the spherical symmetry (assumed in CNT) resembling more a "weblike" porous structure spanning the whole system. It has been recently shown[16,13] that when studying bubble cavitation one can use the volume of the largest bubble as a local order parameter. In Ref.[16] the authors studied the same system as in Ref. 12 using a local order parameter (the volume of the largest bubble) and forward flux sampling, and concluded that the vapour nucleation process instead involved

the formation of rather compact bubbles.

There have been in the literature several works approximating the critical bubble to an empty spherical cavity[19,1,20,8,21,22,23,24]: therefore, one could estimate the bubble nucleation free-energy by calculating the work needed to generate a cavity with a radius as large as the critical one.

When nucleation happens spontaneously, the Mean First Passage Time (MFPT)[25] is a useful technique to quantify both nucleation rates and free-energies barriers. It has been recently used to investigate vapour nucleation in metastable over-stretched water[2], where bubbles were identified by means of Voronoi polyhedra. The order parameter presented in Ref.[2], i.e. the volume of the largest bubble identified with the Voronoi polyhedra, relies on targeting structural properties of the liquid phase, exploiting the differences between these and the properties of liquid-vapor interface. Given that such properties can be very different when comparing a molecular to a simple fluid, one could not use the same Voronoi-based order parameter to study bubble cavitation from very different fluids.

To be able to ientify the same order parameter in different metastable fluids, we now identify the largest among all *spherical cavities* that spontaneously form in metastablewater or simple fluids, and use the radius of the largest cavity as an order parameter to study vapor nucleation from over-stretched liquids.

The concept of "cavity" has been widely used to quantify the characteristic structure of fluids. A cavity approximates the critical nucleus as a spherical volume without particles. It obviously represents a simplification of a real nucleus which might contain atoms in the emerging vapour phase, featuring a shape that deviates from a spherical geometry. Few decades ago, Reiss *et al.*[26,27] developed the *Scaled Particle Theory* (SPT), that provides a direct link between statistical distribution of cavities in a fluid and the work needed to create a cavity with a particular radius. The connection between cavity nucleation and free-energy has been already exploited to investigate both cavitation from simple fluids[20,8,21,22,23,24], and the relevance of Coulomb interactions in cavity formation[28] or solute solubility[29]. The latter example is of particular relevance, as the SPT provides important insights in the hydrophobic behaviour of nanoscale solutes[29,30]. In what follows we will show that the concept of cavity can be used to construct a reasonable order parameter that is valid at the same time for water and simple fluids, not being based on specific structural features of the liquid of interest.

The chapter is structured as follows. We start with discussing the theoretical background needed to obtain the cavities'free-energy from the cavity probability distribution and both nucleation rates and free-energy barriers from MFPT. Next, we study bubble nucleation in over-stretched water and

Lennard-Jones and compare with existing results.

8.3. Methods

8.3.1. Theoretical background

When equilibrating a liquid at a pressure below coexistence, it becomes over-stretched and metastable and eventually will phase transform into the thermodynamically stable vapor via a nucleation mechanism. According to Classical Nucleation Theory, the top of the free-energy for bubble nucleation is given by

$$\beta\Delta G^* = \frac{16\pi\gamma^3}{3\left(P_s - P\right)^2} \tag{8.1}$$

where γ is the liquid-vapor interfacial free-energy, $\beta = 1/k_B T$ (T the temperature and k_B is the Boltzmann constant), P the pressure and P_s the saturated pressure, whereas the nucleation rate, J, can then be written as

$$J = k \exp\left(-\beta\Delta G^*\right) \tag{8.2}$$

being k the kinetic prefactor ($k = \rho\left(\frac{2\gamma}{\pi m B}\right)$, being ρ the density of the liquid, γ the liquid-vapor surface tension, m the mass of a molecule and B a factor that takes into account the mechanical equilibrium of a bubble, set to 1 in cavitation experiments[31]).

When the liquid is over-stretched at a pressure not so far from the spinodal one, it becomes metastable and nucleates spontaneously (being the nucleation free-energy barrier to overcome quite low). The MFPT technique[14,32] has been recently developed to calculate both the nucleation rate or the free-energy barrier from the analysis of many spontaneously nucleating trajectories. It focuses on the evaluation of the *first* time (τ) of appearance of a given value of the order parameter (for instance, the volume of the largest bubble V) averaged over a large number of nucleating trajectories. Therefore, following Ref.[14], the volume dependence of $\tau(V)$ can be fitted to

$$\tau(V) = \frac{\tau_J}{2}\{1 + erf\left[c(V - V^*)\right]\} \tag{8.3}$$

where τ_J is the nucleation time, V^* the volume of the critical bubble and c a constant proportional to the Zeldovich's factor $Z = c/\sqrt{\pi}$ (that takes into account the curvature at the top of the free-energy barrier). Thus the nucleation rates can be obtained as[14,15]

$$J = \frac{1}{\tau_J V_s} \tag{8.4}$$

being V_s the mean system's volume. The nucleation free-energy is then give by[25],

$$\beta\Delta G(V) = \ln B(V) - \int \frac{dV'}{B(V')} + D \tag{8.5}$$

where D is a reference free-energy that needs to be determined (see below), and

$$B(V) = -\frac{1}{P(V)}\left(\int_V^{V_m} P(V')dV' - \frac{\tau(V_m)-\tau(V)}{\tau(V)}\right)$$

being $P(V)$ the normalized probability function of finding a bubble of volume V in the metastable state and V_m has been set to an arbitrary large value of $4nm^3$.

When studying bubble cavitation one can use the volume of the largest bubble as a local order parameter. This has been estimated via a grid-based method [16,13] or via a Voronoi construction[2]. In this work, we approximate this volume as that of a sphere with radius equal to the *largest cavity radius* R_{max} (thus $V = \frac{4}{3}\pi R_{max}^3$). This radius can be readily computed with algorithms already used to compute cavity probability distributions (see eg. Ref.[28]).

8.3.2. Radius of the largest spherical cavity (LSC) as a local order parameter

Similarly to Ref.[28], our approach relies on the identification of the *largest spherical cavity* (LSC) spontaneously appearing in the metastable liquid, both in a simple fluid (Lennard-Jones) and in water. The procedure is the following:

Step 1 We build a three dimensional cubic grid that is mapped onto the simulation box, choosing 20^3-30^3 cubic cells for both water and Lennard-Jones (since these grid sizes provide accurate probability distributions). When simulating a NpT ensemble, we fix the number of mesh per box edge, and change their size when scaling the simulation box.

Step 2 For a given cell, we calculate the shortest distance between the cell's geometrical center and each liquid's atom or water's Oxygens.

Step 3 Having computed all distances, we detect the largest one that corresponds to the radius of the largest cavity, R_{max}. Therefore, we estimate its volume as $4/3\pi R_{max}^3$. We can also estimate the cavity probability

distribution as a function of the corresponding radius, and from this extract the one for the corresponding volumes $P(V)$. Thus, it is straightforward to compute $\beta\Delta G(V)$ using equation (8.5).

Step 4 To compute the cavity size distribution functions for small cavities with radius $R < 0{,}5\sigma$ (being σ the particle's diameter), we compute $P_t(V)$ (the probability of finding any cavity of volume $V = 4/3\pi R^3$ in the metastable liquid, irrespectively of its volume) using the Scaled Particle Theory[26,27]. (Therefore, $P(V)$ belongs to a subset of $P_t(V)$.)

In Ref.[28], the authors first analytically determine $P_t(R) = 4\pi R^2\rho$ for small cavities, where rho is the system's density. Next, they show that the reversible work needed to form a cavity can be computed using the cavity size distribution function

$$\Delta\mu = -k_B T \ln P_t^{ex}(R) \tag{8.6}$$

where $P_t^{ex}(R)$ is the cavity exclusion probability distribution function

$$P_t^{ex}(R) = 1 - \int_0^R P_t(R')dR'. \tag{8.7}$$

where $P_t(R')$ is the normalized cavity probability distribution function. Given that $P_t(R) = 4\pi R^2\rho$, Eq.8.7 becomes $P_t^{ex}(R) = 1 - \frac{4\pi R^3}{3}\rho$, where $V = 4/3\pi R^3$ is the volume of the largest cavity (used as the order parameter in our work). Thus, we compute $P_t^{ex}(V)$ from $P_t(V)$ using the Eq. (8.7).

Step 5 Having computed D, we now calculate the relative free-energy barrier using the MFPT technique based on the subset of the largest cavity volume ranging from V_0 to V_{max}, where $V_0 = \frac{4\pi R_0^3}{3}$ is the smallest cavity volume of the subset and V_{max} is the volume of a post-critical cavity. The value of D in Eq. 8.5 corresponds to the work needed to create the smallest cavity with a volume of V_0. Equation (8.6) can then be used to calculate the constant D in equation (8.5), i.e., $D = \Delta\mu(V_0) = G(V_0) \equiv -k_B T \ln P_t^{ex}(V_0)$. This procedure will be explained in more details in the next section.

Both sampling of $P(V)$ and $P_t(V)$ are performed in the isothermal-isobaric ensemble following the procedure discussed above. In the results section we will show that the NVT ensemble would not be a good choice for such calculation.

8.3.3. Simulation details

We study spontaneous bubble cavitation from over-stretched liquids characterised by significantly different thermodynamical and structural properties. We choose a truncated and shifted Lennard-Jones (ts-LJ)[33] as a model of a simple fluid, and TIP4P/2005 water model[34] as a model of a molecular liquid. Both systems have been extensively investigated and their liquid-vapor phase diagrams are well known[35,36,37]. and different challenges to the largest cavity approach used in this work. Our order parameter assumes a spherical symmetry for the cavities, hence the ts-LJ system will be a good benchmark to assess the accuracy of our approach (given the debate on the sphericity of the critical bubble Ref.[12,16,13]). Water, on the other hand, is a liquid not only with a lower coordination number than ts-LJ, but also with stronger orientational correlations. Thus, it will be of great interest to test the validity of our approach in such very different systems.

We simulate a 800 particles metastable ts-LJ fluid in an NpT ensemble at a reduced temperature of $T^* = k_BT/\epsilon = 0{,}8$ and a reduced pressure of $p^* = p\sigma^3/\epsilon = -0{,}53$. The simulated state point is above the spinodal line ($p^* = -0{,}6$[33] at $T^* = 0{,}8$)[33,19], and at these thermodynamic conditions the system spontaneously cavitates. We choose to equilibrate the system at this state point to be able to compare with Ref.[1]. We run 200 independent molecular dynamics trajectories starting from random configurations with initial velocities extracted from a Maxwell-Boltzmann distribution. We also simulate a 500 TIP4P/2005 water molecules metastable liquid in an NpT ensemble at $T = 280$ K and $p = -2250$ bar. The simulated state point is above the spinodal line of the model[38,2] and at these thermodynamic conditions the system spontaneously cavitates. We choose to equilibrate the system at this state point to be able to compare with Ref.[2]. We run 200 independent molecular dynamics trajectories starting from random configurations with initial velocities extracted from a Maxwell-Boltzmann distribution. For both the ts-LJ and TIP4P/2005 models the equations of motion were integrated with a leap frog algorithm and a timestep of 1 fs. The velocity rescaling thermostat[39] and the Parrinello-Rahman (PR) barostat[40] were employed to generate the NpT trajectories. The Lennard-Jones was truncated and shifted at 4σ, corresponding to a cut-off of 9,5 Å (being $\sigma = 3{,}405$Åthe atoms'diameter). Whereas the TIP4P/2005 potential was truncated at a cut-off of 9,5 Å and long range corrections were included in the simulations. The molecular geometry of water was preserved using the SHAKE constraint algorithm[41]. All the simulations were performed with the molecular dynamics package GROMACS v. 4.5[42]. The long range electrostatic interactions in water were evaluated with the Particle Mesh Ewald method[43].

8.4. Results and discussion

To start with, we investigate the ability of the LSC order parameter to follow the vapour nucleation process. Figure 8.1 shows the volume of the largest cavity (computed as $4/3\pi R^3_{max}$) as a function of time for both water and ts-LJ liquid along two independent nucleating trajectories.

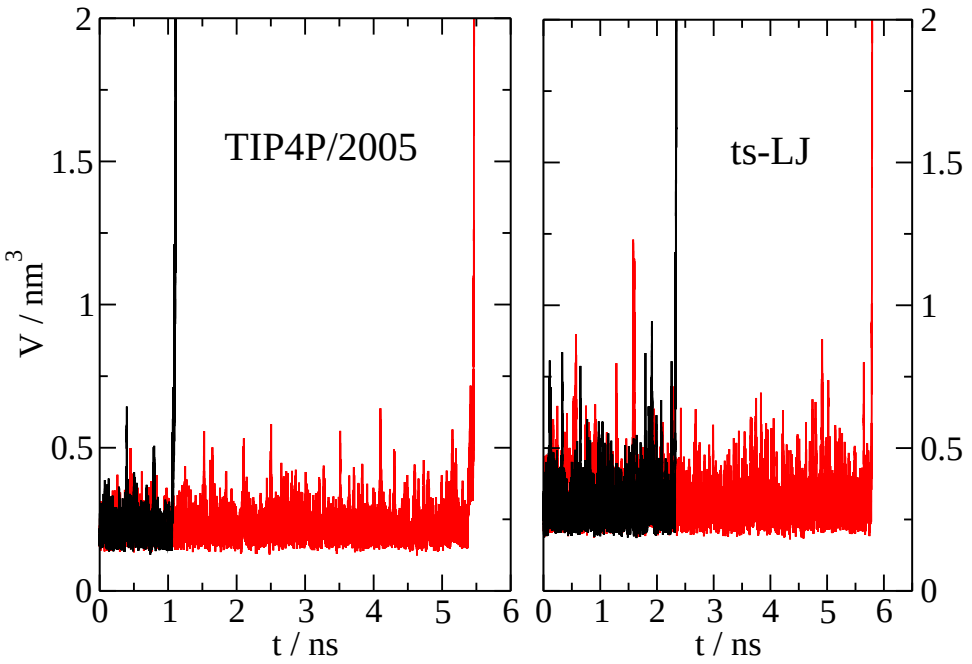

Figure 8.1: Volume (in nm^3) of the largest cavity as a function of time (in ns) for TIP4P/2004 water (left) and the ts-LJ (right) for two independent trajectories (in black and red). Note that the scale on the y-axis is the same for the two systems.

All trajectories feature the characteristic stochastic behaviour expected in a spontaneously nucleating process. The largest cavity undergoes large volume fluctuations until the transition to the vapor phase, characterized by the sharp volume jump, takes place. Therefore, the LSC order parameter captures the volume fluctuations of the background cavities and nicely identifies the onset of nucleation (where the cavity radius indefinitely grows). The time at which the transition occurs defines the nucleation time for that specific trajectory.

Figure 8.2 shows a typical snapshot featuring a postcritical cavity in metastable over-stretched water.

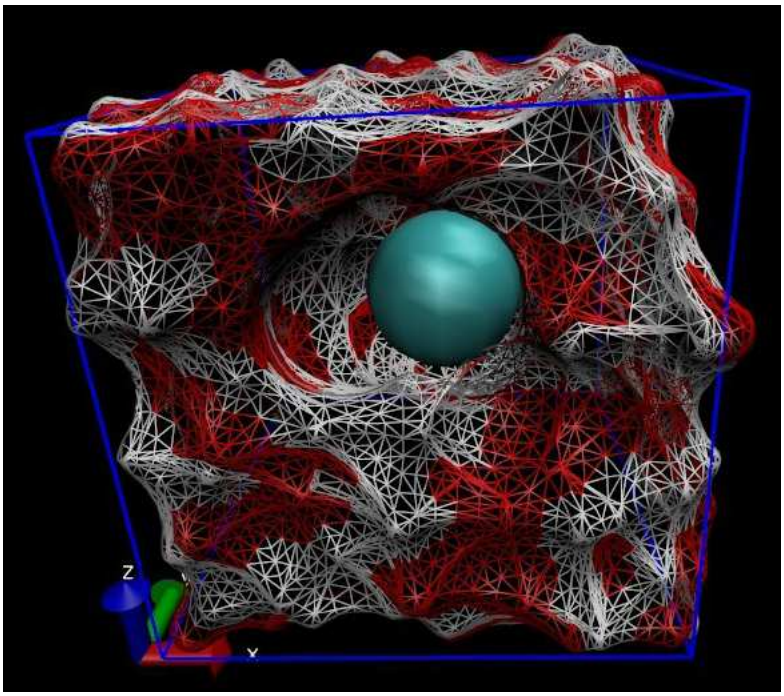

Figure 8.2: Snapshot of metastable water showing a post-critical cavity. Red and white lines represent Oxygen and Hydrogen atoms, respectively. The blue translucent sphere is the largest cavity detected by the LSC method.

Comparison of the fluctuations in cavity volume of the two liquids (see Figure 8.1) shows that water tends to generate cavities with a smaller volume than Lennard-Jones. On the one side, it is well know that nucleation of large cavities is more difficult in water[29,2], and this accounts for the low solubility of gases in aqueous solutions. On the other side, the different thermodynamics conditions between water and LJ can account for the smaller volume observed in the former: our LJ liquid simulations correspond to a temperature that is closer to the critical point than those of water, $T_c/T_{ts-LJ} \approx 1{,}3$ vs. $T_c/T_{water} \approx 2{,}3$. Moreover, the isothermal compressibility of water is much lower than that of a simple fluid, hence inhibiting large cavities volume fluctuations. Despite all these difference the LSC method accurately captures the nucleation times irrespectively of the system under study.

We now run 200 independent spontaneously nucleating trajectories and compute the probability distribution for the largest cavity $P(V)$ (see Figure 8.3).

In Figure 8.3 we observe that the most probable cavity volume, corresponding to the maximum of $P(V)$, is larger for the ts-LJ ($\approx 0{,}28\ nm^3$) than

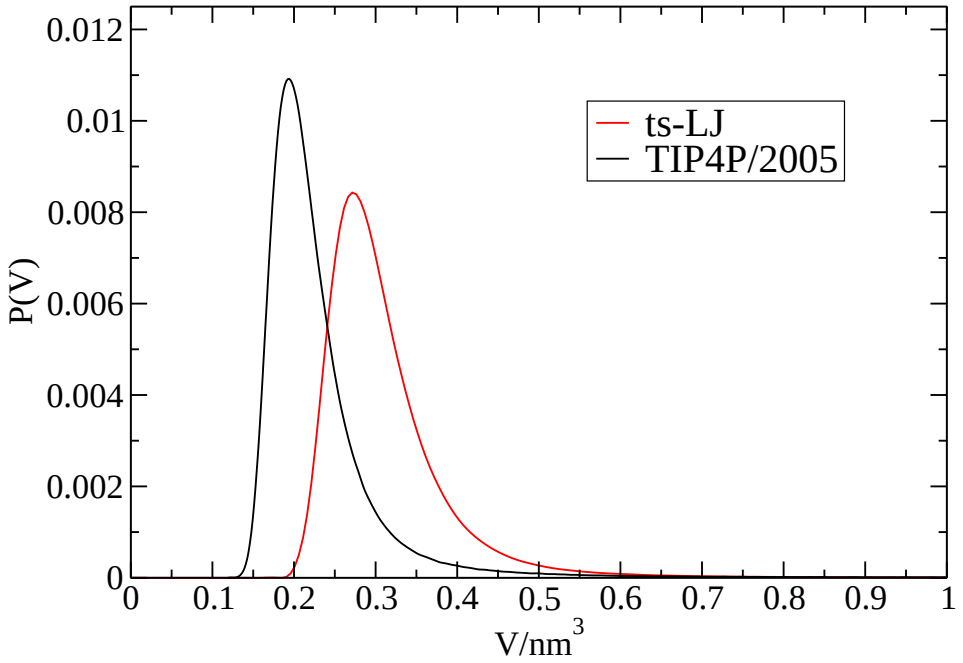

Figure 8.3: Normalized probability distribution of finding the largest cavity of volume V, for the TIP4P/2005 water (black) and ts-LJ (red).

for water ($\approx 0{,}19\ nm^3$), confirming once more what previously mentioned.

Next, we compute the MFPT using the method discussed in sections II-A and B. Figure 8.4 represents the MFPT as a function of the largest cavity volume for water (compared with the MFPT as a function of the largest bubble volume determined via a Voronoi construction Ref.[2]) and for Lennard-Jones.

From Figure 8.4 we estimate the nucleation time (as the time where MFPT converges to a plateau) and find that the nucleation time for water is in excellent agreement with earlier estimates using the Voronoi construction[2], with a noticeable advantage in CPU time.

The main difference between the Voronoi and the LSC approaches lies in the calculation of the volume of the nucleating bubble/cavity. On the one side, the Voronoi construction approximates the growing bubble to a polyhedron, emphasizing the bubble irregularities, thus predicting slightly larger volumes. On the other side, the LSC method approximates the bubble to a sphere and this results in estimating lower volumes. This difference clearly appears at the inflection point of $\tau(V)$ (that corresponds to the value of the critical volume V^*), which is reached at the same time using either

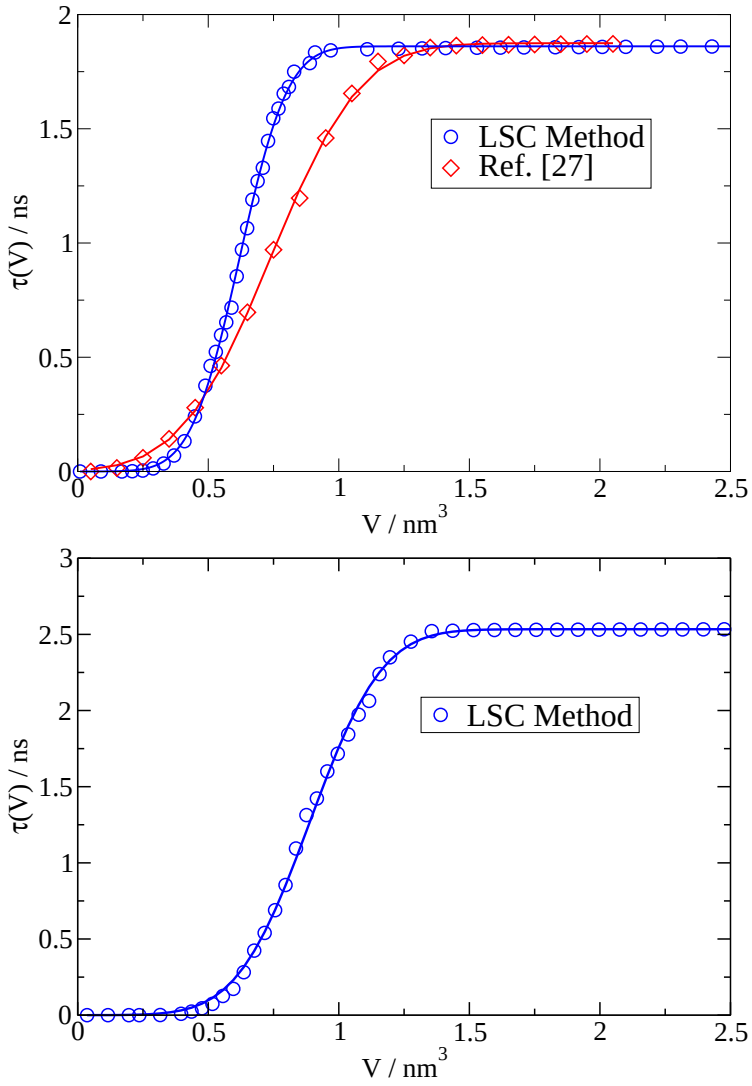

Figure 8.4: (Top) MFPT for TIP4P/2005 water with the LSC method (circles). Results obtained with the Voronoi method are from Ref.[2] (rhombus), at the same thermodynamic conditions of T=280K and p=-2250 bar. (Bottom) MFPT for the ts-LJ at $T^* = 0{,}8$ and $p^* = -0{,}53$.

Voronoi (0.94 ns) or LSC (0.93 ns), while the corresponding value of the critical volume estimated with the Voronoi is ∼15 % larger than that coming from the LSC calculations. This corresponds to a critical radius of 0,56 nm for the Voronoi assuming a spherical geometry, and 0,54 nm for the LSC.

The critical nucleus volume of the Lennard-Jones leads to a radius of

0,592 nm in agreement with the result estimated by Punnathanam and Corti[1], 0.44 nm, using density functional theory. Moreover, when comparing the critical nucleus volume, we observe that the Lennard-Jones one is of the same order of magnitude as that of water. This results is somehow surprising, given the different thermodynamic state and cavity structure between the two liquids and that the LSC method does not capture well bubbles whose symmetry significantly departs from a sphere. Whereas when comparing the nucleation time obtained for water (top panel) to the one obtained for Lennard-Jones, we observe that τ of the latter is slightly larger than of the former, due to their different thermodynamic conditions .

According to Ref.[1], using DFT one could estimate the critical radius as a function of the supersaturation (see Fig. 8.4 in Ref.[1]). One convenient way to do this[44] is to consider $\Delta\mu/\Delta\mu_{spin}$, where $\Delta\mu = \mu - \mu_{sat}$ and $\Delta\mu_{spin} = \mu_{spin} - \mu_{sat}$, being μ the chemical potential of the thermodynamic state of interest, μ_{sat} the chemical potential at the saturation line and μ_{spin} the one at the spinodal line. We have employed the equation of state from reference[33] to compute the chemical potentials defined above. One advantage of using the ratio $\Delta\mu/\Delta\mu_{spin}$ as reference parameter for further comparison across different simulation results is that the ratio is independent of the temperature or the cut-off employed to truncate the pair potential interactions[44,1]. Therefore, since in our case $\Delta\mu/\Delta\mu_{spin} = 0{,}87$, our critical radius would be 0.57 nm, in good agreement with what we measure using MFPT.

The obtained results are summarized in Table 8.1.

		τ_J[ns]	Z[nm^{-3}]	V^* [nm^3]	J[10^{28}cm^{-3}s^{-1}]
Water	LSC	1.86	2.73	0.63	3.15
Water	Voronoi[2]	1.87	1.48	0.74	3.10
ts-LJ	LSC	2.62	1.84	0.87	8.46
ts-LJ	DFT[1]	–	–	0.36	–

Table 8.1: Nucleation time (τ_J), Zeldovich factor (Z), critical volume (V^*) and nucleation rate (J) for TIP4P/water at 280K and -2250 bar from this work (LSC) and from Ref.[2], and for ts-LJ at T*=0.8 and p*= -0.53 from this work (LSC) and from Ref.[1].

Next, we compute the nucleation rate making use of Eq. 8.4, where V_s is 17,1 nm^3 and 45,1 nm^3 for water and the ts-LJ, respectively. The nucleation rate computed for water is in very good agreement with previous estimates at the same thermodynamic state point[2]. As already discussed in Ref.[2], CNT

underestimates the nucleation rate (giving a value of $0{,}031 \times 10^{28} \mathrm{cm}^{-3}\mathrm{s}^{-1}$, using Eq.8.2). A possible reason for this result concerns the CNT estimate of the free-energy barrier height. The CNT expression of the top of the free-energy barrier (Eq.8.1) presents a cubic dependence on the surface tension γ, where one assumes that γ is the surface tension of the liquid-vapor planar interface at coexistence. However, it has been shown that curvature effects influence the surface tension at nanometer length-scales, relevant to the critical radius size[45,46]. When comparing the water's Zeldovitch factor computed with the two methods, we observe that the one obtained with LSC is larger than the one coming from Voronoi calculations. Given that the Zeldovitch factor is proportional to the curvature of the free-energy barrier near the top, the curvature of the barrier in the LSC case is larger than the one in the Voronoi case.

To conclude, we calculate the nucleation free-energy barrier as a function of the volume of the largest cavity (where the largest cavity radius computed with LSC) using the MFPT and the analysis of the largest cavity distribution (Eq. (8.5)[25,15] and (8.6)[28]).

As previously mentioned, to get the value of D in Eq. (8.5) we use the *total* cavity probability distibution P_t obtained from Scaled Particle Theory, and the chemical potential associated to the nucleation of a cavity with radius R.

Figure 8.5(top) shows the cavity probability distribution function P_t for TIP4P/2005 water sampled in both NpT and NVT ensembles, using *only* the volumes evaluated before the phase transition was reached. (the Lennard-Jones systems behaves in the same way). Whereas Figure 8.5(bottom) shows the associated chemical potential used to obtain the value of D in Eq. (8.5), which defines the shift of the free-energy curve.

As shown in the figure, P_t is independent on the chosen ensemble for small cavities, whereas for larger ones P_t in the NpT ensemble presents a long tail. When simulating the system in a NVT ensemble, we fix its total volume thus inhibiting nucleation of large cavities. Therefore, from now onward we will prepare the system in the NpT ensemble.

The corresponding chemical potential for the cavities as a function of volumes can be obtained from Eq. 8.6 (see Fig. 8.5 (bottom)).

The values of chemical potential for both NVT and NpT ensemble are different as soon as V is about 0,1 nm^3. In the first case, a cavity cannot freely grow, since the volume of the simulation box is kept constant.

This constraint contributes as an added work in the chemical potential for volumes beyond 0,1 nm^3. When studying cavity nucleation in the NpT ensemble each bubble can grow unlimitedly, since the simulation box can freely fluctuate. Thus, the chemical potential calculated in these conditions

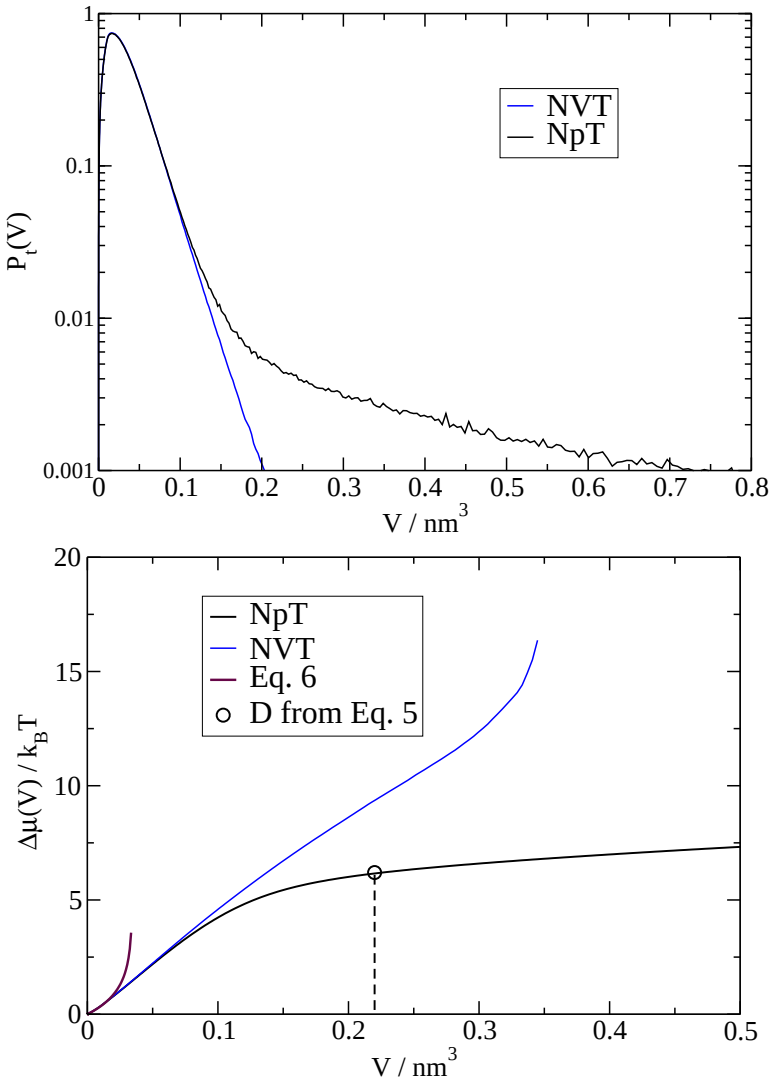

Figure 8.5: Top: Normalized cavity probability distribution function, P_t sampled in both NpT (black) and NVT (blue) ensembles for TIP4P/2005 water. Bottom: associated chemical potential in the same ensembles together with the analytical solution from Eq. (8.6) (Scaled Particle Theory, in brown) which becomes exact at small radii (from $V = 0$ up to 0,02nm^3). D from Eq. 8.5 corresponds to the value of 6 k$_B T$ at $V_0 = 0{,}23$ nm^3 (for water).

is lower than the one calculated in the NVT ensemble.

Therefore, in what follows we will make use of the chemical potential obtained from the NpT ensemble, so our simulation will be performed in this ensemble.

Having determined the constant D for both TIP4P/2005 and for ts-LJ, we calculate their nucleation free-energy barriers (Figure 8.6). The curves have been shifted using the value of D for the smallest cavity sampled in the metastable liquid, i.e. for water $D = 6$ k_BT and $V_= = 0{,}23$ nm^3 and for ts-LJ $D = 5{,}5$ k_BT and $V0 = 0{,}28$ nm^3, respectively.

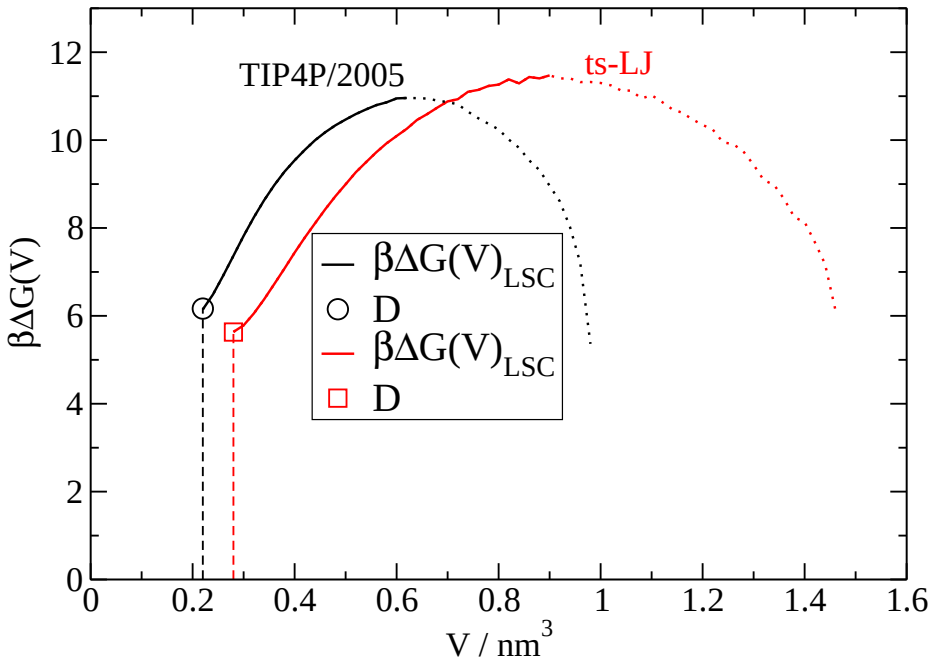

Figure 8.6: Nucleation free-energy as a function of the bubble volume (nm^3) for the TIP4P/2005 (solid black line) and ts-LJ (solid red line). D has been obtained by Scaled Particle Theory.

In both cases, the nucleation free-energies present a maximum ($\beta\Delta$G*) at the critical volume. The main results are summarized in the following table.

		$\beta\Delta$G*			$\beta\Delta G^*$
Water	LSC	11	ts-LJ	LSC	11
Water	Voronoi[2]	10	ts-LJ	DFT[1]	10

Table 8.2: Top of the nucleation free-energy barrier for TIP4P/water at 280K and -2250 bar from this work (LSC) and from Ref.[2], and for ts-LJ at T*=0.8 and p*= -0.53 from this work (LSC) and from Ref.[1].

The free-energy barrier for both water and ts-LJ is $\sim 1k_BT$ higher than that estimated in Ref[2] and[1], within the uncertainty of free-energy computations. Hence the LSC approach provides an efficient route to estimate nucleation free-energy barriers.

8.5. Conclusions

We have employed a generic order parameter to investigate and quantify vapor nucleation in two metastable over-stretched liquids, TIP4P/2005 water and a Lennard-Jones liquid. The structure of these two liquids is significantly different as denoted by their coordination numbers and orientational correlations. The structure in Lennard-Jones is dominated by packing constrains, whereas that of water is determined to a large extent by hydrogen bonding. Our order parameter is based on the identification of the *largest spherical cavitiy* (LSC) that nucleates spontaneously in an "over-stretched" mestastabe liquid. The implementation of this order parameter requires the calculation of a radial distance only, avoiding additional criteria such as coordination numbers or the use of more intensive computational approaches to map the cavity volume into polyhedra. The LSC method can be used together with Mean First Passage Time technique to estimate the nucleation rate and free-energy barrier.

We have shown that using LSC and MFPT we can compute the critical bubble radius, free-energy barrier and nucleation rate for both Lennard-Jones and water that agree with published results (obtained with the Voronoi construction and Umbrella Sampling). As compared with the Voronoi the LSC method tends to slightly underestimate the radius of the critical cavity, by about 15 %. We find that the activation free-energy estimates for the critical cavity are within $\sim 1k_BT$ of literature results, which is well within the expected uncertainty in computational estimates of the free energies. The nucleation rate for the water is similar in both methods.

One clear advantage of the LSC method is its generality. As we have shown it can be used to investigate liquids with significant structural differences. Existing methodologies target specific structural features (such as Ref.[2]), or rely on the use of clustering criteria to identify the largest vapor bubble[16,23,24], whereas the LSC approach allows us to use the same criterion for different liquids (whether simple or molecular). Its computational cost scales with the number of grid points, $\sim N^2$, used to identify the largest cavity. Our analysis of structurally different liquids indicates that moderate grid sizes produce accurate results, making the method inexpensive from a computational point of view. The LSC method can be extended to investi-

gate heterogeneous vapor nucleation involving complex substrates. Work in this direction is in progress.

Acknowledgments

All authors thank the Imperial College High Performance Service for providing computational resources. MAGG acknowledges both the "Thomas Young Center" for the award of a Junior research Fellowship and the "Pan-European Research Infrastructure on High Performance Computing (HPC-EUROPA2)" for the award of a travelling Fellowship. FB thanks the EPSRC for the award of a Leadership Fellowship. CV acknowledges Spanish grant JCI-2010-06602 and EU grant 303941-ANISOKINEQ-FP7-PEOPLE-CIG-2011. MAG, CV and JLFA acknowledge Spanish grant FIS2013-43209-P.

Bibliografía

1. S. Punnathanam and D. S. Corti, J. Chem. Phys. **119**, 10224 (2003).
2. J. Abascal, M. Gonzalez, J. Aragones, and C. Valeriani, J. Chem. Phys. **138**, 084508 (2013).
3. M. Volmer and A. Weber, Zeitschrift Physik. chemie–stochiometrie und verwandtschaftslehre **119**, 277 (1926).
4. P. G. Debenedetti, *Metaestable liquids* (Princeton University Press, Princeton, New Jersey, 1996).
5. C. F. Delale, J. Hruby, and F. Marsik, J. Chem. Phys. **118**, 792 (2003).
6. X. C. Zeng and D. W. Oxtoby, J. Chem. Phys. **94**, 4472 (1991).
7. V. Talanquer and D. Oxtoby, J. Chem. Phys. **102**, 2156 (1995).
8. M. J. Uline and D. S. Corti, Phys. Rev. Lett. **99**, 076102 (2007).
9. R. Y. Yang, R. P. Zou, and A. B. Yu, Phys. Rev. E **65**, 041302 (2002).
10. G. Torrie and J. Valleau, Chem. Phys. Lett. **28**, 578 (1974).
11. S. Auer and D. Frenkel, Nature **409**, 1020 (2001).
12. V. K. Shen and P. G. Debenedetti, J. Chem. Phys. **111**, 3581 (1999).
13. S. L. Meadley and F. A. Escobedo, J. Chem. Phys. **137**, 074109 (2012).
14. J. Wedekind, R. Strey, and D. Reguera, J. Chem. Phys. **126**, 134103 (2007).
15. J. Wedekind, G. Chkonia, J. Woelk, R. Strey, and D. Reguera, J. Chem. Phys. **131**, 114506 (2009).

16. Z.-J. Wang, C. Valeriani, and D. Frenkel, J. Phys. Chem. B **113**, 3776 (2009).

17. K. S. Suslick, Science **247**, 1439 (1990).

18. Y. Chen and J. Israelachvili, Science **252**, 1157 (1991).

19. S. Punnathanam and D. S. Corti, Ind. Eng. Chem. Res. **41**, 1113 (2002).

20. S. Punnathanam and D. S. Corti, J. Chem. Phys. **120**, 11658 (2004).

21. M. J. Uline and D. S. Corti, J. Chem. Phys. **129**, (2008).

22. K. Torabi and D. S. Corti, J. Chem. Phys. **133**, 134505 (2010).

23. K. Torabi and D. S. Corti, J. Phys. Chem. B **117**, 12479 (2013).

24. K. Torabi and D. S. Corti, J. Phys. Chem. B **117**, 12491 (2013).

25. J. Wedekind and D. Reguera, J. Phys. Chem. B **112**, 11060 (2008).

26. H. Reiss, H. Frisch, E. Helfand, and J. Lebowitz, J. Chem. Phys. **31**, 369 (1959).

27. H. Reiss, *Scaled Particle Methods in the Statistical Thermodynamics of Fluids* (John Wiley & Sons, Inc., 2007).

28. F. Bresme and J. Alejandre, J. Chem. Phys. **118**, 4134 (2003).

29. A. Pohorille and L. Pratt, J. Am. Chem. Soc. **112**, 5066 (1990).

30. L. Pratt and A. Pohorille, Proc. Nat. Acad. Sci. **89**, 2995 (1992).

31. M. Blander and J. L. Katz, AICHE J. **21**, 833 (1975).

32. G. Chkonia, J. Woelk, R. Strey, J. Wedekind, and D. Reguera, J. Chem. Phys. **130** (2009).

33. J. K. Johnson, J. A. Zollweg, and K. E. Gubbins, Mol. Phys. **78**, 591 (1993).

34. J. L. F. Abascal and C. Vega, J. Chem. Phys. **123**, 234505 (2005).

35. C. Vega, J. L. F. Abascal, and I. Nezbeda, J. Chem. Phys. **125**, 034503 (2006).

36. J. L. Aragones, L. G. MacDowell, and C. Vega, J. Phys. Chem. A **115**, 5745 (2011).

37. M. M. Conde, M. A. Gonzalez, J. L. F. Abascal, and C. Vega, J. Chem. Phys. **139** (2013).

38. M. A. Gonzalez, Master's thesis, Fac. Ciencias Quimicas, Univ. Complutense, Madrid (2011).

39. G. Bussi, D. Donadio, and M. Parrinello, J. Chem. Phys. **126**, 014101 (2007).

40. M. Parrinello and A. Rahman, J. Appl. Phys. **52**, 7182 (1981).

41. J. P. Ryckaert, G. Ciccotti, and H. J. C. Berendsen, J. Comput. Phys. **23**, 327 (1977).

42. B. Hess, C. Kutzner, D. van der Spoel, and E. Lindahl, J. Chem. Theory Comput. **4**, 435 (2008).

43. U. Essmann, L. Perera, M. L. Berkowitz, T. Darden, H. Lee, and L. G. Pedersen, J. Chem. Phys. **103**, 8577 (1995).

44. V. K. Shen and P. G. Debenedetti, J. Chem. Phys. **114**, 4149 (2001).

45. F. Bresme and N. Quirke, J. Chem. Phys. **110**, 3536 (1999).

46. F. Bresme, H. Lehle, and M. Oettel, J. Chem. Phys. **130**, 214711 (2009).

Results: Chapter 9

Heterogeneous bubble nucleation: a water + carbon nanotube system at negative pressure. Preliminary results

Miguel A. González[1,2], *Jose L. F. Abascal*[1], *F. Bresme*[2,3] *and C. Valeriani*[1]

(1) Departamento de Química Física, Facultad de Ciencias Químicas, Universidad Complutense de Madrid, 28040 Madrid, Spain.

(2) Chemical Physics Section, Department of Chemistry, Imperial College London, London SW7 2AZ.

(3) Department of Chemistry, Norwegian University of Science and Technology, Trondheim, Norway.

9.1. Abstract

In this chapter, we are presenting preliminary results of the heterogeneous bubble nucleation of TIP4P/2005 water in the presence of a single-wall carbon nanotube (SWCNT) using molecular dynamics. Our system consists of a nanotube immersed in a bulk of over-stretched water at the same thermodynamic conditions as the ones used in Chapter 6. At these conditions bubbles nucleate spontaneously in the pure water system. Therefore, we can use either a brute-force method or MFPT to compute the nucleation rate. Next, we compare the heterogeneous nucleation rate with the value obtained in the homogeneous nucleation case (Chapter 6).

9.2. Introduction

Water is undoubtedly the most relevant liquid for living organisms both at macroscopic (the human body contains 65-70 % of water and a tree 20-70 %) and microscopic scales (a human cell contains 70-80 % of water). How does water behave when it is confined at very small scales (e.g. in the growth environment of the cell, inside a protein, or inside nanomaterials) is a question of fundamental interest in materials applications and biological processes.

Recent developments in the manufacture of nanomaterials offer good opportunities to systematically investigate the behaviour of water under nanoscale confinement. Carbon nanotubes have been targeted as models for biological channels, building blocks for molecular nanovalves, electrophoretic and thermophoretic channels or DNA sequencing and therapeutic tools. Water is present in all these applications; hence it is necessary to understand its behaviour.

Nanoconfinement and nanoscale roughness provide unique conditions to control the properties of water, which are expected to significantly depart from the bulk properties[1]. Nanoscale roughness can induce capillary evaporation, a physical effect that can be used to make superhydrophobic surfaces. Under non equilibrium conditions, away from the coexistence line, negative pressures can induce cavity nucleation[2], which influences transport processes in trees and in microfluidic devices[3]. The first spontaneous cavitation of water in experiments under tension has been reported very recently using hydrogel pores[4].

In this chapter investigate the cavitation of water in heterogeneous conditions provided by synthetic nanocapillaries, i.e., single wall carbon nanotubes. Computer simulation provide an excellent approach to investigate the cavitation process from a microscopic perspective. Recent works have indeed shown the possibility of monitoring vapour nucleation in water when it is confined between hydrophobic surface[5]. The impact of the nanopore size and geometry (edges, kinks and roughness) on the nucleation barrier and evaporation rate has also been addressed[6,7]. We are therefore in an ideal position to investigate the mechanism and dynamics of water cavitation in carbon nanotubes as a function of the nanotube structure: SWCNT radius, length and topology (zig-zag or armchair). To perform such investigation we employ molecular dynamics simulations of water-nanotube systems modelled at an atomistic level.

We set out to investigate the thermodynamics of the water-carbon nanotube system using the recently developed and accurate TIP4P/2005 water model[8], and compute the spinodal and the binodal curves as a function of

the confining nanotube structure. We also intend to investigate the cavity nucleation mechanism for different thermodynamic states around the spinodal line. To properly identify the morphology of the growing bubbles we will use an "ad hoc" order parameter to quantify the behaviour of confined water with high accuracy such as the one based on detecting the largest cavity in the system, already introduced in this Thesis.

9.3. Simulations and Methods

We have carried out 100 independent molecular dynamics trajectories of liquid water at 280 K and at −2250 bar surrunding a single-wall carbon nanotube. This state, above the spinodal line of the water model, has already been studied in recent works[9,10,11] of homogeneous bubble nucleation (see Chapter 6). SWCNT with a 2,034 nm diameter, 15x15 chirality (armchair) and a 6 nm length were considered in our work. The SWCNT was constructed with the nanotube modelling program of VMD[12] and the OPLS-AA force field has been used to describe the intermolecular forces of carbon atoms. The structure of SWCNT was hydrated with 19079 water molecules. The water potential used was TIP4P/2005[8]. This water model predicts quantitative of many water properties,[13,14] both dynamics properties[15] and thermodynamic anomalies[16]. It is also relevant goes a satisfactory account of the our study of bubble nucleation that this model to vapour-liquid equilibrium[17]. In a recent work, the TIP4P/2005 model has been used to analyse the droplets formation into a metastable vapour[18].

The simulations have been performed in the NpT ensemble using the Molecular Dynamics package GROMACS 4.5[19] with a 1 fs time step. We evaluated the long range electrostatic interactions with the Particle Mesh Ewald method[20]. The geometry of the water molecules has been maintained using the SHAKE algorithm[21]. However, no constrans has been imposed to the SWCNT geometry. Temperature has been kept constant with a velocity rescaling thermostat[22] and, the pressure is set constant using the Parrinello-Rahman barostat[23].

9.4. Heterogeneous Nucleation

Classical nucleation theory can be extended to the case of heterogeneous nucleation. Considering the formation of a vapour embryo at a solid-liquid interface (see Ref. (24)), the top of the associated free-energy barrier is given

by

$$\Delta G^* = \frac{16\pi}{3}\frac{\gamma^3}{(\rho_A|\Delta\mu|)^2}\frac{(1+\cos\theta)^2(2-\cos\theta)}{4} = \frac{16\pi}{3}\frac{\gamma^3}{(\rho_A|\Delta\mu|)^2}\psi(\theta) \quad (9.1)$$

where ρ_A is the density of the stable phase (vapour), $\Delta\mu$ corresponds to the difference between the chemical potentials of the phases (vapour and liquid), the contact angle is represented by θ, $\psi(\theta)$ is a geometric correction factor and the the global surface tension, γ, is a combination of the surface tensions of all interfaces implicated in the process.

$$\gamma = \frac{\gamma_{vl}A_{vl} + (\gamma_{vs} - \gamma_{ls})A_{vs}}{\pi R^2\left[2(1+\cos\theta) + \sin^2\theta\cos\theta\right]} \quad (9.2)$$

the subscripts indicate the appropriate interface (lv: liquid-vapour, vs: vapour-solid, and ls: liquid-solid), A is the surface area and R is the radius associated to the curvature of the nucleating bubble.

Therefore, we can define the ratio between heterogeneous and homogeneous nucleation rate as,

$$\frac{J_{het}}{J_{hom}} \approx \frac{a}{N_{tot}^{1/3}} exp\left\{\frac{\Delta G^*}{k_B T}\left[1-\psi(\theta)\right]\right\} \quad (9.3)$$

where J_{het} and J_{hom} are the heterogeneous nucleation rate and the homogeneous nucleation rate, respectively; a is the minimum value of the contact angle needed for heterogeneous nucleation to become the predominant mechanism and $N_{tot}^{1/3}$ is the total number density of the bulk metastable phase. For example, this relation increases from 3,2x10^{-8} to 3,2x10^3 when θ changes from 10° to 70°, keeping the rest parameters constant.

9.5. Preliminary results

We set up different diameters of the nanotube, changing the chirality of the SWCNT. The chiralities used in thes work were 10x10 (1,356 nm), 15x15 (2,034 nm), 20x20 (2,712 nm), 30x30 (4,068 nm), 40x40 (5,425 nm), being the numbers between parenthesis the diameter of the nanotube in nanometer. The idea behind using these huge carbon nanotubes is to determine the effect of the nanotube's curvature in the bubble nucleation process, when the metastable water surrounding the nanotube is simulated at the same thermodynamic conditions. We have started running 100 trajectories of the 15x15 case within the metastable liquid water at 280 K and at −2250 bar to study spontaneous cavitation.

Fig. 9.1 and Fig. 9.2 show two different snapshots along a randomly chosen trajectory. The first figure represents the side-view of the nanotube embedded in water. Fig. 9.1 shows that the structure of the nanotube remains constant, with an almost perfect spherical section. Fig. 9.2 is a picture of the same system, but much later in time, showing a bubble growing during the nucleating trajectory. The presence of the bubble at the surface of the nanotube deforms its cylindrical shape by compressing it.

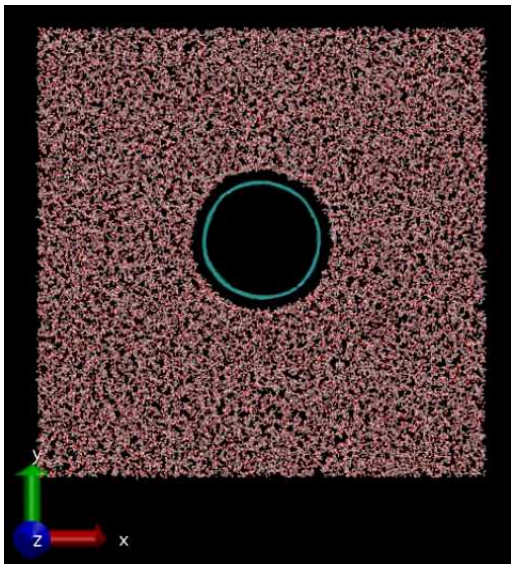

Figure 9.1: Side-view section of the water+SWCNT system at 280 K and at −2250 bar. In these conditions the overall structure of the nanotube is cylindrical and does not clearly change for short time scales.

Next, we have determined the nucleation rate at 280 K and −2250 bar via a brute force method. This method is different from the MFPT technique, used in Ref.[9]. Here the nucleation rate s evaluated by computing the inverse of the first time (τ_J) that the total volume of the system crosses a chosen threshold in each trajectory, and dividing it by the total system's volume at the same metastable conditions. Thus, differently from previous studies, we are now using a global order parameter (the total volume of the system) instead of a local one (the size of the largest bubble in the system). The threshold of this global order parameter (total system's volume) was set to 22 nm^3. Although somewhat arbitrary, this volume has been fixed once the critical bubble is known (see Chapter 6). Notice that the time it takes for critical bubble to form is much longer than the time it takes to growth (e.g. see Fig. (6.10) of Chapter 6). In our case, this information was known for the

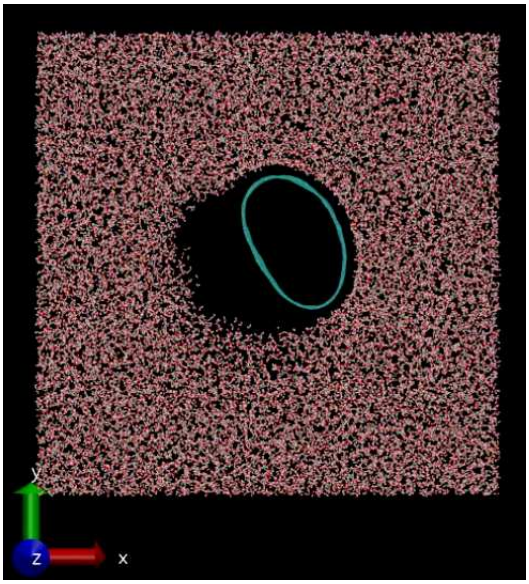

Figure 9.2: Side-view section of the water+SWCNT system at the same thermodynamic conditions as in Fig.9.1. Note the compression of and the nanotube caused by the bubble growth, when spontaneous nucleation takes place. The structure of the nanotube has been distorted by the bubble and the nanotube has now lost its cylindrical shape.

homogeneous nucleation case previously studied[9]: the critical bubble volume was estimated to be 0,74 nm^3 and the mean system volume was 17 nm^3. For the water+SWCNT system, the mean total volume is 54 nm^3 and the threshold is set to 68,5 nm^3.

The results of the nucleation rate are shown in Fig. 9.4 and in Table. 9.1. As one might expect, the nucleation rate in the heterogeneous case is higher than the one computed in the homogeneous case. These results are only the first step of a comprehensive study about heterogeneous bubble nucleation which will be carried out in the near future.

In particular, in future studies on heterogeneous nucleation, using the systems presented above, we will apply the *Largest Spherical Cavity* method to detect the local order parameter, the largest cavity. We will focus on several factors, such as the curvature and stiffness of the nanotube, which we foresee will have strong influence in the nucleation process. At the same time, we are also interested in computing the liquid-vapour phase diagram of water confined in nanotubes, and to study heterogeneous nucleation "from the inside" of the confined surface (differently from what we presented above, where cavitation always happens on the outside of the nanotube).

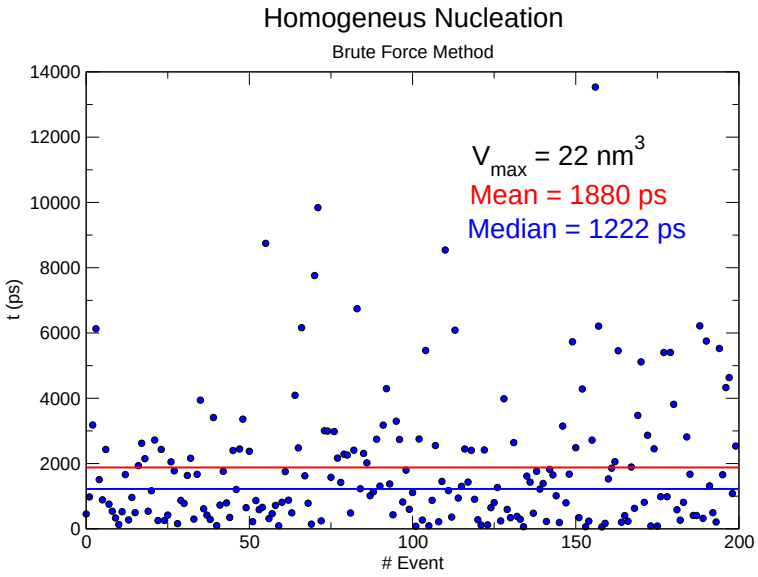

Figure 9.3: First time at which the system's volume crosses the threshold of 22 nm^3 in each trajectory (blue dots) in the homogeneous nucleation case (Ref.9) The red solid line is the mean of 200 trajectories and the blue solid line corresponds to the median of the same values.

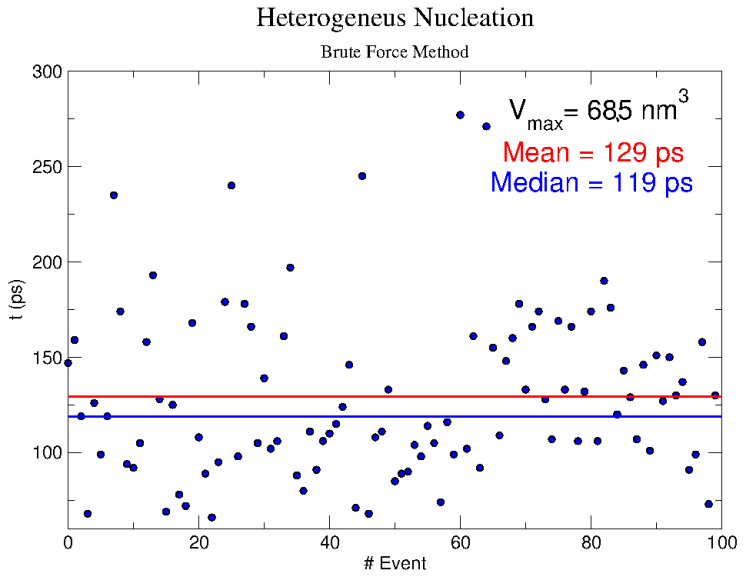

Figure 9.4: First time at which the system's volume crosses the threshold of 68,5 nm^3 in each trajectory (blue dots) in the heterogeneous nucleation case. The red solid line is the mean of 100 trajectories and the blue solid line corresponds to the median of the same values.

280 K −2250 bar	τ_J	V^*	J
Homogeneous Nucleation			
Local Order Parameter (MFPT)[24,25,9]	1.87	0.74	3.10
Homogeneous Nucleation			
Global Order Parameter Brute Force Method	1.88	–	3.10
Heterogeneous Nucleation			
Global Order Parameter Brute Force Method	0.129	–	14.3

Table 9.1: Simulation results of spontaneous bubble homogeneous and heterogeneous nucleation of over-stretched TIP4P/2005 water. All simulations have been carried out at 280 K and at −2250 bar. Results reported in the first line of the table, have been obtained using MFPT and the volume of the largest bubble as a local order parameter. The results reported in the second and third lines have been obtained using brute force and the total volume of the system as a global order parameter. τ_J corresponds to nucleation time (ns) (see Ref.[24,25]), V^* the volume of the critical bubble V^* (nm^3) and J ($10^{28} cm^{-3} s^{-1}$) nucleation rate.)

Bibliografía

1. H. Kyakuno, K. Matsuda, H. Yahiro, Y. Inami, T. Fukuoka, Y. Miyata, K. Yanagi, Y. Maniwa, H. Kataura, T. Saito, et al., J. Chem. Phys. **134**, 244501 (2011).

2. E. Herbert, S. Balibar, and F. Caupin, Phys. Rev. E **74**, 041603 (2006).

3. T. D. Wheeler and A. D. Stroock, Nature **455**, 208 (2008).

4. O. Vincent, P. Marmottant, P. A. Quinto-Su, and C.-D. Ohl, Phys. Rev. Lett. **108**, 184502 (2012).

5. N. Giovambattista, P. J. Rossky, and P. G. Debenedetti, Phys. Rev. E **73**, 041604 (2006).

6. S. Sharma and P. G. Debenedetti, Proc. Nat. Acad. Sci. **109**, 4365 (2012).

7. J. Russo, S. Melchionna, F. De Luca, and C. Casieri, Phys. Rev. B **76**, 195403 (2007).

8. J. L. F. Abascal and C. Vega, J. Chem. Phys. **123**, 234505 (2005).

9. J. Abascal, M. Gonzalez, J. Aragones, and C. Valeriani, J. Chem. Phys. **138**, 084508 (2013).

10. M. A. Gonzalez, G. Menzl, J. L. Aragones, P. Geiger, G. Pallare, M. Azouzi, F. Caupin, C. Dellago, J. Abascal, C. Vega, et al., In preparation (????).

11. M. A. Gonzalez, J. Abascal, C. Vega, C. Valeriani, and F. Bresme, In preparation (????).

12. W. Humphrey, A. Dalke, and K. Schulten, J. Mol. Graphics **14**, 33 (1996).

13. C. Vega, J. L. F. Abascal, M. M. Conde, and J. L. Aragones, Faraday Discuss. **141**, 251 (2009).

14. C. Vega and J. L. F. Abascal, Phys. Chem. Chem. Phys. **13**, 19663 (2011).

15. M. A. Gonzalez and J. L. F. Abascal, J. Chem. Phys. **132**, 096101 (2010).

16. H. L. Pi, J. L. Aragones, C. Vega, E. G. Noya, J. L. F. Abascal, M. A. Gonzalez, and C. McBride, Mol. Phys. **107**, 365 (2009).

17. C. Vega, J. L. F. Abascal, and I. Nezbeda, J. Chem. Phys. **125**, 034503 (2006).

18. A. Perez and A. Rubio, J. Chem. Phys. **135**, 244505 (2011).

19. B. Hess, C. Kutzner, D. van der Spoel, and E. Lindahl, J. Chem. Theory Comput. **4**, 435 (2008).

20. U. Essmann, L. Perera, M. L. Berkowitz, T. Darden, H. Lee, and L. G. Pedersen, J. Chem. Phys. **103**, 8577 (1995).

21. J. P. Ryckaert, G. Ciccotti, and H. J. C. Berendsen, J. Comput. Phys. **23**, 327 (1977).

22. G. Bussi, D. Donadio, and M. Parrinello, J. Chem. Phys. **126**, 014101 (2007).

23. M. Parrinello and A. Rahman, J. Appl. Phys. **52**, 7182 (1981).

24. J. Wedekind, R. Strey, and D. Reguera, J. Chem. Phys. **126**, 134103 (2007).

25. J. Wedekind, G. Chkonia, J. Woelk, R. Strey, and D. Reguera, J. Chem. Phys. **131**, 114506 (2009).

Parte III

Conclusiones

Conclusiones

Después de cuatro años de trabajo predoctoral en el grupo de investigación de la Universidad Complutense de Madrid, se ha adquirido por parte del candidato unas herramientas básicas en Mecánica Estadística y Simulación Molecular. Además, el conocimiento dentro de estas ramas de la Ciencia se ha centrado en determinar una amplia lista de propiedades termodinámicas del agua, en desarrollar nuevos modelos de potencial de agua y nuevos métodos de localización de burbujas y en estudiar de forma rigurosa el proceso de nucleación, tanto en procesos espontáneos como en eventos raros.

Se pueden extraer tres conclusiones generales de esta memoria. El modelo de potencial TIP4P/2005 predice las propiedades termodinámicas en condiciones extremas y también el comportamiento anómalo del agua. Por lo tanto podemos construir un escenario termodinámico del modelo avalado por datos experimentales. Los datos de simulación avalan la existencia de un punto crítico líquido-líquido en el agua (aunque éste pudiera aparecer a 0 K. La presencia del segundo punto crítico del agua como explicación a las propiedades anómalas del agua.

La incorporación de la flexibilidad molecular a los modelos rígidos de potencial de agua no es una mejora sustancial en el ámbito de la Simulación Molecular, aunque logra mantener la calidad de las predicciones aumentando los grados de libertad moleculares.

Se demuestra que el estudio de nucleación de burbujas en agua a presiones negativas con el modelo TIP4P/2005 es realizable de forma rigurosa. Existen muchos problemas en este estudio debidos a la naturaleza del agua. El agua líquida tiene una estructura abierta, basada en la del hielo Ih, la cual permite la existencia de cavidades naturales hasta en el agua termodinámicamente estable, que se pueden confundir con burbujas en el análisis de los primeros momentos del proceso de nucleación. Después de desarrollar nuevos métodos para el análisis riguroso de burbujas, y aplicar estos resultados a las técnicas de nucleación, observamos que existe concordancia entre nuestros valores y los propuestos por la CNT, como el radio de la burbuja crítica, aunque existen discrepancias tanto en la tasa de nucleación como en la al-

tura de la barrera de nucleación. Esto puede deberse a que la CNT utiliza el valor de una superficie plana, mientras que la burbuja de la fase vapor (termodinámicamente estable) que crece en el agua metaestable no tiene esa geometría.

Ahora pasaremos a especificar capítulo a capítulo las conclusiones concretas de cada uno de ellos:

1. La técnica usada en este capítulo ha sido la Dinámica Molecular, con la cual se ha simulado el comportamiento del modelo TIP4P/2005 a diferentes rangos de presión y temperatura. Las predicciones del modelo en el cálculo de la **TMD**, la temperatura del máximo de densidad, han sido muy satisfactorias. Además de reproducir el valor experimental a presión ambiente, el modelo predice la tendencia y dependencia de esta propiedad con la presión. Para la isóbara de 1 bar se ha extendido el estudio a bajas temperaturas, encontrando un mínimo alrededor de los 200 K.

   También se ha simulado la **compresibilidad isoterma** a dos presiones distintas,1 y 1000 bar. El TIP4P/20005 predice en las dos isobara la presencia de un mínimo y su localización en términos de temperatura son similares a los encontrados experimentalmente, 37 ^{o}C en el modelo y 46,5 ^{o}C en el experimento. También se evaluó este mismo mínimo para otros modelos rígidos de agua y los resultados se encontraban alejados de los experimentales.

   El modelo TIP4P/2005 predice el comportamiento anómalo del agua en condiciones extremas a excepción de la **capacidad calorífica a presión constante**, C_p. Esto se debe a que este propiedad está afectada por contribuciones cuánticas que hay que tener en cuenta a temperaturas bajas.

2. Los cálculs para una propiedad dinámica, **la viscosidad**, para los modelos de agua más utilizados muestran una superioridad del modelo TIP4P/2005 frente a otros potenciales. El valor de la viscosidad experimental en condiciones ambiente es de 0,896 mPa s, los modelos analizados predicen valores desde 0,321 mPa s a 0,729 mPa s y el TIP4P/2005 reproduce el valor más cercano al experimental, 0,855 mPa s.

   Se simuló esta propiedad en tres isotermas y en un rango de presiones concreto para encontrar el mínimo experimental. El modelo predice este mínimo en la misma localización del experimental y además se observa la misma dependencia del mínimo con la temperatura. Por todo ello se puede decir que el TIP4P/2005 es también capaz de reproducir el comportamiento anómalo de las propiedades dinámicas del agua.

3. Se presenta un **nuevo modelo flexible de agua**, TIP4P/2005f, basado en el modelo rígido y no polarizable, TIP4P/2005. Se calcularon una serie de propiedades estructurales, termodinámicas y dinámicas para el modelo flexible y se comparó con el modelo rígido y el experimento con un resultado satisfactorio.

   La temperatura de fusión del modelo mejora al incorporar los grados de libertad del modelo rígido, de 252 K a 254 K frente al valor experimental 273 K. Mientras que la constante dieléctrica se aleja ligeramente del dato experimental. La ventaja del desarrollo del modelo flexible, TIP4P/2005f, es que reproduce el resto de propiedades del agua con la misma robustez y fiabilidad que el TIP4P/2005, pero incorporando la flexibilidad molecular.

   Este hecho contradice con lo observado en otros modelos flexibles que se basan en un homólogo rígido. En el caso del modelo flexible SPC/Fw, la mejora frente al potencial rígido SPC/E, es considerable. Pero no se puede concluir que la flexibilidad molecular mejore los resultados en Simulación Molecular sino que mejora las predicciones de los modelos rígidos. Y estas mejoras por incorporar la flexibilidad no son apreciables si las predicciones del propio modelo rígido son excelentes.

   La utilización de modelos flexibles se hace imprescindible en estudios concretos, tales como estudios espectroscópicos o condiciones estrictas de simulación donde no se puedan utilizar los algoritmos de *constraints* de la moléculas.

4. La construcción del **escenario termodinámico del modelo TIP4P/2005** es fundamental para la explicación de las anomalías del agua. Por ello se han calculado una serie de propiedades termodinámicas en un amplio rango de temperaturas y presiones. La función respuesta que se ha simulado ha sido la compresibilidad isoterma, tanto a presiones positivas como a presiones negativas. El modelo TIP4P/2005 es capaz de predecir los máximos y los mínimos de esta propiedad a presiones positivas. Si seguimos la línea de máximos encontramos el punto crítico líquido-líquido del modelo a 193 K y 1350 bar. Si se simula el modelo bajo presiones negativas, también encuentra esos máximos y mínimos en la compresibilidad isoterma. Además, y también en presiones negativas, la buena predicción del comportamiento anómalo del agua se comprueba al extender el estudio de la línea que marca las temperaturas máxima de densidad dentro de una isobara dada, línea de TMD o LDM (*Line of Density Maxima*). El aspecto más importante de este estudio es que el modelo tiene un punto reentrante en la línea de TMD, lo cual implica

que la espinodal líquido-vapor no puede ser reentrante y aumentar la presión de la misma cuando disminuimos la temperatura como sugiere Speedy en su escenario termodinámico.

Con el punto reentrante de la LDM y la presencia del segundo punto crítico del agua se llega a la conclusión de que el escenario que reproduce el TIP4P/2005 es coincidente con el escenario propuesto por Poole *et al.* Por lo tanto las anomalías que presenta el agua en las funciones respuesta y en la densidad se deben a la presencia del punto crítico líquido-líquido. También es posible la compatibilidad de nuestros resultados con el cuarto escenario, propuesto por Sastry *et al.*

5. Los datos experimentales expuestos en este capítulo son la primera prueba de la existencia de un mínimo en la velocidad del sonido a presión negativa en dos isócoras. Estas isócoras presentan un mínimo en el valor de la velocidad del sonido que corresponde con el máximo de compresibilidad isoterma según su definición termodinámica. Se ha podido acceder a este mínimo sin que la muestra cristalice gracias a que en presiones negativas la línea de Widom tiene valores de temperatura mayores que la línea de nucleación homogénea.

   Este mismo comportamiento está avalado por los datos de simulación del modelo TIP4P/2005, el cual reproduce los mínimos de la velocidad del sonido en las mismas isócoras.

6. El algoritmo ajustado para la localización y análisis de **nucleación de burbujas en agua**, basado en los poliedros de Voronoi reproduce fielmente el volumen de las burbujas dentro del sistema. Se ha comprobado la capacidad del algoritmo con distintos sistemas. Primeramente se ha construido una burbuja de volumen perfectamente conocido y se ha obtenido ese valor por medio del análisis por los poliedros de Voronoi. Seguidamente se reproducen los mismo buenos resultados para un sistema metaestable de agua como para uno termodinámicamente inestable. Con el volumen de la burbuja más grande del sistema como parámetro de orden, se han calculado con la técnica *Mean First Passage Time* el tamaño de la burbuja crítica y la tasa de nucleación. Los dos parámetros se han comparado con los valores ofrecidos por la teoría clásica de nucleación.

   Además este algoritmo ofrece una alternativa a las estándares para distinguir entre moléculas líquidas y moléculas interfaciales (de tipo vapor). La utilización del parámetro de esfericidad α en combinación con el volumen de los poliedros de Voronoi asociado a cada partícula genera una herramienta muy útil para clasificar las moléculas.

7. Se presentan los resultados de dos métodos alternativos para identificar burbujas en agua. Los dos métodos se basan en un primer paso de construcción de una trama bajo el sistema. Posteriormente se clasifica cada una de las celdillas de la trama, entre celdillas líquidas y celdillas vapor. Cada método utiliza diferentes criterios para realizar esta clasificación pero, la predicción de los parámetros de nucleación es similar. Además si comparamos el estudio de nucleación espontánea con los resultados obtenidos por el método basado en los poliedros de Voronoi podemos concluir que los tres métodos son válidos para el estudio del proceso de nucleación de vapor a partir de agua a presión negativa. En este capítulo se presentan también resultados del estudio de la nucleación de eventos raros (no espontánea). Por dos técnicas diferentes, por un lado el *Hybrid Monte Carlo + Umbrella Sampling* y por otro una aproximación del *Hybrid Monte Carlo* acoplada con el *Umbrella Sampling*, se ha calculado la barrera de nucleación utilizando como parámetro de orden el volumen de la burbuja más grande pero en el primer caso de calculó ese volumen con el método propuesto en el grupo de Viena y en el segundo caso fue usado el método de nuestro grupo en Madrid. Los dos método son igualmente validos y útiles para estudiar y describir la nucleación de burbujas en agua.

8. Se presenta otro método alternativo a los presentados anteriormente para identificar burbujas en agua. En esta ocasión el método se basa en la localización de la cavidad más grande con un algoritmo más fácil de implementar en cualquier sistema, tanto estudiando nucleación homogénea como heterogénea. Este método además es muy útil en la transición líquido-vapor, ya que permite combinarse con la *Scaled Particle Theory*. Esta versatilidad salva el problema que nos encontramos en otros métodos cuando calculamos el primer tramo de la barrera de nucleación.

   Este método es válido tanto en líquidos moleculares (agua), como en líquidos simples (Lennard-Jones), como se demuestra en el apartado de resultados. La desventaja de este método es la suposición de una burbuja esférica y siempre vacía de moléculas vapor. La consecuencia de esta desventaja es una disminución del volumen respecto a la burbuja real, pero la sencillez de implementación y versatilidad en cualquier tipo de sistemas compensa estas desventajas.

9. Por ultimo, hemos estudiado un caso de nucleación heterogénea, preparando un sistema de agua TIP4P/2005 metastable (en las mismas condiciones termodinámicas consideradas anteriormente) en presencia

de un nanotubo de carbono. Hemos medido la tasa de nucleación y observado que, como previsible con la teoría clásica de nucleación, en condiciones heterogéneas la tasa es más alta (siendo la barrera más baja) que en condiciones homogéneas, o de agua de *bulk*.

También, nuestros resultados preliminares parecen sugerir que la burbuja que se desarrollará como crítica tiende a surgir en sitios del nanotubo caracterizados por una elasticidad mayor. De todas formas, es necesario trabajar en esta dirección.